2014

Functional and Structural Studies of the Human Voltage-Gated Proton Channel

James Anthony Letts

FUNCTIONAL AND STRUCTURAL STUDIES OF THE HUMAN VOLTAGE-GATED PROTON CHANNEL

A Thesis Presented to the Faculty of

The Rockefeller University

in Partial Fulfillment of the Requirements for

the degree of Doctor of Philosophy

by

James Anthony Letts

June 2014

FUNCTIONAL AND STRUCTURAL STUDIES OF THE HUMAN VOLTAGE-GATED PROTON CHANNEL

James Anthony Letts, Ph.D.

The Rockefeller University 2014

The activity of voltage-gated cation channels underlies the action potentials that allow for neuronal signaling and muscle contraction. The canonical family of voltage-gated K^+, Na^+ and Ca^{2+} channels has been the subject of extensive electrophysiological, biophysical, genetic, biochemical and structural characterization since the 1950s. These channels all share a conserved six-transmembrane helix topology (S1-S6) in which the first four transmembrane helices (S1-S4) form the regulatory voltage-sensor domain and the last two transmembrane helices (S5 and S6) comprise the ion-conducting pore domain. It was thought that all voltage-gated cation channels shared this conserved domain architecture. However, this scheme was challenged by the discovery of the gene for the voltage-gated H^+ channel. This voltage-gated cation channel has a four transmembrane helix topology that is homologous to the voltage-sensor domain of the canonical voltage-gated cation channels alone, without a separate pore domain.

In this thesis, I present my work, which constitutes the first ever biochemical characterization of the human voltage-gated H^+ channel (hH_V1). First, I demonstrate by site-specific cross-linking that hH_V1 is a dimer in the membrane and define the oligomerization interface. Then, by developing methods for the heterologous expression, purification and reconstitution of hH_V1, I establish that the four transmembrane helix

voltage-sensor-domain-like putative channel protein is in fact responsible for H^+ conduction. Next, I present my work on the structural characterization of hH_V1 by X-ray crystallography. I solved a low-resolution structure of a chimeric voltage-gated proton channel but then demonstrated that although this channel is functional in a membrane, the conformation seen in the crystal is non-native. Finally, I present my work on the analysis of hH_V1 by solution state NMR in detergent micelles. This technique allowed us to define the secondary structure of the channel for the first time but full three-dimensional structural characterization was determined to be unfeasible. From these studies, I conclude that the H_V channel structure is dependent on the constraints imposed by the lipid bilayer and is destabilized upon detergent solubilization. Future structural studies of H_V channels will have to focus on channels imbedded within a membrane-like environment.

To my parents, my brothers and my darling wife.

ACKNOWLEDGEMENTS

To do science is to be involved in humanity, to be completely dependent on the people who came before you as well as on your contemporaries. Because of the amazing caliber of science and people in Rod's lab there is no better place to get involved. I consider myself very lucky to have had the opportunity to learn from Rod and to work along side some of the best scientists alive today. Rod I have been truly inspired by your passion for great science and your ability to make it happen, thank you.

Throughout my time as a student I have worked closely with postdoctoral fellows in the lab. I would like to thank Seok-Yong and Joel with whom I worked side-by-side for many years. My thanks to Ernie, Matt, Liang, Steve, Xiao, Peng, Josefina and Daniel for all their help troubleshooting the many various techniques and methodologies I learned and developed during my tenure in Rod's lab. Everyone in the lab contributed to my work and wellbeing in some way and I greatly appreciate all of you.

Thanks to my collaborators Yuko Arita and Dev Sidhu for all your help and hard work.

I would like to thank Júlio Padovan in Brian Chait's lab for assitance with mass spectrometry, and Deena Oren of the Structural Biology Resource center for help with the robots and home source.

Thanks to David Gadsby, Seth Darst, Fred Cross and Tom DeCoursey for their time and attention as members of my thesis committee.

Most of all I would like to thank my beautiful wife María for helpful discussions and tireless editing.

TABLE OF CONTENTS

LIST OF TABLES

LIST OF FIGURES

CHAPTER 1: INTRODUCTION

In order to support the highly complex processes required for life, cells must be able to isolate desired components such as ions, small-molecule nutrients and biological macromolecules and precisely control their concentrations such that the chemistry of life, which derives from their interactions, can occur. This problem was solved in part by the evolution of the cellular membrane; an oily barrier composed of a bilayer of amphipathic phospholipids, which envelopes and defines the cell. Unlike the aqueous medium inside and surrounding cells, which allows for the free diffusion and interaction of biological molecules and ions, the membrane interior excludes water and hence creates an energetic barrier for passage of hydrophilic components. In this way, the membrane solves the problem of keeping the cells' contents from diffusing away, allowing for the chemistry of life to occur.

However, the existence of the membrane creates a new problem: it blocks the release of waste products from inside the cell and the uptake of nutrients from outside. The evolution of "membrane proteins" that express hydrophobic exteriors and therefore are able to insert and reside within the cellular membrane, allowed cells to fully exploit

the membrane's properties. Indeed, some membrane proteins have evolved to catalyze the specific conduction or transport of hydrophilic ions and molecules across the membrane, thus helping the cell gain precise control over its contents.

Another property of the cellular membrane that cells have evolved to utilize is its ability to separate electrical charge, i.e. its capacitance. Cells can store energy across the membrane by controlling the relative concentrations of ions inside and outside the cell. This energy manifests itself as an electrical potential across the membrane, which the cell can then use to do work. In most cells, this work is performed locally on a specific class of voltage-sensitive ion channels or enzymes, allowing for the fast transmission of signals along the cell membrane. Moreover, in certain organisms, specialized electrogenic organs have evolved that use biologically generated electric fields from an organized array of cells to detect the electric fields of other organisms, a process known as electroreception. In extreme cases, such as the electric knifefish (a.k.a. electric eel) and the electric rays, biological electricity is used in hunting to stun or even kill prey.

In this chapter, I will discuss how cells generate and control electrical potentials across the membrane using ion channels and transporters. I will introduce the canonical voltage-gated ion channels and how cells can use them to directly tie the membrane potential to membrane permeability. Then, I will introduce the biophysics of the voltage-gated proton channel and discuss its diverse physiological roles. Finally, I will discuss the motivation and aims for my research on the human voltage-gated proton channel.

1.1 Generation and Control of Cellular Electricity

1.1.1 Channeling Ions – the charge carriers of bioelectricity

The inorganic ions Na^+, K^+, Ca^{2+} and Cl^- are the major charge carriers used to generate electrical potentials across the membranes of cells (Hille 2001). The relative abundance of these ions on either side of the membrane is regulated by the activity of two classes of membrane proteins: ion channels and ion transporters (a.k.a. ion pumps).

Ion channels allow only for the passive diffusion of ions down their electrochemical gradient and are defined (and named) by two major properties: selectivity and gating. Selectivity refers to the fact that different channels show a preference for the conduction of specific ionic species. For example, a K^+ channel allows for the easy passage of K^+ ions across the membrane but not the easy passage of Na^+ ions. Gating refers to the ability of the channels to open and close, that is, to transition between conductive and non-conductive states. The stimulus that causes a channel to gate varies widely between channels. Some channels are gated by the binding of ligands (for example the ATP-gated K^+ channel, K_{ATP}), others are gated by the transmembrane potential (for example the voltage-gated K^+ channel, K_V), others, by the mechanical state of the membrane itself (e.g. tension) and others, by environmental cues such as temperature and light (Hille 2001). Many channels are gated to varying degrees by the combination of different stimuli, for example the Slo1 K^+ channel is gated both by transmembrane voltage and by binding of intracellular Ca^{2+} ions (Barrett *et al*. 1982).

Ion pumps use cellular energy (usually in the form of ATP) to pump ions against their concentration gradient (Albers 1967). For example, the Na^+ K^+ ATPase pumps three

Na^+ ions out of the cell while at the same time pumping two K^+ ions into the cell and hydrolyzing an ATP molecule to form ADP and inorganic phosphate (Post *et al*. 1972). Since the number of ions pumped in each direction is uneven and the charge on each ion is the same, this pumping cycle is electrogenic. Thus, the Na^+ K^+ ATPase separates charge across the membrane, thereby charging the membrane capacitor and contributing to the membrane potential (Albers 1967). In the next section, I will describe how the activity of ion channels and pumps working in concert can be used to control the electrical potential of the cell.

1.1.2 Electro-diffusion – how the membrane voltage is set

Ion pumps consume cellular energy to pump ions against their concentration gradients and thereby establish an uneven distribution of ions across the membrane (Albers 1967). For example, in mammalian skeletal muscle the distribution of ions is such that $[Na^+]$ is high outside relative to inside, $[K^+]$ is low outside relative to inside, $[Ca^{2+}]$ is high outside relative to inside and $[Cl^-]$ is high outside relative to inside (Table 1.1; Hille 2001).

Because each ion carries a charge, the free diffusion of the ions across the semi-permeable membrane does not depend solely on the concentration difference and does not go to equilibrium when the concentration of the specific ionic species reaches the same value on either side of the membrane (Nernst 1888; Nernst 1889; Hille 2001). For example, diffusion of a single K^+ ion down its concentration gradient removes a positive charge from the inside of the cell and adds a positive charge to the outside. Therefore, diffusion of ions across the membrane creates an electrical potential resulting in a force opposing the further diffusion of similarly charged ions. Equilibrium is reached when the

strength of the electrical potential results in balanced diffusion, such that there is no net flux of ions across the membrane. The electrical potential at which this balance is reached is known as the Nernst equilibrium potential (E_S) and is calculated for each ionic species (S) using the Nernst equation (equation 1.1), where R is the gas constant, T is the temperature, z_S is the charge on the ionic species, F is Faraday's constant, $[S]_o$ is the external concentration of the ion and $[S]_i$ is the internal concentration (Nernst 1888). The Nernst equilibrium potentials for each of the four major biologically important inorganic ionic species in muscle cells at 37°C are shown in Table 1.1 (Hille 2001).

$$E_S = \frac{RT}{z_S F} \ln \frac{[S]_o}{[S]_i} \qquad \{1.1\}$$

Table 1.1 Free ion concentrations and equilibrium potentials for mammalian skeletal muscle (adapted from Hille 2001)

Ion	Extracellular Concentration (mM)	Intracellular Concentration (mM)	$\frac{[S]_o}{[S]_i}$	Equilibrium Potential[a] (mV)
Na^+	145	12	12	+67
K^+	4	155	0.026	-98
Ca^{2+}	1.5	100 nM	15,000	+129
Cl^-	123	4.2[b]	29[b]	-90[b]
H^+ [c]	4×10^{-5}	1×10^{-3}	0.04	-86

[a]Calculated from equation 1.1 at 37°C

[b]Calculated assuming a -90 mV resting potential for the muscle membrane and that Cl- is at equilibrium at rest.

[c]Values from Carter *et al*. 1967

Because the cell membrane separates many different ionic species, the reversal potential (E_{rev}) at which there is no net ion flux across the membrane is not found at the Nernst equilibrium potential of a single ion, but at a weighted mean of all the Nernst potentials (Goldman 1943; Hodgkin & Katz 1949). The different Nernst potentials are weighted by the relative permeability of the different ions according to the Goldman-Hodgekin-Katz voltage equation, which if K^+, Na^+ and Cl^- are the permeant ions gives equation 1.2, where P_S is the permeability of the membrane to the specific ionic species ($S = K^+, Na^+, Cl^-$) and all other terms are defined as in equation 1.1 (Goldman 1943; Hodgkin & Katz 1949; Hille 2001).

$$E_{rev} = \frac{RT}{F} \ln \frac{P_{K^+}\left[K^+\right]_o + P_{Na^+}\left[Na^+\right]_o + P_{Cl^-}\left[Cl^-\right]_i}{P_{K^+}\left[K^+\right]_i + P_{Na^+}\left[Na^+\right]_i + P_{Cl^-}\left[Cl^-\right]_o} \qquad \{1.2\}$$

Equation 1.2 holds only in the simplified case in which there are no active electrogenic pumps in the cell and all of the permeant ions carry the same absolute value of charge (the equation takes an alternate form when divalent cations such as Ca^{2+} are taken into account; Hille 2001). Although P_S is defined as the rate of flux of ion S across the membrane (in units of cm/s), it is proportional (though non-linearly) to the conductance of ion S across the membrane (g_S, with units of Siemens [$kg^{-1} \cdot m^{-2} \cdot s^3 \cdot A^2$]), which is a function of the number of open ion channels that can conduct ion S and the driving force for the conduction of that ion (Hodgkin & Huxley 1952c; Hille 2001). If the membrane is only permeable to a single ionic species, equation 1.2 simplifies to the Nernst equilibrium potential for that ion (equation 1.1).

In the average resting cell, the presence of inward rectifying K^+ channels makes the membrane far more permeable to K^+ than to any other ionic species; therefore, E_{rev} is close to E_K (approximately -60 to -90 mV, see Table 1.1; Hille 2001). Through changes in the permeability of the membrane to the different ionic species (i.e. opening and closing of K^+ and Na^+ ion channels), the cell can control its E_{rev}, allowing it to set the membrane potential to any value between $E_K \approx$ -98 mV and $E_{Na} \approx$ +67 mV (Table 2; Goldman 1943; Hodgkin & Katz 1949; Hille 2001). Voltage-gated cation channels, whose open probability is a function of the membrane potential, directly tie the permeability of the membrane to K^+, Na^+ and Ca^{2+} to the membrane potential, which allows for the rapid propagation of electrical signals across the membrane known as action potentials (Hodgkin & Huxley 1952a).

1.2 Voltage-Gated Ion Channels and the Voltage Sensor Domain

1.2.1 Discovery and common features of voltage-gated cation channels

Hodgkin and Huxley first described voltage-gated cation currents in their classical studies on the action potentials of the giant squid axon in the 1950s (Hodgkin & Huxley 1952c; Hodgkin & Huxley 1952b; Hodgkin & Huxley 1952d; Hodgkin & Huxley 1952a). As their name suggests, the opening and closing (i.e. gating) of the voltage-gated cation channels is strongly dependent on the transmembrane potential. It wasn't until the 1980s that the first genes of a voltage-gated Na^+ (Na_V) channel and a voltage-gated K^+ (K_V) channel were identified and cloned (Noda *et al*. 1984; Tempel *et al*. 1987). These

sequences were then followed by the sequences of many more voltage-gated Na^+, K^+ and Ca^{2+} channels from many different species (for a review see Yu & Catterall 2004).

Analysis of these sequences identified a simple pattern: K_V channels were made up from a short polypeptide subunit, whereas, Na_V and Ca_V channels were made up of a longer polypeptide containing four "K_V-channel like" domains (Rehm & Tempel 1991; Guy & Durell 1994). Each one of the subunits or domains shared a conserved six-transmembrane-helix (6-TM) architecture (S1-S6) with a conserved series of positively charged arginine or lysine amino acid residues along the fourth transmembrane helix (S4), as well as conserved negatively charged residues on (S1 and S2; Fig 1.1; Rehm & Tempel 1991; Guy & Durell 1994; Yu & Catterall 2004; Bezanilla 2000). For the K_V channels, it was shown that the last two transmembrane helices (S5 and S6) comprise the pore of the channel (Fig. 1.1; Mackinnon & Miller 1989; Mackinnon *et al*. 1990; Mackinnon & Yellen 1990; Yellen *et al*. 1991). The discrepancy between the length of the K_V channel and Na_V/Ca_V channel genes was resolved when it was found that four identical K_V channel subunits come together in the membrane to form a four-fold symmetric tetramer (Mackinnon 1991). Based on sequence analysis, the first four transmembrane helices (S1-S4) were proposed to fold into a separate domain that was thought to be responsible for voltage sensing, and hence was coined the voltage-sensor domain (VSD; Fig. 1.1; Greenblatt *et al*. 1985; Nelson *et al*. 1999).

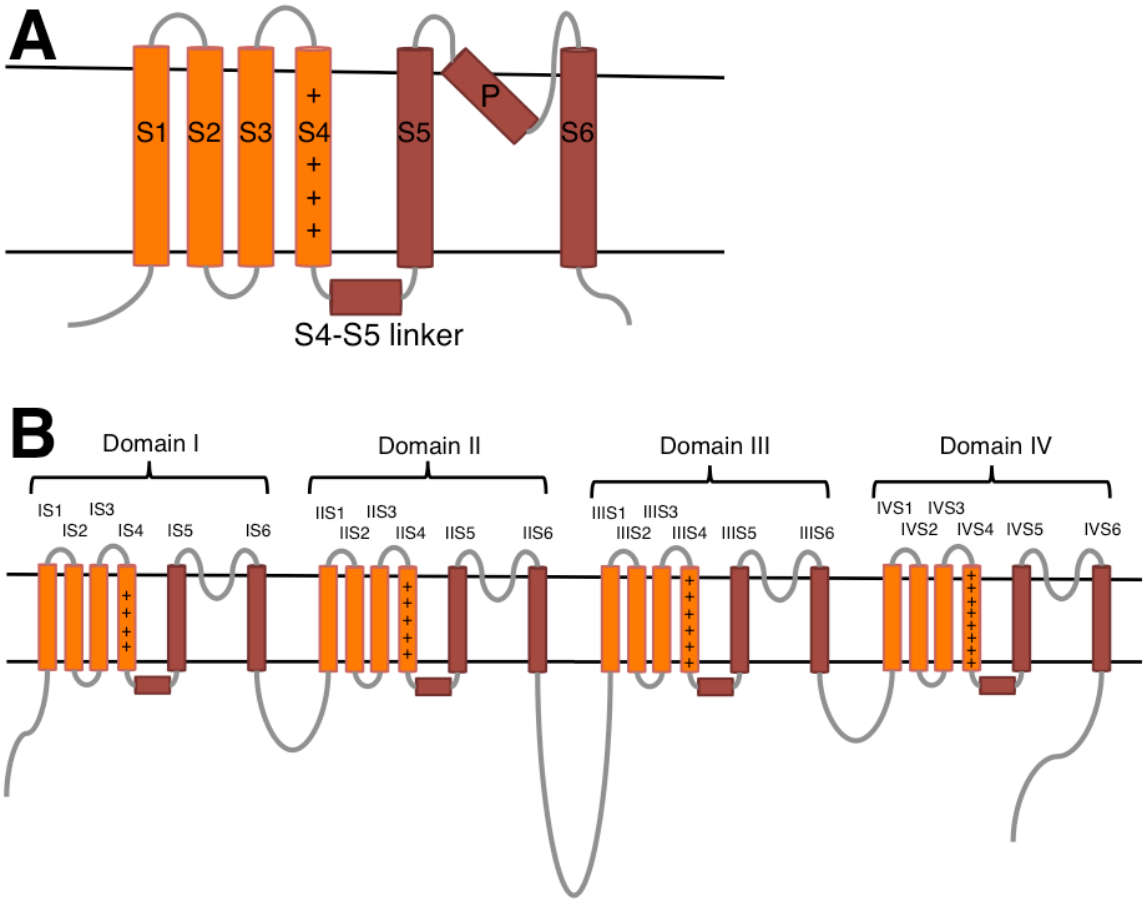

Fig. 1.1 Topology of voltage-gated channels

(**A**) Schematic representation of the six-transmembrane helix topology of K_V channels which become concatenated to form the topology of the Na_V or Ca_V channels (**B**). The helices that comprise the voltage-sensor domain (S1-S4) in each domain are shown in orange while the helices that comprise the pore (S5 and S6) are shown in brown. The conserved gating-charge residues on S4 are indicated by "+" signs. Horizontal black lines denote the membrane boundaries (cytoplasm side down).

One of the most well characterized families of voltage-gated cation channels is the voltage-gated K^+ channel family $K_V1.1$ (for a review see Fedida & Hesketh 2001). This channel is closed at hyperpolarized membrane potentials (negative inside relative to outside) and opens upon depolarization (Fig. 1.2). By measuring the instantaneous current-voltage relation from the tail currents and plotting the normalized current (I/I_{max}) as a function of transmembrane potential (V), it is possible to get an estimate of the open probability of the channel at the different values of V (Fig. 1.2; Hodgkin & Huxley 1952c; Hille 2001). This normalized current-voltage (IV) curve can be modeled by the two-state Boltzmann function shown in equation 1.3, where z is the effective gating charge on the channel (see below), V_{mid} is the voltage at which half the channels are open and F, R and T are defined as in equation 1.1.

$$\frac{I}{I_{max}} = \frac{1}{1 + \exp\left(-\frac{zF}{RT}\left(V - V_{mid}\right)\right)} \qquad \{1.3\}$$

As this equation shows, at V greater than V_{mid} the exponential term approaches zero and the ratio I/I_{max} goes to one, at V less than V_{mid} the exponential term approaches infinity and I/I_{max} goes to zero, at V equals V_{mid} the exponential term equals one and I/I_{max} equals 0.5.

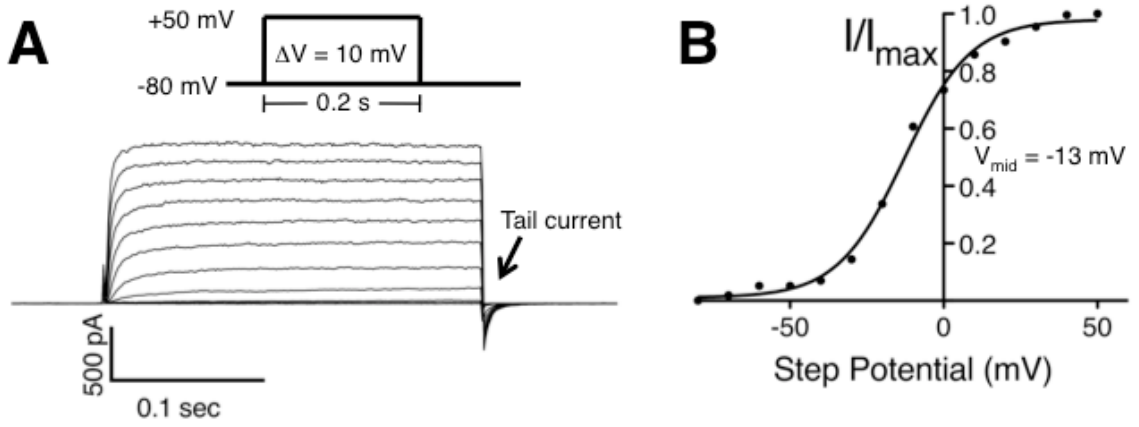

Fig. 1.2 K_V1.1 channel activity

(**A**) Whole-cell current elicited from CHO cells expressing rat K_V1.1 according to the voltage-step protocol depicted in the schmatic. (**B**) Current-Voltage plot (IV curve) of tail currents elicited by stepping back to the resting potential of (-80 mV) after each voltage step corrected for leak and fitted to the two-state Boltzmann (equation 1.3). Data provided by Josefina del Mármol.

In order to sense and undergo conformational changes in response to changes in the transmembrane voltage, the channels must contain "gating charges" within the membrane interior, which move in response to changes in the transmembrane potential, resulting in channel gating (Hodgkin & Huxley 1952a). Gating charges have been directly observed during the gating of voltage-gated channels (Armstrong & Bezanilla 1973; Taglialatela & Stefani 1993; Perozo *et al*. 1992; Perozo *et al*. 1993). As equation 1.3 shows, this gating charge (z) is a scalar multiplier of the voltage difference ($V-V_{mid}$). Therefore, the gating charge modifies the steepness at which changes in voltage near V_{mid} alter the I/I_{max} ratio: the larger the gating charge, the smaller the voltage difference ($V-V_{mid}$) is required to bring I/I_{max} to one or zero. These gating charges were measured to be 12 to 14 elementary charges per channel (3.0 to 3.5 per subunit) and identified to be the

conserved positively charged amino acid residues on the S4 helix with contributions from a conserved negatively charged residue on S2 (Seoh *et al*. 1996; Aggarwal & Mackinnon 1996).

Although these charges are required for the proper functioning of voltage-gated cation channels, due to the low electrical permittivity of the membrane interior, charges are unstable within its depths (Yaroshchuk 2000). How voltage-gated channels circumvent this energetic barrier and stabilize the gating-charge arginines in the membrane was not fully understood until the elucidation of the eukaryotic K_V channel structures (Long *et al*. 2005; Long *et al*. 2007).

1.2.2 Structure of the K_V channel – the VSD revealed

The first structures of the prokaryotic K_V channel K_VAP established the domain arrangement of the channel's fold (Jiang *et al*. 2003a). As was previously demonstrated, the K_V channel was seen to be a four-fold symmetric tetramer with the tetramerization interface completely comprised of the last two transmembrane helices (S5 and S6) (Mackinnon 1991; Jiang *et al*. 2003a). The S5 and S6 helices from each subunit come together to form a central pore, with the ion conduction pathway down the central four-fold symmetry axis (Fig. 1.3A) (Jiang *et al*. 2003a). This pore structure was nearly identical to the structures of the non-voltage-gated K^+ channels that had previously been solved (Doyle *et al*. 1998; Zhou *et al*. 2001; Jiang *et al*. 2002).

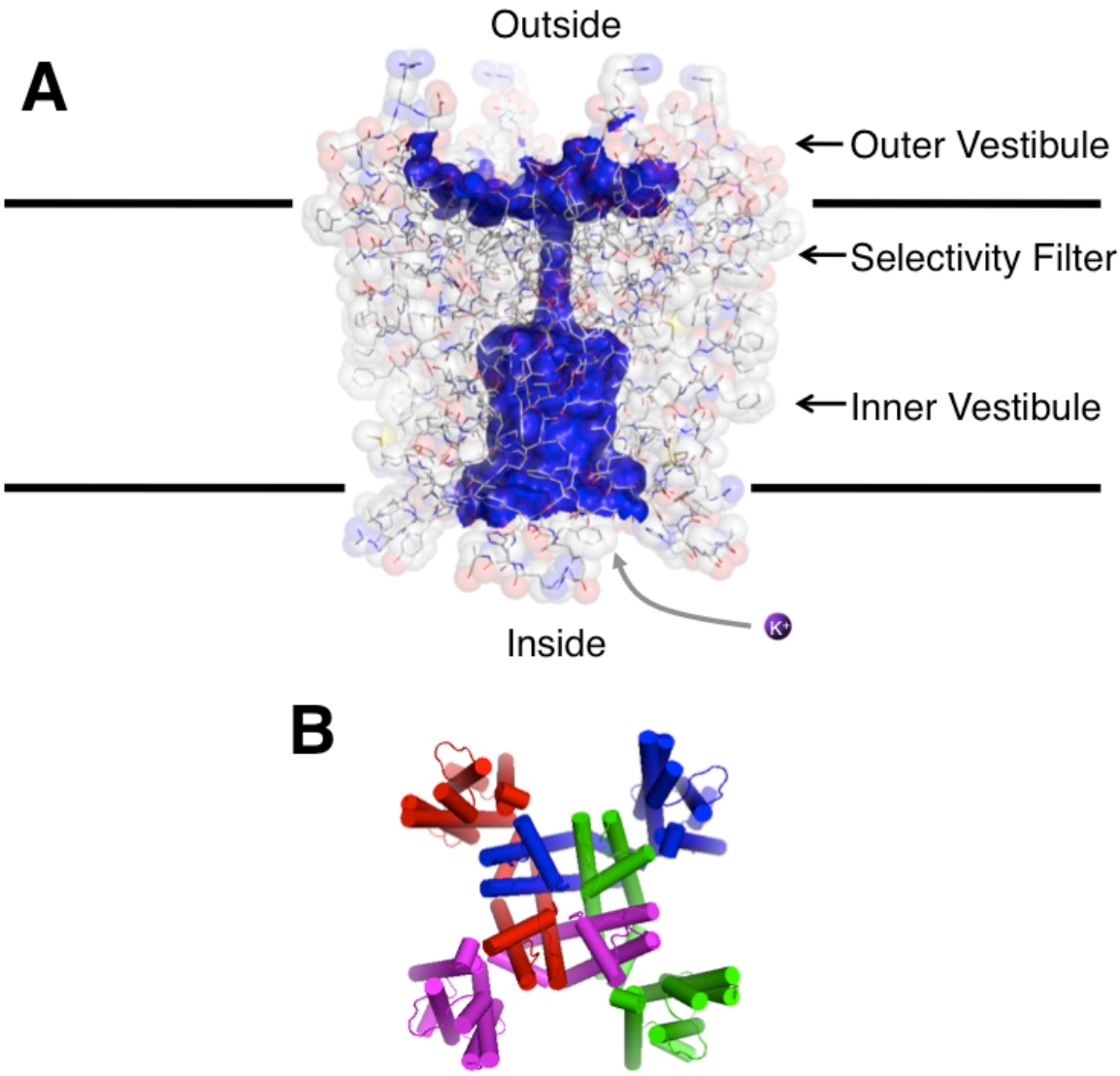

Fig. 1.3 K_V channel Structure

(A) The pore domain of the K_V1.2 channel shown in stick representation surrounded by translucent atom space filling spheres with carbon grey, nitrogen blue, oxygen red and sulfur yellow. VSDs have been removed for clarity (Long *et al*. 2007). The surface of the pore is shown in blue drawn with the program HOLLOW (Ho & Gruswitz 2008). (B) The K_V channel tetramer looking down from the extracellular medium showing the peripheral arrangement of VSDs around the central pore domain, each subunit is colored differently with each α-helix represented as a cylinder (Long *et al*. 2007).

The first four transmembrane helices (S1-S4) arrange themselves around the periphery of the pore and form the VSD, which is responsible for voltage dependent conformational changes (Fig. 1.3B) (Greenblatt *et al*. 1985; Caprini *et al*. 2001). Although it was demonstrated that the conformation of the VSD seen in the full-length K_VAP structure was in a non-native conformation (Jiang *et al*. 2003a; Lee *et al*. 2005; Long *et al*. 2005; Long *et al*. 2007), the structure did allow for the identification of the functionally important S3-S4 helix-turn-helix motif coined the "voltage-sensor paddle" (Jiang *et al*. 2003a). It has subsequently been shown that this motif is found in all VSD containing proteins and that it can be swapped between different VSDs and still result in functional voltage-gated channels (Alabi *et al*. 2007). Structures of the isolated VSD from K_VAP and, later, the structure of eukaryotic K_V channels revealed the native four-helix bundle fold of the VSD (Fig. 1.4; Jiang *et al*. 2003a; Long *et al*. 2005; Long *et al*. 2007). These structures allowed the first understanding of how the gating-charge arginines are stabilized within the membrane and were later followed by the structures of prokaryotic Na_V channels (Payandeh *et al*. 2011; Zhang *et al*. 2012; Payandeh *et al*. 2012).

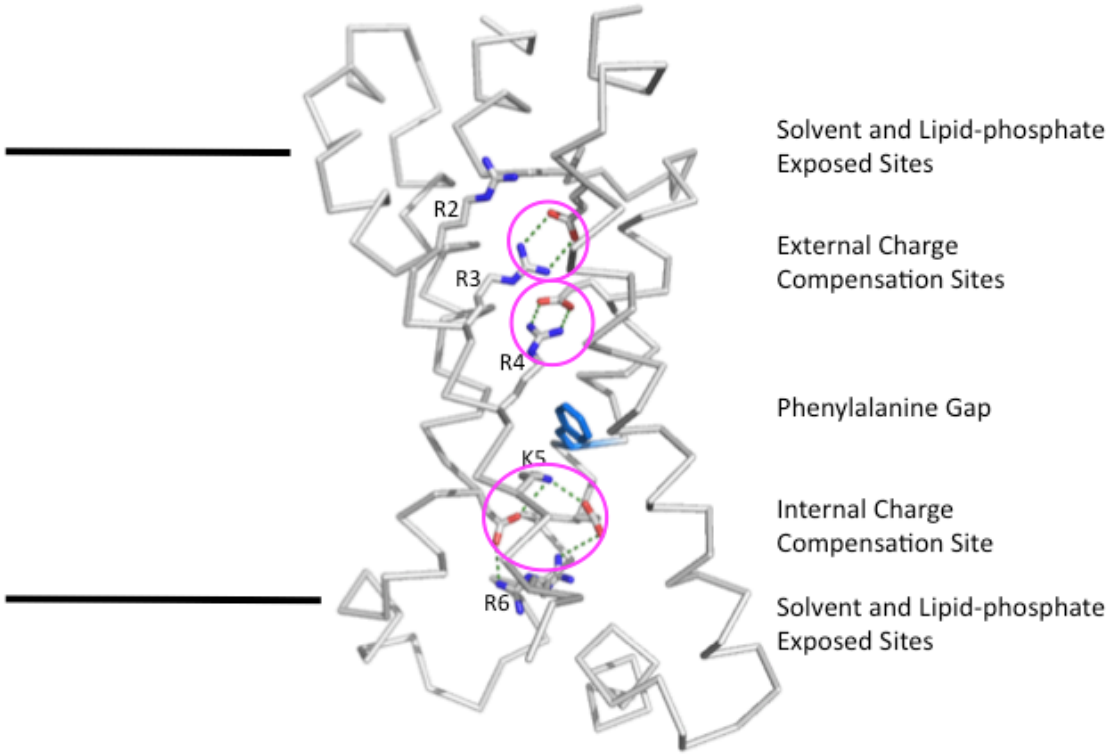

Fig. 1.4 The VSD structure from the K_V1.2-2.1 Paddle Chimera

Structure of the VSD is shown in ribbon representation with the side chains of charged amino acid residues within the transmembrane region shown as sticks with carbon grey, nitrogen blue and oxygen red (Long *et al*. 2007). The side chain of F233 is shown in blue. The S4 gating-charge residues are numbered according to the equivalent positions along the S4 of Shaker (Tempel *et al*. 1987). Horizontal black lines denote the approximate membrane boundaries (cytoplasm side down). The sites of charge compensation within the membrane are highlighted by pink circles.

Because of the large energy cost of burying a charge in the low permittivity medium of the membrane interior, membrane proteins have evolved to minimize the number of charged amino acid side chains within their transmembrane segments (Eisenberg *et al*. 1984). However, if —such as in the case of a VSD— the presence of a charged residue in the membrane is mechanistically required, then compensation for the charge must be provided by the protein structure. In many cases, this compensation is provided by the presence of oppositely charged residues protruding from other parts of the protein. Charge compensation of this type can readily be seen in the structures of VSDs. As shown in Fig. 1.4, all of the positively charged S4 gating charges that are buried within the hydrophobic membrane are paired with a conserved negatively charged residue from one of the other transmembrane helices (Glu183 on S1, Glu226 and Glu236 on S2 and Asp259 on S3a). This pairing stabilizes the charges in the membrane, hence stabilizing the structure of the VSD itself.

1.2.3 Mechanism of voltage sensing – the charge transfer center

The internal charge-compensation site occupied by K5 in Fig. 1.4 is known as the charge transfer center (Tao *et al*. 2010). This site differs from the external charge-compensation sites by the presence of two negatively charged side chains and the proximity to the "phenylalanine gap" (represented by the blue side chain of F233 in Fig. 1.4). This phenylalanine gap forms a hydrophobic barrier that separates the external and internal charge compensation clusters and is considered the most constrictive point within the VSD structure (Fig. 1.3; Tao *et al*. 2010; Starace & Bezanilla 2004).

The structure shown in Fig. 1.4 is the depolarized conformation of the Kv1.2-2.1 paddle chimera VSD (Long *et al*. 2007). It is thought that, during gating, the S4 gating charge residues that occupy each of the charge compensation sites changes. For example, in the hyperpolarized state immediately preceding the depolarized state, R2 would be in the external charge compensation site occupied by R3 in Fig. 1.4, R3 would be in the site occupied by R4 and R4 will be in the internal charge transfer center occupied by K5. This coordinated movement between the sites would allow for sustained charge compensation throughout the gating conformational changes of the VSD. In more hyperpolarized conformations, it is thought that R2 or even R1 would occupy the charge transfer center (Tao *et al*. 2010). This model of gating charge motion provides a structural and mechanistic understanding for the existence of multiple closed states of the VSD, the existence of which was first proposed by Cole and Moore in 1960 to explain the observed delay in channel activation after prolonged strong hyperpolarizations (Cole & Moore 1960). The clear mechanistic importance of the pattern of charged residues within the transmembrane region of the VSD is demonstrated by the conservation of this pattern of charges throughout evolution (Yu & Catterall 2004; Bezanilla 2000).

The H_V channel constitutes a unique member of the voltage-gated cation channel family. The remainder of this chapter will introduce the properties of this channel, its many important physiological roles and the scientific questions it poses.

1.3 VOLTAGE-GATED H^+ CHANNELS

1.3.1 Discovery of H_V channels

Voltage-gated H^+ channels were first proposed to exist by Fogel and Hastings in 1972 for their model of bioluminescence in the single cellular eukaryotic algae *Noctiluca miliaris* (Fogel & Hastings 1972). However, the first biophysical characterization of voltage-gated H^+ currents was not until ten years later when Thomas and Meech published their voltage-clamp studies on snail neurons (Thomas & Meech 1982). Thomas and Meech found that, upon depolarization, the membranes of these cells greatly increase their permeability to H^+, which led them to propose that "H^+ channels may be more widespread than hitherto suspected" (Thomas & Meech 1982). This proposal was confirmed by the subsequent discovery of H_V channels in many different cell types from a diverse set of organisms (Barish & Baud 1984; DeCoursey 1991; DeCoursey & Cherny 1993; Kapus *et al*. 1993; Demaurex *et al*. 1993; Taylor *et al*. 2011; Smith *et al*. 2011).

The Clapham and Okamura groups published the first genes for H_V channels in 2006. As explained in the previous section, the pattern of evolutionarily conserved charges within the VSD makes up a signature sequence. By using the sequences of known VSDs, Ramsey *et al*. and Sasaki *et al*. searched the human and mouse genomes with the aim of identifying any previously unknown VSD containing proteins (Ramsey *et al*. 2006; Sasaki *et al*. 2006). In 2006, both groups published the discovery of the previously unknown gene of the voltage-gated H^+ (H_V) channel (Ramsey *et al*. 2006; Sasaki *et al*. 2006).

1.3.2 Domain overview of H_V channels—not your canonical voltage-gated channel

The sequence of hH_V1 is shown in Fig.1.5A and is very different from all previously described voltage-gated cation channels in that it does not have a 6-TM topology (see Fig 1.1). H_V channels contain the first four transmembrane helices (S1-S4) of the VSD but lack the last two transmembrane helices that comprise the pore domain in the canonical 6TM channels (K_V, Na_V and Ca_V channels, Fig. 1.1). Nonetheless, when these genes are expressed in HEK cells, robust depolarization-dependent, Zn^{2+}-sensitive, H^+ currents can be measured (Ramsey *et al*. 2006; Sasaki *et al*. 2006).

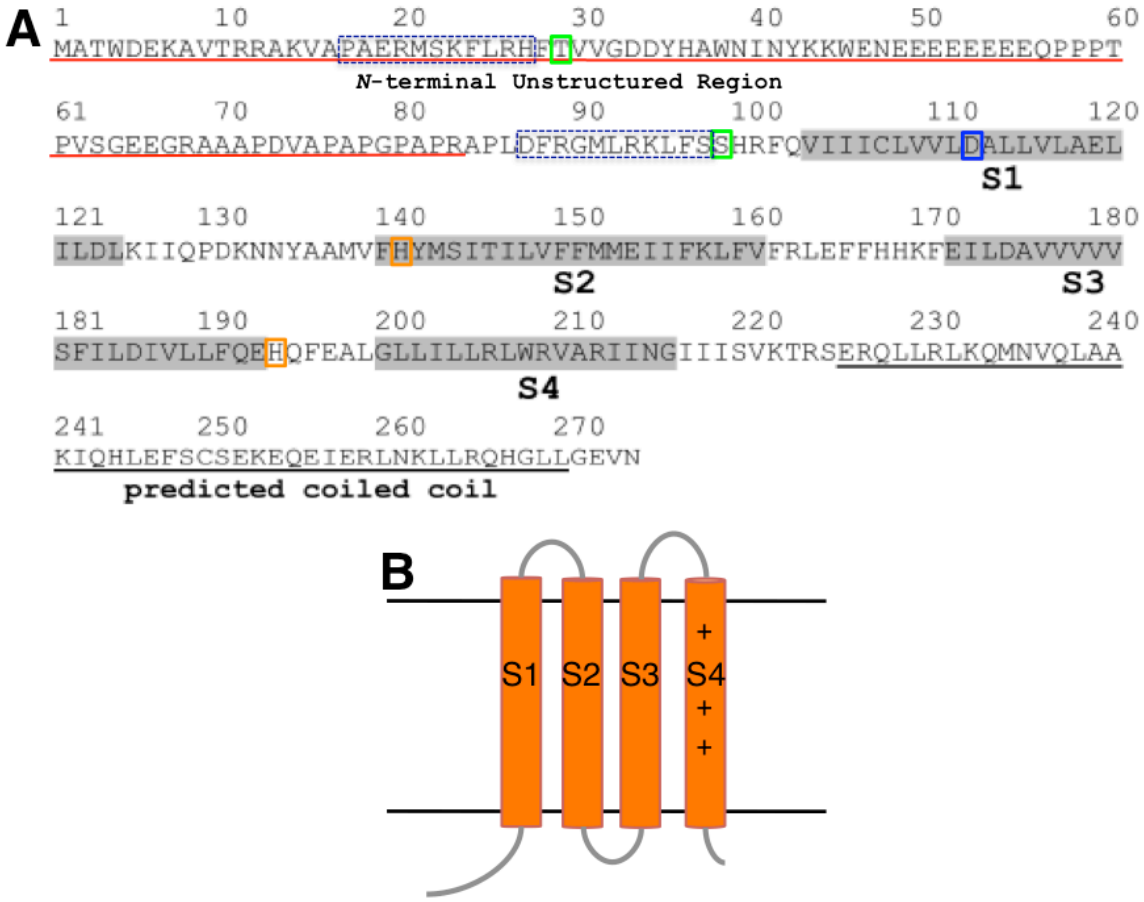

Fig. 1.5 Primary structure and transmembrane topology of hH_V1

(A) Amino acid sequence of hH_V1. The predicted unstructured N-terminus is underlined in red, the predicted transmembrane helices are highlighted in grey and labeled S1-S4, the predicted C-terminal coiled-coil (Lupas *et al*. 1991) is underlined in black, the putative short helices within the N-terminus are boxed by blue dashed lines, the two known phosphorylation sites are boxed in green (Musset *et al*. 2010a) and the two histidines that are known to bind Zn^{2+} are boxed in orange (Ramsey *et al*. 2006). Critical residue D112 in S1 is boxed in blue. (B) Transmembrane topology of the hH_V1 channel. Horizontal black lines denote the approximate membrane boundaries (cytoplasm side down). The S4 gating charge residues are represented as "+" signs.

Human H_V1 (hH_V1) is comprised of 273 amino acid residues with both the N- and C-termini residing in the cytoplasm (Fig. 1.5B). Secondary structure prediction identifies the four transmembrane helices of the VSD fold (highlighted in grey in Fig. 1.5A and labeled S1 through S4). Although it is very clear that these four transmembrane helices are present in the structure of the channel, the exact boundaries (i.e. the amino acid positions at which the helices start and terminate) are unknown. The first ~90 amino acid residues of hH_V1 are predicted to be mostly disordered (Fig. 1.5A). The high proportion of negatively charged glutamate (E) and aspartate (D) residues, as well as the many proline (P) residues in the N-terminus, suggest an unstructured random coil. However, secondary structure prediction algorithms indicate that two short helices may be present in the N-terminus: one spanning residues A18-H27 (distant from the transmembrane helices in primary sequence) and the other spanning residues D87-S97, directly preceding S1 (Cole *et al*. 2008). Short amphipathic helices preceding the S1 have been observed in the structures of other voltage-sensor domains (VSDs) and have been termed S0 (Long *et al*. 2007; Butterwick & Mackinnon 2010). Therefore, it is possible that hH_V1 also contains a S0 helix preceding S1. It is also interesting to note that a phosphorylation site that affects channel gating has been identified at T29, adjacent to the short predicted N-terminal helix. This suggests that this region of the protein may interact closely with the transmembrane domain (Musset *et al*. 2010a). The C-terminal end of human H_V1 is predicted to comprise one half of a coiled-coil structure; a number of structural and biochemical studies examining this isolated sequence demonstrate that it forms a homodimer coiled-coil structure (Li *et al*. 2010; Fujiwara *et al*. 2012; Fujiwara *et al*. 2013a).

1.3.3 Biophysical features of H_V channels

In addition to exhibiting near perfect selectivity for H^+ (DeCoursey 2003b), the voltage-gated H^+ currents measured in a variety of organisms share specific biophysical features, as described below.

ΔpH dependence of gating

Very early on, it was found that the gating of the depolarization activated H^+ current was not solely dependent on the transmembrane potential, but that it also strongly depended upon the pH difference across the membrane (ΔpH, defined as external pH [pH_o] minus internal pH [pH_i]; Byerly *et al*. 1984). An example of currents elicited from whole-cell patch clamp recordings of HEK cells expressing hH_V1 is shown in Fig. 1.6 at three different values of pH_o (Fig. 1.6A pH_o = 7.0, Fig. 1.6B pH_o = 6.5 and Fig. 1.6C pH_o = 6.0). It is clear from the current recordings that the different pH_o has an effect on the rate of channel opening and closing (Fig. 1.6A-C). By plotting an IV curve from the normalized tail currents, it becomes clear that the different pH_os also have a strong effect on the voltage dependence of the gating (Fig. 1.6D). Reducing pH_o (increasing the external concentration of H^+) results in a significant shift of the threshold voltage (V_{thr}, defined as the voltage at which you begin to see H^+ current) to more depolarized potentials (rightward shift on the IV plot; Fig. 1.6D). This ΔpH dependence is also seen upon changes of pH_i and results in the channels only ever opening at membrane potentials more positive than the Nernst equilibrium potential for H^+ (E_H; Fig. 1.6D; Cherny *et al*. 1995; DeCoursey 2003b).

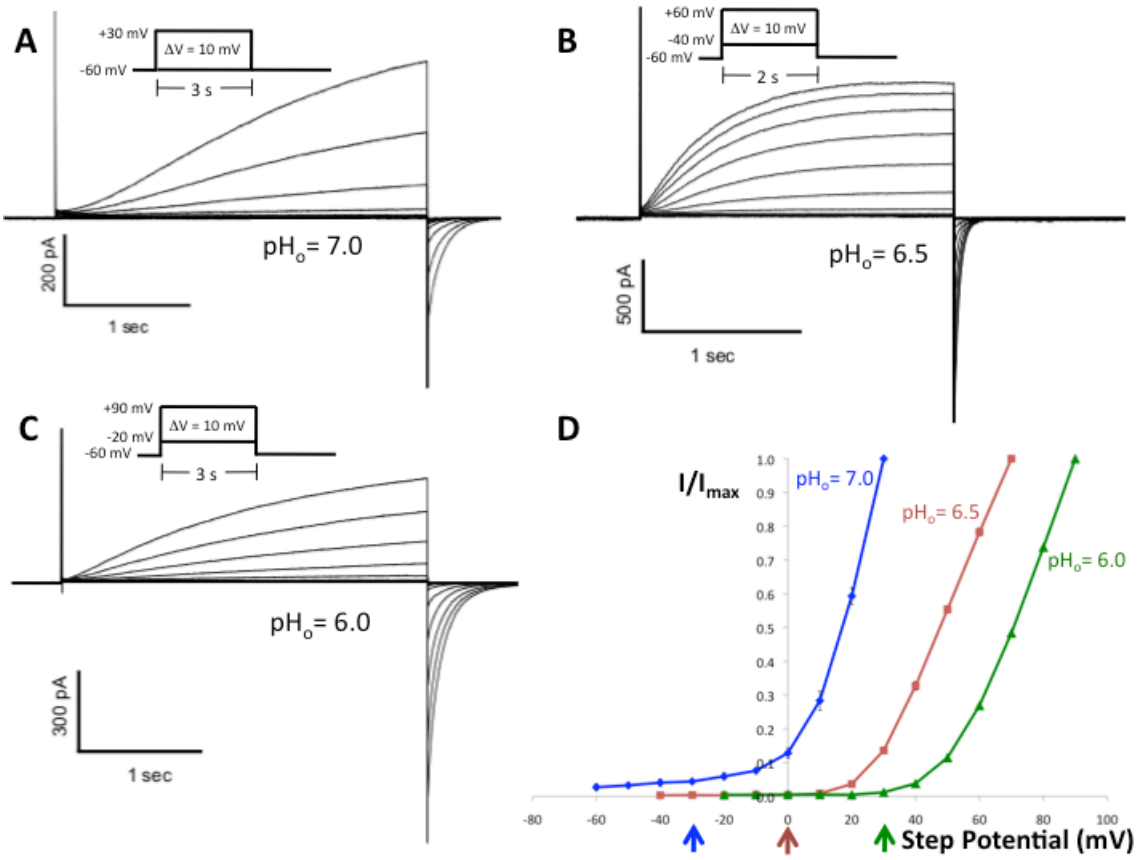

Fig. 1.6 Whole cell patch clamp recording of HEK cells expressing hH$_V$1 channels
Current recordings from the same HEK cell expressing hH$_V$1 channels at different pH$_o$ (A) pH$_o$ = 7.0, (B) pH$_o$ = 6.5 and (C) pH$_o$ = 6.0; pH$_i$ = 6.5 for each recording. Voltage step protocols are represented schematically above each recording. (D) Normalized IV curves plotted from tail-currents. The arrows at the bottom indicate the different values of E_H for each ΔpH shown (calculated by equation 1.1).

Through their dependence on ΔpH, these channels become outward rectifiers: they only ever open in resting mammalian cells such that the electrochemical potential for H^+ conduction is outward. In other words, H_V channels are acid extruders, only opening to allow H^+ to leave the cytoplasm. This property defines the many physiological roles played by the H_V channels (discussed in the next section). Although models have been proposed for how this gating behavior could be achieved (Cherny *et al*. 1995; DeCoursey 2003b), the mechanism remains unknown and the amino acid residues involved in pH sensing on both sides of the membrane remain to be identified.

Inhibition by Zn^{2+}

To varying degrees, all H_V channels thus far characterized are inhibited by polyvalent metal cations, with Zn^{2+} in general being the most potent inhibitor (Byerly *et al*. 1984; Mahaut-Smith 1989; DeCoursey 2003b). It is thought that the major mechanism of inhibition is through the direct binding of Zn^{2+} to an extracellular receptor site on the channel, which stabilizes the hyperpolarized (closed) conformation and thereby shifts the voltage-dependence of gating to more depolarized potentials (Cherny & DeCoursey 1999; DeCoursey 2003b). The binding of Zn^{2+} was found to be highly sensitive to pH_o and detailed competition studies indicated that H^+ and Zn^{2+} compete for binding to the same site composed of multiple groups (Cherny & DeCoursey 1999). Furthermore, since both external H^+ or Zn^{2+} binding stabilize the closed conformation, it was proposed that the groups responsible for Zn^{2+} binding may also be responsible in part for the ΔpH dependence of gating (Cherny & DeCoursey 1999).

After the discovery of the H_V gene, Ramsey *et al*. identified the Zn^{2+} binding site in hH_V1 (Ramsey *et al*. 2006). The binding site bridges two histidine residues, one at position 140 (near the extracellular end of S2) and the other at position 193 (within the voltage-sensor paddle motif; see Fig. 1.5A). When either or both of these two histidines are mutated to alanine, Zn^{2+} inhibition is alleviated (Ramsey *et al*. 2006). However, a systematic study of the role of these histidine residues on the ΔpH dependence of gating has yet to be published. It is also interesting to note that the H_V channel found in calcifying coccolithophores (see below) does not have histidine residues at these positions and yet remains inhibited by extracellular Zn^{2+} ions, indicating that an alternative receptor exists for Zn^{2+} in these channels (Taylor *et al*. 2011).

Conduction via protein mediated hydrogen-bonded chain

The conduction of H^+ both in water and through proteins is dissimilar to that of other ions in that it does not occur *via* simple diffusion but *via* the formation of transient covalent bonds (de Grotthuss 1806; Cukierman 2006; DeCoursey 2003b). Channel-mediated conduction of H^+ across the membrane has commonly been found to occur by two distinct mechanisms: as H_3O^+, *via* a continuous water wire as in the gramicidin channel (Cukierman 2000), or as H^+ *via* a hydrogen-bonded chain (the transfer of the H^+ to a titratable amino acid side chain in the channel which then passes it to water on the other side of the membrane) as in the influenza M2 channel (Pinto *et al*. 1992; DeCoursey 2003b).

Which mechanism do H_V channels utilize for H^+ conduction? By measuring the effect of buffer concentration, temperature and the deuterium (^2H) isotope on proton

conduction, DeCoursey and Cherny established that the rate of H^+ conduction through H_V channels is not diffusion-limited (DeCoursey & Cherny 1996; DeCoursey & Cherny 1998; DeCoursey & Cherny 1997). This indicates that there is a rate-limiting step for H^+ conduction as it permeates the channel. When comparing the temperature and deuterium isotope effects to other channels with established conduction mechanisms, such as the gramicidin and influenza M2 channels, the values found for hH_V1 are more consistent with a hydrogen-bonded chain mechanism, as opposed to a continuous water-wire mechanism (DeCoursey 2003b). This titratable residue was later identified in hH_V1 to be D112 on the S1 helix (Fig. 1.5A; Hille 2001; Musset *et al*. 2011). Mutation of this residue to valine results in a defective H^+ channel unable to conduct H^+; mutation to other amino acid residues results in Cl^- leakage through the channel (see Chapter 3 for a more complete discussion; Musset *et al*. 2011).

1.3.4 H_V channels diverse physiological roles

Although the first description of H_V channel currents was from snail neurons, the role that the channels play in neuronal physiology remains poorly understood. In humans, H_V channels are mainly found in cells of the immune system and in sperm cells (Barrett *et al*. 1982; DeCoursey 2010; Capasso *et al*. 2010; Lishko *et al*. 2010). In addition, a potentially significant role of H_V channel activity is being uncovered in cancer cells (Wang *et al*. 2012; Wang *et al*. 2013a). In this section I will briefly discuss a selection of the physiological roles that H_V channels play in humans, as well as some of the important roles they play in single-celled eukaryotes.

Phagocytes

H_V channels have been best characterized physiologically for the role they play in stabilizing the activity of the NADPH oxidase during oxidative bursts in phagocytes' phagosomes (DeCoursey 2010). Upon encountering a bacterium, a phagocyte engulfs it into a specialized vacuole known as the phagosome. Through the activity of the NADPH oxidase (which transfers electrons from NADPH to molecular oxygen, generating $NADP^+$ and H^+ in the cytoplasm and the superoxide ion [O_2^-] in the phagosome), the macrophage attacks the bacterium with reactive oxygen species (ROS; DeCoursey 2010). In this way, the activity of the NADPH oxidase results in the depolarization of the phagosome membrane (inside negative with respect to the cytoplasm) and the acidification of the cytoplasm. Because of the voltage-dependence of NADPH oxidase activity, this activity would be self-inhibitory in the absence of any compensatory mechanism (DeCoursey *et al*. 2003). H_V channels in the phagosome membrane provide the required compensatory mechanism: they open in response to the NADPH-oxidase-induced membrane depolarization and conduct H^+ into the phagosome, simultaneously repolarizing the membrane and deacidifying the cytoplasm (DeCoursey *et al*. 2003; DeCoursey 2003a).

Human sperm cells

The H_V channel is integral for regulation of the internal pH of the sperm cell (Lishko *et al*. 2010; Lishko & Kirichok 2010). The pH of the sperm cytoplasm is a major regulator of sperm cell motility, capacitation, hyperactivation and the acrosome reaction, all essential processes for the fertilization of the egg (Lishko *et al*. 2012). For example, the

capacitation process (by which sperm cells go from a quiescent state to an actively swimming state) was known to involve the extrusion of protons out of the sperm cytoplasm (Giroux-Widemann & Jouannet 1991; Hamamah & Gatti 1998). In 2010, Lishko *et al*. showed this proton efflux in human sperm cells is facilitated by H_V channels (Lishko *et al*. 2010).

Upon the identification of role played by H_V chanels in sperm cell physiology, a potential mechanism for the role of Zn^{2+} in sperm cell activation was proposed (Lishko *et al*. 2010). Since the very early characterization of H_V current, it was shown that Zn^{2+} is a potent inhibitor of the channel (see above; Mahaut-Smith 1989). It is telling that the highest concentration of Zn^{2+} in the human body is found in the seminal fluid (Saaranen *et al*. 1987; Lishko *et al*. 2012). Through inhibition of H_V channels, a high concentration of Zn^{2+} would prevent premature sperm capacitation; conversely, removal of Zn^{2+} would promote proton efflux from the sperm cytoplasm. It has been demonstrated in rats that, upon entering the female reproductive tract, the Zn^{2+} from the seminal fluid is rapidly diluted (Gunn & Gould 1958). There is also evidence that the lipid-derived hormone anandamide present in the human reproductive system (Schuel & Burkman 2005) may have a direct activating influence on H_V channels (Lishko *et al*. 2010).

Cancer

The metabolism of cancer cells is markedly different than that of normal cells (for a review see Griffin & Shockcor 2004). Cancerous cells require a large amount of energy to fuel their expansive growth. Therefore, many cancers are characterized by increased levels of metabolism, specifically increased activity of the glycolytic pathway (Gatenby

& Gillies 2007). Furthermore, because of the high cell density of tumors, cancer cells tend to be hypoxic (Knowles & Harris 2001). Therefore, due to their high metabolism and their hypoxic environment, cancer cells start to accumulate high levels of H^+ (a byproduct of anaerobic glycolysis) in their cytoplasm (Gatenby & Gillies 2007). Without a mechanism for extruding protons out of the cytoplasm, these cells would not be able to continue proliferating or to metastasize.

The discovery of the expression of hH_V1 in highly metastatic breast and colorectal cancer cells, both from human cancer biopsies and established cancer cell lines, has led to the hypothesis that these channels are responsible for the regulation of cytoplasmic pH that allows the high proliferation of these cells (Wang *et al*. 2011; Wang *et al*. 2012; Wang *et al*. 2013a). Additionally, it has been demonstrated that H_V channels are overexpressed in the highly metastatic glioma cell SHG-44 and that inhibition of H_V channel activity by Zn^{2+} when these tumors are implanted into nude mice results in significantly smaller tumor size (Wang *et al*. 2013b). These findings indicate that H_V channels might be effective targets for anticancer drugs.

Calcification in Coccolithophores

Coccolithophores comprise a large group of phytoplankton that is found in all oceans around the globe (Winter & Siesser 1994). These unicellular algae generate elaborate calcium carbonate scales (coccoliths) of unknown physiological function (Marsh 1999). Nonetheless, because of the tendency of coccolithophores to grow into immense blooms, they are the most numerous calcifying organisms in the ocean. Coccolithophores significantly impact marine biogeochemical cycling and atmospheric chemistry by

incorporating inorganic carbon into their coccoliths and carrying it to the bottom of the ocean when they die (Rost & Riebesell 2004).

The process of coccolith formation occurs within an intracellular compartment and involves the combination of Ca^{2+} and bicarbonate (HCO_3^-) to produce calcite ($CaCO_3$), releasing one mole of H^+ for every mole of $CaCO_3$ produced (Marsh 1999; Brownlee & Taylor 2004; Paasche 2001). Without a mechanism for H^+ removal from the cytoplasm, it is predicted that coccolith production would acidify the cell at a rate of ~0.3 pH min^{-1} (Taylor *et al*. 2011). The mechanism of H^+ dumping from the coccolithophores was not understood until the discovery that these cells express H_V channels (Taylor *et al*. 2011). The activity of these H_V channels allows for the maintenance of calcification by regulating cytoplasmic pH homeostasis, thereby influencing the composition of the atmosphere on a global scale.

Bioluminescence in dinoflagellates

In 1972, Fogel and Hastings first proposed the existence of voltage-gated proton channels as a component of their theoretical model describing the process of bioluminescence in dinoflagellates (Fogel & Hastings 1972). It was not until 2011 that the existence of H_V channels in dinoflagellates was experimentally confirmed (Smith *et al*. 2011). The H_V channels found in these single cellular algae are unique in that they activate at membrane potentials negative to the Nernst equilibrium potential for H^+, thus allowing for inward H^+ current (Smith *et al*. 2011). This feature is necessary for this H_V channel to fulfill its proposed role in the triggering of bioluminescence by rapid H^+ influx into the specialized small organelles known as scintillons (Fogel & Hastings 1972). Additionally, this

distinctive gating behavior allows these H_V channels to participate in the production of action potentials that carry the H^+ signals along the algal membranes to the scintillon organelles (Smith *et al*. 2011).

1.4 Motivation and Aims of Thesis Research

1.4.1 Many fundamental questions to tackle

Hv's significant deviations from the canonical voltage-gated domain structure, namely, its lack of separate voltage-sensing and pore domains, raised a number of fundamental questions as to its mechanism of gating, conduction and regulation. How does the channel conduct H^+ without a pore domain? Is the gene identified actually the H^+ channel, or does the protein associate with some unknown factor in the HEK cell membrane to mediate H^+ conduction? Given that the pore helices create the multimerization interface in the K_V channels, what is the multimeric state of the H_V channel?

I joined the MacKinnon laboratory in 2008, less than two years after the first discovery of the H_V genes by Ramsey and Sasaki (Ramsey *et al*. 2006; Sasaki *et al*. 2006). At the time, all that was known about the H_V channel protein was its sequence and the histidine residues that were responsible for Zn^{2+} binding (Ramsey *et al*. 2006); many of the biophysical and physiological studies mentioned in the previous sections had yet to be performed. In this thesis, I describe my efforts on the investigation of the molecular mechanisms of H_V channel gating and conduction through attempts at functional and structural characterization.

In Chapter 2, I describe my work on the multimeric state of the hH_V1 channel in membranes. Together with the postdoctoral fellow Dr Seok-Young Lee, I demonstrated that H_V channels form dimers in the membrane and we identified the dimerization interface to be along the S1 helix in the membrane and along the coiled-coil in the cytoplasm (Lee *et al*. 2008).

In Chapter 3, I describe our approach of studying the purified H_V channels in detergent and reconstituted into vesicles. Whereas all other research on H_V channels has been performed in cells, we decided to biochemically characterize the purified channel, taking advantage of the expertise in membrane protein expression and purification in the MacKinnon laboratory. By studying the purified protein reconstituted in lipid vesicles, we demonstrated for the first time that the hH_V1 gene alone is able to conduct H^+ (Lee *et al*. 2009b). Furthermore, to identify amino acid residues that play an important role in H^+ conduction, we purified and reconstituted mutated hH_V1 channels and subjected them to functional analysis. We identified D112 as a candidate residue involved in H^+ conduction and showed that the mutation of an equivalent position to aspartate in the isolated VSD of the prokaryotic K_V channel K_VAP increases the rate at which this protein conducts H^+.

In Chapters 4 and 5, I describe my efforts towards the structural characterization of H_V channels. Determining the atomic resolution structure of a protein and using it to generate experimentally testable hypotheses is one of the most powerful ways to produce mechanistic understanding. Needless to say, this would be particularly useful for many of the poorly understood H_V-channel biophysical properties. Encouraged by our development of expression and purification methods for hH_V1 as well as by our colleague's determination of the K_VAP isolated VSD structure (Jiang *et al*. 2003a), we

decided to pursue the structure of hH_V1 by x-ray crystallography. Our efforts to this end are discussed in detail in Chapter 4.

In addition to the crystallographic approach, together with postdoctoral fellow Dr Joel Butterwick, I also examined H_V channels in detergent by solution state NMR. Because of its sensitivity to the protonation state of amino acid residue side chains, NMR constitutes an ideal methodology for probing the conduction mechanism of H_V channels. Additionally, NMR can be used to calculate protein structures and since Dr Butterwick had solved the structure of K_VAP isolated VSD by this method (Butterwick & Mackinnon 2010), we thought this would be a complementary approach to solving the hH_V1 structure. Our efforts on the NMR of H_V channels are discussed in detail in Chapter 5.

Although the attempts at complete structural characterization of H_V both by crystallography and NMR have thus far been unsuccessful, we were able to define the secondary structure of the channel for the first time and determine that the channel requires a lipid bilayer for the stabilization of its three-dimensional fold. Ongoing and future research into H_V channel structure must focus on membrane like environments. For crystallography this includes detergent-lipid mixtures, bicelles and lipidic cubic phase crystallography. For NMR solution state studies can be performed on the channel in lipid nanodisks or solid state NMR can be attempted on pellets of reconstituted channels.

Significant progress has been achieved in the last 7 years since the H_V genes were identified. However, many fundamental questions still remain. Complete mechanistic understanding of H_V conductance and gating will ultimately require the atomic description of the protein in multiple states. As such, structural characterization of H_V remains a pressing goal for the voltage-gated ion-channel field. Understanding of this

unique voltage-gated channel will contribute to our understanding of the diverse mechanisms that have evolved which allow voltage-gated cation channels to fulfill their diverse and important physiological roles.

CHAPTER 2: H_V IS A DIMER IN THE MEMBRANE

Voltage-gated six-transmembrane (6-TM) cation channels (Na^+, K^+, and Ca^{2+}) contain voltage-sensor and pore domains (Hille 2001). In the case of voltage-gated K^+ (K_V) channels, four 6-TM subunits come together in the membrane to form a four-fold symmetric tetramer (Mackinnon 1991; Long *et al*. 2007). The last two transmembrane helices (S5 and S6) from each subunit come together to form the pore domain, with the ion conduction pathway through the central four-fold access of symmetry (Yellen *et al*. 1991; Doyle *et al*. 1998). The first four transmembrane helices (S1-S4) form the voltage-sensor domain (VSD); the four VSDs of the tetramer arrange themselves around the periphery of the pore (see Fig. 1.3B on page 15; Long *et al*. 2007). The multimeric interface of the K_V channel is completely composed of the pore domain (S5 and S6) without any contribution from the VSDs (Long *et al*. 2007).

Until the cloning of voltage-gated proton (H_V) channels, it was thought that all voltage-gated cation channels had a 6-TM architecture, containing distinct VSDs and pore domain (Yu & Catterall 2004). However, the work of Ramsey *et al*. and Sasaki *et al*. revealed that the voltage-sensor domain can also exist independently, as the cloned sequences showed that H_V channels contain only a voltage-sensor domain in the

membrane without a separate pore domain (Ramsey *et al*. 2006; Sasaki *et al*. 2006). Because the pore domain of other voltage-gated cation channels is instrumental in generating higher-order structure in the membrane (e.g. the tetramerization of the K_V channels), the oligomeric state of the H_V channel was unknown. This fundamental property of the channel can have significant repercussions for our mechanistic understanding of the channel's gating and conduction. It has been shown that in order for VSDs to function properly in K_V channels two interfaces are necessary between the VSD and the pore (Lee *et al*. 2009a). Do H_V channels require support from other protomers in the membrane in order to properly function? The conduction pathway for other voltage-gated cation channels is found at an assembly interface (Yellen *et al*. 1991; Long *et al*. 2007). Where is the conduction pathway of H_V channels? Does it form at an oligomeric interface or do H^+ conduct through the VSD itself?

In this chapter I will discuss my work carried out together with Dr Seok-Yong Lee, which addressed these questions through evaluation of the subunit stoichiometry of the human H_V1 (hH_V1) channel. By site-specific cross-linking in cell membranes we were able to demonstrate that hH_V1 is a dimer in the membrane and we were able to define the dimeric interface (Lee *et al*. 2008).

2.1 HUMAN H_V1 IS A DIMER IN THE MEMBRANE

2.1.1 Non-specific cross-linking in HEK cells

To probe the oligomeric state of hH_V1, cell membranes isolated from HEK cells transfected with hH_V1 cDNAs were subjected to the amino-group specific bifunctional cross-linker disuccinimidyl suberate (DSS) and visualized by western blot analysis using antibodies directed against the hH_V1 channel coiled-coil. Amino-group specific cross-linkers have been successful in defining the oligomeric status of several membrane proteins (Albright *et al*. 2007; Aller *et al*. 2004). Recombinant H_V1 makes functional channels in HEK cells (Ramsey *et al*. 2006; Sasaki *et al*. 2006; Musset *et al*. 2008). hH_V1 migrated at approximately 35 kDa in SDS-PAGE under reducing conditions, which is consistent with the molecular weight of a monomer (32 kDa; Fig. 2.1A). As the concentration of the cross-linker (DSS) was increased, a band migrating near 73 kDa appeared with a concomitant decrease in the monomer band. Further increase of cross-linker concentration yielded a series of weak bands corresponding to higher oligomers in addition to the strong dimer band. These were probably due to non-specific cross-linking with other membrane proteins or cross-linking between the hH_V1 dimers. However, the appearance of strong dimer bands at low concentrations of DSS suggested that hH_V1 forms a homo-dimer in the membrane. Dimerization in hH_V1 is not a consequence of disulfide bond formation because mutants lacking cysteines showed the same DSS-mediated cross-linking pattern as wild type (Fig. 2.1B).

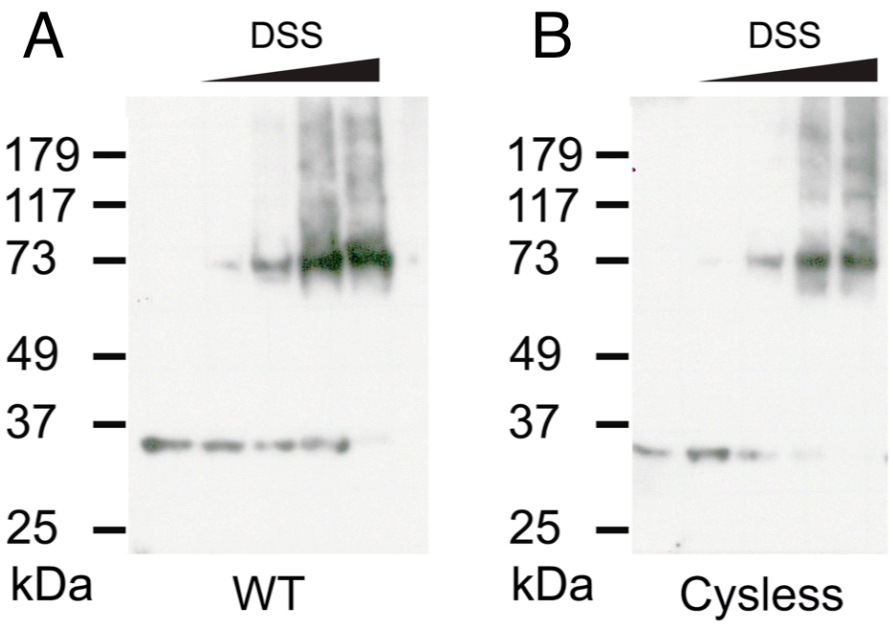

Fig. 2.1 hH_V1 is a dimer

Western blots of membranes from tsA201 cells transfected with (**A**) wild type and (**B**) cysless hH_V1 cDNAs and exposed to increasing concentrations of the amino-group specific cross-linker DSS (from left to right: No DSS, 25 μM, 75 μM, 250 μM, 2.5 mM). Membrane samples were run on SDS-PAGE under reducing conditions as per methods. All the gels that were used are 12 %. Molecular weight markers are shown on the left side of each blot.

2.2 Probing the Dimeric Interface

2.2.1 Design of site-specific cross-links

The finding of a dimeric subunit stoichiometry for hH_V1 leads to the question of how two voltage sensors arrange relative to each other in the membrane. If the hH_V1 homo-dimer contains a two-fold rotation axis normal to the membrane, a single cysteine mutation close to the dyad axis should form a cross-linked dimer under oxidizing conditions, or in the presence of a bifunctional cross-linker. By sequence analysis, hH_V1 can be dissected

into three subdomains: an N-terminal acid- and proline-rich region, a transmembrane voltage-sensor domain, and a C-terminal coiled coil domain (see Fig. 1.5 on page 22 and Fig. 2.2). Using the voltage sensor of the $K_V1.2$-$K_V2.1$ paddle chimera structure as a reference (Long *et al*. 2007), we examined both the two naturally existing cysteine residues and a series of substituted cysteines on a natural-cysteine-free background (Fig. 2.2). Positions that were mutated to cysteine included: R100 (preceding S1), C107 and L120 (S1), I127 and N132 (S1-S2 loop), T145 and I155 (S2), E164 (S2-S3 turn), L173 and V187 (S3), Q194 (S3-S4 turn), L203 and I212 (S4), T222 (after S4), and C249 (putative coiled coil; Fig. 2.2). Limited proteolysis and preliminary biochemical data suggested that the N-terminal region is largely unstructured and does not affect the oligomeric state of the protein. Therefore, although the full-length hH_V1 was used, the N-terminal region was not investigated in this cross-linking study.

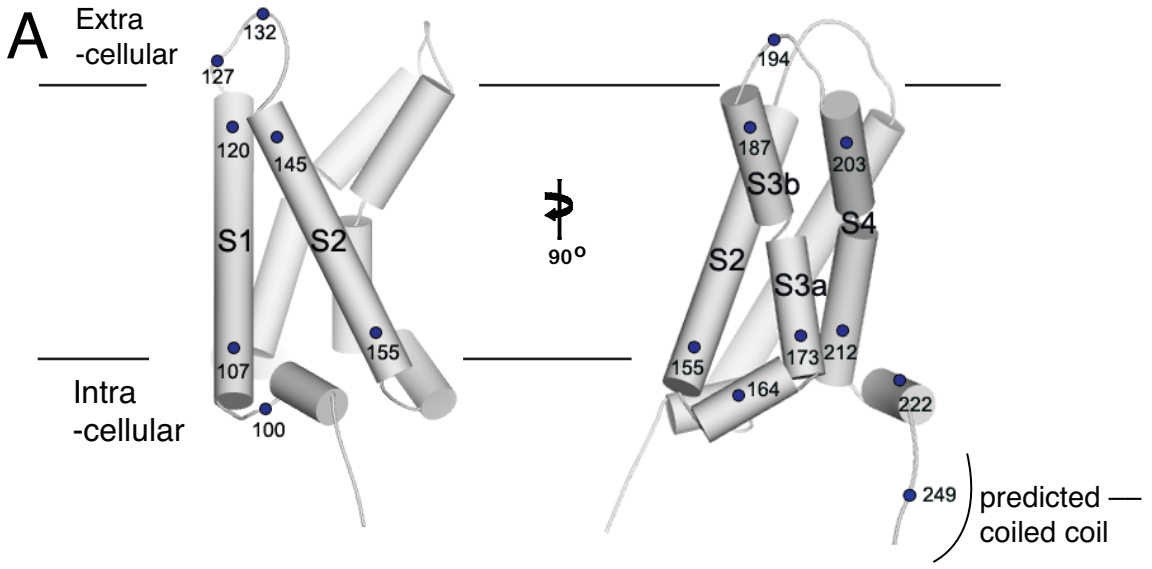

B

```
1          10         20         30         40         50         60
MATWDEKAVTRRAKVAPAERMSKFLRHFTVVGDDYHAWNINYKKWENEEEEEEEEQPPPT

61         70         80         90         100        110        120
PVSGEEGRAAAPDVAPAPGPAPRAPLDFRGMLRKLFSSHRFQVIIICLVVLDALLVLAEL
                                                          S1
121      130        140        150        160        170        180
ILDLKIIQPDKNNYAAMVFHYMSITILVFFMMEIIFKLFVFRLEFFHHKFEILDAVVVVV
                                  S2                          S3
181      190        200        210        220        230        240
SFILDIVLLFQEHQFEALGLLILLRLWRVARIINGIIISVKTRSERQLLRLKQMNVQLAA
                                  S4
241      250        260        270
KIQHLEFSCSEKEQEIERLNKLLRQHGLLGEVN
```

predicted coiled coil

Fig. 2.2 Introduction of cysteine mutations into hH_V1

(**A**) The positions that were mutated to cysteine are indicated by filled circles on the voltage-sensor structure of the $K_V1.2$-2.1 paddle chimera (PDB ID: 2R9R). The S1-S2 loop from the paddle chimera was drawn as a shorter loop to match the length of hH_V1. (**B**) The amino acid sequence of hH_V1. Predicted transmembrane regions, based on the structure of the paddle chimera and hydropathy, are highlighted gray. Residues mutated to cysteine are colored red. C107 and C249 are natural cysteines. The region corresponding to the coiled coil was calculated by the program COIL (Lupas *et al*. 1991).

2.2.2 Dimer interface of H_V channels

Each of the 14 cysteine-mutant cDNAs was transfected into tsA201 cells and membranes isolated from these cells were subjected to cross-linking reactions. The oligomeric state of each mutant was assessed by western blot analysis. Among the 15 mutants that we tested for cross-linking, only R100C failed to be expressed, by western blot analysis. As shown in Fig. 2.3A, all mutants migrated as a monomer under reducing conditions on SDS-PAGE. However, several mutants migrated as a dimer under non-reducing conditions (Fig. 2.3B). I127C, which is located in the loop between S1 and S2, formed an almost complete spontaneous disulfide bond, whereas C249—a natural cysteine located in the predicted coiled-coil domain—formed a significant quantity of spontaneous disulfide bond. N132C and T222C also showed some degree of disulfide bond formation. This pattern of disulfide bond formation suggests that S1 and the adjacent loop form a dimer interface on the extracellular side of the cell membrane and that the C-terminus, through a coiled-coil, forms a dimer interface on the intracellular side of the membrane.

Oligomer formation was also studied under conditions that 'force' cross-linking, either by the addition of the oxidant $CuSO_4$ and o-phenanthroline (CuP) or by the addition of the bifunctional cross-linker 1,3-propanediyl bismethanethiosulfonate (M3M), which has a 13 Å spacer separating the two cysteine-reactive methanethiosulfonate functional groups (Fig. 2.3C and D). Both reagents drove cross-links at I127C and at C249 nearer to completion. They also produced cross-linked cysteines to a lesser extent at positions near I127 (position 120 within S1 and position 132 in the S1-S2 loop) and near 249 (position 222 within the C-terminus).

Fig. 2.3 Dimer interface of hH_V1

Western blots of membranes from tsA201 cells transfected with 14 individual hH_V1 cysteine-containing mutant cDNAs that were subjected to (**A**) reducing reagent (5 % (v/v) b-mercaptoethanol), (**B**) air oxidation, (**C**) CuP-induced cross-linking, or (**D**) M3M-mediated cross-linking as per methods. Cross-linked dimers migrate at approximately 73 kDa while monomers migrate at approximately 35 kDa. Other weak bands probably correspond to proteolytic fragments of hH_V1. A mutant hH_V1 in which the native cysteines were removed was included as a control (cysless). The number represents the amino acid position of the cysteine residue.

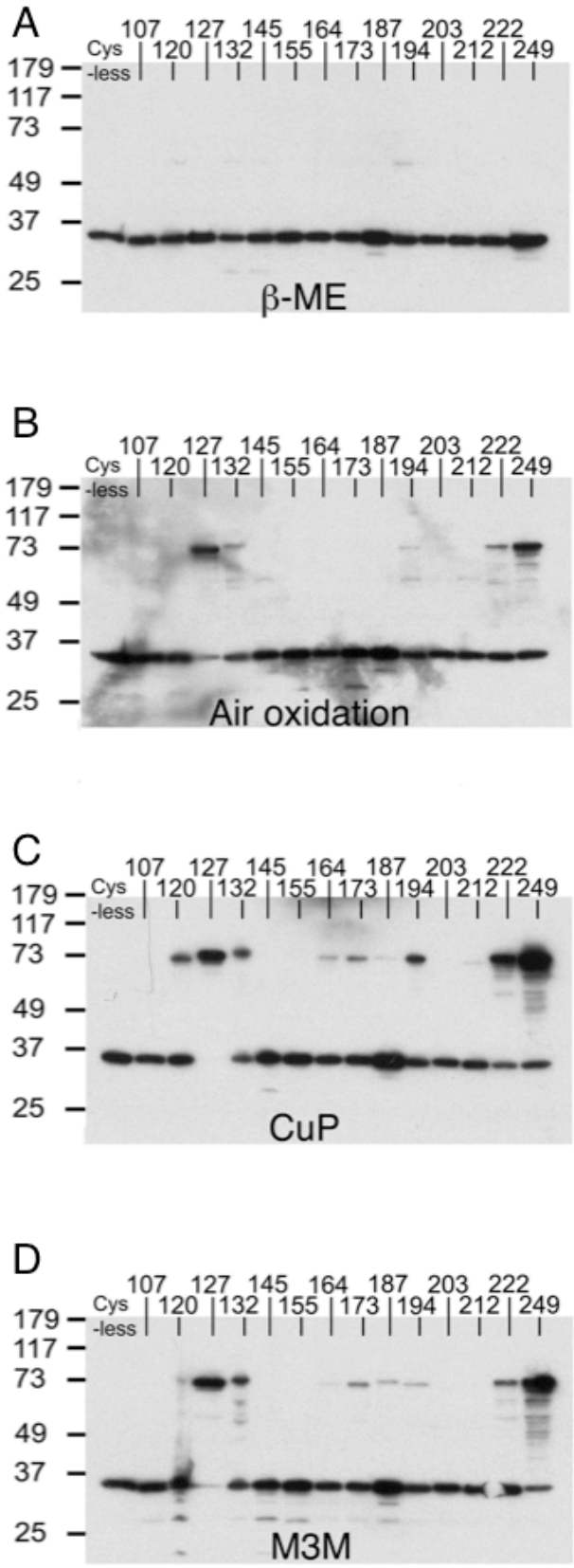
A
107 127 145 164 187 203 222
Cys | 120 | 132 | 155 | 173 | 194 | 212 | 249
-less
179
117
73
49
37
25
β-ME
B
107 127 145 164 187 203 222
Cys | 120 | 132 | 155 | 173 | 194 | 212 | 249
-less
179
117
73
49
37
25
Air oxidation
C
107 127 145 164 187 203 222
Cys | 120 | 132 | 155 | 173 | 194 | 212 | 249
-less
179
117
73
49
37
25
CuP
D
107 127 145 164 187 203 222
Cys | 120 | 132 | 155 | 173 | 194 | 212 | 249
-less
179
117
73
49
37
25
M3M

Forcing conditions also resulted in weak cross-links in two new regions: the S2-S3 turn—also known as the membrane interface anchor (positions 164 and 173) (Lee *et al*. 2005)—and the tip of the voltage sensor paddle (positions 187 and 194; Fig. 2.3C and D; Jiang *et al*. 2003a; Jiang *et al*. 2003b).

By covalently trapping rare conformations or molecular arrangements, forcing conditions can sometimes result in cross-link formation between residues that are only rarely in close proximity to each other. An example of this would be intermolecular cross-links (in this case inter-dimer cross-bridge formation between pairs of dimers). The blot in Figure 2.4A provides evidence for such dimer pairing by cross-linking of cysteines at position 173. When combined with a cysteine at 127 (which by itself formed a cross-linked dimer to near completion; Fig. 2.3B), cysteine at 173 resulted in the appearance of bands near the size of a tetramer (Fig. 2.4A). This observation is explicable if cross-links between position 173 cysteines formed between S2-S3 loops from separate dimers, because cross-links within a dimer would not produce a tetramer. A similar analysis of cysteine at position 194 in the background of a cysteine at 127 produced a different, yet equally interesting result. Cysteine at 194 did not produce tetramers in this setting, but reduced the degree to which cysteine at 127 formed a cross-linked dimer (compare Fig. 2.3C and D with Fig. 2.4A). The location of position 194 at the tip of the voltage sensor paddle, which is adjacent to the S1-S2 loop within a single voltage sensor of the dimer (see Fig. 2.2A), offers a possible explanation for this cross-linking outcome. By forming an intramolecular cross-link with cysteine 127 within the same subunit, cysteine at 194 would compete with cysteine 127-mediated dimer cross-linking. These more subtle aspects of the blots suggest that the S2-S3 turn and the voltage sensor paddle

are not actually part of the tight dimer interface, but that less specific cross-links are formed under forcing conditions.

A more extensive inspection of covalent dimer formation via cysteine residues within the S1 and S1-S2 loop showed differential propensities to react (Fig. 2.4B and C). Even among amino acids that we expect to reside outside the membrane (positions 124-128), positions 126 and 127 reacted to a greater extent, as if they were most optimally positioned to form a disulfide bridge relative to their molecular symmetry equivalents. Position 120, which we expect is buried in the membrane, formed a disulfide partially in the presence of CuP. Disulfide formation in a low dielectric environment suggests that position 120 is probably very near its molecular symmetry partner (Schwem & Fillingame 2006; Yu & Oprian 1999).

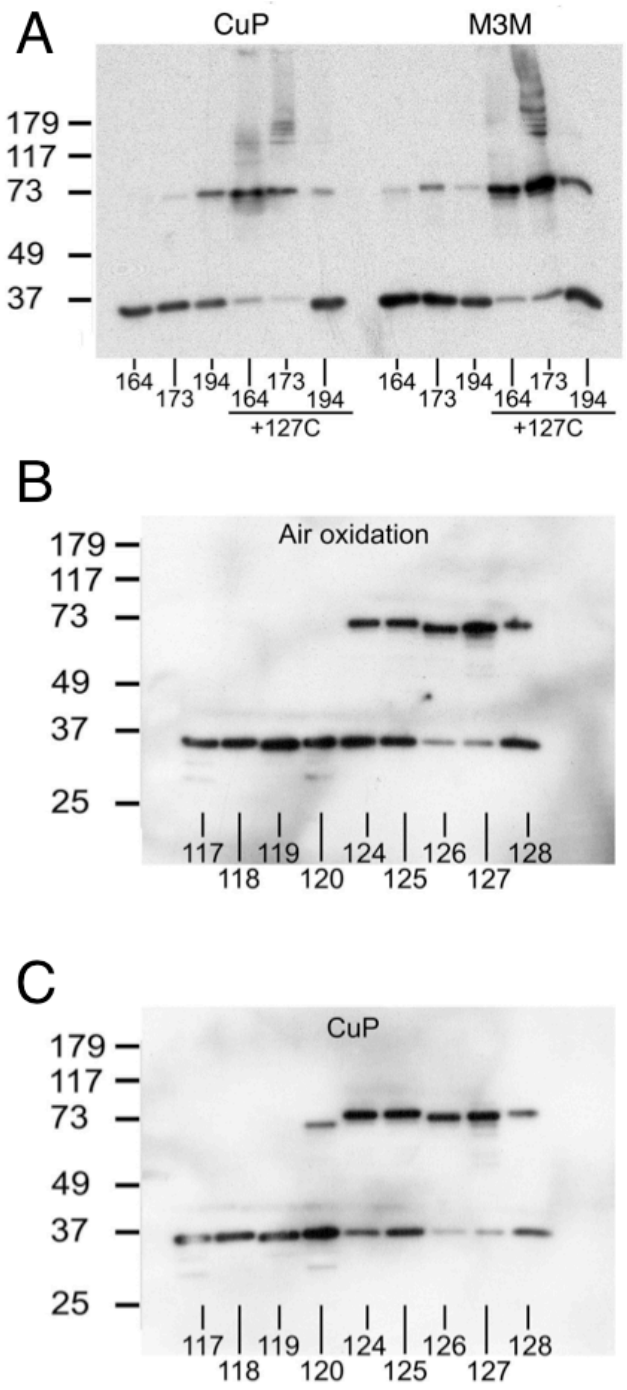

Fig. 2.4 Further study of the dimer interface.

(**A**) Distinguishing intra- from inter-dimer cross-linking. Numbers at the bottom of each gel indicate the cysteine position. (**B**) Specificity of cross-linking in the S1-S1 dimer interface. Transmembrane region of S1 (117 to 120) and the adjacent loop (124 to 128) were subjected to (**B**) air oxidation and (**C**) CuP - mediated oxidation.

2.3 Discussion of Results and Subsequent Literature

2.3.1 Schematic representation of the hH_V1 dimer

These cross-linking data support the conclusion that H_V1 exists in the cell membrane as a dimer of identical voltage sensor protomers. Two regions of contact between the voltage sensors correspond to the extracellular C-terminal side of S1 and the adjoining S1-S2 loop and intracellular C-terminus, which may form a coiled coil structure. The native cysteine at position 249 may help to stabilize the dimer at the coiled coil but a disulfide bridge at this position is not essential for holding the dimer together. We conclude that two voltage sensor protomers of a dimer come into direct contact at both the extracellular and intracellular side of the membrane. A schematic representation of the H_V1 dimer, based on the known crystal structures of K_V channel voltage sensors and the contact surfaces identified in this study, is shown in Fig. 2.5 (Jiang *et al*. 2003a; Long *et al*. 2005; Long *et al*. 2007).

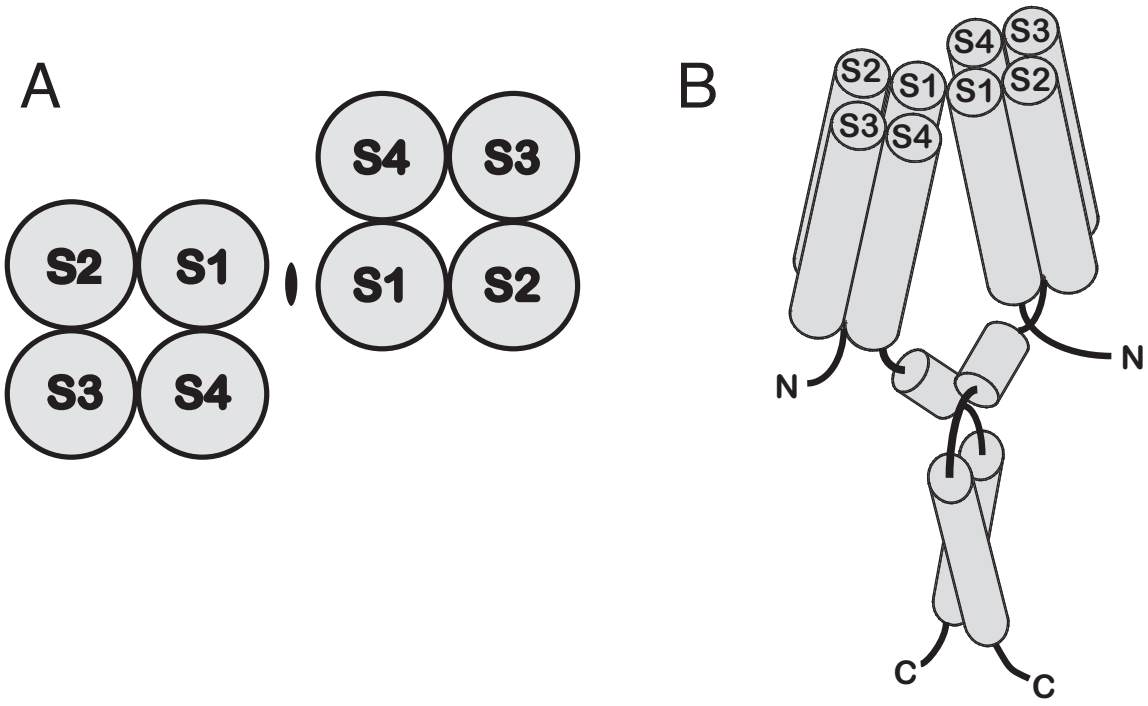

Fig. 2.5 A model of the hH_V1 dimer

(**A**) Topology diagram showing the dimer arrangement of hH_V1 transmembrane regions based on the cross-linking data, viewed from the extra-cellular side. An ellipsoid denotes the 2-fold rotation axis normal to the membrane. (**B**) A cartoon representation of the hH_V1 dimer. Transmembrane helices are labeled. The helical representation of the putative interfacial region (after S4) and the predicted coiled coil region are also included.

Contemporary publications from two groups corroborated and complemented our discovery that H_V channels are dimers in the membrane (Koch *et al*. 2008; Tombola *et al*. 2008). By expressing two differentially tagged mouse H_V channels subunits in HEK cell and performing pull-down experiments, Koch *et al*. showed complex formation between the two H_V constructs (Koch *et al*. 2008). Furthermore, they demonstrated that the amount of detectable complex is significantly reduced by deletion of the C-terminal coiled coil, providing further evidence for the importance of the coiled-coil in stabilizing the dimer interface (Koch *et al*. 2008). Using single molecule photobleaching on GFP-tagged hH_V1, Tombola *et al*. also demonstrated that H_V channels are dimers in *Xenopus* oocyte membranes (Tombola *et al*. 2008). Our work, together with the work from these other two groups, established that H_V channels are dimers in the membrane.

2.3.2 Each subunit has a separate H^+ conduction pathway

Many membrane proteins exist as oligomers of identical or similar subunits. In many cases, the need for an oligomeric structure is clear: potassium channels, for example, require four subunits to form a single ion conduction pathway in between the subunits (Doyle *et al*. 1998). In other membrane proteins, the reason for an oligomeric structure is less clear: in aquaporin channels (Murata *et al*. 2000) and in ClC Cl^- channels (Dutzler *et al*. 2002), the water and ion conduction pathways are formed entirely by atoms of a single protomer and yet these transport proteins are tetramers and dimers of identical protomers, respectively.

Into which category does the H_V channel fall? Based on electrophysiological studies showing that mutant K_V channel voltage sensors can themselves conduct ions

(Tombola *et al*. 2005) or H^+ (Starace & Bezanilla 2004) across the membrane, and based on atomic structural studies showing that K_V channel voltage sensors contain protonatable chemical groups extending most of the way across the membrane (Long *et al*. 2007), it is not difficult to imagine that H^+ flows through individual voltage sensors in H_V channels. In other words, each sensor might contain its own H^+ conduction pathway.

The contemporary work by Tombola *et al*. provided evidence for this claim (Tombola *et al*. 2008). By generating tandem hH_V1 dimers (i.e., both subunits expressed on a single polypeptide) with specific cysteine mutations in each subunit and reacting them with a cysteine-specific reagent that disrupted H^+ conduction, they demonstrated that each subunit contributed approximately 50% of the total H^+ current (Tombola *et al*. 2008). Moreover, by making a chimeric H_V channel in which the N- and C-termini were replaced by those of the voltage-sensor phosphatase from *Ciona intestinalis* (Ci-VSP), Tombola *et al*. were able to monomerize the channel and demonstrate that the monomerized channel was still able to conduct H^+ (Tombola *et al*. 2008).

More recently mutagenesis studies on hH_V1 by Musset *et al*. found that a single point mutation, D112V, is able to completely abolish H^+ conduction (Musset *et al*. 2011). Further mutagenesis data on hH_V1 suggest that D112 interacts with the S4 gating-charge arginines, indicating that this side chain is directed into the central cavity of the VSD itself and not located at the dimeric interface (Berger & Isacoff 2011). This finding further supports the notion that each subunit contains a separate conduction pathway.

2.3.3 H_V channel dimer and cooperativity

Sometimes, multiple subunits allow active sites to function in a non-independent manner. Hemoglobin is a well known example in which an oligomeric structure underlies cooperativity (Perutz 1989), allowing a steep relationship between oxygen saturation and oxygen partial pressure. In ClC Cl^- channels, one form of gating might arise from its dimeric architecture (Bykova *et al*. 2006). Thus, oligomeric architectures in both soluble and membrane proteins can allow for much more than the multiplicity of active sites.

Electrophysiological studies have demonstrated strong cooperativity between the two subunits of the H_V channel dimer (González *et al*. 2010; Tombola *et al*. 2010; Musset *et al*. 2010b). Using voltage-clamp fluorometry and specifically labeling *Ciona intestinalis* H_V channels on S4 with a fluorescent probe, Qui *et al*. demonstrated that each subunit undergoes independent conformational changes prior to a concerted opening of the H^+ conduction pathway (Qiu *et al*. 2013). It has also been noted that truncation of the channel on the N- and C-terminus (or the C-terminus alone) removes the cooperativity of H_V channel gating, which has been argued to be due to monomerization of the channel (González *et al*. 2010; Tombola *et al*. 2010; Musset *et al*. 2010b).

Although it is clear from Koch *et al*.'s pull down experiments that truncating the termini of H_V channels reduce the proportion of dimer observed, there is still some dimer present, indicating that the truncated channel subunits may still be associated in the membrane and may only come apart during the many washes of the pull-down protocol (Koch *et al*. 2008). Furthermore, Fujiwara *et al*. demonstrated that mutation of three amino acid residues in the C-terminal coiled coil is sufficient for disruption of the cooperative gating without disruption of the dimer (Fujiwara *et al*. 2012). Therefore, the

cooperativity of gating can be modulated independently of channels' multimeric state in the membrane. Hence, simply because deletion of the C-terminus removes cooperative gating does not necessarily mean the channel has become monomeric. In fact, evidence is mounting that, by affecting the oxidation state of a native cysteine residue in the coiled coil, C249 in hH_V1 (shown in Fig. 2.3B to be able to spontaneously form a inter-subunit disulfide bond), the cell is able to tune the cooperativity of the channel, thereby physiologically linking channel activity to the redox state of the cell (Fujiwara *et al*. 2012; Fujiwara *et al*. 2013b).

2.3.4 Mechanistic Implications of the dimer

In H_V1 channels, a dimeric architecture might be related to the mechanics of channel gating. It is interesting to note that the location of the extracellular dimer interface in the H_V1 channel corresponds well to the region of contact between voltage sensor and pore in K_V channels (Long *et al*. 2007). In K_V channels, the contact between S1 and the pore at the extracellular surface is proposed to serve as a mechanical fixed point so that motions of the voltage sensor paddle (S3 and S4) are efficiently transmitted to the pore's gate (Long *et al*. 2007; Lee *et al*. 2009a). By analogy, contacts between S1 helices in the H_V1 dimer might serve a similar function by fixing S1 and S2, thus permitting the voltage sensor to move and open a conduction pathway within each voltage sensor.

However, the work of Tombola *et al*. on the monomerized H_V-channel chimera, in which both N- and C-termini are replaced by sequences from Ci-VSP, indicates that H_V channels are able to function in the absence of the dimer (Tombola *et al*. 2008). Additionally, the voltage-sensor phosphatase (VSP) functions as a monomer in the

membrane, indicating that not all VSDs require a fixed support at the extracellular side of S1 to function (Kohout *et al*. 2008). If they are able to function as monomers, what makes the mechanism of H_V channels and VSP different from the 6-TM voltage-gated cation channels, which have been shown to require a fixed support at the extracellular side of S1 in order to function (Lee *et al*. 2009a)?

All VSDs are able to change conformation in response to changes in the transmembrane voltage. However, the VSDs of the 6-TM voltage-gated cation channels are electromechanical force transducers: the conformational changes need to be transmitted to the pore helix, *via* the S4-S5 linker and the S6 helix bundle, in order to open and close the ion conduction pathway (Long *et al*. 2007; Lee *et al*. 2009a). In order to efficiently transmit force to the pore domain, a fixed anchor in the membrane is required (Lee *et al*. 2009a). Are the VSDs of H_V channels and VSPs electromechanical force transducers? The conformational changes of these VSDs are not coupled to opening or closing of a separate pore as in the case of the canonical 6-TM voltage-gated cation channels. If the role of these non-canonical VSDs were simply to undergo conformational changes and not to transmit force, they would not require a fixed anchor in the membrane. Since the conduction pathway for H^+ in H_V channels is located within the VSD itself, conformational changes of the VSD without force transduction should be sufficient to open the channel. Therefore, the purpose of the H_V dimer would not be to provide a fixed anchor to allow force transduction but to allow for modulation of gating through the regulation of cooperativity discussed in the previous section, and hence the channels would still be functional as monomers.

2.3.5 Implications of the dimer on future structural studies

In order to fully understand the mechanism and regulation of cooperativity in H_V channels structures of both the reduced and oxidized dimers would be required (Fujiwara *et al*. 2013b). However, Tombola *et al*. show that a monomerized H_V-VSP chimera is functional as a monomer (Tombola *et al*. 2008). Therefore, it should be possible to gain insight concerning the gating and conduction of H_V channels from the structure of a monomerized channel. In order to confirm that the monomeric channel is functional, constructs that disrupt dimerization should be built in the absence of chimerization and functionally characterized. These channels will have to be shown to be monomeric in membranes by their inability to form site-specific cross-links along S1. The C-terminally truncated channels (discussed above) that lack cooperativity during gating have not been experimentally shown to be monomeric and therefore may still exist as dimers in the membrane. If the truncated channels are found to still be dimeric in the membrane it may be possible to disrupt the dimer by introduction of tryptophan amino acid residues along the S1 dimer interface. Due to its large bulky side chain tryptophan has been used successfully in other studies to disrupt membrane protein structure (Sharp *et al*. 1995). Alternatively, it has been suggested that due to its lack of a C-terminal coiled-coil the H_V channel found in the dinoflagellates *Karlodinium veneficum* may exist as a monomer (Smith *et al*. 2011). However, this has yet to be experimentally verified. As discussed above, a definitive demonstration that monomeric H_V channels are functional would significantly contribute to our understanding of the mechanism of gating and greatly improve our confidence in interpretations of structural studies on monomerized channel in detergent (see Chapters 4 and 5).

CHAPTER 3: FUNCTIONAL RECONSTITUTION OF HUMAN H_V1

Due to the complexity of the proteic component of a cell's cytoplasm and membrane, it can be very difficult to determine the function of each of the individual proteins. When Sasaki *et al*. and Ramsey *et al*. expressed the putative H_V channel proteins in HEK cells, they observed the robust generation of voltage-gated H^+ currents (Ramsey *et al*. 2006; Sasaki *et al*. 2006). However, whether this H^+ conduction occurred through the putative H_V gene product was unclear. Given that the H_V protein has homology to the regulatory voltage sensor domain (VSD) of canonical voltage-gated cation channels, but lacks the pore domain responsible for ion conduction, it remained possible that H_V was not an ion channel at all, but, instead, an accessory subunit for the modulation of a separate, unknown endogenous HEK cell membrane protein. In order to determine whether or not the putative H_V channel is in fact responsible for H^+ conduction a reductionist approach was necessary; the activity of the putative channel had to be assessed in isolation from all other cellular proteins.

In this chapter, I will discuss my work in collaboration with Dr Seok-Yong Lee addressing this issue (Lee *et al*. 2009b). Working with the eukaryotic expression vector *Pichia pastoris*, we were able to develop a protocol for the purification and reconstitution of human H_V1 (hH_V1) into lipid vesicles. By assaying the activity of the purified

reconstituted channel using a fluorescence-based concentrative uptake assay, we were the first to demonstrate that the putative H_V channel gene product alone is in fact responsible for H^+ conduction. By reconstituting the protein at different protein-to-lipid ratios, we were able to demonstrate that the majority of the hH_V1 channels that we purified were functional, validating our purification protocol for use in more detailed biochemical and structural studies. As controls, we reconstituted several other voltage-gated channels to prove that the H^+ flux observed was specific to H_V channels and not due to non-specific leaks caused by the presence of protein in the membranes. Extensive mutagenesis studies of purified and reconstituted hH_V1 identified D112 on S1 as an important amino acid residue for H^+ conduction. Furthermore, mutation of the equivalent position to aspartate on the K_VAP isolated VSD increased the rate of H^+ flux through this protein, indicating that this residue is sufficient to promote H^+ conduction through VSDs. A model of H^+ uptake qualitatively recapitulated our experimental results. These findings will be discussed in the context of the more recent H_V channel electrophysiological literature.

3.1 THE PUTATIVE H_V CHANNEL MEDIATES H^+ FLUX IN VESICLES

3.1.1 Expression, Purification and Reconstitution of Human H_V1

Heterologous expression of hH_V1 channels was attempted in both prokaryotic (*Escherichia coli*) and eukaryotic vectors (*Pichia pastoris* yeast, Sf9/baculovirus insect cells and HEK mammalian cells). Although expression of extractable channel was low in each system, it was determined that *Pichia pastoris* provided sufficient protein for the reconstitution experiments. Due to the poor expression, the high affinity C-terminal 1D4-tag was needed to isolate the low-abundance channel protein from high-abundance endogenous contaminants. The channels were extracted from the yeast membranes using dodecylmaltoside (DDM) detergent and purified by affinity chromatography on an anti-1D4 antibody resin, followed by size exclusion chromatography (see Materials and Methods for details). Purified protein appeared as a single band corresponding to the expected size of a monomer on gel electrophoresis under denaturing and reducing conditions (Fig. 3.1A). Reconstitution of H_V protein into lipid vesicles was carried out by detergent removal from channel-detergent-lipid mixtures *via* dialysis, using different protein to lipid ratios. As a control for tight lipid bilayer formation, reconstitution of empty vesicles was carried out in parallel in the absence of protein, allowing us to measure any non-specific membrane leakage.

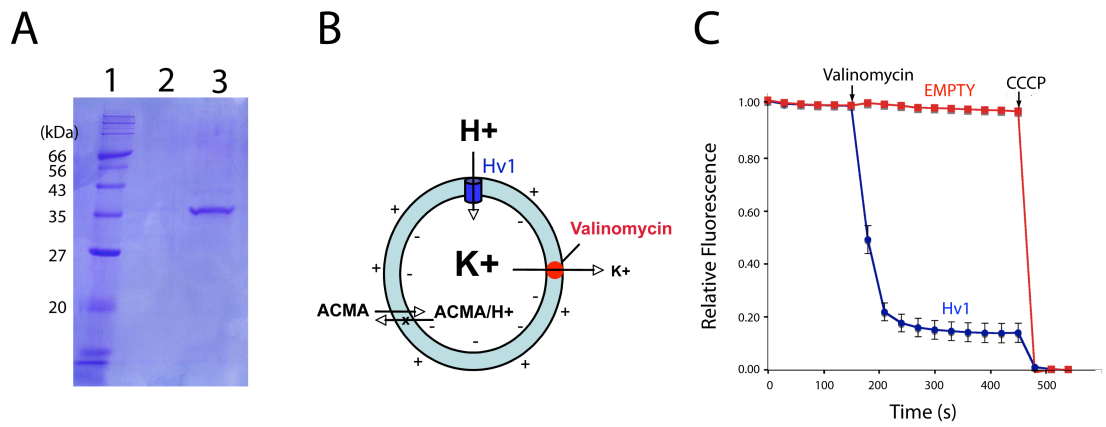

Fig. 3.1 H^+ flux into vesicles containing recombinant Hv channels

(A) SDS-PAGE gel showing purified H_V channels. Lane 1: molecular weight marker, 2: final wash, and 3: hH_V-1D4 eluted with 0.4 mg/ml 1D4 peptide. **(B)** Fluorescence-based H^+ flux assay. Vesicles (cyan) loaded with high concentration of K^+ are diluted into low concentration K^+ buffer containing the fluorescence dye ACMA (9-amino-6-chloro-methoxyacridine). Addition of valinomycin (red), a K^+ selective ionophore, results in K^+ efflux, which generates a driving force for H^+ influx. If there is a H^+ channel (blue) in the vesicle membrane, pH inside the vesicle will decrease. This pH decrease is monitored by ACMA because the protonated form, which becomes trapped inside vesicles, loses fluorescence whereas unprotonated ACMA diffuses freely across the membrane (Zhang & Forgac 1994). **(C)** Fluorescence-based H^+ flux assay for vesicles with and without hH_V1 colored blue and red, respectively (n = 5). Error bars indicate standard error of the mean. Valinomycin and CCCP are added at the indicated time points.

3.1.2 Monitoring H_V channel conduction by fluorescence

To study H^+ flux into lipid vesicles containing human H_V channels, we used the fluorescence-based concentrative uptake H^+ flux assay depicted in Fig. 3.1B. This assay was originally developed to study H^+ flux through V-ATPase (Zhang & Forgac 1994). Vesicles were reconstituted in the presence of 150 mM K^+ and diluted 20-fold into buffer containing 7.5 mM K^+ generating a 10-fold K^+ gradient across the membranes. Upon addition of the K^+ selective ionophore valinomycin, the K^+ diffuses out of the vesicles, generating an electric potential across the vesicular membrane of approximately -60 mV (negative inside relative to outside, calculated by equation 1.1). If a H^+ conduction pathway is present in the membrane, the negative electrical potential inside the vesicles will cause H^+ to enter, lowering the internal pH. We monitored the changes in pH by a H^+-induced quenching of the fluorophore 9-amino-6-chloro-2-methoxyacridine (ACMA).

Fig. 3.1C shows the fluorescence change caused by the addition of valinomycin to a sample of empty vesicles and to a sample of hH_V1 reconstituted vesicles at a protein to lipid ratio of 1:100 (wt:wt). The empty vesicles exhibited a very gradual fluorescence change, consistent with there being a very slow non-specific leak for H^+ entry until the proton ionophore carbonyl cyanide m-chlorophenyl hydrazone (CCCP) is added. Vesicles containing H_V channels showed a robust change in fluorescence upon addition of valinomycin, consistent with the H_V channel providing a specific pathway for H^+ entry. The further reduction in fluorescence brought about by the addition of CCCP reflects a small fraction of empty vesicles. The ~15% of empty vesicles seen even at high protein-to-lipid ratios stems from a population of vesicles that appear incapable of incorporating functional H_V channels (see below). Similar fractions of reconstitution deficient vesicles

have been described previously in studies of other channels and transport proteins (Eytan 1982; Goldberg & Miller 1991; Heginbotham *et al*. 1998).

3.1.3 The Majority of Reconstituted H_V Channels are Functional

In order to further investigate the functioning of H_V channels, we performed the reconstitution at various protein-to-lipid ratios (Fig. 3.2A). The fluorescence-based assay, which indirectly measures H^+ flux through an unknown relationship between H^+ concentration and fluorescence, precludes quantitative determination of H^+ conduction rates (Fiolet *et al*. 1974). The assay does, however, allow us to estimate the fraction of total channels in the reconstitution that are functional, as explained below.

The fluorescence decay brought about by the addition of valinomycin (F_{Hv}) is proportional to the number of vesicles that contain at least one functional H_V channel. The fluorescence decay brought about by valinomycin plus CCCP (F_{total}) is proportional to the total number of vesicles. Given that we know the mass protein to mass lipid ratio in the reconstitution, and that the reconstitution occurs efficiently (Fig. 3.2B), with a few assumptions we can calculate the mean number of channels per vesicle μ from equation 3.1, where g_{Hv} and g_L are the grams of Hv channel and lipid added, r is the estimated average radius of a vesicle, M_L is the molecular weight of the average lipid molecule (754 Da), σ is the estimated area per lipid molecule and M_{Hv} is the molecular mass of the Hv channel dimer (70,000 Da).

$$\mu = \frac{8 g_{Hv} \pi r^2 M_L}{g_L \sigma M_{Hv}} \qquad \{3.1\}$$

Fig. 3.2 H^+ flux into vesicles containing H_V channels at various protein-to-lipid ratios (**A**) Fluorescence-based H^+ flux assay for vesicles containing a decreasing number of H_V channels. Protein-to-lipid ratios of 1:100 (dark blue, n = 5), 1:500 (pink, n = 2), 1:1000 (orange, n = 3), 1:5000 (yellow, n = 3), 1:10,000 (cyan, n = 4), 1:20,000 (light green, n = 3), 1:40,000 (green, n =4), 1:60,000 (violet, n = 3) and empty vesicles (red squares, n = 4) are plotted (error bars represent the standard error of the mean, range of mean for 1:500). (**B**) Sucrose cushion of vesicles containing H_V channels. Numbers denote the fractions collected from top to bottom. (**C**) Determination of the fraction of functional H_V channels. Plot of μ versus the ratio of fluorescence decay contributed by H_V containing vesicles over the total fluorescence decay by addition of CCCP where μ is the ratio of the number of channels over number of vesicles calculated with equation 3.1. The two curves are derived from equation 3.2 with ϕ (fraction of functional H_V) = 1.0, θ (fraction of reconstitution deficient vesicles) = 0.15 (red) and $\phi = 0.5$, $\theta = 0.15$ (green).

A

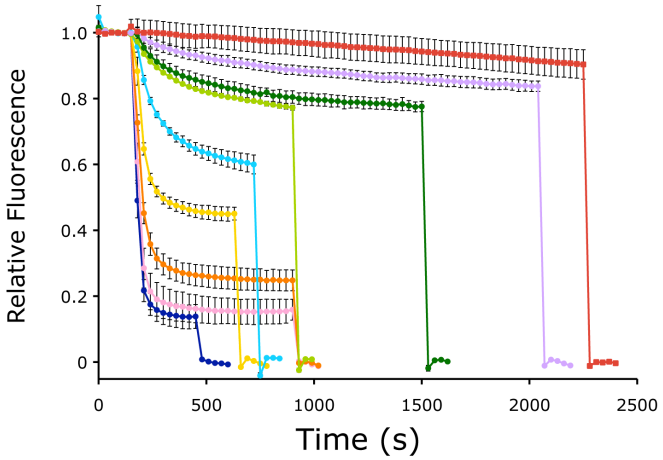
Relative Fluorescence
1.0
0.8
0.6
0.4
0.2
0
0
500
1000
1500
2000
2500
Time (s)

B

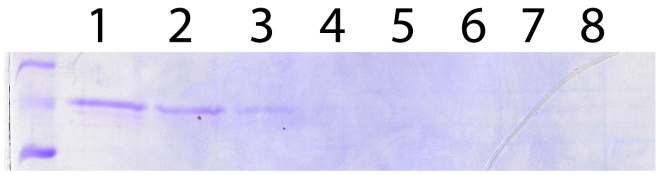
1 2 3 4 5 6 7 8

C

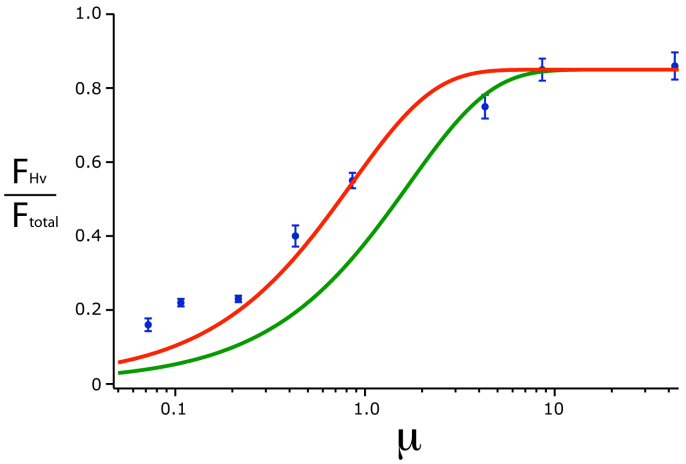
1.0
0.8
0.6
0.4
0.2
0
F Hv
F total
0.1
1.0
10
μ

The main assumptions are that the lipid head group area is 63 $Å^2$ (DeCoursey 2003b; Rand & Parsegian 1989) and that the vesicles are uniform in size with a radius of 100 nm (Moffat *et al*. 2008). If incorporation of H_V channels into vesicles is random, then we expect equation 3.2 to be true, where θ is the fraction of reconstitution deficient vesicles (~15%, measured directly from the data) and ϕ is the fraction of channels that are functional (Heginbotham *et al*. 1998).

$$F_{Hv}/F_{total} = (1-\theta)\left[1-\exp\left(\frac{-\phi\mu}{(1-\theta)}\right)\right] \qquad \{3.2\}$$

The red curve in Fig. 3.2C corresponds to the curve generated from equation 3.2 with ϕ = 1.0. To ensure that this conclusion is not mistakenly based on an incorrect assumption of the vesicle radius (which we have not measured but estimate from values in the literature), we fit the data using alternative values. At 70 nm, vesicles would be too numerous given the number of channels: ϕ would have to be greater than 1.0, which is physically impossible. At 130 nm, the best fit still corresponds to a ϕ value of approximately 0.75. Therefore, even given the degree of uncertainty introduced by our assumptions of vesicle radius, uniformity, and lipid molecule surface area, the data support the conclusion that the majority of H_V channels in the reconstitution are functional.

3.1.4 H^+ Flux is Specific to H_V Channels

The small conductance inferred from this study (see the section on modeling the flux below), raises the concern that the H^+ flux into the vesicles may be due to a non-specific leak resulting from the presence of protein in the membranes. To examine this possibility, we expressed, purified and reconstituted three additional proteins at equivalent protein to lipid ratios (to match the number of VSDs per vesicle): full-length K_VAP (K_VAP), K_VAP isolated VSD (K_VAP VSD), and K_V1.2-2.1 paddle chimera (paddle chimera). The fluorescence-based H^+ flux analysis of these proteins showed that vesicles containing either K_VAP or paddle chimera generated very little fluorescence decay (Fig. 3.3). Because both K_VAP and paddle chimera contain K^+ pores, the K^+-driven membrane potential may be established before valinomycin addition. Initial fluorescence values with vesicles containing these channels were very similar to other vesicle preparations (H_V or empty), suggesting that no H^+ influx occurred before the first point of data collection. Interestingly, vesicles containing K_VAP VSD exhibited fluorescence decay but at a significantly slower rate than vesicles containing H_V channels (Fig. 3.3). Sucrose cushions of these vesicles confirmed efficient reconstitution of all proteins. These data suggest that the H^+ flux through H_V is not simply a manifestation of membrane protein reconstitution into the vesicles: rapid H^+ flux is specific to H_V. The slower H^+ flux observed for K_VAP VSD might reflect an intrinsic H^+ conduction potential of the VSD, which is suppressed by its association with the K^+ channel pore.

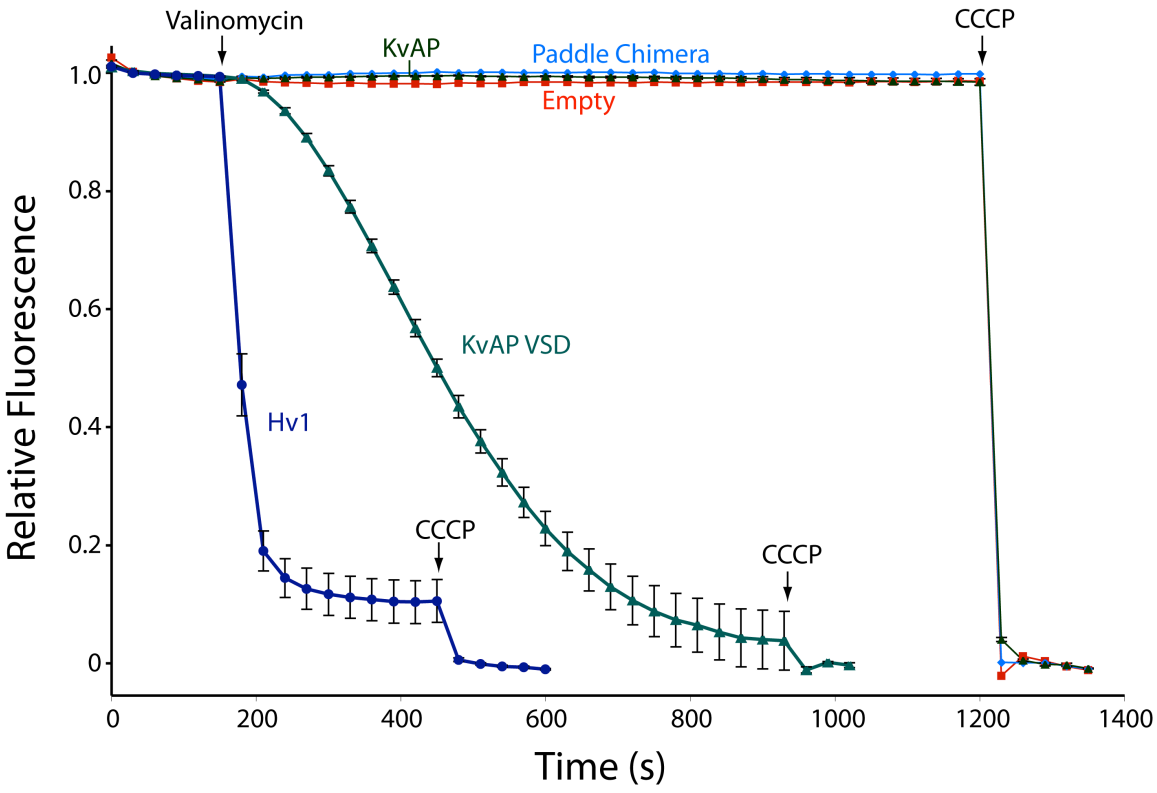

Fig. 3.3 Specific H^+ permeation through hH_V1

Fluorescence-based H^+ flux assay for vesicles containing hH_V1 (dark blue, n=5), K_VAP VSD (green, n=4), K_VAP (dark green, n=4), paddle chimera (cyan). Empty vesicles are shown in red. Error bars indicate standard error of the mean. Valinomycin and CCCP are added at the indicated time points. K_VAP, K_VAP VSD, and paddle chimera channels were expressed and purified according to published procedures (Jiang *et al*. 2003a; Long *et al*. 2007). Reconstitutions were carried out as described in materials and methods with the following protein to lipid ratios (wt:wt) 1:200 (KvAP VSD), 1:100 (KvAP), and 1:50 (paddle chimera).

3.2 MUTAGENESIS OF THE H_V CHANNEL TRANSMEMBRANE DOMAIN

3.2.1 H^+ flux through mutant hH_V1 channels

In order to find the amino acid residues responsible for H^+ conduction through the transmembrane domain of H_V channels, we conducted extensive mutagenesis studies. Because hydrophilic residues are required for specific interaction with ions in the hydrophobic interior of the membrane, we focused our mutagenesis on polar and charged amino acids within the transmembrane domain. Fig. 3.4 shows the transmembrane sequence of hH_V1 aligned to the equivalent sequence of the $K_V1.1$ channel Shaker, highlighting the 14 positions that were individually mutated to alanine or leucine. Each of the mutant channels was expressed, purified and reconstituted into lipid vesicles at a protein to lipid ration of 1:100 (wt:wt). To ensure that the mutations did not significantly affect the reconstitution efficiency of the channel, we ran sucrose cushion flotation assays on each of the reconstituted mutant channels.

The activity of each mutant was tested by the fluorescence-based concentrative uptake flux assay described in Fig. 3.1B and compared to that of reconstituted wild type hH_V1 and empty vesicles. Mutation of a residue that is required for H^+ conduction should result in the absence of fluorescence quenching. The data from the reconstituted mutant channels presented in Fig. 3.5A-D are organized by the transmembrane helix (S1-S4) on which the mutated residue resides. However, the mutants can also be organized by their effect on H^+-mediated fluorescence quenching and it is in this context that I will discuss them below.

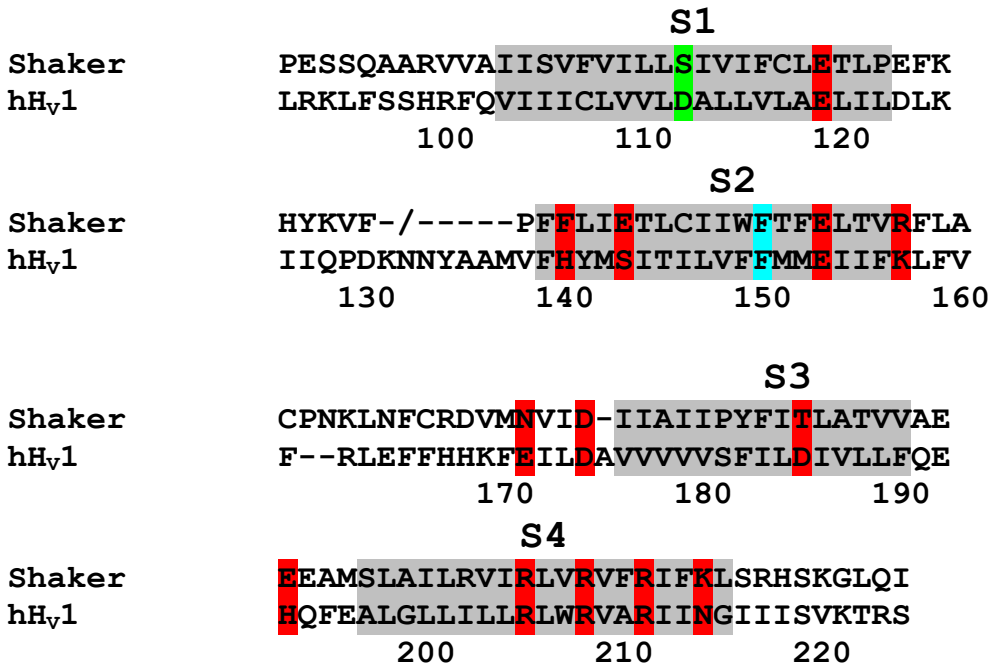

Fig. 3.4 hH_V1 transmembrane residues targeted for mutagenesis

The transmembrane sequence of hH_V1 is shown aligned to the equivalent sequence of the $K_V1.1$ channel Shaker. Numbering at the bottom corresponds to the hH_V1 amino acid position. The putative transmembrane helices are highlighted in grey and labeled S1-S4. The sites of the mutations are highlighted in red with the exception of position D112 that is highlighted in green. The phenylalanine that corresponds to the phenyalanine gap in S2 is highlighted in cyan (see Fig. 1.4).

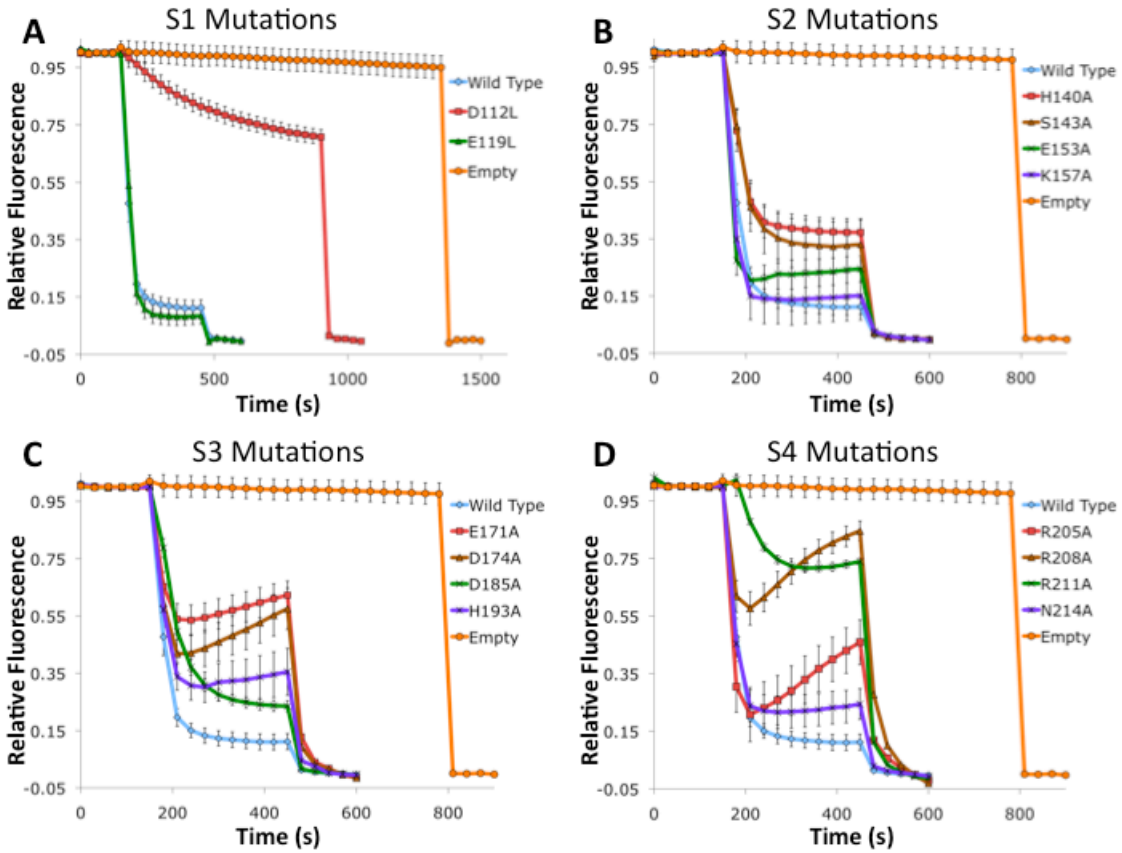

Fig. 3.5 H^+ flux into vesicles containing mutant hH_V1 channels

Fluorescence-based H^+ flux assay for vesicles containing mutant hH_V1 channels compared to vesicles containing wild type channels and empty vesicles. (A) Mutations along S1. (B) Mutations along S2. (C) Mutations along S3. (D) Mutations along S4. In each case valinomycin was added after 150 s and CCCP was added after 450s except in the case of D112L were CCCP was added after 900s. For empty vesicles CCCP was added at 1350 s (A) and 780 s (B C and D). All channels were reconstituted at a protein-to-lipid ratio of 1:100 (wt:wt). Each curve corresponds to the average of 3-4 repetitions with the error bars indicating the standard error of the mean.

3.2.2 Mutations with small or no effect on H^+ conduction

Many of the mutations investigated had little or no effect on the H^+ conduction when compared to the wild type channel (Fig. 3.5A-D). These included E119L on S1 (Fig. 3.5A), all residues tested on S2, H140A, S143A, E153A and K157A (Fig. 3.5B), D185A and H193A on S3 (Fig. 3.5C), as well as N214A on S4 (Fig. 3.5D). Although many of these mutants showed some effect on either the initial rate of H^+ conduction (e.g. D185A on S3; Fig. 3.5C) or on the fraction of empty vesicles measured (e.g. H140A on S2; Fig. 3.5B), none of these mutants completely abolished H^+ conduction. Differences in the fraction of empty vesicles indicated a higher proportion of non-functional channels in the vesicles. However, in each case, a significant proportion of the channels remained functioning and we are able to clearly observe H^+ conduction. Small effects of the mutations on the initial rate of fluorescence quenching may indicate a role for those amino acids in H^+ conduction; however, those roles are not critical, given that conduction is only slightly affected.

One H_V channel mutation that was reported to disrupt H^+ conduction in oocyte membranes expressing hH_V1 channels is N214R (Tombola *et al*. 2008). However, when we expressed purified and reconstituted this mutant at different protein-to-lipid ratios and tested it in our flux assay, we did not observe any significant difference in H^+ conduction compared to wild type hH_V1 channels (Fig. 3.6A). Another mutagenesis study on the mouse H_V (mVSOP) channel expressed in HEK cells and characterized by whole-cell patch clamp electrophysiology also found that the equivalent mutation N210R results in functional channels (Sakata *et al*. 2010).

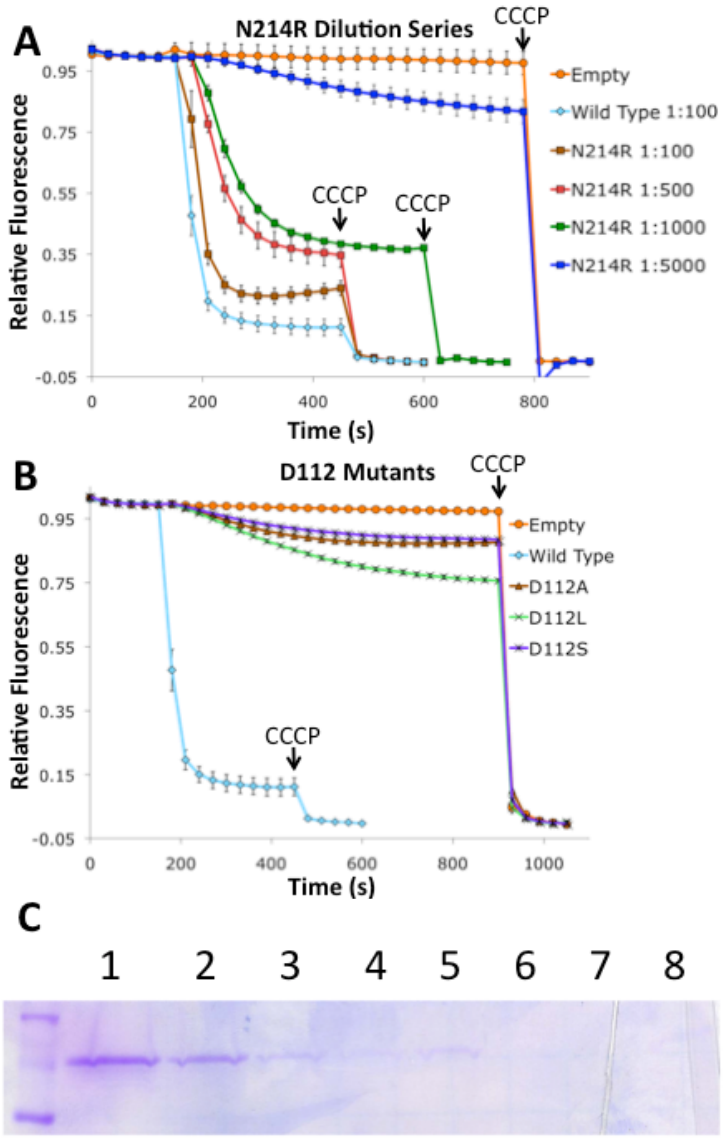

Fig. 3.6 H^+ flux into vesicles containing additional mutants of the hH_V1 channel

Fluorescence-based H^+ flux assay for vesicles containing mutant hH_V1 channels compared to vesicles containing wild type channels and empty vesicles. (**A**) Dilution series of the N214R mutation on S4. (**B**) Mutations at position D112 on S1; all channels were reconstituted at a protein-to-lipid ratio of 1:100 (wt:wt). In each case valinomycin was added at 150 s and CCCP was added where indicated. Each curve corresponds to the average of 3-4 repetitions with the error bars indicating the standard error of the mean. (C) Sucrose cushion of vesicles containing D112L hH_V1 channels demonstrating efficient reconstitution. Numbers denote the fractions collected from top to bottom.

3.2.2 Mutations that generate leaky vesicles

Another class of mutations, e.g. E171A and D147A on S3 (Fig. 3.6C); and R205A, R208A and R211A on S4 (Fig. 3.6D), showed an initial decrease in fluorescence that was followed by a slow recovery. This may be explained by the mutations causing a membrane leak that allowed the passage of Na^+ or Cl^-, both of which are present in high concentrations in these experiments. After addition of valinomycin, the membrane potential was clamped at the equilibrium potential for K^+ (approximately -60 mV, negative inside relative to outside, calculated with equation 1.1). This negative potential creates a driving force for the entrance of H^+ into the vesicles. However, the negative electrical potential also creates a driving force for Cl^- to exit the vesicles (the concentrations of Cl^- is nearly symmetric across the vesicular membrane) and an even stronger driving force for Na^+ entry (there is a large Na^+ gradient across the membrane: 150 mM Na^+ outside vs. ~0 mM Na^+ inside). Therefore, if the mutation resulted in the generation of a leak for either of these ions, they would cross the membrane and dissipate the driving force for H^+ uptake into the vesicles.

Depending on the rate of the leak, it might still be possible to see the fast influx of H^+ followed by a slower dissipation of the H^+ driving force caused by the leak, after valinomycin addition. This would result in the slow efflux of H^+ from the vesicles and a slow recovery of the fluorescence signal (see below for a comparison between experiment and theory for leaky vesicles). To varying degrees, this is exactly what was observed for these mutant H_V channels (e.g. R205A in Fig. 3.5D), indicating that the mutation resulted in a Cl^- or Na^+ leak through the VSD. If the leaky VSD were permeable to K^+ in addition to Na^+ or Cl^-, a collapse of the K^+ gradient would begin prior to addition

of valinomycin, resulting in a lower overall fluorescence signal upon addition of valinomycin. This is what was observed for the R208A and R211A mutants (Fig. 3.6D). In fact, more recent electrophysiological experiments on R211 in hH_V1 indicate that mutation to Ser or Cys results in the leak of the organic guanidinium cation through the channel (Berger & Isacoff 2011).

Mutations of VSDs that result in a leak current through the VSD itself (the so-called "omega current") are relatively common and have been characterized in both K_V and Na_V channels (Tombola *et al*. 2006; Sokolov *et al*. 2005). Given the delicate structural balance that the VSD must fulfill— compensating the charges of the gating residues within the low electrical permittivity of the membrane— it is not surprising that mutation of charged residues within the transmembrane domain leads to disruption of the structure, producing a leak pathway for the conduction of ions. It is interesting to note that all of the mutations that caused significant leak resulted from the removal of a charged amino acid side chain (Fig. 3.5C and D).

3.2.3 D112 an interesting position

A single mutation significantly slowed the H^+ flux into the vesicles: D112L on S1 (Fig. 3.5A). Interestingly, an aspartate at this position on S1 is highly conserved in H_V channels, but the equivalent position in the VSDs of other voltage-gated cation channels is a serine (Fig. 3.5; Musset *et al*. 2011). If this mutation only affected the rate of H^+ conduction, we would expect that, given enough time to equilibrate, the same H_V dependent fluorescence quenching (F_{Hv}) would be observed when compared to wild type. However, even if the experiment is run over long time courses, the fluorescence

quenching seen in the D112L mutation never reached the same levels as wild type (Fig. 3.6B). Since the D112L reconstitution occurs efficiently (Fig. 3.6C), this indicates either that there are a larger proportion of non-functional channels in the vesicles, or that there is a leak current that results in partial dissipation of the electrical driving force, resulting in a stable steady state level of H^+ uptake and fluorescence-quenching (see below for a theoretical analysis incorporating Cl^- leak).

To further investigate the potential role of D112 in the mechanism of H^+ conduction, two additional mutations were made: D112S and D112A, both of which also displayed a significant decrease in H^+ flux (Fig 3.6B). More recent electrophysiological experiments have demonstrated that mutation of D112 can make the channel leak Cl^- ions (Musset *et al*. 2011). In that study, both the D112S and D112A mutations were shown to have a strong Cl^--dependent shift in the reversal potential of the measured current, indicating Cl^- conduction through the H_V channels (Musset *et al*. 2011). The D112L mutation was not investigated in that study; however, Musset *et al*. did generate D112N and D112F, both of which also showed Cl^- conduction (Musset *et al*. 2011). Therefore, it is likely that the D112L mutation also results in Cl^- leak, which would account for our observations in the flux assay that this mutant doesn't show the same steady state level of H_V dependent fluorescence quenching (F_{Hv}) as wild type channels (Fig. 3.5A and 3.6B).

Because the D112L mutation alters H^+ conduction through the channel in the flux assay (Fig. 3.5A and 3.6B) and the D112V mutation, examined by Musset *et al*., completely abolished conduction though the channel (Musset *et al*. 2011), it has been postulated that D112 is critical to both the conduction and selectivity of H_V channels. However, whether the aspartate is sufficient remained unknown. To determine if an

aspartate at the equivalent position as D112 in S1 is sufficient to induce H^+ flux through VSDs, we generated the S38D mutation in the isolated-VSD of K_VAP (Fig. 3.7). As shown in Fig. 3.3, removal of the K_VAP VSD from the pore domain revealed a possible intrinsic potential for H^+ conduction: a slow H^+ conduction was observed in the reconstituted isolated VSD. However, when we made the mutation S38D, we saw a significant increase in the rate of H^+ conduction through the isolated VSD (Fig. 3.7). This indicates that an aspartate at this position on S1 is sufficient to promote H^+ conduction through the VSD.

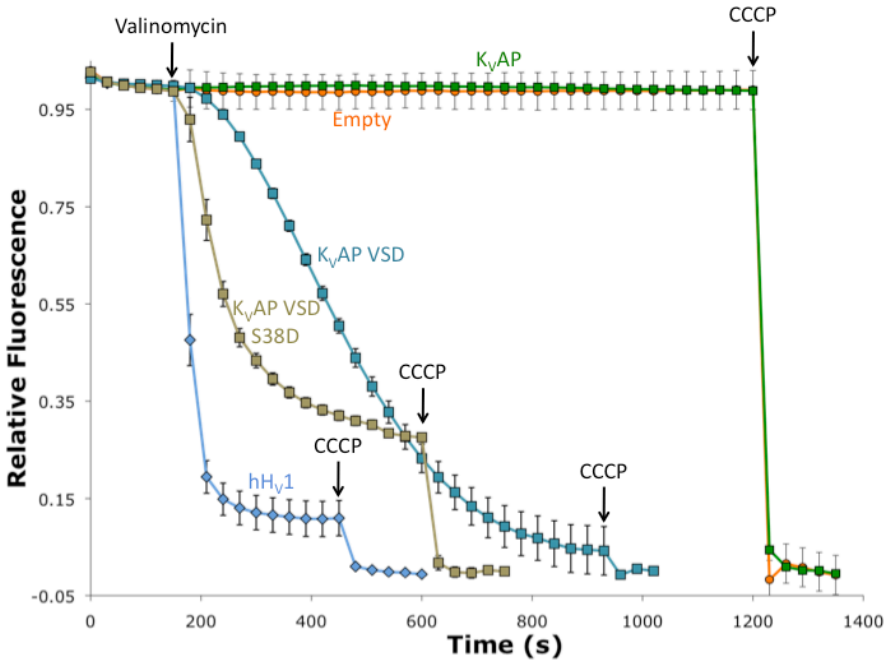

Fig. 3.7 D112 in S1 is sufficient for H^+ conduction

Fluorescence-based H^+ flux assay for vesicles containing the wild type (blue) and S38D mutant (brown) K_VAP isolated VSD compared to vesicles containing full-length K_VAP (green) channels, hH_V1 channels (cyan) and empty vesicles (orange). Each curve corresponds to the average of 3-4 repetitions with the error bars indicating the standard error of the mean. Valinomycin and CCCP are added at the indicated time points. K_VAP channels, K_VAP VSD, and K_VAP VSD S38D were expressed and purified according to published procedures (Jiang *et al*. 2003a). Reconstitutions were carried out as described in materials and methods with the following protein to lipid ratios (wt:wt) 1:100 (KvAP), 1:200 (KvAP VSD), and 1:200 (KvAP VSD S38D).

3.3 MODELING H^+ CONDUCTION THROUGH RECONSTITUTED H_V CHANNELS

3.3.1 Understanding the time course of fluorescence decay

Although we are unable to determine the H^+ conduction rate we can ask to what degree the time course of fluorescence decay is at least qualitatively consistent with our expectation based on theory. We simulated H^+ flux into a population of vesicles with a mean number of μ channels per vesicle assuming that a vesicle will have n channels with subset m facing outside-in with a frequency:

$$f(n,m) = \frac{n!}{m!(n-m)!}\left(\frac{1}{2}\right)^n \frac{\mu^n}{n!} e^{-\mu} \qquad \{3.3\}$$

Upon addition of valinomycin, the membrane potential is driven to very near the Nernst equilibrium potential for K^+ (about -60 mV inside calculated from equation 1.1) because the K^+ permeability exceeds H^+ conductance under all conditions in the simulation (see equation 1.2). We modeled H_V voltage-dependent gating with a two-state Boltzmann function with midpoint activation voltage V_{mid} = 40 mV and valence 3 (Ramsey *et al*. 2006; DeCoursey 2008).

The change in internal H^+ concentration was calculated using the algorithm described in Moffat *et al*. with slight modifications (Moffat *et al*. 2008). To account for the voltage-dependent gating property of the H_V channels, the proton flux (J_H) was calculated by equation 3.4, where G_H is proton conductance, V is the membrane potential, E_H is the equilibrium potential for H^+, F is Faraday's constant, z is the effective gating charge (a value of 3.0 e_0 was used; (DeCoursey 2008; Qiu *et al*. 2013; González *et al*.

2013), V_{mid} is the midpoint voltage of activation for H_V (a value of 40 mV was used; Ramsey *et al*. 2006), R is the ideal gas constant and T is the absolute temperature in Kelvin (298 K).

$$J_H = \frac{G_H(V - E_H)}{F\left(1 + \exp\left(\frac{-zF(V - V_{mid})}{RT}\right)\right)} \qquad \{3.4\}$$

The algorithm was run successively for a unit volume of one vesicle of radius 100 nm with n channels (where n = 1, 2, 3,...,30), either facing outside-in or outside-out (expressed as a multiplier of either 1 or -1 on the V in the two-state Boltzmann). This basic set of 60 time courses representing the internal pH change of the vesicle was combined to generate the expected flux of a population of vesicles each containing n channels according to equation 3.5, where n signifies the total number of channels and m the number of channels facing outside-in.

$$f(n,m) = \frac{n!}{m!(n-m)!}\left(\frac{1}{2}\right)^n \qquad \{3.5\}$$

Since the flux from channels facing outside-in is much greater than the flux due to channels facing outside-out (by more than 3 orders of magnitude), we applied the simplifying assumption that flux into any vesicle containing channels in both orientations was equal to the flux generated by only the channels facing outside-in. This operation results in a new basis set of 30 time courses that correspond to the H^+ flux into

populations of vesicles with total of n channels in either orientation (where n = 1, 2, 3,…,30). This new basis set was then applied to the distribution of vesicles with n channels at the various protein-to-lipid ratios used according to equation 3.6, where $f(n)$ is the fraction of vesicles with n channels, ϕ is the fraction of functional H_V channels (a value of 1.0 was used), θ is the fraction of reconstitution deficient vesicles (a value of 0.15 was used) and μ is the ratio of number of channels to number of vesicles (see equation 3.1).

$$f(n) = \left(\frac{\phi}{(1-\theta)}\right)^n \frac{\mu^n}{n!} \exp\left(\frac{-\phi\mu}{(1-\theta)}\right) \qquad \{3.6\}$$

All simulations were performed using MATLAB and the code can be found in Appendix I.

3.3.2 Comparing Experimental Results and Simulations

Fig. 3.8A graphs the simulation results for populations of vesicles with channels distributed according to equation 3.3. If one focuses on a single vesicle, a value 1.0 on the y-axis corresponds to a free (unbound) internal H^+ concentration of 10^{-7} M and a value 0 corresponds to a free internal H^+ concentration of 10^{-6} M. During the simulation, the free internal H^+ concentration in the given vesicle changes from 10^{-7} to 10^{-6} (approximately), following a time course that depends on the number of channels and their orientation in the vesicle. The graph shows the weighted sum of time courses for all vesicles (including empty) in the population for a 200 s interval. The curves show a fast decay followed by a

slower one at smaller values of μ: the slower component is attributable mainly to a fraction of vesicles with only outside-out channels, which have a very low open probability. The curves also show a negative second derivative (curvature) at early time points, due to H^+ buffering inside the vesicles. These same qualitative features are observed in fluorescence decay data (Fig. 3.8B).

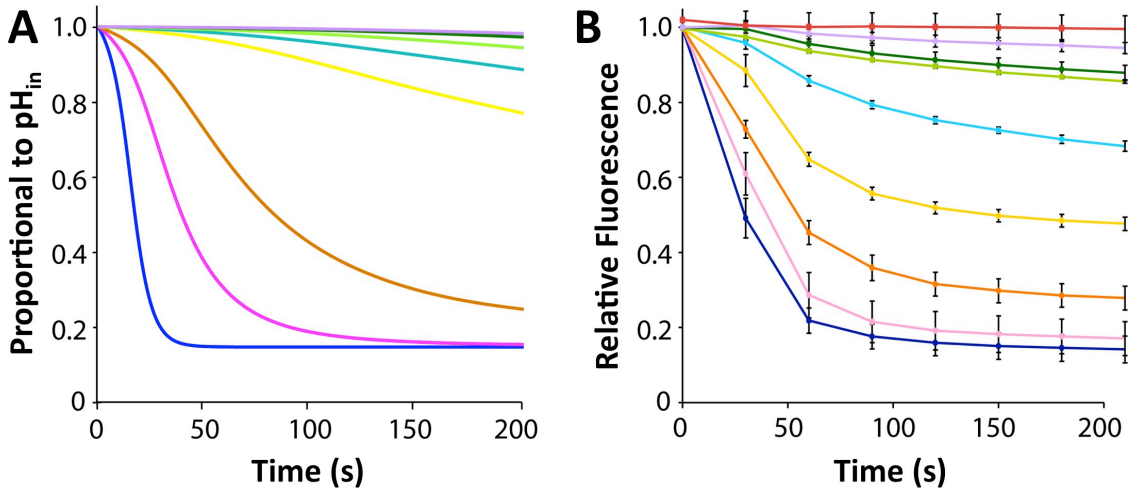

Fig. 3.8 Comparison of dilution series data with theory

(A) Theoretical curves for the decrease of internal pH over time at the equivalent protein to lipid ratios as in Fig 3.2A, scaled with the theoretical fraction of empty vesicles. Curves are colored to match the equivalent experimental traces in Fig 3.8B; a theoretical curve corresponding to empty vesicles is not shown. Simulations were all performed using MATLAB. **(B)** Experimental fluorescence traces from Fig. 3.2A highlighting the first 200 seconds after the addition of valinomycin.

The theoretical and experimental curves are different in two obvious respects. As a function of μ, the curves do not exhibit the same spacing between them. We think this most likely reflects the nonlinear (and unknown) relationship between free internal H^+ concentration and fluorescence (Fiolet *et al*. 1974). We emphasize that this unknown relationship prevents us from determining H^+ flux rates, but it does not prevent us from determining the fraction of vesicles with no channels versus vesicles with at least one channel (Fig. 3.2A and equation 3.2). The second difference between theory and experiment is a more prominent slow component of fluorescence change in the data, which is consistent with channel-independent H^+ leak in the vesicles (which we have not included in the model).

In the simulation, the curves correspond to an open channel conductance of 0.1 fS. This value should not be taken as an accurate determination of H_V channel conductance for the reasons discussed above. However, this value is smaller than the reported conductance measured electrophysiologically – 10-100 fS (Cherny *et al*. 2003; DeCoursey 2008) – by a factor too large to be accounted for by the unknown relationship between H^+ concentration and fluorescence. One possibility is that the values used for V_{mid} in our two-state Boltzmann distribution (equation 3.4) result in an overestimation of the open probability of the channel. Although these values were taken from the literature (Ramsey *et al*. 2006; DeCoursey 2008), it is well established that, due to H^+ depletion effects and the strong dependence of H_V channel gating on the transmembrane pH gradient, it is difficult to get an accurate measure of V_{mid} (DeCoursey 2008). Also, there is debate as to what the exact value of the valence of H_V channels gating (z) is, with experimental values ranging 2-3 (Fujiwara *et al*. 2012; González *et al*. 2013). The

ambiguity in these values would only have a minor effect on the results from our model; however, they are sources of uncertainty that could contribute to underestimation of the unitary conductance. Additionally, our model treats each subunit of the dimeric H_V channels as independently gating, whereas more recent data in the literature has established that the subunits behave cooperatively (González *et al*. 2010; Tombola *et al*. 2010; Musset *et al*. 2010b). Cooperativity would also affect the open probability of the channels in our simulation.

3.3.3 Simulating the effect of Na^+ and Cl^- leak on H^+ uptake

Because some of the mutations we have investigated with the flux assay have been shown to cause leak through the hH_V1 channel (Berger & Isacoff 2011; Musset *et al*. 2011), we can ask how much does the time course of fluorescence signal observed for these mutants agree with theory incorporating a Na^+ or Cl^- leak in the membrane? Na^+ and Cl^- leak can be easily incorporated into equivalent circuit flux algorithm described in section 3.3.1 (and by (Moffat *et al*. 2008) by the addition of flux terms for the permeant ions. These flux terms are defined in equation 3.7 for Na^+ flux (J_{Na}) and equation 3.8 for Cl^- flux (J_{Cl}), where G_{Na} is the conductance of Na^+, E_{Na} is the Nernst equilibrium potential for Na^+, G_{Cl} is the conductance of Cl^-, E_{Cl} is the Nernst equilibrium potential for Cl^- and all other terms are defined as in equation 3.4.

$$J_{Na} = \frac{G_{Na}}{F}\left(V - E_{Na}\right) \qquad \{3.7\}$$

$$J_{Cl} = -\frac{G_{Cl}}{F}\left(V - E_{Cl}\right) \qquad \{3.8\}$$

For simplicity the added Na^+ and Cl^- leak conductances were modeled as independent of H_V channel gating. Versions of the algorithm that incorporated H_V channel state dependence into the leak currents did not alter the shapes of the curves calculated but only slightly altered the kinetics and final steady state positions for the theoretical pH_i. This modified algorithm can be found in Appendix I.

Fig. 3.9A shows theoretical curves calculated from the algorithm used for simulation of the H^+ flux into the vesicles with the addition of Na^+ leak. These curves recapitulate the main features of the data for the leaky mutants E171A, D147A, R205A and R208A (compare Fig. 3.5C and D to Fig. 3.9A). Additionally, by increasing g_{Na} in the simulation, theoretical curves similar to the data for R211A can also be produced. Fig 3.9B shows the theoretical curve for the simulation of H^+ flux into the vesicles with the addition of Cl^- leak. The theoretical curve in Fig. 3.9B (bottom) differs from the data in that the H^+ flux reaches a steady state more quickly than what is seen in the D112L mutant fluorescence data. This discrepancy can be understood if the D112L mutation also decreased the H^+ conductance. In order to reduce bias, the H^+ conductance was kept the same as for the simulations in Fig 3.8 during the leak simulations (Fig. 3.8).

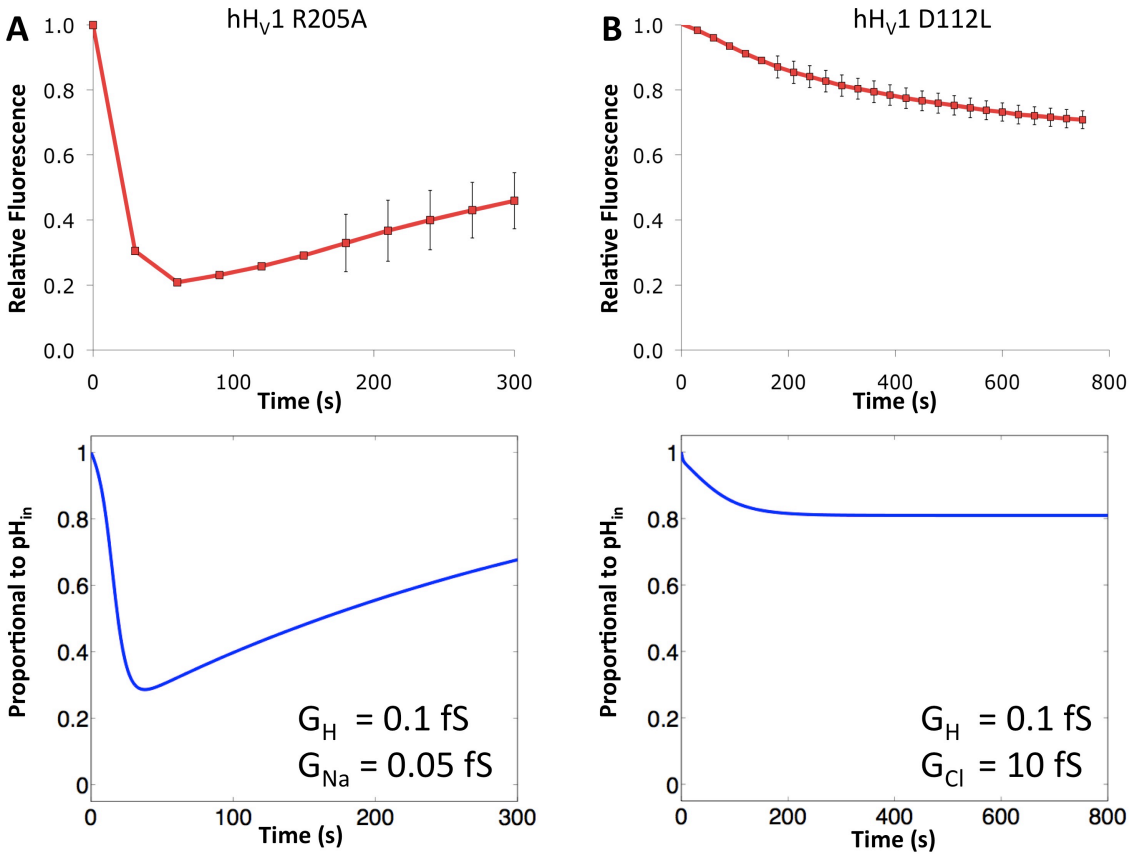

Fig. 3.9 Comparison of mutant data to theory incorporating leak conductances

(A) Comparison of R205A mutant channel flux data (top) to theoretical curves for the decrease followed by slow recovery of internal pH over time incorporating a Na^+ conductance (G_{Na}) in the membrane of 0.05 fS scaled with the theoretical fraction of empty vesicles (0.15, bottom). Simulations were all preformed using MATLAB. **(B)** Comparison of D112L mutant channel flux data (top) to theoretical curves for the decrease of internal pH over time incorporating a Cl^- conductance (G_{Cl}) in the membrane of 10 fS scaled with the theoretical fraction of empty vesicles (0.15, bottom). Simulations were all preformed using MATLAB according to the protocol described in section 3.2 with protein-to-lipid ratios of 1:100 (wt:wt).

3.4 DISCUSSION AND FUTURE DIRECTIONS

The data presented in this chapter clearly establish the ability of the putative hH_V1 channel to conduct H^+ (Lee *et al*. 2009b). Furthermore, through mutagenesis studies on the transmembrane domain, we identified an interesting amino acid residue position— D112 on S1— which, when mutated, impairs the channel's ability to conduct H^+. This finding has since been confirmed electrophysiologically by Musset *et al*., who demonstrated that mutation of this position can lead to Cl^- leak through hH_V1 and that the D112V mutant is incapable of conducting ions (Musset *et al*. 2011). By mutating the equivalent position on S1 of the K_VAP isolated VSD to aspartate (S38D), we demonstrated that an aspartate at this position is sufficient to promote H^+ conduction through VSDs.

Going forward, it would be interesting to generate, purify and reconstitute the D112V mutant and to test it for H^+ flux in our assay. Given that Musset *et al*. failed to see any conduction through the D112V mutant channel even though it was efficiently expressed to the cell membrane (Musset *et al*. 2011), we would expect that this mutant would completely abolish H^+ flux in our assay. In order to fully understand the role of D112 in conduction, it would be ideal to solve the structure of the channel in both the conductive and non-conductive states. Because of the delicate charge balance that is found in VSDs, one may expect that mutations of D112 to an uncharged residue may disrupt the protein's stability. However, given that the D112L mutant channel displayed greater stability in detergent than wild type hH_V1 in our expression and purification experiments, we believe that the D112L mutant may constitute a good structural target.

Many of the mutants we characterized in our flux assay show behavior consistent with the generation of a leak conductance through the membranes (Fig. 3.9). However, in order to confirm whether these mutations cause the production of leaky VSDs these mutants will have to be expressed in cell membranes and characterized electrophysiologically. The cases in which the indicated mutants or similar mutants have been characterized electrophysiologically have demonstrated that leak currents exist through the channel (Berger & Isacoff 2011; Musset *et al*. 2011).

CHAPTER 4: CRYSTALLOGRAPHY

One major goal of my doctoral work was to obtain the structure of the human voltage-gated H^+ channel (hH_V1), in order to shed light on the unique properties of H_V channels. Although structures may not provide direct mechanistic insight, they do provide a model for hypothesis generation, which can then be followed up by functional studies. Before I joined the lab, Dr Seok-Yong Lee had done initial construct design and crystallization screening on hH_V1. My work described here follows from Dr Lee's initial work, and we worked as a team for the first three years.

In our efforts to crystallize the hH_V1 channel, Dr Lee and I generated many different constructs (discussed below), which were tested for expression and biochemical stability. Biochemical stability here is defined as monodispersity on a size exclusion chromatography (SEC) column after remaining in solution undisturbed at high concentrations for 5-7 days, as monodispersity on SEC has been shown to correlate well with crystallizability (Kawate & Gouaux 2006). Only biochemically stable constructs were pursued in crystallization trials.

In addition to hH_V1, 21 other putative H_V channel genes were synthesized and screened for biochemical stability. Appendix II contains the sequences of all genes synthesized and shows a multiple sequence alignment between all of the putative H_V channel genes as well as the voltage sensor domain of rat $K_V1.2$. Dr Scott Hansen a

postdoctoral fellow in the lab joined Dr Lee and I in this effort, which unfortunately failed to identify any other promising functional targets. The putative H_V channel from the plant genus *medicago* was biochemically well behaved but when reconstituted into lipid vesicles did not result in any H^+ conduction and was therefore set aside.

4.1 Native and Fusion Protein Crystallographic Attempts

4.1.1 Crystallography of wild type truncated channels

Despite many attempts, crystals of the full-length hH_V1 never grew. This is not surprising, given that the acid-and-proline-rich N-terminus of hH_V1 is predicted to be disordered. To increase crystallizability by removal of the unstructured regions, Dr Lee worked with Dr Qingjun Wang (Laboratory of Mass Spectrometry and Gaseous Ion Chemistry at the Rockefeller University) to define the structural core of the hH_V1 channel by limited proteolysis and by mass spectroscopy. Upon the identification of two trypsin-sensitive sites (at amino acid R83 in the N-terminus, preceding the transmembrane domain, and at K221, between the transmembrane domain and the coiled coil), Dr Lee designed two truncated constructs: one with the C-terminal coiled coil removed ($hH_V\Delta C$) and one with both N- and C-termini removed ($hH_V\Delta N\Delta C$).

Expressing these constructs in *Pichia pastoris* and using the high affinity 1D4-tag for purification, Dr Lee was able to purify both constructs and grow small crystals of the $hH_V\Delta N\Delta C$ construct (Fig. 4.1A). These truncated channels crystallized under many conditions; however, none diffracted better than ~10 Å (Fig. 4.1B). Nevertheless, this was encouraging, since similar diffraction had been previously observed for the isolated

voltage-sensor domain (VSD) of the voltage-gated K^+ channel K_VAP. When an antigen-binding fragment (Fab) of an antibody raised against the isolated VSD of K_VAP was used as a crystallization chaperone, Jiang *et al*. were able to solve the structure of isolated VSD to 1.9 Å resolution (Jiang *et al*. 2003a). Therefore, by analogy, we reasoned that, if we could obtain a Fab against the hH_V1 channel and use it in crystallization, we should be able to obtain crystals with improved diffraction.

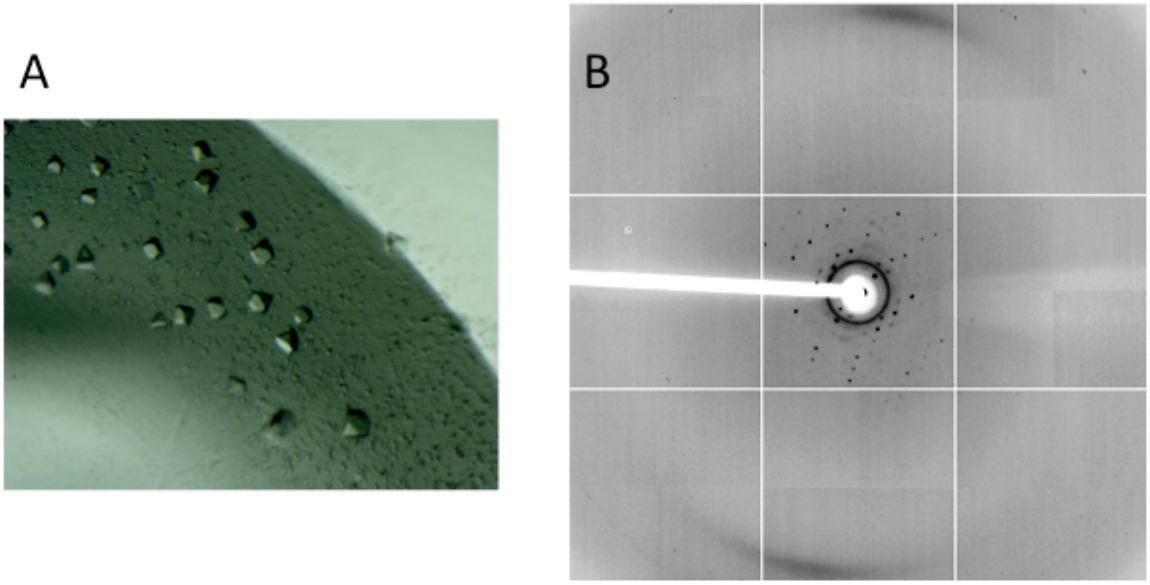

Fig. 4.1 Best diffracting crystals of $hH_V\Delta N\Delta C$

(A) Representative crystals of $hH_V\Delta N\Delta C$ grown in DM/HEGA9 detergent at 30% PEG400, 50 mM NaAcetate pH 4.5. (B) Best diffraction from crystals shown in (A), resolution extends to 9.6 Å, apparent space group is F23 a=b=c=169.7 Å. Weak diffraction is also seen for a unit cell with an alternate orientation indicating possible twinning. These crystals were grown and their diffraction tested by Dr Seok-Yong Lee.

4.1.2 Raising antibodies against hH_V1

We attempted raising antibodies against both the wild type and truncated ($hH_V\Delta N\Delta C$) hH_V1 channels by mouse injection. The only anti-hH_V1 antibodies that were isolated were against an intracellular C-terminal coiled-coil epitope, which, according to the limited proteolysis studies, is connected to the transmembrane domain by a flexible linker. Although these antibodies worked well in Western blots and were used for the stoichiometry studies discussed in Chapter 2, no crystals of hH_V1-Fab complex grew in our crystallization trials. Given that Fabs that were successful for the crystallization of the K_VAP isolated VSD were targeted towards an extracellular loop of the transmembrane domain (the S3-S4 helix-turn-helix motif known as the voltage-sensor paddle), an anti-hH_V1 antibody that targeted the voltage-sensor paddle of hH_V1 was desirable. An additional round of mouse injections was performed with the $hH_V\Delta N\Delta C$ doubly truncated construct, with injections of the channel reconstituted in lipid vesicles, followed by boosters of detergent-solubilized channels. As in the wild type case, we were unable to isolate any anti-hH_V1 antibodies.

Because mouse injection has been very successfully applied in the MacKinnon laboratory for raising antibodies against membrane proteins (Zhou *et al*. 2001; Dutzler *et al*. 2003; Jiang *et al*. 2003a; Brohawn *et al*. 2013), a purely technical reason for our failure was unlikely. A possible explanation is that, given the human and mouse H_V channel sequence-similarity (78% identical over the entire sequence and 84% identical within the transmembrane domain alone), the hH_V1 channel may not be sufficiently immunogenic in mice to produce a strong antibody response.

In order to address this possible issue, we attempted another round of mouse injections using chimeric channels that contained the voltage-sensor paddle of hH_V1 spliced into the K_VAP isolated VSD, reasoning that the H_V sequence presented in this context should increase the immunogenicity. We built and characterized six chimeras based on three possible K_VAP/hH_V1 alignments (Fig. 4.2A and B). Although the chimeric channels expressed well and were biochemically well behaved (Fig. 4.2C), they were not sufficiently immunogenic for us to be able to isolate any anti-hH_V1 Fabs.

More recent work in the literature has demonstrated that hH_V1 channels play a physiological role in B-cell receptor signaling: hH_V1 knockdown in B-cells results in impaired antibody production (Capasso *et al*. 2010). Thus, it is likely that there is a negative selection against B-cells that produce high-affinity anti-H_V1 antibodies that are able to bind to extracellular epitopes. Such negative selection is a possible explanation as to why we were unable to raise any antibodies by mouse injection.

Despite these setbacks, we still reasoned that it should still be possible to improve the diffraction of hH_V1 crystals with a crystallization chaperone. Two additional strategies were attempted to this end: fusion proteins and epitope-swapped chimera. The fusion protein strategy was ineffective and I will only discuss it briefly below. The epitope-swapped chimera will be more fully discussed in the following section.

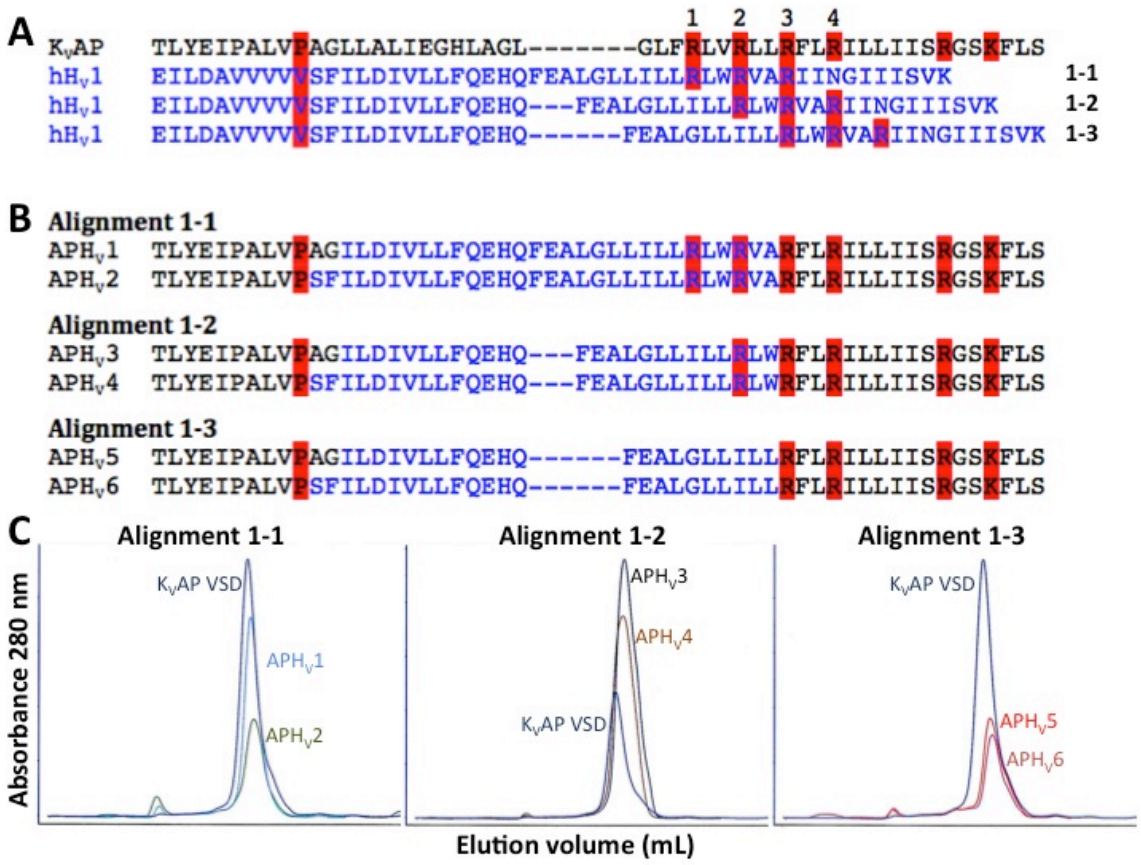

Fig. 4.2 Sequences and biochemical stability of K_VAP VSD-hH_V1 paddle chimeras

(A) Three possible registers for sequence alignments between the S3-S4 paddle motif of K_VAP (in black) and hH_V1 (in blue). The numbers above the K_VAP sequence denote the positions of the gating-charge arginines (highlighted red in all sequences) for the first alignment. The alignments are named based on the relative position of the first hH_V1 gating-charge arginine with respect to the K_VAP gating-charge arginines. For example alignment 1-1 aligns the first arginine of hH_V1 with the first arginine of K_VAP, alignment 1-2 aligns the first arginine of hH_V1 with the second arginine of K_VAP etc. (B) Paddle sequences of the six chimeric (APH_V) constructs built, organized by the alignment that was used for their construction. (C) SEC profiles of each chimeric construct organized by alignment. Each chromatogram contains the K_VAP VSD curve (blue) to allow for comparison of expression levels. From these data it is clear that, although all constructs are monodisperse, we are able to purify larger quantities of APH_V3 and APH_V4 from the 1-2 alignment.

4.1.3 Lysozyme Fusion Proteins

The fusion of the highly crystallizable enzyme lysozyme into the transmembrane domain loops of membrane proteins has been used as a chaperone strategy to crystallize difficult membrane protein targets. For instance, this strategy was used to determine the structure of the first G-protein coupled receptor (GPCR; Rosenbaum *et al*. 2007). We attempted this strategy by splicing lysozyme into both extracellular loops of the $hH_V\Delta N\Delta C$ construct (the S1-S2 and S3-S4 loops). At low concentrations, the lysozyme fusions looked promising; however, they readily aggregated at high concentration. Optimization of linker length between the hH_V1 and lysozyme sequences was carried out, but no construct was sufficiently well behaved for large-scale crystallization attempts. Because of this tendency for aggregation, the lysozyme fusion strategy was abandoned.

4.1.4 Dimerization Fusion Proteins

Since we knew from our cross-linking studies that hH_V1 is a dimer in the membrane, we reasoned that by fusing readily crystallizable dimeric protein onto hH_V1 we might be able to promote crystallization. A major criterion for the fusion partner would be for it to have its N- or C-terminus arranged in the dimer such that it would be positioned to align with our experimental model of the hH_V1 dimer (see Fig. 2.5 on page 48). Four top candidates were identified from the protein data bank: secretion chaperone CsaA (accession code 2NZH; Shapova & Paetzel 2007), F420H2:$NADP^+$ oxidoreductase (FnO; accession code 1JAX; Warkentin *et al*. 2001), the bleomycin resistance determinant (Bleo; accession code 1ECS; Maruyama 2000) and 4-diphosphocytidyl-2-C-methylerythritol synthetase (CDP; accession code 1INJ; Richard *et al*. 2001). Two of these proteins were selected for

N-terminal fusion (FnO and CDP) and two for C-terminal fusion (Bleo and CsaA) to the $hH_V\Delta N\Delta C$ construct. For each fusion, four or five different constructs were built to optimize linker length. After much effort, however, and although some of the constructs generated well-behaved dimeric chimera, no fusions gave crystals. Therefore, this approach was also abandoned.

4.2 H_V1-K_VAP Epitope-Swapped Chimera

4.2.1 Design and selection of hH_V1-K_VAP paddle chimera

As discussed in the previous section, by analogy to the K_VAP isolated VSD, we reasoned that Fab-mediated crystallization would facilitate structure determination of $hH_V\Delta N\Delta C$. Since we were unable to raise antibodies against wild type hH_V1 channels by mouse injection or to obtain crystals by the fusion protein strategy, we needed to innovate. It occurred to us that it should be possible to make a hH_V1-K_VAP (HAP) chimera in which the paddle epitope that is responsible for binding anti-K_VAP Fabs is spliced into the hH_V1 sequence. It has been previously demonstrated that the paddle motif can be swapped between different VSD of voltage-gated cation channels and still produce functional voltage-gated cation channels (Alabi *et al*. 2007). In this way, we could generate functional chimeric H_V channels that would bind to the anti-K_VAP Fabs, allowing us to use the anti-K_VAP Fabs as crystallization chaperones.

Due to the ambiguity in the sequence alignment between hH_V1 and K_VAP along the S4 helix, many different constructs needed to be built and characterized before crystallization trials could proceed. Based on three different possible hH_V1 and K_VAP S4

alignments, 17 chimeras were constructed (Fig. 4.3) and each was expressed in both full length and C-terminally truncated forms (ΔC). Small-scale purification and biochemical characterization using size exclusion chromatography (SEC) was carried out to gauge the stability of each chimeric channel. Two chimeras each with different alignment—HAP5ΔC and nHAP3ΔC—were chosen as the best candidates for structure determination, based on their biochemical stability and Fab-binding. When probed for binding with the anti-K_VAP antibodies 33H1 and 6E9, both chimeras were ELISA- and Western-blot-positive, indicating that the antibodies were able to recognize the paddle epitope of the chimeric constructs (Fig. 4.4).

The HAP5ΔC chimera was highly stable, giving a stable monodisperse peak on the SEC column after several days at high concentrations at room temperature in DM (Fig. 4.5A-C). However, when mixed with anti-K_VAP Fabs and run over the SEC column, only a small complex peak was formed, with most of the protein eluting at positions characteristic of the channel and Fab alone (Fig 4.5D and E). This is in contrast to what is observed with wild type K_VAP channel or isolated VSD, which elute completely as VSD-Fab complex. This indicated that, although HAP5 is ELISA-positive for binding to 33H1 and 6E9 Fabs (Fig. 4.4), the interaction is much weaker than the binding of the Fabs to the wild type K_VAP VSD.

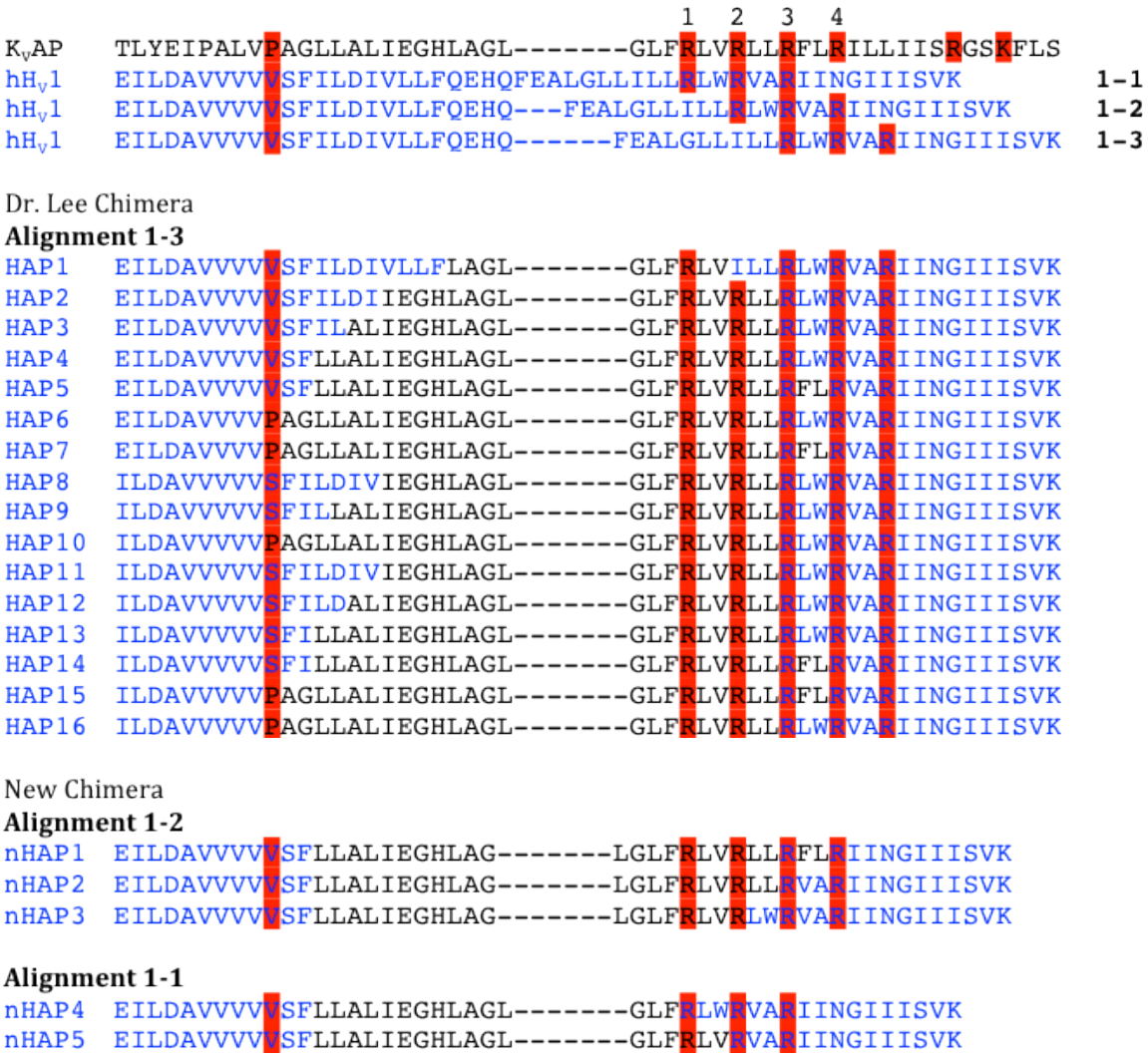

Fig. 4.3 HAP chimera construct sequences

(Top) Three possible registers for sequence alignments between the S3-S4 paddle motif of K_VAP (in black) and hH_V1 (in blue). The numbers above the K_VAP sequence denote the positions of the gating-charge arginines (highlighted red in all sequences) for the first alignment. The alignments are named as in Fig. 4.2. The first 16 HAP chimeras were generated and characterized by Dr Seok-Yong Lee and were all based on the 1-3 alignment. The "New Chimera" designated with an "n" were constructed based on the 1-2 and 1-1 alingments.

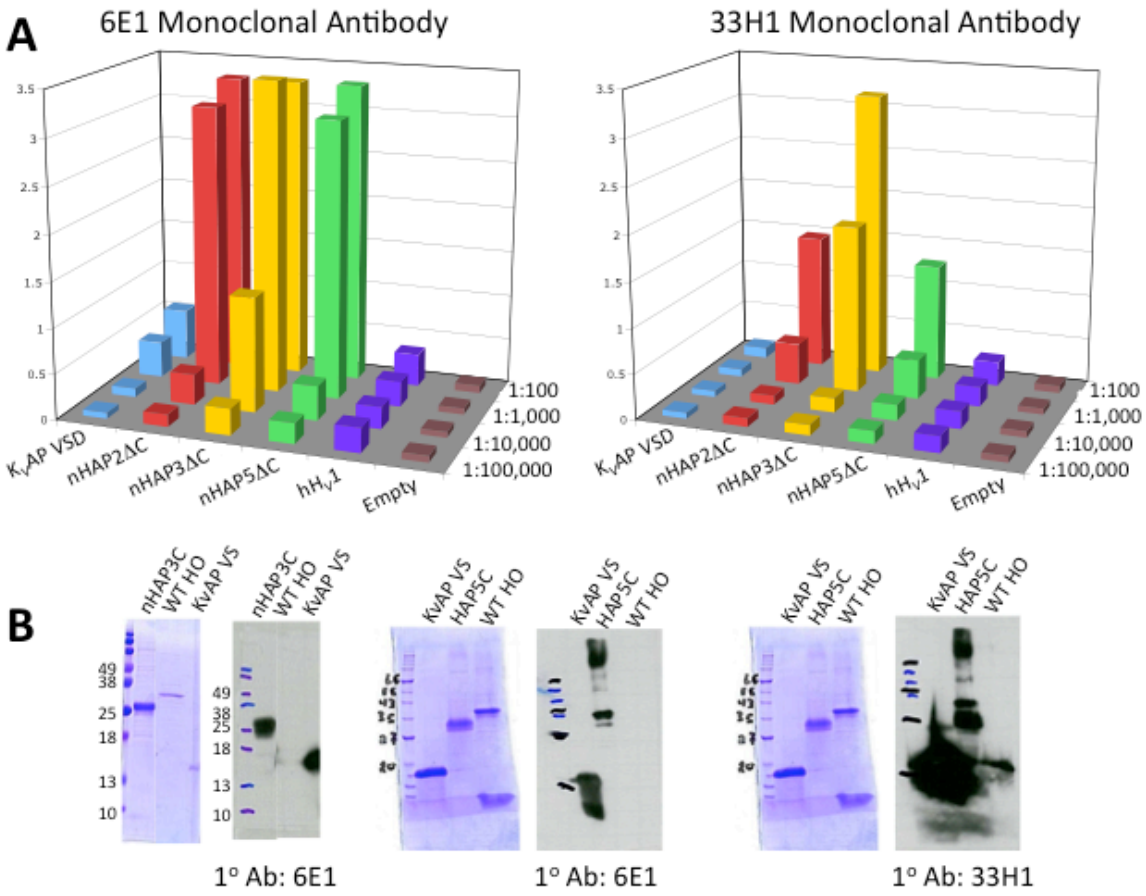

Fig. 4.4 ELISAs and western blots of chimeras using αK$_V$AP paddle antibodies

(**A**) Bar graphs of ELISA signal intensity as a function of Ab dilution (indicated on right) for K$_V$AP VSD (cyan), nHAP2ΔC (red), nHAP3ΔC (yellow), HAP5ΔC (green) and hH$_V$1 (purple) using the αKVAP monoclonal antibodies 6E1 (left) and 33H1 (right). The low signal seen for the K$_V$AP VSD is due to poor binding of this protein to the plates. (**B**) SDS-PAGE gels and corresponding western blots against the indicated chimera using the αKVAP monoclonal antibodies 6E1 (left and center) and 33H1 (right).

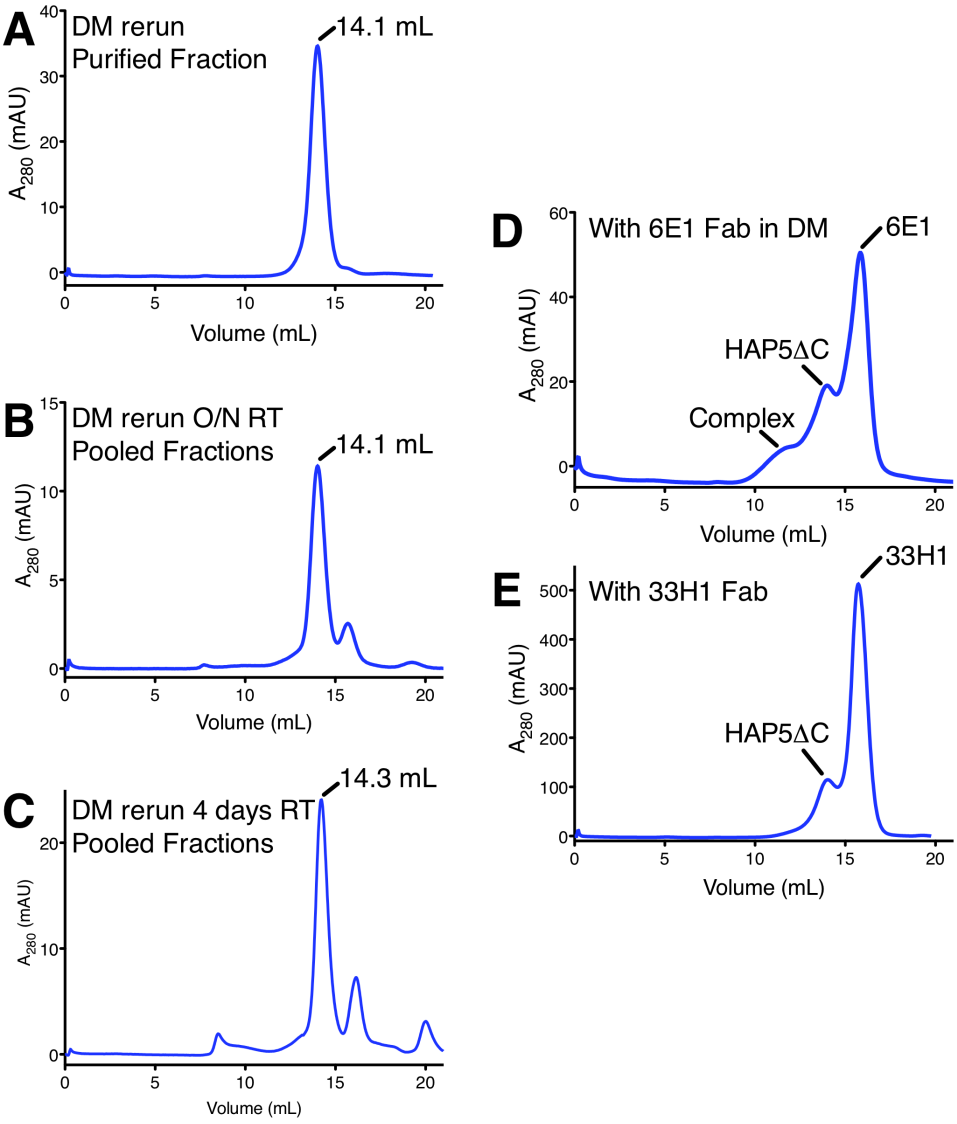

Fig. 4.5 Biochemical stability of HAP5ΔC and binding of αK$_V$AP paddle antibodies

(**A**) SEC chromatogram of rerun single concentrated fraction after initial SEC purification. (**B**) SEC chromatogram of pooled fractions from initial SEC run concentrated and left overnight (O/N) at room temperature (RT). (**C**) SEC chromatogram of pooled fractions from initial SEC run concentrated and left for 4 days at RT. (**D**) SEC chromatogram of HAP5ΔC with 6E1 Fab indicating some weak complex formation in DM. (**E**) SEC chromatogram of HAP5ΔC with 33H1 Fab indicating no significant complex formation. All SEC runs were done in DM.

The nHAP3ΔC chimera was less stable than the HAP5ΔC construct; nHAP3ΔC readily aggregated at high concentrations in DM (Fig 4.6A and B). However, in the more dispersive detergent LDAO nHAP3ΔC was more stable (Fig4.6C-E) and it eluted completely as complex with the anti-K_VAP 6E1 Fab on the SEC column (Fig. 4.6F), similar to the wild type K_VAP VSD. Because of the differences in the biochemical behavior of these two chimeras, it was decided that both would be pursued for structure determination.

In order to explore possible crystallization conditions, the detergent-stability profiles of the two chimeras was examined. After purification of the constructs in decylmaltoside (DM), small volumes of the protein were injected onto a SEC column equilibrated in the detergent of interest. Stability in the new detergent was judged based on the monodispersity of the protein peak eluting from the SEC column. In this way, 19 detergents were examined (Table 4.1). Consistent with the differential stability of the chimeras in DM (see Fig. 4.5A-C vs. 4.6A and B), the HAP5ΔC chimera was stable in a diverse array of detergents, whereas the nHAP3ΔC chimera was only highly stable in dispersive and lipid-like detergents (Table 4.1).

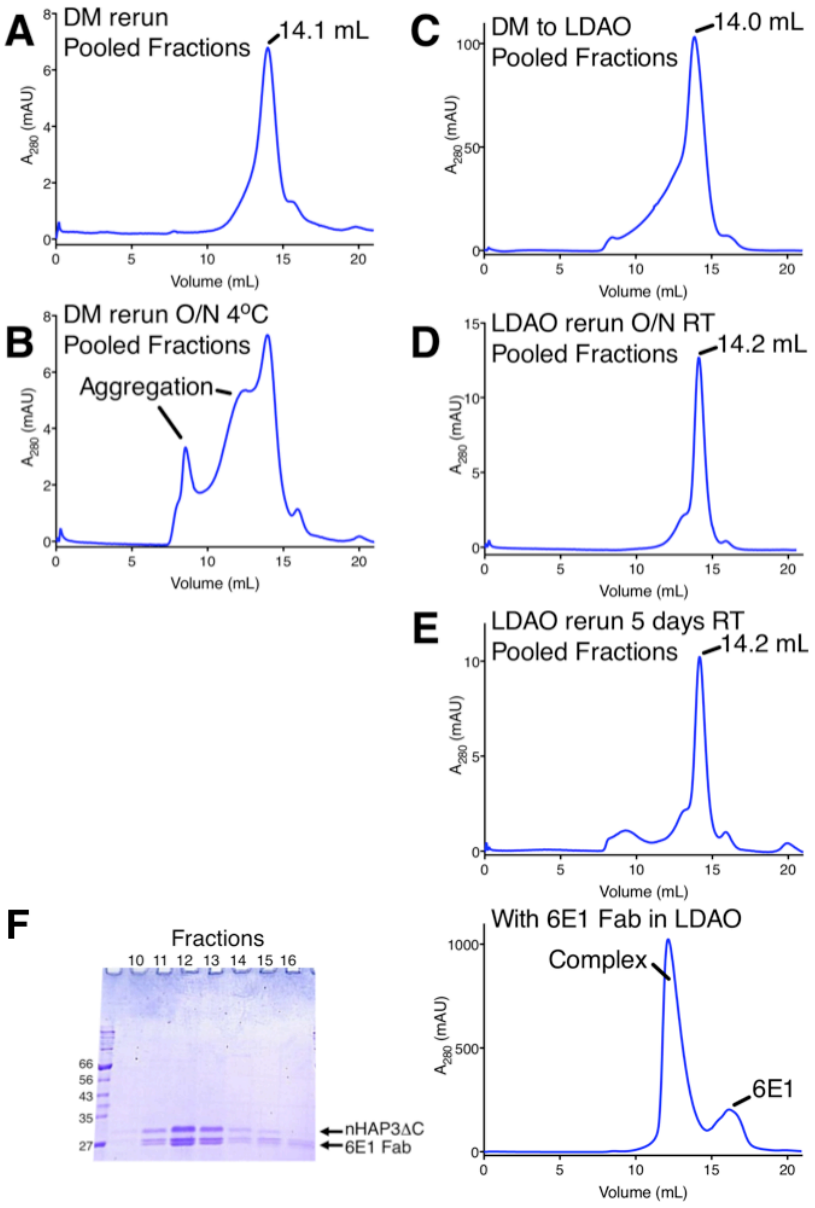

Fig. 4.6 Biochemical stability of nHAP3ΔC and binding of αK$_V$AP paddle antibodies (**A**) SEC chromatogram of rerun single concentrated fraction after initial SEC purification in DM. (**B**) SEC chromatogram of pooled fractions from initial SEC run concentrated and left O/N at RT in DM. (**C**) SEC chromatogram of detergent exchange from DM to LDAO. (**D**) SEC chromatogram of pooled fractions from (**C**) concentrated and left O/N at RT in LDAO. (**E**) SEC chromatogram of pooled fractions from (**C**) concentrated and left for 5 days at RT in LDAO. (**F**) Reducing SDS-PAGE gel (left) of SEC chromatogram (right) fractions for nHAP3ΔC with 6E1 Fab indicating complex formation in LDAO (right)

Detergent	HAP5DC	nHAP3DC
Maltosides		
DDM	A	D
UDM	A	C
DM	A	C
NM	B	-
OM	C	D
Glucosides		
DG/NG	A	-
NG	C	-
OG	F	F
Cymals		
Cymal-7	A	-
Cymal-6	A	D
Cymal-5	A	-
Polyoxyethers		
ANAPOE-C12E8	A	F
ANAPOE-C10E6	B	-

Detergent	HAP5DC	nHAP3DC
Miscelaneous		
DHPC	A	A
LDAO	A	A
Fos-12	A	B
Zwittergent 3-12	B	A
HEGA-9	D	-
LPPG	-	A

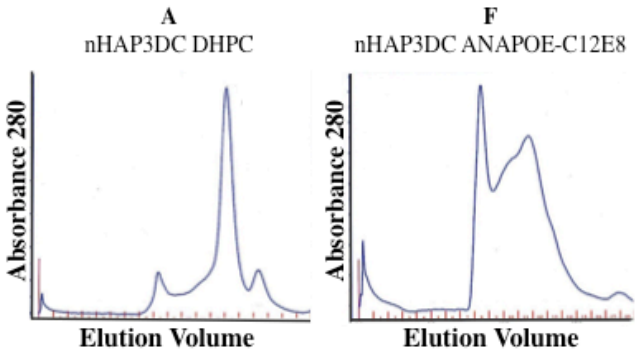

Table 4.1 Detergent stability profiles of HAP5ΔC and nHAP3ΔC chimeras

Detergent stability is graded qualitatively from A to F based on peak monodispersity during detergent exchange experiments on SEC. A dash (-) indicates that the experiment was not done. Inset shows an example A grade (left) vs. an example F grade (right).

Given the diversity of detergent conditions in which the chimeras were stable, many conditions needed to be explored for crystallization. Initial crystallization trials of HAP5ΔC and nHAP3ΔC with the 6E1 anti-K_VAP Fab gave small crystals in the case of the HAP5ΔC construct in DM (Fig. 4.7), but did not give any crystals in the case of the nHAP3ΔC in DM, LDAO or DHPC. However, crystalline precipitate was seen in many drops of the nHAP3ΔC/6E1 crystallization screens, indicating that it might be possible to further optimize the conditions to produce crystals. For HAP5ΔC, I was unable to

successfully refine the initial hits from 6E1 crystal screens, suggesting that alterations to the construct might be required to facilitate efficient crystallization.

Although the C-terminally truncated wild type hH_V1 ($hH_V\Delta C$) construct gave some crystals, truncation of both the N- and C-termini improved crystallizability (Fig. 4.1). Therefore, we reasoned that removal of the N-terminus might also be required to improve crystal formation of the chimeric constructs, as described below.

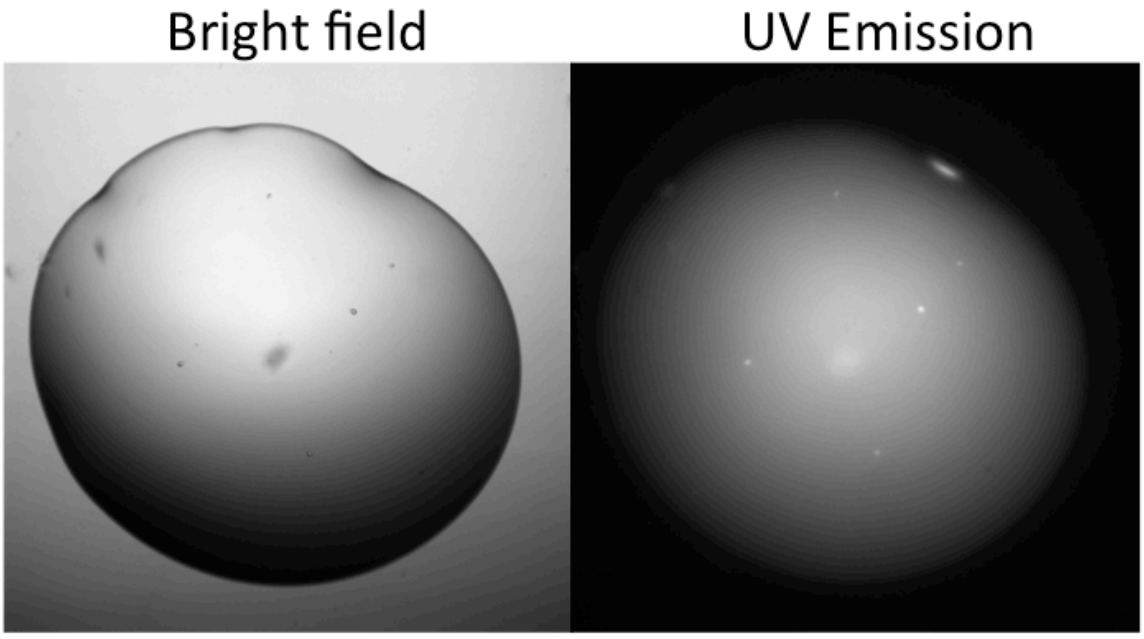

Fig. 4.7 Initial crystal hits for HAP5ΔC in complex with 6E1 Fab

Bright field (left) and UV emission (right) images of small crystals that grew in drops containing HAP5ΔC/6E1 in DM with 10-30% PEG400, 200 mM $CaCl_2$, 50 mM NaAcetate, pH 4.5. The fluorescent signal see in the UV emission image indicates that the crystals are protenacious.

4.2.2 Construct optimization and improvement of the initial crystals

In order to optimize the chimeric constructs in an unbiased manner, we performed limited proteolysis on both HAP5ΔC and nHAP3ΔC. In this way, any differences in the protease-resistant regions of the constructs could be examined and compared to wild type hH_V1 channels. By defining the protease resistant core of the chimeras, we would be able to redesign the constructs to remove any flexible or unstructured regions that might be interfering with crystallization.

Limited proteolysis was carried out for each chimera using four proteases: trypsin, chymotrypsin, elastase and subtilisin (Fig. 4.8). For both chimera, one hour of trypsinization resulted in the smallest stable fragment. These fragments were then analyzed by both N-terminal sequencing and mass spectrometry, which revealed that the trypsin cleavage site was located between amino acids R83 and A84. This is the same position at which limited proteolysis removes the N-terminus of the wild type hH_V1 channel, indicating that the beginning of the structured transmembrane domain is unaltered in the chimeric constructs.

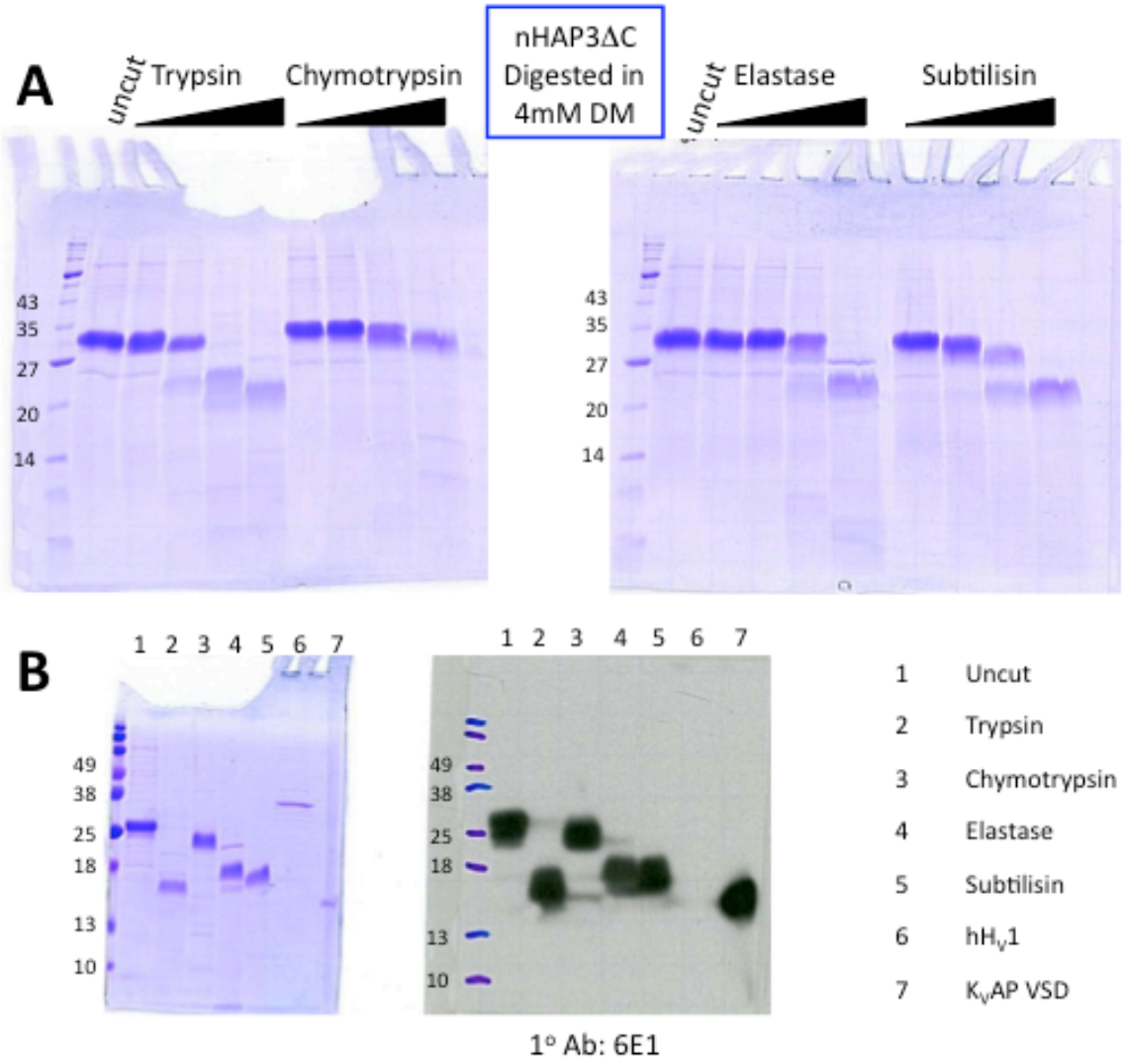

Fig. 4.8 Example limited proteolysis experiments for nHAP3ΔC in DM

(**A**) nHAP3ΔC was mixed with the indicated proteases at ratios ranging from 0.0001 mg protease/mg channel to 0.1 mg protease/mg channel for 1 hour at room temperature. Digestions were stopped by addition of 5 mM PMSF. (**B**) Western blot analysis of the proteolysis fragments generated at the highest protease concentrations in (**A**). SDS-PAGE gel (left) indicating the presence of each of the fragments as well as wild type hH_V1 and K_VAP VSD controls. Western blot (middle) using the αK_VAP-paddle mAb 6E1 as primary Ab indicating that each proteolysis fragment contains the paddle epitope indicating that the transmembrane region is resistant to proteolysis. The contents of each well are indicated in the legend (right). Trypsin fragment was further characterized by N-terminal sequencing and mass spectrometry.

After initial proteolysis experiments, a trypsinization time-course was carried out to compare the relative stabilities of HAP5ΔC and nHAP3ΔC (Fig. 4.9). These experiments indicated that the trypsin-digested HAP5ΔC was highly stable: no further proteolysis was observed after the initial cleavage even at very high trypsin concentrations (Fig. 4.9B). In contrast, the nHAP3ΔC continued to degrade over time, indicating instability (Fig. 4.9A). However, by stopping the trypsin digestion of nHAP3ΔC at an early time point by addition of phenylmethanesulfonylfluoride (PMSF), it was possible to isolate the transmembrane fragment before it was further digested (Fig. 4.9A).

Since it was possible to isolate a stable transmembrane fragment of both chimeric constructs, preparative trypsinization was attempted as a possible method for protein production for crystallization. Using this methodology, the protein was digested by addition of trypsin during the purification, the digestion was stopped by addition of PMSF, the transmembrane fragment was isolated by SEC, mixed with the anti-K_VAP Fabs (6E1 or 33H1) and then set up in crystallization screens. This process resulted in the growth of crystals of trypsinized-HAP5ΔC (tHAP5ΔC) in complex with 6E1. No crystals were observed for the nHAP3ΔC construct with either 6E1 or 33H1 Fabs.

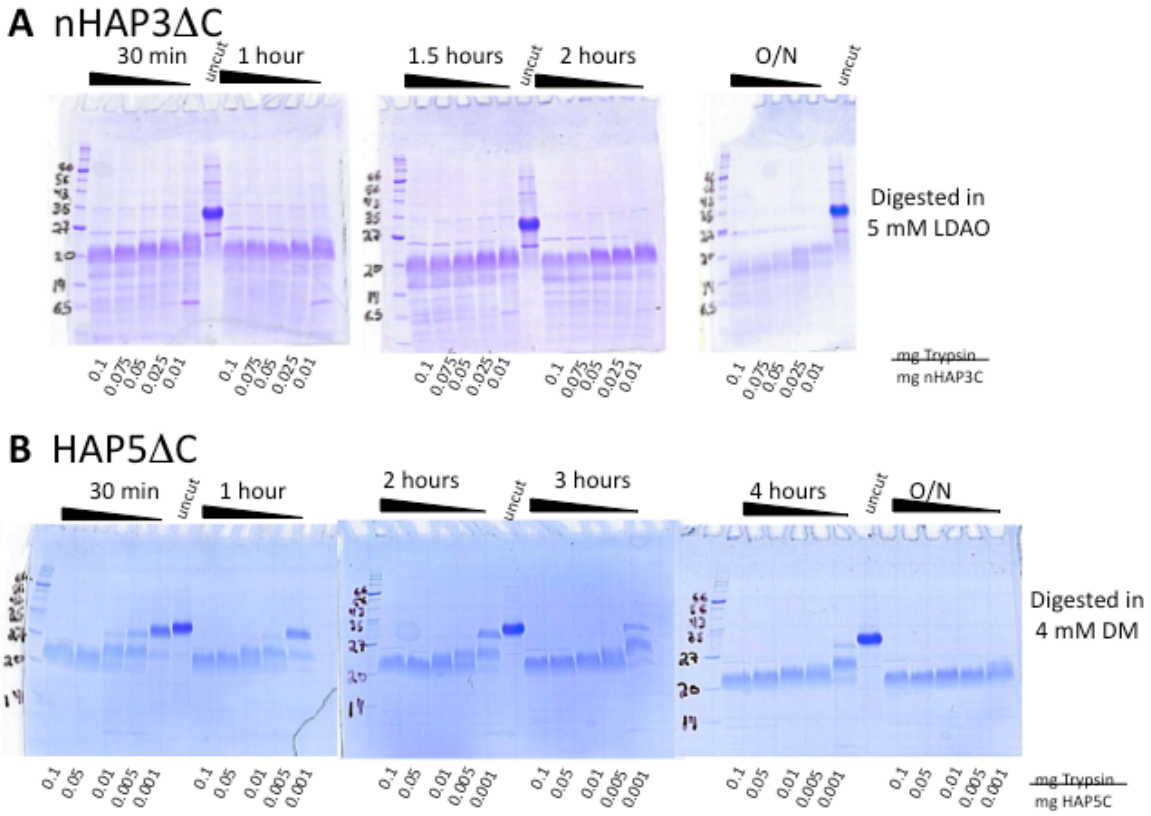

Fig. 4.9 Trypsinization time-course to compare stability of chimeric constructs

(A) nHAP3ΔC in LDAO and (B) HAP5ΔC in DM were subjected to trypsinization at the indicated trypsin-to-channel ratios (bottom of gels). At the indicated time points an aliquot was taken and quenched with PMSF then run on the SDS-PAGE gel. LDAO was used for nHAP3ΔC since the channel is more stable in this detergent than in DM (see Table 4.1).

Refinement of the tHAP5ΔC/6E1 crystallization conditions resulted in the growth of large (~0.4 x 0.2 x 0.1 mm) crystals (Fig. 4.10A). In order to confirm that these crystals contained both channel and Fab, crystals were harvested, washed and run on an SDS-PAGE gel, which was developed using silver staining (Fig. 4.10B). This gel indicated that the crystals contained both Fab and tHAP5ΔC (Fig. 4.10B), demonstrating that, even though the interaction between this construct and the Fabs are too weak to purify complex on the SEC column, complex does form under crystallization conditions.

The X-ray diffraction properties of these tHAP5ΔC/6E1 crystals were examined at the synchrotron. The crystals diffracted anisotropically to ~3.5 Å in the good direction and ~9 Å in the other two directions (Fig. 4.10C). Although I was unable to index this data set, it was encouraging to see diffraction from these crystals. We decided it would be best to focus efforts on improving this crystal form and to forego working on the nHAP3ΔC chimera, which had yet to produce any crystals.

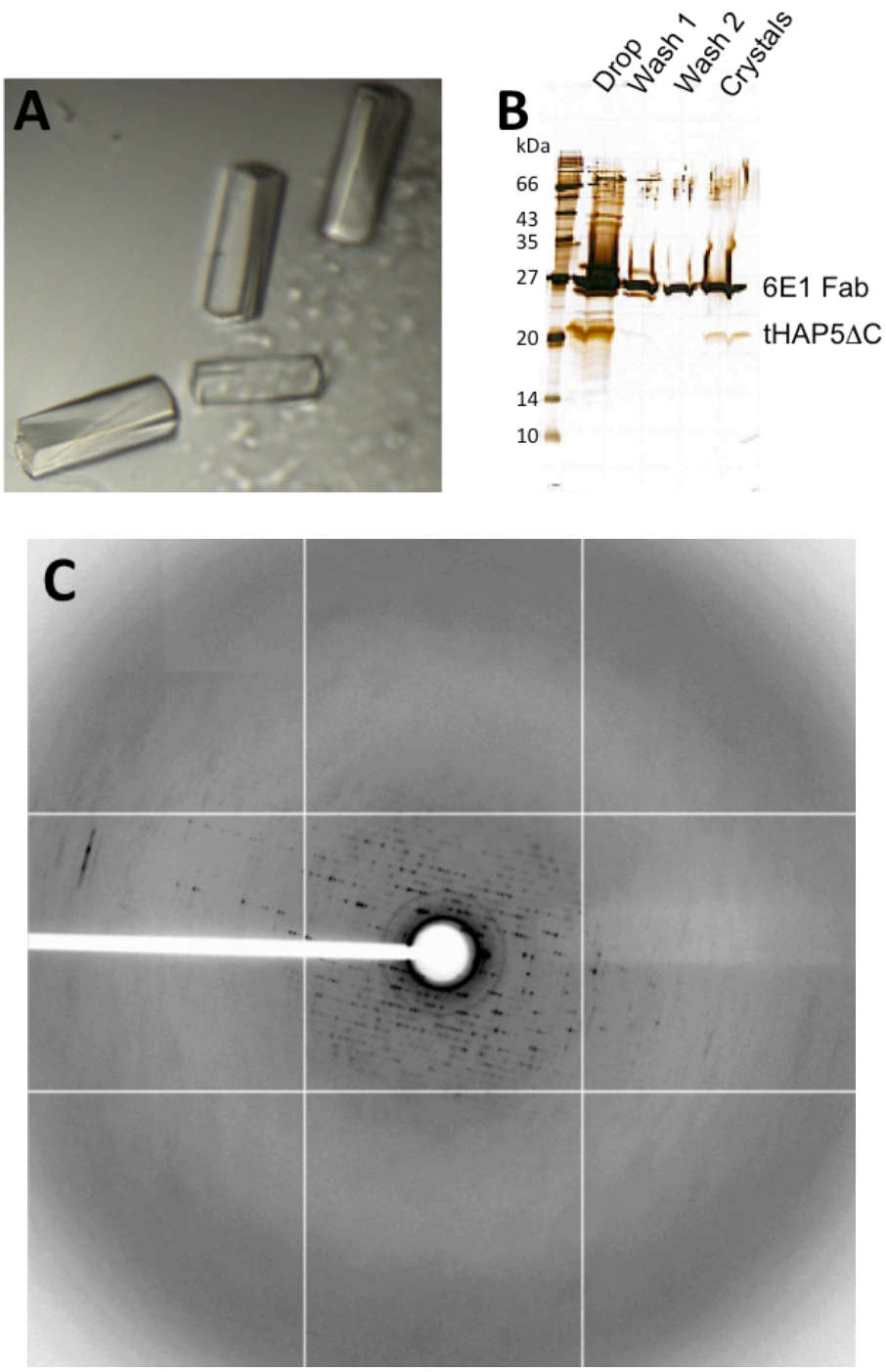

Fig. 4.10 Crystals of trypsinized HAP5ΔC in complex with 6E1

(A) Crystals of trypsinized-HAP5ΔC (tHAP5ΔC) in complex with 6E1 Fab grown in 30% PEG400, 50 mM potassium phosphate pH 7.0. (B) Silver stained SDS-PAGE gel of crystals from these conditions indicating that the crystals contain both 6E1 Fab and tHAP5ΔC. (C) Best diffraction pattern generated by crystals from these conditions.

To improve the diffraction, I needed to eliminate any source of heterogeneity originating from the protein preparation. To generate channel protein for these crystals, the construct was expressed as a C-terminal GFP-1D4 fusion, with the channel and GFP-1D4 tag separated by a PreScission protease cleavage site. The channel was purified by 1D4-affinity chromatography followed by PreScission protease digestion to remove the GFP-1D4 tag, followed by an additional round of 1D4-affinity chromatography to separate the cleaved GFP-1D4 from the channel, trypsinization to remove the N-terminus and then SEC to isolate the transmembrane fragment. PreScission protease is a highly specific protease isolated from human rhinovirus that cleaves the sequence LEVLFQ/GP where the "/" indicates the site of cleavage (Cordingley *et al*. 1990). Because of the eight amino acid residue long recognition site and an additional three amino acid residues introduced for cloning purposes, removal of the C-terminal GFP-1D4 tag by PreScission protease resulted in the presence of nine non-H_V derived amino acid residues (SNSLEVLFQ) following the final native lysine residue (K221 in wild type channels) on the C-terminus of the HAP5ΔC construct. Mass spectrometry of the trypsinized channel indicated that not only did the trypsin cut at position R83 on the N-terminus, but it also cut much more slowly at the final native lysine residue, producing a mixture of C-termini (Fig 4.11). We reasoned that removal of this source of heterogeneity by redesign of the expression construct should improve crystal growth.

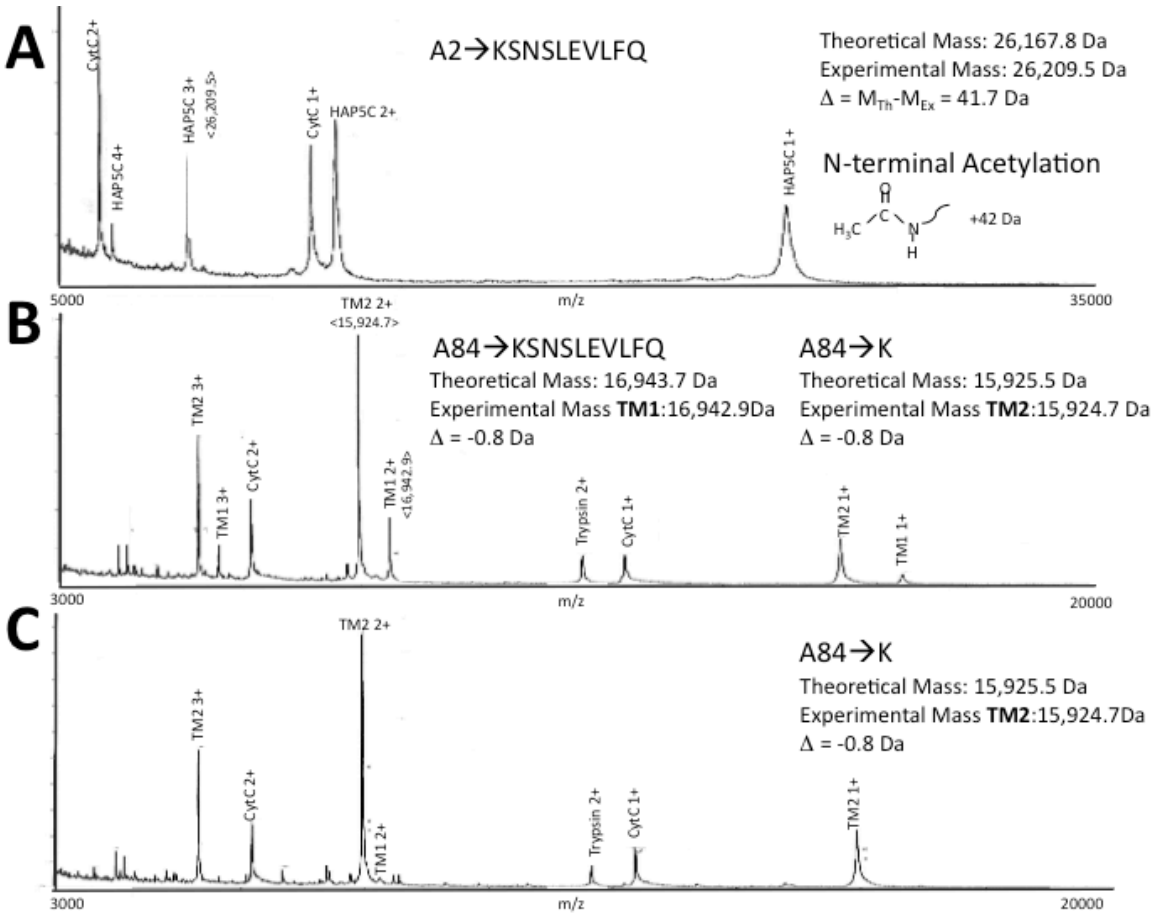

Fig. 4.11 Mass Spectrometry of HAP5ΔC trypsinization time course

(**A**) Mass spectrum of undigested HAP5ΔC generated using the ultrathin-layer method (Cadene & Chait 2000). The experimental mass agrees well with the theoretical mass for the full-length construct with the N-terminal methionine removed. The additional ~42 Da mass difference between the theoretical and experimental masses indicates that the protein contains a post-translational modification, most likely N-terminal acetylation. (**B**) Mass spectrum of HAP5ΔC after 3 hours of trypsin digestion indicating that the N-terminus has been completely removed by trypsin digestion at R83. Two distinct peaks corresponding to the transmembrane (TM) fragment are visible. The masses of the two fragments TM1 and TM2 correspond to within 1 Da of the theoretical masses of the HAP5ΔC TM fragment plus/minus the nine non-native amino acid residues left over from the PreScission protease site on the C-terminus. (**C**) Mass spectrum of HAP5ΔC after overnight trypsin digestion at 0.1 mg trypsin/mg channel indicating that given enough time the nine non-native amino acid residues are completely removed.

To bypass preparative trypsinization, the GFP tag was moved to the N-terminus, making the PreScission site N-terminal to the transmembrane domain. Since the N-terminal site of trypsinization was located between R83 and A84, through overlapping of the PreScission cleavage site with this trypsin site, it was possible to generate a final PreScission-digested N- and C-terminally truncated chimera that only differed from the wild type $H_V\Delta N\Delta C$ by having a glycine instead of an alanine at position 84 and by terminating at the lysine position 221 (and, of course, by having the KvAP paddle swap). However, because the 1D4 affinity tag is C-terminal, moving the tag to the N-terminus required using a different affinity purification protocol. At first, an N-terminal FLAG tag was used, which also allows antibody affinity for the purification of low-yield proteins. However, after initial expression and purification trials, it was found that moving the GFP tag to the N-terminus greatly improved the protein expression and more than doubled the yield. Therefore I was able to switch the affinity tag from a FLAG tag to a Deca-His tag and thus use immobilized metal-affinity chromatography (IMAC) in the purification.

By making the above modifications to the expression construct, I was able to simplify the purification protocol by removing the need for preparative trypsinization. With this construct, the purification protocol after protein extraction consisted of IMAC using Co^{2+} resin, PreScission digestion to cleave off the His-GFP tag, another round of IMAC to separate the cleaved tag and the HAP5ΔNΔC construct, followed by a final SEC purification. Mass spectrometry confirmed that this new construct and purification protocol resulted in the production of a homogenous protein sample without any additional proteolysis or post-translational modifications.

Setting up crystallization screens with this construct in the presence of the 33H1 Fab in DM resulted in two new crystal forms both of which contained Fab and HAP5ΔNΔC (Fig 4.12). After refinement of the crystal growth conditions and initial diffraction analysis, it was determined that the crystal form shown in Fig. 4.12A did not diffract better than ~9 Å resolution, whereas the other crystal form, shown in Fig. 4.12B, displayed greater variability with some crystals diffracting better than 4 Å. Screening of many different crystals from these conditions resulted in collection of a complete, though anisotropic, data set to 3.9 x 5.1 x 3.8 Å resolution (Fig. 4.13, Table 4.2).

Before discussing the structure of HAP5ΔNΔC that I obtained from this data set, I will use the following section to describe the functional work that was performed in conjunction with the biochemistry described in the previous sections. Throughout the design and modification of the chimeras, great care was taken to insure that each new construct was a functional voltage-gated proton channel. The functional data presented in the next section are essential for interpretation of the structural work.

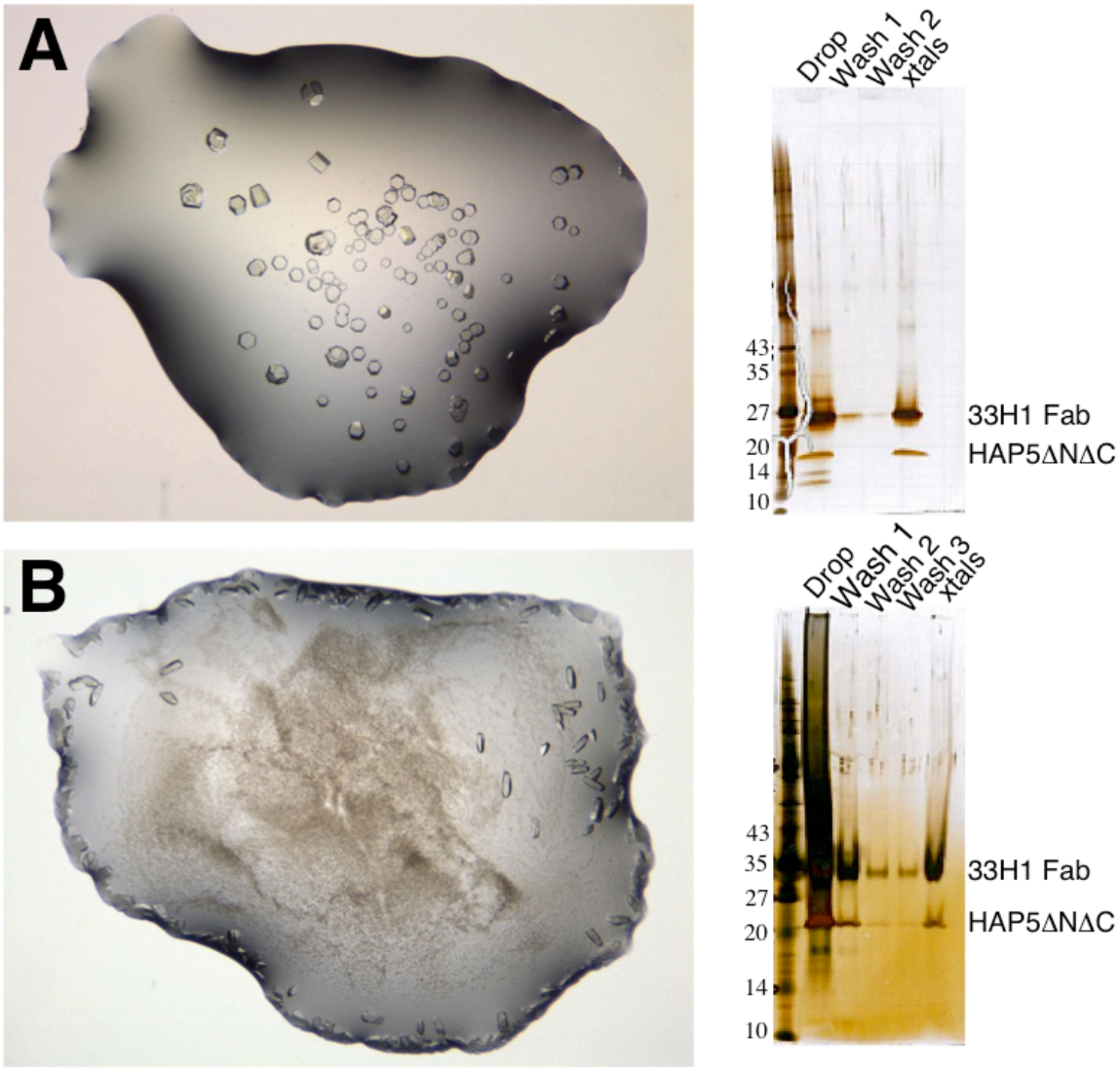

Fig. 4.12 Crystals grown from HAP5ΔNΔC construct in complex with 33H1 Fab

(**A**) Crystals grown in 30% PEG400, 50 mM MES pH6.5, 100 mM $NaLiSO_4$. (**B**) Crystals grown in 30% PEG400. The silver stained gels of the crystals (right) indicate that the crystals contain both 33H1 Fab and HAP5ΔNΔC.

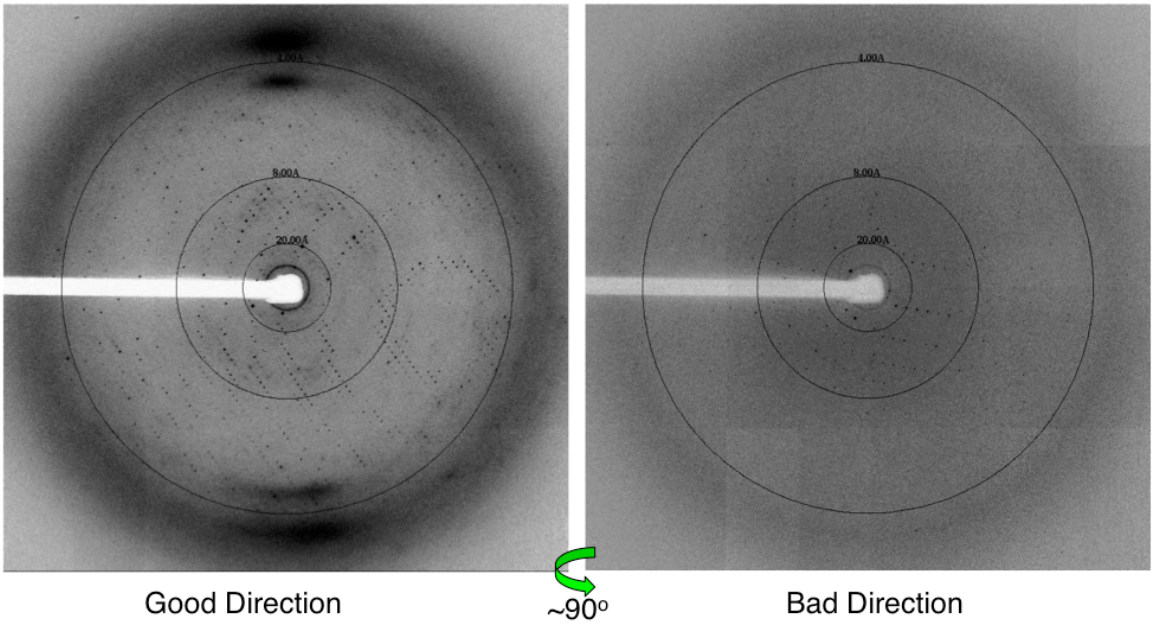

Fig. 4.13 Diffraction from crystals of HAP5ΔNΔC/33H1 complex crystals

Two diffraction images from the same crystal grown in 30% PEG400 taken at ~90° separation clearly showing anisotropy. The concentric circles indicate resolution shells, going from the center outwards 20 Å, 8 Å and 4 Å are shown.

Table 4.2 Summary of data collection for HAP5ΔNΔC/33H1 complex

Data Set	**HAP5ΔNΔC/33H1**
Resolution (Å)	3.9, 5.1, 3.8
Space Group	P1
Source	BNL X29
Cell Dimensions: a, b, c (Å)	99.8, 136.1, 148.1
α, β, γ (°)	82.2, 89.4, 76.6
Unique reflections	53,138
I/σI	7.33 (2.47)

Ellipsoid truncation and anisotropic scaling was performed on the data set using the UCLA MBI diffraction anisotropy server (Strong *et al*. 2006).

4.2.3 The best candidates for structure determination are functional

By reconstituting the chimeric channels into lipid vesicles and using the fluorescence-based concentrative uptake flux assay described in Chapter 3, I determined that HAP5ΔC, nHAP3ΔC and the trypsinized HAP5ΔC were able to conduct H^+ (Fig. 4.14A and B). In each case, the H^+ conduction observed from these constructs was qualitatively similar to that of the reconstituted wild type hH_V1 channel (Fig. 4.14A and B). The fact that the fluorescence quenching time courses went to completion without any slow recovery or intermediate level of quenching indicated that the chimeric constructs also maintained H^+ selectivity (see Chapter 3 for a more in depth discussion on implications concerning selectivity from this assay). These functional data from the flux assay were sufficient for me to pursue these chimeric constructs as possible structural targets; however, once a complete data set was obtained for the HAP5ΔNΔC, a more rigorous electrophysiological characterization was desired.

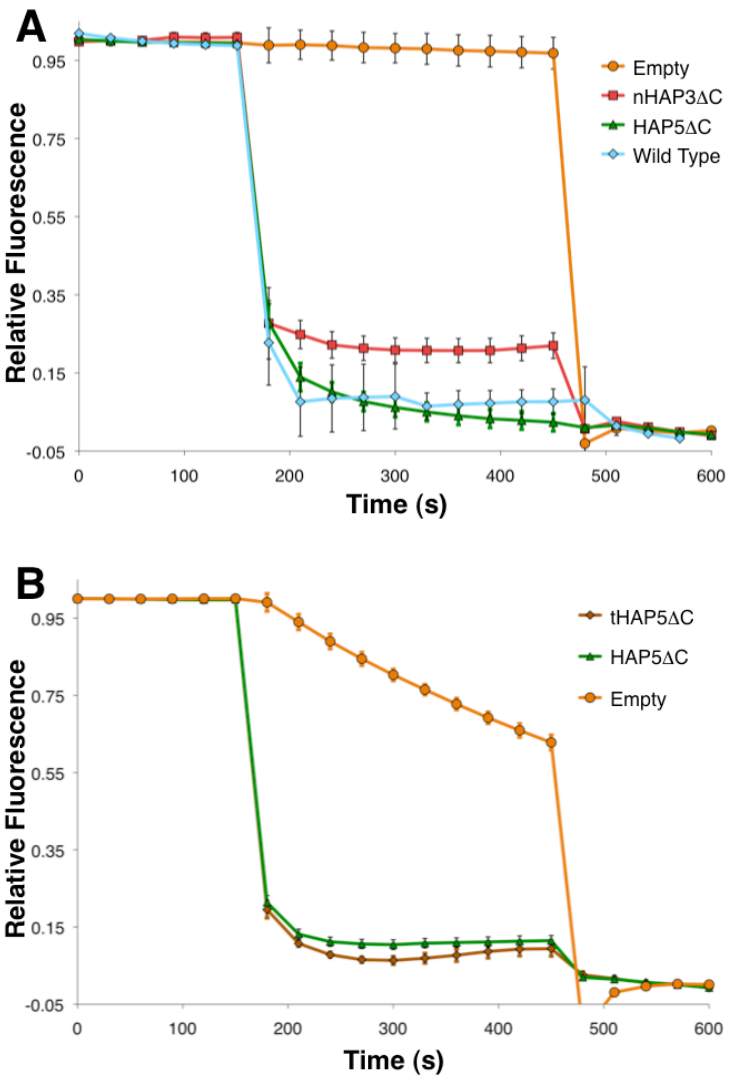

Fig. 4.14 H^+ uptake into vesicles containing the chimeric constructs

(**A**) Fluorescence-based H^+ flux assay for vesicles containing HAP5ΔC (green), nHAP3ΔC (red) compared to empty vesicles (orange) and wild type hH_V1 containing vesicles (cyan). (**B**) Fluorescence-based H^+ flux assay for vesicles containing HAP5ΔC (green) and trypsinized-HAP5ΔC (tHAP5ΔC, brown). In each case valinomycin was added after 150s, CCCP was added at 450s and the fluorescence measurements were repeated 3-4 times (error bars represent the standard error of the mean). The significant fluorescence quenching seen for the empty vesicles in (**B**) indicate that this batch of vesicles was more leaky than usual.

To test the voltage-gating properties of the HAP5 chimera, the full-length sequence was cloned into a HEK-cell expression vector and the activity of the channel was compared to wild type hH_V1 in HEK cells by the whole-cell patch clamp method. Although both channels generated robust voltage-gated currents, the gating properties of the HAP5 chimera are significantly different from that of hH_V1 channels (Fig. 4.15A and B). Both the rate of opening and closing were significantly faster in the HAP chimeric channel (Fig. 4.15B). The rate of closing of the HAP5 chimera was so fast that, when using a similar voltage step protocol as for hH_V1, tail current was not observable (Fig. 4.15B). Due to the speed of channel closing when the voltage was stepped to negative potentials, the reversal potential of the currents elicited by opening of the HAP5 channel could not be accurately measured. This precluded definitive determination of the ion selectivity for this channel; however, as mentioned above, the stability of fluorescence quenching seen in the flux assay suggests that the HAP5 channel maintained its H^+ selectivity.

Further characterization of the chimeric channel under different external and internal pH and ionic conditions may have allowed for accurate measurement of reversal potentials; however, further structural and biochemical analysis described in the following sections precluded the need for further functional characterization of this channel. Although the functional changes elicited by the paddle swap are interesting unto themselves (the channel gating actually more resembles that of K_VAP than hH_V1), my major focus was to solve the structure of a H_V channel and, thus, only confirmation that the HAP5 chimera was a functional voltage-gated H^+ channel was needed. The data presented in Fig. 4.14 and 4.15 demonstrate that the HAP5 chimera is functional.

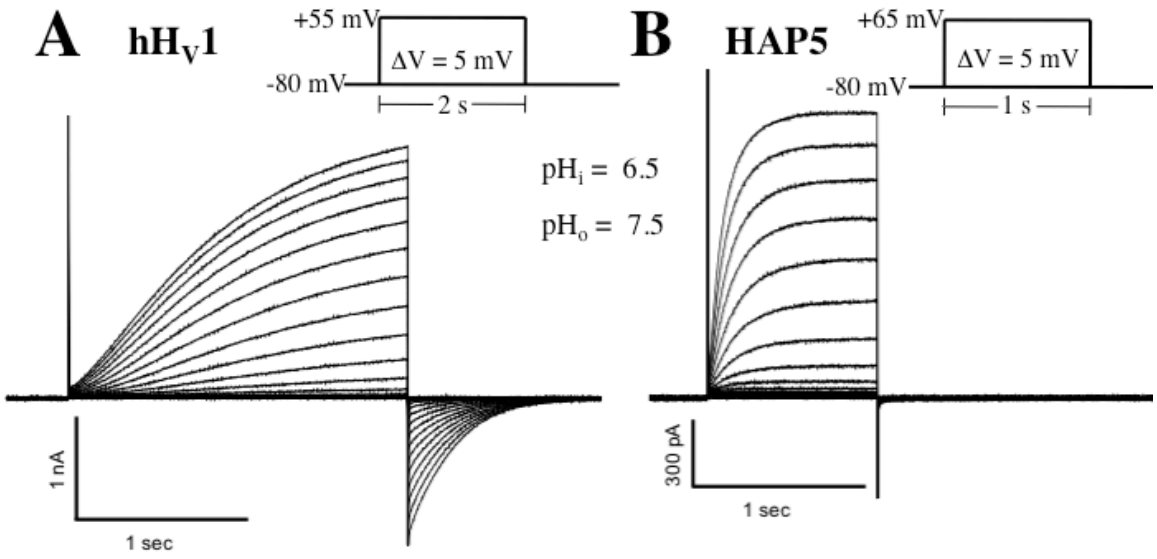

Fig. 4.15 HAP5 is a voltage-gated H^+ channel

(A) Whole-cell patch clamp recording from a HEK cell expressing hH_V1. Voltage-step protocol was as indicated in the schematic. (B) Whole-cell patch clamp recording from a HEK cell expressing HAP5. Voltage-step protocol was as indicated in the schematic.

4.2.4 Structure of the HAP5ΔNΔC chimera

Using the separate constant (F_C) and variable regions (F_V) of the Fab as search models for molecular replacement, it was possible to phase the low-resolution anisotropic data set. The unit cell (which was the asymmetric unit, since the space group was P1) was large enough to fit eight HAP5ΔNΔC/33H1 complexes; however, clear density was observed for only five and a half Fabs (6 F_Vs and 5 F_Cs), with the remainder of the cell being disordered. From the initial molecular replacement solution, tubular density was observed extending from the 33H1 binding sites, which unambiguously corresponded to the four transmembrane helices of the HAP5ΔNΔC channel (Fig. 4.16).

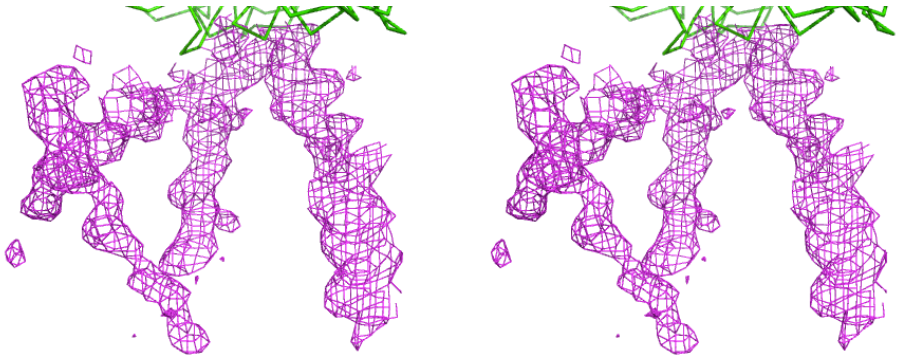

Fig. 4.16 Example of helical electron density observed in a 33H1 Fab binding site
Stereo image of 1σ electron density from 2Fo-Fc map calculated from 33H1 Fab molecular replacement solution prior to any refinement or model building. Strands corresponding to 33H1 binding site are shown as green ribbons. Map was generated from data set summarized in Table 4.2 at 4 Å.

It was possible to fit the transmembrane helices into the density without any refinement of the initial search model (Fig. 4.17). Due to the low resolution and internal disorder of the data set, it was not possible to unambiguously determine the connectivity between the different transmembrane helices. However, due to the known interaction between the K_VAP paddle sequence and the 33H1 Fab (Jiang *et al*. 2003a), it was possible to identify and register the S3 and S4 helices. Additionally, it was clear from the density that the channels were arranged as dimers.

Comparing the arrangement of the four transmembrane helices of each HAP5ΔNΔC subunit it was evident that the observed structure was very different from that of known VSDs (Jiang *et al*. 2003a; Long *et al*. 2005; Long *et al*. 2007; Payandeh *et al*. 2011; Payandeh *et al*. 2012; Zhang *et al*. 2012). Additionally, the dimer interface in the structure was extensive, with the S3 helices wrapping around each other and

intercalating between the S3 and S4 helices of the opposite subunit in the dimer, causing a splaying of the paddle motif when compared to the K_VAP structure (Fig. 4.18). The presence of this dimer interface along S3 disagreed with our site directed cross-linking studies of the wild type hH_V1 in membranes, which demonstrated that the dimer interface was along the S1 helix (see Chapter 2 and Lee *et al*. 2008).

In spite of these discrepancies seen in the model of HAP5ΔNΔC (Fig. 4.17) and the cross-linking data presented in Chapter 2, we knew from the electrophysiology and the flux assay of the reconstituted channel that the chimera was functional. However, the inconsistency between structural and biochemical data had to be resolved before further interpretation and refinement of the structure could be carried out.

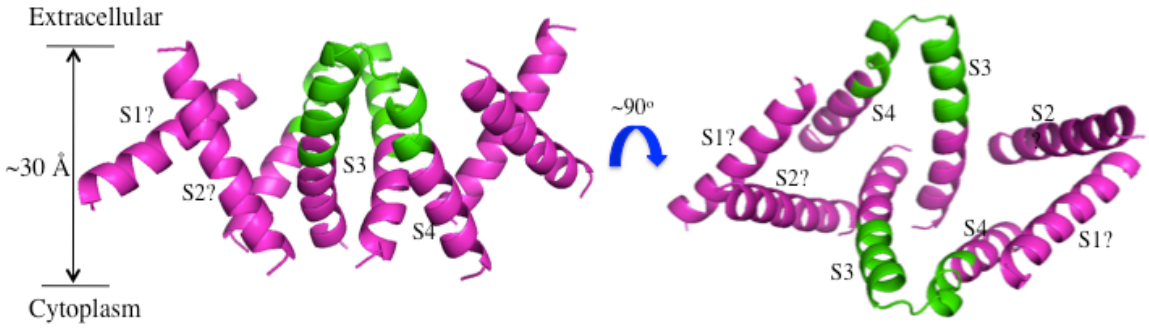

Fig. 4.17 Helical model of HAP5ΔNΔC

Model of transmembrane helices generated by fitting polyalanine α-helices into the electron density found at the 33H1 binding site. Left, side view looking from within the expected membrane plane, right, top view looking down from the hypothetical extracellular side. The amino acid residues that corresponds to K_VAP sequence are colored green, whereas hH_V1 derived residues are magenta.

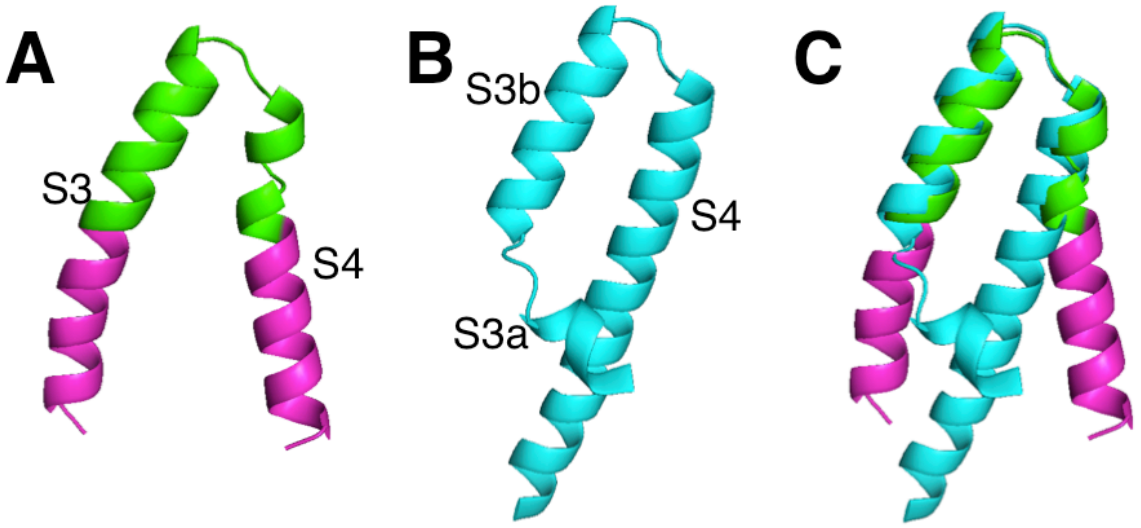

Fig. 4.18 Comparison of paddle structures between HAP5 and K_VAP isolated VSD

(A) Structural model of the HAP5ΔNΔC paddle colored as in Fig. 4.17. (B) Structural model of K_VAP paddle from (Jiang *et al*. 2003a). (C) Overlay of paddle structures demonstrating that the paddle motif in HAP5ΔNΔC is splayed open compared to the equivalent sequence in K_VAP. Also no kink is observed in the S3 helix of HAP5ΔNΔC.

4.2.5 Cross-linking indicates HAP5ΔNΔC chimera structure is not native

To probe the functional dimeric state of the HAP5 chimera, the channel was expressed in HEK cells in both full-length and C-terminally truncated forms and the pattern of site specific cross-linking was investigated and compared side-by-side with wild type hH_V1 channels. In addition to the positions along S1 that were shown to form robust disulfide cross-links in hH_V1, the amino acid residue positions along S3 that form the dimer interface in the structure (Fig. 4.17) were also mutated to cysteine one at a time and probed for cross-linking.

In both cases, the full-length and C-terminally truncated HAP5 chimera showed robust spontaneous disulfide bond formation along the top of the S1 helix, exactly recapitulating the pattern seen for wild-type hH_V1 (Fig. 4.19C). Because of the lack of the C-terminus from the truncated channels, the less specific anti-K_VAP antibody 6E1 was used in the western blots, which resulted in some non-specific signal in spite of which clear dimer was observed (Fig. 4.19E and G). Addition of oxidizing reagents and cysteine reactive cross-linkers to the membranes pushed cross-linking at these S1 sites to completion, just as was seen for the wild type hH_V1 channel (Fig. 4.19G; Chapter 2; Lee *et al*. 2008).

When the positions along S3 were probed for spontaneous cross-link formation, no disulfide bond formation was observed (Fig. 4.19B and F). Furthermore, addition of oxidizing reagents and cysteine-reactive cross-linkers still did not result in the observation of any cross-linked dimer (Fig. 4.19D and H). These data clearly indicated that the HAP5 chimera is a dimer in membranes even in the absence of the C-terminus, and that its dimer interface is along the S1 helix (i.e. similar to wild type hH_V1), not along the S3 helix as seen in the structure.

Fig. 4.19 Site-specific cross-linking studies of HAP5 and HAP5ΔC in membranes

(**A**) Cross-linking of the native coiled-coil cysteine (position 249) in both wild type hH_V1 and HAP5. Production of a cys-less (CL) construct in which the two native cysteines have been mutated to serine precludes disulfide-mediated cross-linking. (**B**) Cysteine mutants of hH_V1 CL along the S3 dimer interface seen in the crystal structure of HAP5ΔNΔC (**C**) Cysteine mutants along the S1-S2 loop dimer interface seen in the cross-linking studies discussed in Chapter 2 for both hH_V1 CL and HAP5 CL constructs (**D**) Same S3 mutants of hH_V1 CL as in (**B**) but under forcing conditions. (**E**) Compaing the effect of C-terminal truncation on the S1-S2 loop cysteine mediated cross-linking of HAP5 CL and HAP5ΔC CL (**F**) Cysteine mutants of HAP5ΔC CL along the S3 dimer interface seen in the crystal structure (**G**) Same S1-S2 mutants of HAP5 and HAP5ΔC CL as in (**E**) but under forcing conditions. (**H**) Same S3 mutants of HAP5ΔC CL as in (**F**) but under forcing conditions. Symbols in blue on the right on gels indicate the approximate positions for the dimer and monomer of the coiled-coil containing constructs (circles with tails) and the truncated constructs (circles without tails). (**A – D**) Use the αhH_V1-coiled-coil antibody 9C1 as the primary antibody (**E – H**) Use the αK_VAP-paddle antibody 6E1 as the primary antibody.

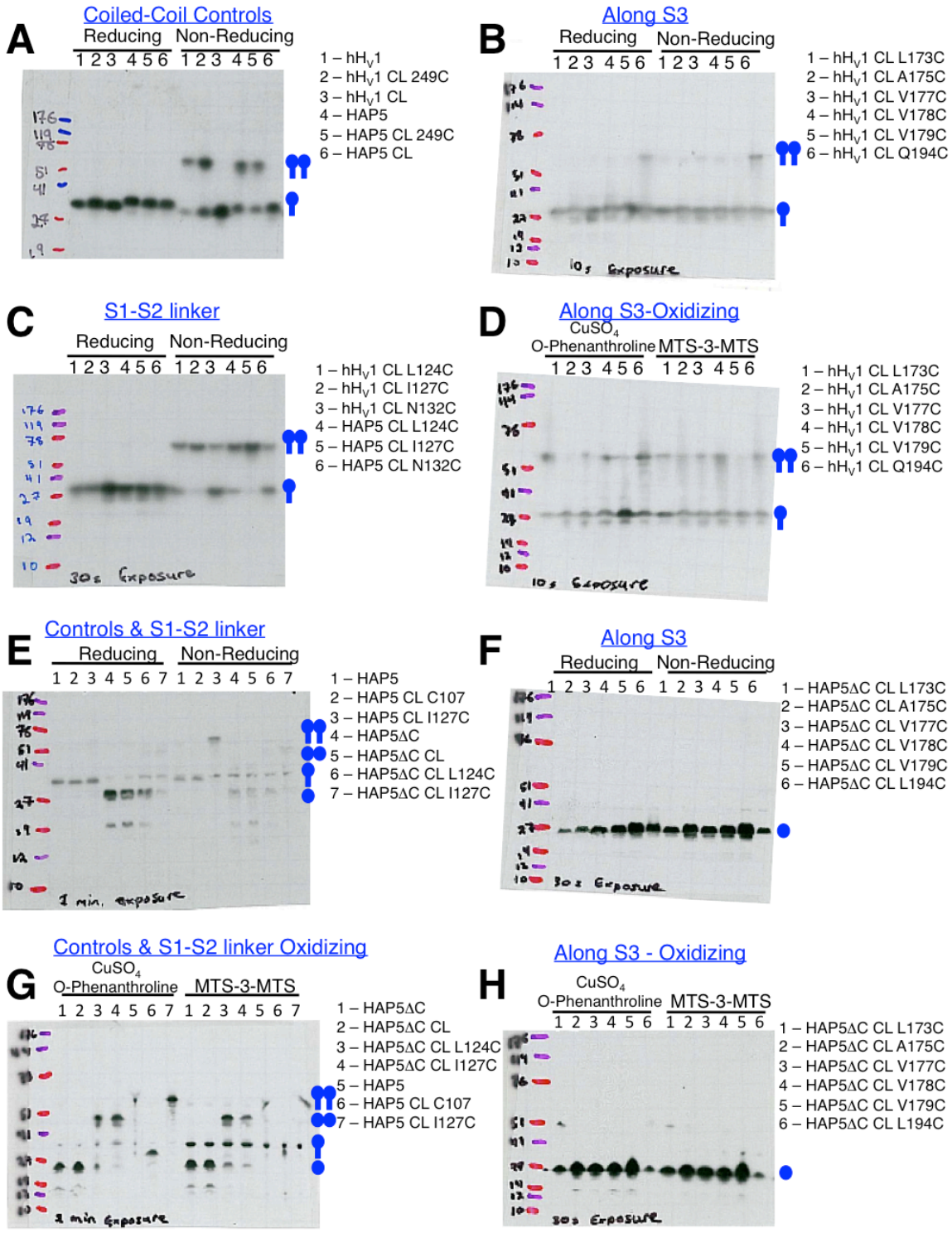
A
Coiled-Coil Controls
Reducing
Non-Reducing
1 2 3 4 5 6 1 2 3 4 5 6
1 – hHV1
2 – hHV1 CL 249C
3 – hHV1 CL
4 – HAP5
5 – HAP5 CL 249C
6 – HAP5 CL
B
Along S3
Reducing
Non-Reducing
1 2 3 4 5 6 1 2 3 4 5 6
1 – hHV1 CL L173C
2 – hHV1 CL A175C
3 – hHV1 CL V177C
4 – hHV1 CL V178C
5 – hHV1 CL V179C
6 – hHV1 CL Q194C
10s Exposure
C
S1-S2 linker
Reducing
Non-Reducing
1 2 3 4 5 6 1 2 3 4 5 6
1 – hHV1 CL L124C
2 – hHV1 CL I127C
3 – hHV1 CL N132C
4 – HAP5 CL L124C
5 – HAP5 CL I127C
6 – HAP5 CL N132C
30s Exposure
D
Along S3-Oxidizing
CuSO4
O-Phenanthroline
MTS-3-MTS
1 2 3 4 5 6 1 2 3 4 5 6
1 – hHV1 CL L173C
2 – hHV1 CL A175C
3 – hHV1 CL V177C
4 – hHV1 CL V178C
5 – hHV1 CL V179C
6 – hHV1 CL Q194C
10s Exposure
E
Controls & S1-S2 linker
Reducing
Non-Reducing
1 2 3 4 5 6 7 1 2 3 4 5 6 7
1 – HAP5
2 – HAP5 CL C107
3 – HAP5 CL I127C
4 – HAP5ΔC
5 – HAP5ΔC CL
6 – HAP5ΔC CL L124C
7 – HAP5ΔC CL I127C
1 min. exposure
F
Along S3
Reducing
Non-Reducing
1 2 3 4 5 6 1 2 3 4 5 6
1 – HAP5ΔC CL L173C
2 – HAP5ΔC CL A175C
3 – HAP5ΔC CL V177C
4 – HAP5ΔC CL V178C
5 – HAP5ΔC CL V179C
6 – HAP5ΔC CL L194C
30s Exposure
G
Controls & S1-S2 linker Oxidizing
CuSO4
O-Phenanthroline
MTS-3-MTS
1 2 3 4 5 6 7 1 2 3 4 5 6 7
1 – HAP5ΔC
2 – HAP5ΔC CL
3 – HAP5ΔC CL L124C
4 – HAP5ΔC CL I127C
5 – HAP5
6 – HAP5 CL C107
7 – HAP5 CL I127C
2 min Exposure
H
Along S3 - Oxidizing
CuSO4
O-Phenanthroline
MTS-3-MTS
1 2 3 4 5 6 1 2 3 4 5 6
1 – HAP5ΔC CL L173C
2 – HAP5ΔC CL A175C
3 – HAP5ΔC CL V177C
4 – HAP5ΔC CL V178C
5 – HAP5ΔC CL V179C
6 – HAP5ΔC CL L194C
30s Exposure

4.2.6 Final attempts at chimera strategy

Here, I will briefly describe my efforts to use the non-native HAP5ΔNΔC structure to design improved chimera with the goal of solving a native structure of the channel. The main question that needed to be addressed was whether the HAP5ΔNΔC was completely disordered in detergent or whether Fab binding was forcing the conformational equilibrium of the chimera into a low occupancy non-native conformation.

Since the Fab was not raised against the HAP5ΔNΔC channel itself but against the K_VAP channel, if the paddle epitope were not properly presented for Fab recognition in the native chimeric construct, we would expect very little binding of the Fab to the native chimera. Therefore, four scenarios can be envisioned for binding of a Fab to an epitope-swapped chimeric channel: 1) the chimera structure is native and highly stable in detergent but does not present the epitope properly. In this case, Fab would not bind and we would see no complex on the SEC column. This may be true even if we saw binding of antibody in ELISAs and Western blots, since under these conditions we expect a higher proportion of unfolded channels. 2) The chimera is native and stable in detergent but does not present the epitope properly; however, it is in equilibrium with a low occupancy non-native (partially unfolded) state in which the Fab is able to bind to the paddle epitope with high affinity. In this case, we may see some incomplete complex formation on the SEC column, but high concentrations of Fab would result in the accumulation of non-native-chimera-Fab complex, which may then crystallize due to the strength of Fab mediated crystal contacts. 3) Although the native chimera doesn't present the paddle epitope properly, the chimera is unstable in detergent and therefore significantly occupies a non-native conformation that is able to bind Fab with high

affinity. In this case, we would expect the chimera to be unstable in most non-dispersive detergents but bind strongly to the Fab resulting in complete complex formation on the SEC column. 4) The native chimera is highly stable in detergent and properly presents the paddle epitope in a way that is easily accessible to the Fab. In this case we would expect a biochemically stable construct and complete complex formation on the SEC column.

To solve the native structure of a chimeric channel we require chimera that fall into scenario 4 above. However, based on the evidence presented in this chapter, I conclude that HAP5ΔNΔC falls into scenario 2: it is biochemically stable in many detergents and it only forms partial complex with Fab on the SEC column. Therefore, the 33H1 Fab is only binding to a small population of non-native channels on the SEC column, but the structure is completely non-native when solved in complex with the 33H1 Fab. In addition, I categorize the nHAP3ΔC chimera into scenario 3: it is unstable in most detergents, but forms complete complex with Fab on the SEC column. The question then becomes: can we use what we see in the structure to build a chimera that falls into scenario 4, i.e. one that is stable in detergent and binds to the Fab in the native conformation?

By examining the structure, it was clear that the S1 and S2 helices were directly adjacent to the Fab; moreover, the S3-S4 helix-turn-helix paddle motif may be buried below these two adjacent helices in the native structure (Fig. 4.20A-C). If the paddle motif were buried, then Fab binding to the native structure would be prevented by steric clash between the Fab and the S1 and S2 helices.

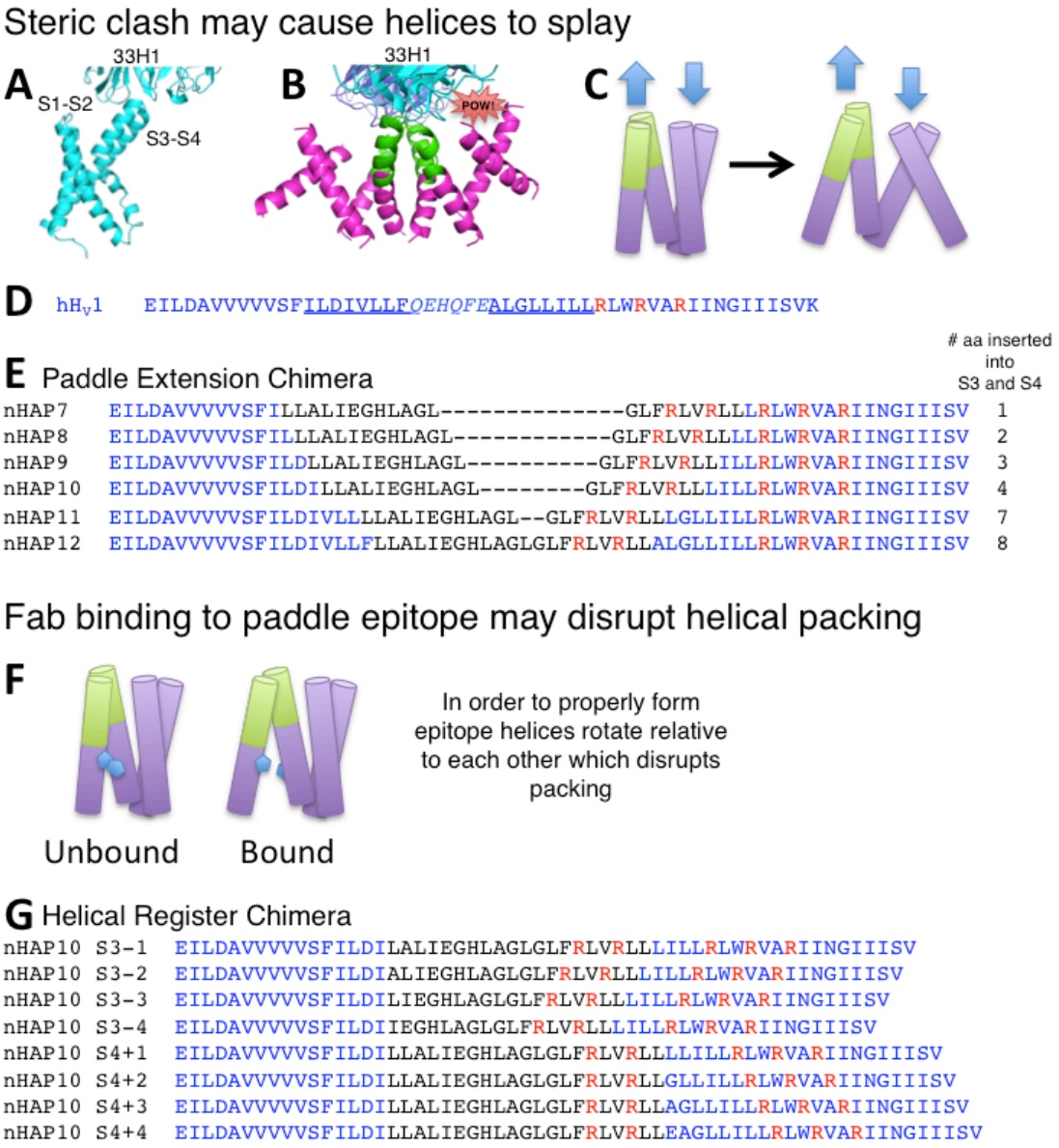

Fig. 4.20 Structure based strategy for design of new chimera

(A) Cartoon representation of K_VAP VSD in complex with 33H1 Fab structure showing that the S3-S4 paddle epitope is extended relative to the S1-S2 loop. (B) Cartoon representation of HAP5ΔNΔC dimer indicating possible source of steric clash between the S1 and S2 helices and 33H1 Fab. (C) Schematic demonstrating how steric clash could lead to helix splaying. (D) Sequence of hH_V1 paddle; underlined portions indicates residues that were added to the paddle extension chimera. (E) Sequences of paddle extension chimera. (F) Schematic demonstrating how Fab binding could lead to disruption of helical packing (G) Sequences of alternate helical register chimera.

Looking back over the sequences of all the chimera constructed (Fig. 4.3), it was determined that, because of the register used to splice in the paddle sequence, the HAP5C construct actually contained the most extended paddle (the longest combined S3-S4 K_VAP/hH_V1 sequence) of all the chimeras originally screened. Therefore, four additional doubly truncated chimeras that shared the same register as HAP5 but with longer S3 and S4 helices were generated (Fig. 4.20E; nHAP8, nHAP10, nHAP11 and nHAP12 were constructed). These chimera were expressed, purified and tested for only the two scenario-4 properties: biochemical stability and complete complex formation with Fab on the SEC column.

With the exception of nHAP10ΔNΔC (which was approximately one helical turn longer on S3 and S4 with respect to HAP5), most of the paddle extensions resulted in decreased stability of the chimeric constructs. Although the nHAP10ΔNΔC chimera was stable, the alterations did not improve Fab binding. The binding of nHAP10ΔNΔC to both 6E1 and 33H1 Fabs looked very similar to that of HAP5ΔNΔC, with only a small proportion of complex formation, likely placing it into scenario 2.

Another possible way in which the paddle epitope may be incorrectly presented for Fab binding on the chimeric channel is if the register of the S3 and S4 helices is wrong relative to that of native K_VAP. If S3 is longer or shorter than S4 in the chimera relative to the equivalent positions of the K_VAP S3 and S4 helices, then the S3-S4 helix turn helix motif may be askew, resulting in poor Fab binding and disruption on helical packing when the Fab does bind (Fig. 4.20F). To address this, eight additional chimeric constructs were built: four in which successive single amino acid residue deletions were carried out in S3 and four in which successive single amino acid residue additions were

carried out in S4 (Fig. 4.20G). These deletions/additions were carried out on the background of the nHAP10ΔNΔC construct, since it was the most stable chimera with the most extended paddle motif. Expression and purification of these eight constructs demonstrated that the nHAP10ΔNΔC S3-1, S3-1 and S4+4 constructs (Fig. 4.20G) were very stable and monodisperse on the sizing column. However, none of these constructs improve binding of either 6E1 of 33H1 Fabs.

Although there are a great number of possible combinations of amino acid residue additions/deletions that could be tested for these paddle chimeras, after failure of this set of eight constructs it was decided that it would be more productive to pursue other avenues for improved Fab binding. Therefore, the paddle chimera strategy was abandoned in favor of raising Fabs against the $hH_V\Delta N\Delta C$ channel by phage display (discussed below) and of nuclear magnetic resonance (NMR) characterization of the wild type channel (discussed in the next chapter).

4.3 Raising Fabs by Phage Display

4.3.1 Phage display selections overview

For soluble proteins, phage display selections are done *via* biotinylation and immobilization of the protein of interest onto streptavidin or neutravidin coated 96-well plates (Sidhu *et al*. 2000). In this way, large phage libraries with $>10^{13}$ sequence diversity can be applied to the sample for selection of binders by successive washing steps (Persson *et al*. 2013). In practice, the phage libraries are applied first to a streptavidin-coated well alone to remove any phage clones with non-specific or streptavidin specific

binding, and then the phage are moved to the wells with the immobilized sample (Sidhu *et al*. 2000). After incubation and 4-5 rounds of washing, the bound phage are eluted from the sample by addition of acid and are then amplified overnight in bacterial culture. This process is repeated in four or five rounds of selection, using higher concentrations of phage in each successive round. Increasing the phage concentration as the selection rounds progress results in greater competition between the remaining phage, selecting for the higher affinity binders (Sidhu *et al*. 2000). After the final round of selection, phage-infected bacteria are plated out in order to isolate single clones, which are then expanded and tested for binding to the antigen by ELISAs. Positive-binding clones are then sequenced and the Fabs present can be easily cloned, expressed and purified for use in structural studies (Sidhu *et al*. 2000).

This process was very much the same for purified membrane proteins, except that each step required the presence of detergents to keep the proteins in solutions. Due to the long time course of the selection process (generally 4-5 days), it is necessary that the membrane protein of interest be highly stable in detergent over long time spans. For most membrane proteins, including hH_V1, this is not the case, complicating the phage-display selection process. Nonetheless, because of our desire for high-affinity antibodies against the hH_V1 transmembrane domain, we initiated a collaboration with the laboratory of Dr Sachdev Sidhu at the University of Toronto. Before going to Dr Sidhu's laboratory, I was able to show that the $hH_V\Delta N\Delta C$ construct was efficiently biotinylated using two different reagents: one that reacts specifically with cysteine residues and one that reacts with primary amines such as the side chains of lysine residues.

Working with postdoctoral fellow Dr Yuko Arita, I carried out five rounds of phage selections against the $hH_V\Delta N\Delta C$ channel in diheptanoyl-glycerol-phosphatidylcholine (DHPC) detergent using two different phage-Fab libraries (Fellouse *et al*. 2007; Persson *et al*. 2013). After several days of selections, it was clear that the channel was becoming unstable, as small amounts of precipitate were seen in the sample tubes. Although we were able to prevent the protein from precipitating by diluting our stock concentration, we were still unsuccessful in isolating any strong binders from our selections. Instead, we obtained a plethora of phage that bound non-specifically to the plates and did not express functional Fab domains: PCR and sequencing analysis indicated either the presence of no Fab, or of frame-shift or nonsense mutations within the complementarity determining regions (CDRs).

An abundance of non-specific "sticky" binders is common where there are no strong specific binders present in the phage library, or if there is heterogeneity in the target sample such that the selection pressure for strong binders is low. Because of the long time course required for the selections and the inherent instability of $hH_V\Delta N\Delta C$ channel in detergent, we concluded that it would be unproductive to continue attempting selections according to this standard protocol. However, due to my experience with channel reconstitution and functional analysis (see Chapter 3) it occurred to me that it would be beneficial to develop a phage-selection protocol using reconstituted channels.

The $hH_V\Delta N\Delta C$ channels in vesicles are highly stable, and reconstituted vesicles can be frozen and stored at -80°C until needed. By using the reconstituted channels, the buffers needed for selections and ELISAs would no longer require detergents, thereby greatly reducing the cost of the entire protocol. Efficient negative selections could be

carried out using vesicles that did not contain any $hH_V\Delta N\Delta C$ channels, thereby removing any phage that non-specifically bound to lipids. Furthermore, the activity of the reconstituted $hH_V\Delta N\Delta C$ channels could be tested by the fluorescence-based concentrative uptake flux assay described in Chapter 3, thus allowing confirmation that the channels were in a functional native state. Therefore, we decided to develop this new phage-display library selection method for reconstituted membrane proteins.

4.3.2 Vesicle-based selections of reconstituted $hH_V\Delta N\Delta C$

Another benefit of using the vesicle-based selections is that it is possible to incorporate biotin-modified lipids into the membrane, thereby bypassing the need for potentially structure-altering modifications (biotinylation) of the protein of interest. In the case of the $hH_V\Delta N\Delta C$, vesicles reconstitution was done in 3:1 1-palmitoyl-2-oleoyl-sn-glycero-3-phosphoethanolamine (POPE): 1-palmitoyl-2-oleoyl-sn-glycero-3-phospho-(1'-rac-glycerol) (POPG) lipids doped with 0.5% 1,2-dipalmitoyl-sn-glycero-3-phosphoethanolamine-N-(cap biotinyl) headgroup modified PE (DPPE-biotin). Assuming an average vesicle radius of 100 nm, this concentration of DPPE-biotin would result in approximately 30-40 DPPE-biotin molecules per vesicle or 15-20 DPPE-biotin per membrane leaflet. Vesicles prepared in this way should be efficiently captured by streptavidin-coated plates.

To test streptavidin binding to the reconstituted DPPE-biotin containing vesicles, sucrose flotation assays were carried out on a sample of the vesicles to determine whether the streptavidin would migrate with the vesicles in the sucrose gradient. In the presence of streptavidin, the DPPE-biotin containing vesicles formed a gel at the interface of the

10% and 30% sucrose solutions in the step gradient. This gel phase was not observed with the DPPE-biotin containing vesicles in the absence of streptavidin or with normal vesicles not containing DPPE-biotin in the presence of streptavidin. Since streptavidin is a tetramer in solution, the gel phase is likely formed by cross-linking from the binding of multiple DPPE-biotin-containing vesicles by single streptavidin tetramers. These observations led me to conclude that the DPPE-biotin was presented on the surface of the vesicles in a way that allows for efficient streptavidin capture of the biotin-modified headgroup.

For the selections, the $hH_V\Delta N\Delta C$ were reconstituted into the DPPE-biotin containing vesicles at a protein-to-lipid ratio of 1:100 (wt:wt). At this ratio, there should be approximately 20 channels per vesicle on average. To confirm efficient incorporation of the channel into the vesicles, a sucrose flotation assay was performed and the functional state of the channels was tested with the fluorescence-based flux assay. These data showed that the $hH_V\Delta N\Delta C$ channels were efficiently incorporated into the vesicles and that the reconstituted channels were functional (Fig. 4.21).

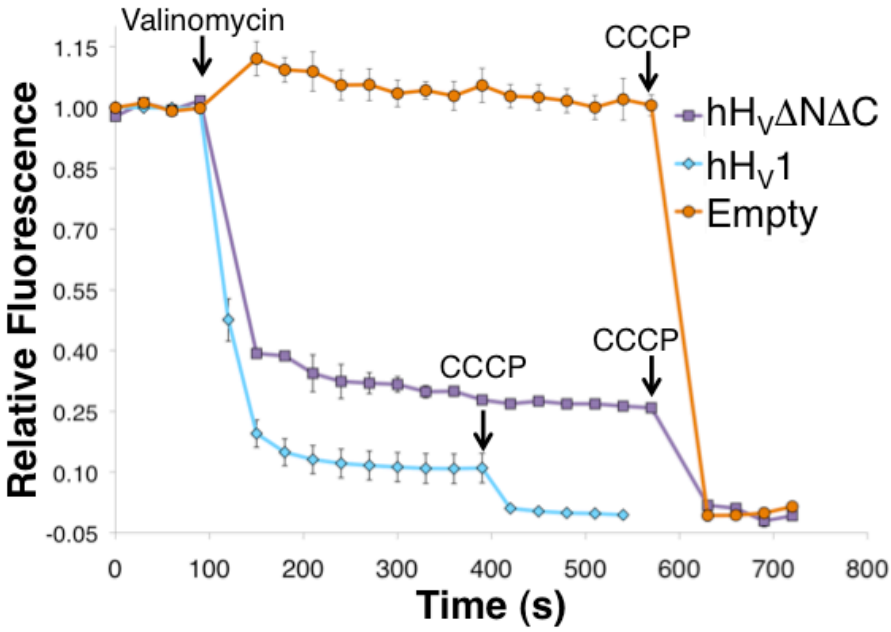

Fig. 4.21 H^+ uptake into vesicles containing truncated hH_V1 channels

Fluorescence-based H^+ flux assay for vesicles containing $hH_V\Delta N\Delta C$ (purple) compared to empty vesicles (orange) and wild type hH_V1 containing vesicles (cyan). Valinomycin and CCCP were added at the indicated time points and the fluorescence measurements were repeated 3-4 times (error bars represent the standard error of the mean).

When Dr Arita performed the phage selections with DPPE-biotin-containing vesicles, the use of empty vesicles for negative selection and of $hH_V\Delta N\Delta C$-containing vesicles for positive selections markedly improved the results compared to those of the detergent-based selections. As opposed to the detergent-based selections (which did not produce any potential H_V binding Fab clones), the vesicle-based selections generated nine Fab clones that showed significant selective binding to $hH_V\Delta N\Delta C$-containing vesicles (Table 4.3). Dr Arita subcloned these Fab genes into an expression vector and I expressed and purified each of the Fabs with the exception of Fab9 (Table 4.3), which did not express.

Table 4.3 ELISA Data for the best Fabs isolated from vesicle based selections

	Raw ELISA Data ‡				Ratios *	
Fab ID	BSA	Empty	FLAG	$hH_V\Delta N\Delta C$	FLAG/BSA	$hH_V\Delta N\Delta C$/Empty
Fab1	0.087	0.332	0.815	1.197	9.4	3.6
Fab2	0.082	0.288	0.839	1.236	10.2	4.3
Fab3	0.086	0.434	0.116	1.664	1.3	3.8
Fab4	0.100	0.164	0.996	1.433	10.0	8.7
Fab5	0.079	0.193	1.065	0.647	13.5	3.4
Fab6	0.075	0.347	0.185	0.856	2.5	2.5
Fab7	0.092	0.148	0.117	0.430	1.3	2.9
Fab8	0.094	0.237	0.644	0.604	6.9	2.5
Fab9	0.086	0.226	0.114	0.695	1.3	3.1

These ELISAs were performed by Dr Yuko Arita

‡ Raw ELISA data corresponds to wells containing BSA control (BSA), Empty Vesicles (Empty), $hH_V\Delta N\Delta C$ containing vesicles probed with an αFLAG Ab (FLAG), $hH_V\Delta N\Delta C$ containing vesicles. All wells were probed with αM13 phage Ab unless otherwise stated. The Fab gene on the phage contains a C-terminal FLAG-tag therefore the αFLAG antibody will only bind to phage that expresses a full-length Fab gene.

* High FLAG/BSA ratio indicates the presence of a bound phage that expresses a full-length Fab gene. High $hH_V\Delta N\Delta C$/Empty ratio indicates specific phage binding to $hH_V\Delta N\Delta C$. The two best $hH_V\Delta N\Delta C$/Empty ratios are highlighted in green.

The remaining eight Fabs were tested for binding to the $hH_V\Delta N\Delta C$ channel in DHPC. Only Fab2 showed evidence of weak binding to the channel on the SEC column in detergent (Fig. 4.22). Although there was almost no complex seen on the SEC column, a shift to lower elution volumes of some Fab2 was observed when the fractions were run on an SDS-PAGE gel (Fig. 4.22C). This shifting of elution volume was not observed for the other best candidate, Fab4 (Table 4.3), indicating that Fab2 did bind weakly to the channel in DHPC. However, the binding observed for Fab2 was very weak and was not considered significant enough to carry forward into full-scale crystallization trials.

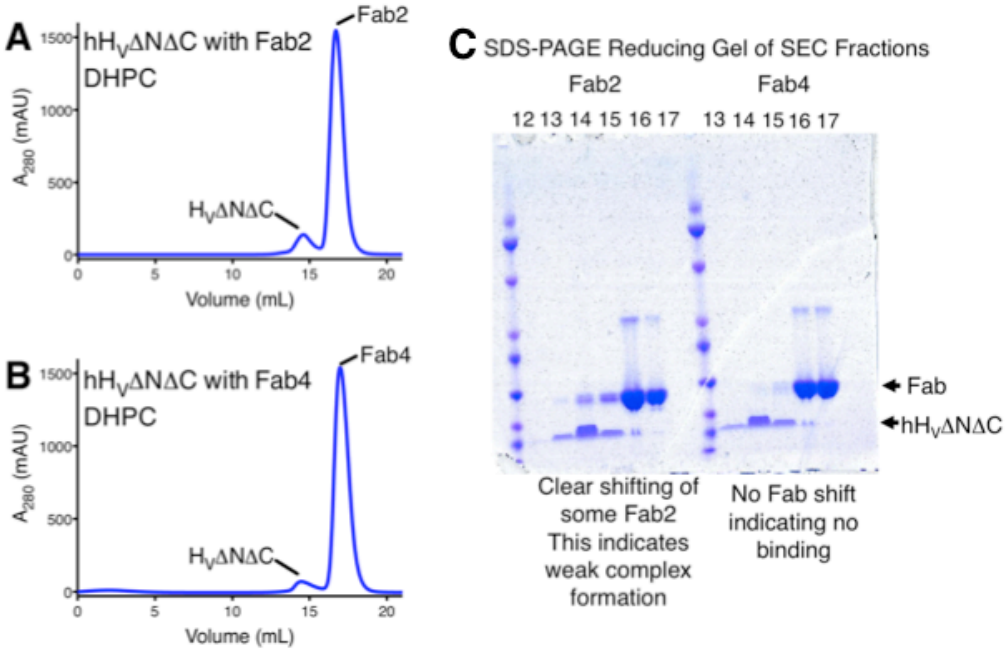

Fig. 4.22 Evidence for weak complex formation between Fab2 and $hH_V\Delta N\Delta C$

(A) SEC chromatogram of $hH_V\Delta N\Delta C$ with Fab2. (B) SEC chromatogram of $hH_V\Delta N\Delta C$ with Fab4. (C) SDS-PAGE reducing gel of SEC fractions showing a shift in the elution volume for Fab2 indicating weak binding of Fab2 to $hH_V\Delta N\Delta C$.

4.3.3 Future directions

Although Fab2 showed some evidence of weak binding, stronger-binding Fabs are needed to justify full-scale crystallization trials. Therefore, Dr Arita is developing affinity-matured libraries based on the sequences of the best binders from the vesicle-based selections (Fab2 and Fab4; Table 4.3). These libraries are currently being screened for Fabs with improved binding to vesicle-reconstituted $hH_V\Delta N\Delta C$. If Fabs with a significant improvement in binding are identified, they will be tested for Fab-channel complex formation by SEC. All promising candidates will be followed up in crystallization trials.

4.4 CONCLUSIONS

In this chapter, I described my efforts to obtain the X-ray crystal structure of a H_V channel. Together with Dr Seok-Yong Lee we attempted crystallization of the wild type channel, lysozyme and dimer fusion constructs, and chimeric channels. Although I did obtain a crystal structure with the HAP5ΔNΔC chimera, I concluded that this structure was non-native. Because of the power of Fab mediated crystallization it is still desirable to isolate high affinity antibodies against the transmembrane domain of hH_V1. My work in collaboration with Dr Yuko Arita in the Sidhu lab at the University of Toronto on the isolation of phage display Fabs has the potential to achieve this goal. However, if we are unable to isolate high affinity antibodies by this method it may still be possible to get high affinity crystallization chaperones by other means. By injecting hH_V1 into llamas it may be possible to generate hH_V1 specific nanobodies. These single-chain camelid antibody fragments have been used successfully for the crystallization of membrane proteins that lack well-structured soluble domains (Rasmussen *et al*. 2010).

As an alternative strategy for structure determination, working with Dr Joel Butterwick in the laboratory, I decided to pursue NMR characterization of hHV1ΔNΔC. As described in the next chapter, this methodology allowed us to define the secondary structure of the channel and we experimentally identified a short N-terminal S0 helix that precedes the transmembrane domain.

CHAPTER 5: NMR

During the final stages of the crystallography work discussed in Chapter 4, I set out to also study the chimeric HAP5ΔC by nuclear magnetic resonance (NMR) with detergent-solubilized channels. Together with postdoctoral fellow Dr Joel Butterwick, I planned to examine the titratable amino acid residues within the transmembrane domain of the channel in order to investigate the conduction mechanism. Because of the sensitivity of NMR to the protonation state of amino acid side chains, this technique complements the crystallographic studies and can provide additional insight into the mechanism of H^+ conduction through H_V.

Although our studies began with the chimeric HAP5ΔC channels, after the crystallography indicated that this channel might not be properly structured in detergent, we decided to work on the wild type truncated hH_VΔNΔC channel. In this chapter, I will briefly discuss our initial NMR work on the HAP5ΔC channel and will then present our efforts to solve the hH_VΔNΔC channel structure.

5.1 NMR ON THE HAP5 CHIMERA

5.1.1 Removal of N-terminus allows for detection of transmembrane peaks

The HAP5ΔC construct was chosen as the best candidate for NMR because of its stability at high concentrations at room temperature (required to maintain its homogeneity during the multi-day length of the experiments) and because of the progress that its structural characterization by X-ray crystallography showed at the time.

To collect a ^{1}H-^{15}N heteronuclear single quantum coherence (HSQC) spectrum, the protein had to be uniformly labeled with the heavy ^{15}N isotope. Since the only source of nitrogen during the expression of the channel in *Pichia pastoris* was from the ammonium sulfate added to the media, we were able to uniformly label the protein by replacing all of the ammonium sulfate with ^{15}N-ammonium sulfate.

The original spectra collected on the HAP5ΔC in LDAO channel showed many peaks (Fig. 5.1). Since every peak on the ^{1}H-^{15}N HSQC spectrum corresponds to a covalently bound ^{1}H-^{15}N pair, the majority of the peaks seen derived from the main chain amide bond, with a subset originating from the side chains of asparagine, glutamine and tryptophan residues (Cavanagh *et al*. 2007). Depending on the local environment of the amino acid residue, it is sometimes possible to see peaks corresponding to the side chains of arginine residues, but it is very rare to see peaks corresponding to histidine and lysine side chains because of their fast rate of H^{+} exchange with the solvent (Cavanagh *et al*. 2007).

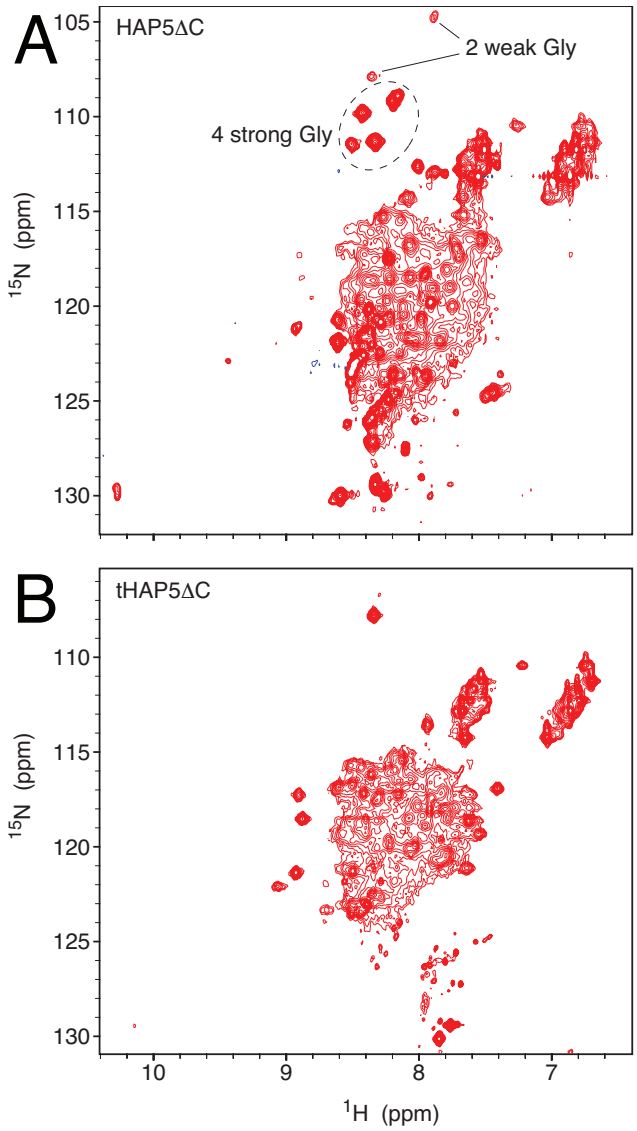

Fig. 5.1 ^{1}H-^{15}N HSQC spectrum of ^{15}N labeled HAP5ΔC and tHAP5ΔC in LDAO

(**A**) ^{1}H-^{15}N HSQC spectrum of HAP5ΔC in N,N-Dimethyldodecylamine N-oxide (LDAO) at 25°C (top) with the glycine resonances highlighted to demonstrate the eclipsing effect of the N-terminus. Four glycine resonances, which likely correspond to the four glycines in the N-terminus are much stronger than two other glycine peaks observed that likely correspond to glycines from the transmembrane segment. (**B**) ^{1}H-^{15}N HSQC spectrum of trypsinized HAP5ΔC (tHAP5ΔC) in LDAO at 25°C (bottom) demonstrating that the majority of the intense peaks derived from the N-terminus.

The intensity of the peaks observed on the ^{1}H-^{15}N HSQC is positively correlated to the flexibility of the protein; thus, loops and unstructured regions might eclipse the more stable parts of the protein (Cavanagh *et al*. 2007). This can be worse with detergent-solubilized membrane proteins since the interactions with the detergent micelle can further broaden peaks corresponding to the transmembrane domain (Butterwick & Mackinnon 2010). Therefore, we suspected that the strong peaks observed in the ^{1}H-^{15}N HSQC spectrum of the HAP5ΔC channel originated from residues within the unstructured N-terminus (Fig. 5.1A). For example six peaks corresponding to glycine resonances can be seen in the ^{1}H-^{15}N HSQC spectrum of the HAP5ΔC (Fig. 5.1A) the four intense glycine peaks likely correspond to the four glycines found in the N-terminus, whereas the two weaker glycine peaks likely correspond to glycines from the transmembrane domain (Fig. 5.1A).

To isolate the peaks originating from the transmembrane domain, we collected a spectrum from trypsinized HAP5ΔC (tHAP5ΔC) channels in which the digested N-terminus had been purified away (Fig. 5.1B). This spectrum clearly indicated that the unstructured N-terminus was indeed eclipsing the transmembrane region in the spectrum of the untrypsinized HAP5ΔC and that, if we wanted to examine the titratable residues in the transmembrane domain, we would have to work with the doubly truncated HAP5ΔNΔC construct.

To improve to resolution of the spectrum, it was desirable to perdeuterate the protein. By using transverse relaxation-optimized spectroscopy (TROSY), it is possible to sharpen the line-width of the peaks, making it easier to make out individual ^{1}H-^{15}N peaks (Cavanagh *et al*. 2007). Although the expression levels were greatly reduced by growing

the *Pichia pastoris* in heavy water (^2H_2O a.k.a. D_2O), we were able to purify a sample of perdeuterated HAP5ΔNΔC. By perdeuteration and by changing detergents from LDAO to the lipid-like detergent 1-palmitoyl-2-hydroxy-sn-glycero-3-phospho-(1'-rac-glycerol) (LPPG) the resolution of this spectrum was greatly improved (Fig. 5.2).

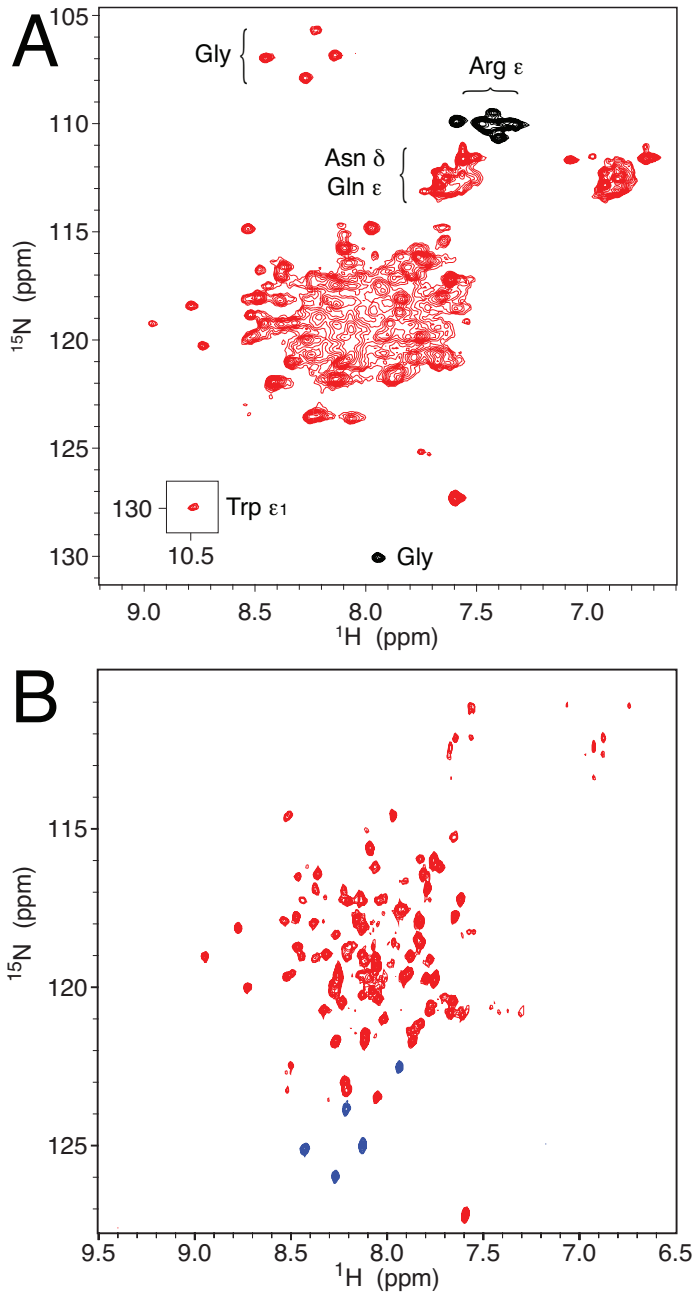

Fig. 5.2 Spectra of HAP5ΔNΔC in LPPG

(**A**) ^{1}H-^{15}N HSQC spectrum of ^{15}N-labeled HAP5ΔNΔC in LPPG at 25°C. Peaks that are aliased in the ^{15}N dimension are shown in black. All five expected glycines can be seen, as well as the side chains of the arginine, asparagine, glutamine and tryptophan (inset)

residues. (B) ^{1}H-^{15}N HSQC TROSY of ^{2}H-^{15}N labeled HAP5ΔNΔC in LPPG at 25°C. Peaks that are aliased in the ^{15}N dimension are shown in blue.

5.1.2 Abandonment of the chimeric channel in favor of wild type

With spectra of perdeuterated, ^{15}N-labeled HAP5ΔNΔC in our hands, we planned to begin the assignment of the ^{1}H-^{15}N HSQC spectrum peaks. However, at this time, the results from the crystallography experiments indicated that, although the HAP5 chimera is a functional H^{+} channel, its structure might be destabilized by extraction from the membrane and solubilization by detergent (see Chapter 4). Therefore we decided that it would be best not to pursue further NMR analysis of the HAP5ΔNΔC chimeric construct.

However, my work with the chimeric proteins, discussed in Chapter 4, required the redesign of the protein expression construct, which resulted in greatly improved yields after purification. We reasoned that if we were to apply the same changes to the wild type hH_VΔNΔC construct (i.e. moving the GFP tag and PreScission protease site to the N-terminus), we should also improve the yield of purified wild type channel. In addition, if detergent conditions could be found in which this channel was highly stable it should be possible to examine the wild type hH_V transmembrane domain by NMR.

Dr. Butterwick had previously solved the structure of the isolated voltage-sensor domain (VSD) of K_VAP by NMR (Butterwick & Mackinnon 2010). Therefore, although we were unable thus far to solve the structure of the hH_VΔNΔC construct by crystallography (see Chapter 4), we reasoned that with improved expression and stability it might be possible to solve the structure by NMR.

5.2 NMR STUDIES OF HUMAN H_V CHANNELS

5.2.1 Truncated hH_V1 channels are functional

In addition to the functional analysis of the reconstituted $hH_V\Delta N\Delta C$ channels by the flux assay presented in Chapter 4 (Fig. 4.21 on page 133), electrophysiological studies were carried out on the truncated versions of the hH_V1 channel. In order to confirm that the $hH_V\Delta N\Delta C$ channel construct used for NMR studies was a functional H^+-selective voltage- and ΔpH-gated channel, whole-cell patch clamp electrophysiology of truncated channels over-expressed in HEK cells was performed. Due to the importance of the ΔpH gating in the physiological functions of the channel and its poorly understood molecular mechanism (see Chapter 1), we wanted to confirm that any construct that we pursued for structural analysis maintained this important mode of regulation. For completeness, all three truncated channel constructs ($hH_V\Delta N$, $hH_V\Delta C$ and $hH_V\Delta N\Delta C$) were characterized and compared to wild type.

The electrophysiological recordings clearly indicated that, although the truncations altered the gating kinetics, all of the truncated channels were functional voltage-gated channels (Fig. 5.3). Furthermore, by perfusion of the external solution with buffers at different pH, it was possible to both measure the ΔpH gating and H^+ selectivity of the channels (Fig. 5.3). These results indicated that, although the truncations did alter ΔpH-gating behavior, the truncated channels were still ΔpH-gated (Fig. 5.3). By comparing the reversal potentials of the measured currents to what is expected for the Nernst equilibrium potential for H^+ at the different ΔpHs, it was possible to show that each of the constructs maintained wild-type-like H^+ selectivity (Fig. 5.4).

Fig. 5.3 Electrophysiological characterization of truncated hH_V1 channels

Examples of currents elicited from whole-cell patch clamp recording of HEK cells expressing (**A**) hH_V1, (**B**) $hH_V\Delta N$, (**C**) $hH_V\Delta C$ and (**D**) $hH_V\Delta N\Delta C$ at symmetric pH (pH_o = pH_i = 6.5; left) according to the voltage-step protocols shown. Average tail current IV curves corresponding to the same cell as shown on the right at three different pH_o (pH_o = 7.0 blue, pH_o = 6.5 brown and pH_o = 6.0 green). Each recording was performed 2-3 times per cell per pH_o with the error bars on the IV curves corresponding to the standard deviation are plotted but are smaller than the graph symbols in most cases.

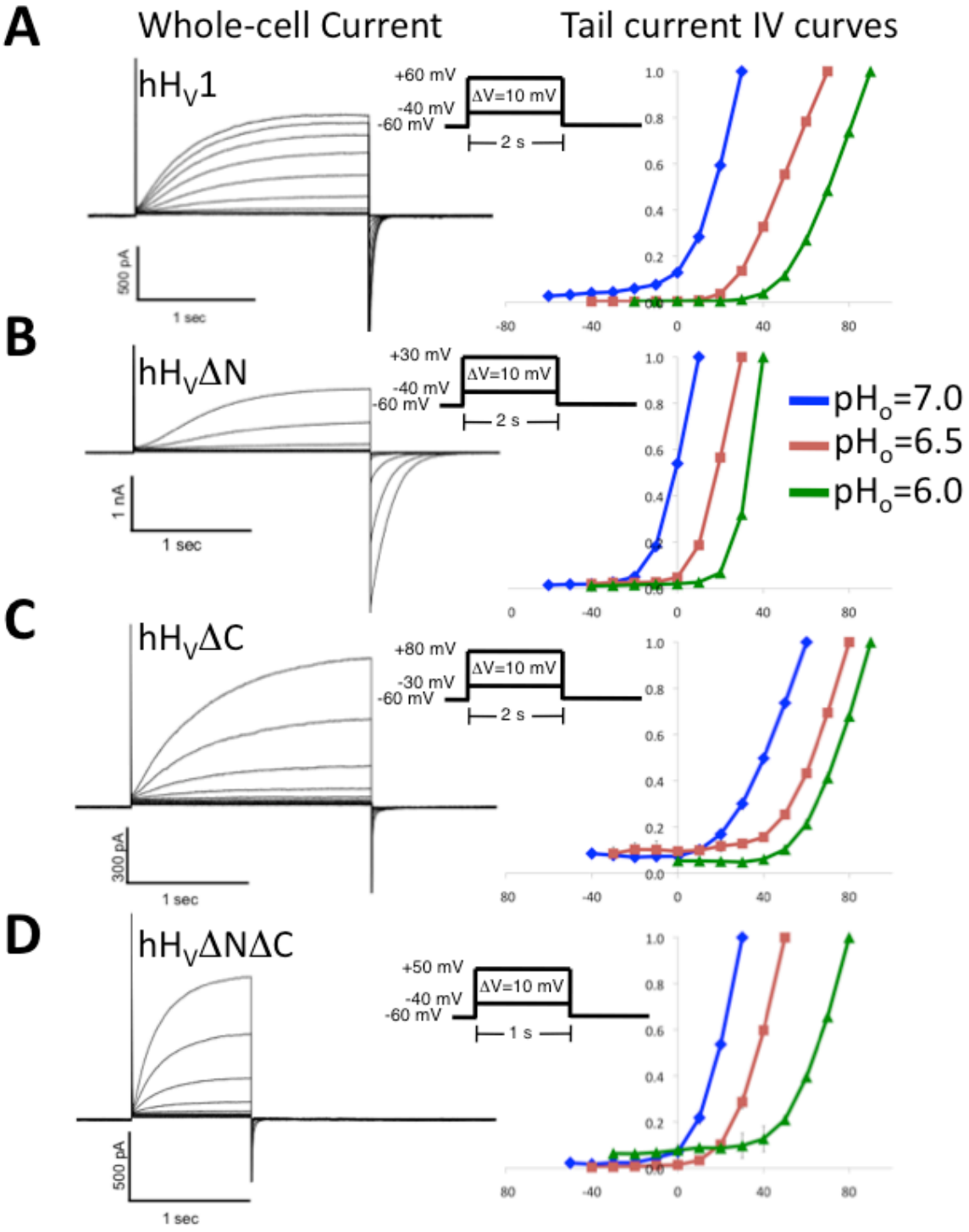
A
Whole-cell Current
Tail current IV curves
hHV1
+60 mV
-40 mV
-60 mV
ΔV=10 mV
2 s
500 pA
1 sec
B
hHVΔN
+30 mV
-40 mV
-60 mV
ΔV=10 mV
2 s
1 nA
1 sec
pHo=7.0
pHo=6.5
pHo=6.0
C
hHVΔC
+80 mV
-30 mV
-60 mV
ΔV=10 mV
2 s
300 pA
1 sec
D
hHVΔNΔC
+50 mV
-40 mV
-60 mV
ΔV=10 mV
1 s
500 pA
1 sec

Fig. 5.4 H^+ selectivity of wild type and truncated hH_V1 channels

Examples of currents elicited from whole-cell patch clamp recordings of HEK cells expressing $hH_V\Delta N\Delta C$ at (**A**) pH_o = 6.0 (**B**) pH_o = 6.5 and (**C**) pH_o = 7.0 according to the voltage-step protocols shown. In each case pH_i = 6.5. (**D**) IV plot of average current elicited shortly after variable voltage-step for hH_V1 (cyan), $hH_V\Delta N$ (red), $hH_V\Delta C$ (green) and $hH_V\Delta N\Delta C$ (purple) according to the same voltage-step protocols show in (**A-C**) at the different values of pH_o. Each recording was performed 3-4 times per cell per pH_o, error bars corresponding to the standard deviation are plotted but are smaller than the graph symbols in most cases. (**E**) Comparison of the reversal potentials for each construct (colored as in **D**) to the Nernst equilibrium potential for H^+ (black line) at each pH_o. Each point represents the average of 3-4 cells with the error bars corresponding to the standard deviation.

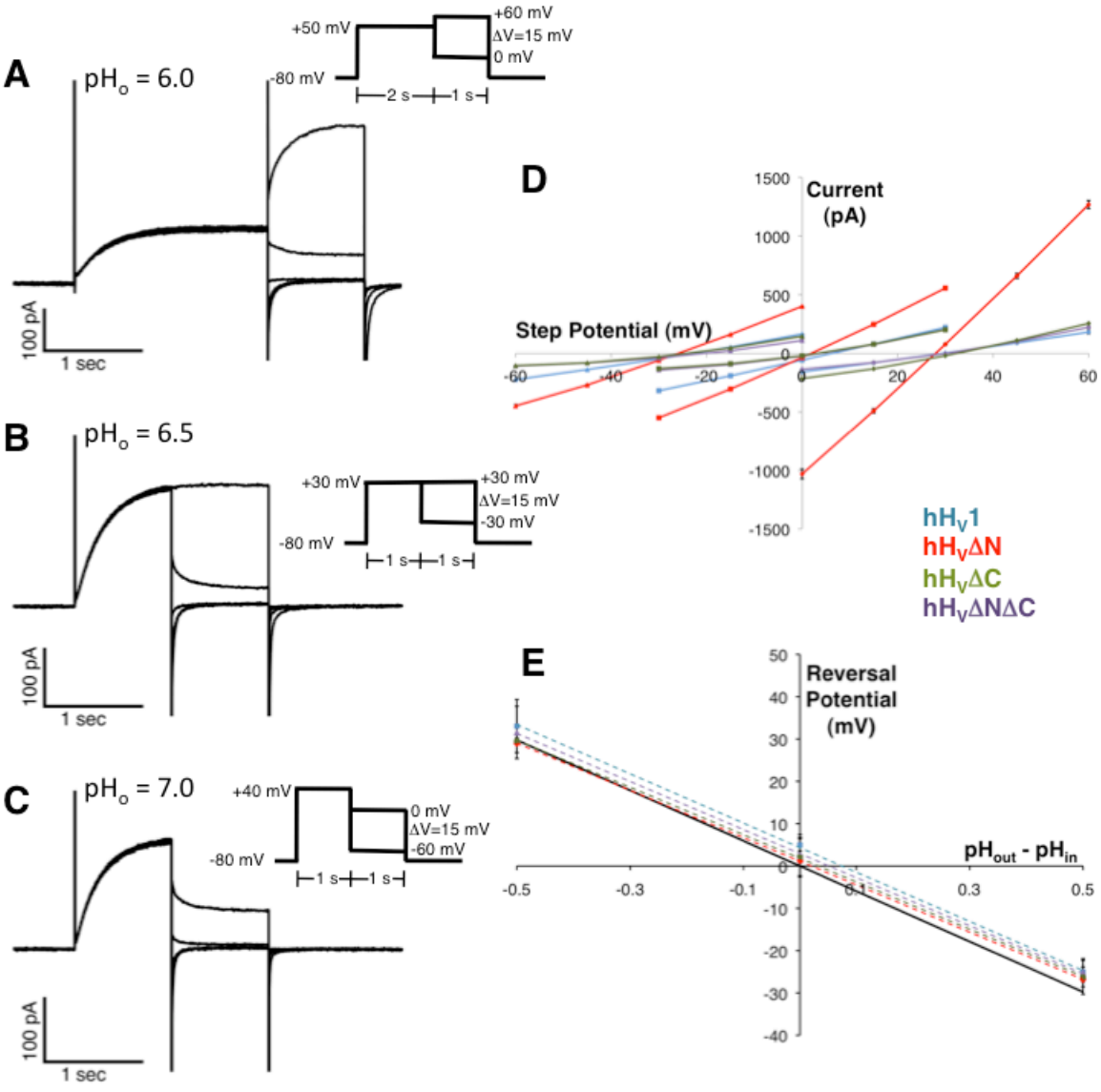
A
pH$_o$ = 6.0
+50 mV
+60 mV
ΔV=15 mV
0 mV
-80 mV
2 s
1 s
100 pA
1 sec
B
pH$_o$ = 6.5
+30 mV
+30 mV
ΔV=15 mV
-30 mV
-80 mV
1 s
1 s
100 pA
1 sec
C
pH$_o$ = 7.0
+40 mV
0 mV
ΔV=15 mV
-60 mV
-80 mV
1 s
1 s
100 pA
1 sec
D
Current (pA)
Step Potential (mV)
1500
1000
500
0
-500
-1000
-1500
-60
-40
-20
0
20
40
60
hH$_V$1
hH$_V$ΔN
hH$_V$ΔC
hH$_V$ΔNΔC
E
Reversal Potential (mV)
pH$_{out}$ - pH$_{in}$
50
40
30
20
10
0
-10
-20
-30
-40
-0.5
-0.3
-0.1
0.1
0.3
0.5

It is interesting to note the opposite effect that the N- and C-terminal truncations have on the gating kinetics and ΔpH-gating. The N-terminal truncation decreased the rate of both opening and closing of the channel (Fig. 5.3B). Additionally, truncation of the N-terminus also shifted the ΔpH-gating of the channel, resulting in channel opening at left-shifted (more negative) voltages relative to wild type channels at the equivalent ΔpH (Fig. 5.3B). Unlike the wild type channel, in which ΔpH-gating ensures that the channel is a perfect outward rectifier (see Chapter 1), this left shift of the delta-N channel allows small inward H^+ currents at high external H^+ concentrations (low external pH). In contrast, the C-terminal truncation increases the rate of both opening and closing of the channel (Fig. 5.3C) and shifts the ΔpH-gating such that channel opening occurs at more right-shifted voltages, strengthening the wild-type-like outward rectification (Fig. 5.3A and C). Although similar to the C-terminal truncation alone in that the rates of channel opening and closing are sped up in the doubly truncated channel ($hH_V\Delta N\Delta C$), the ΔpH-gating more resembles that of wild type channels (Fig. 3D).

These data support a potential interaction between the N-terminus and transmembrane domain in wild type channels. Such an interaction has been previously proposed by Musset *et al*., based on modulation of the gating of wild type hH_V1 by phosphorylation of amino acid residue T29 on the N-terminus (Musset *et al*. 2010a). A simple explanation for the changes in channel gating observed upon N-terminal truncation or phosphorylation could be that the unphosphorylated N-terminus binds to the transmembrane domain and stabilizes the hyperpolarized conformation. If true, this would mean that disruption of the interaction between the N-terminus and the transmembrane domain by either removal or phosphorylation of the N-terminus would

destabilize the hyperpolarized conformation, resulting in the observed left-shift in the voltage activation of the channel (Fig. 5.3B; Musset *et al*. 2010a).

More research is required to fully understand the interactions between the termini and the transmembrane domain and to identify the amino acids residues involved. However, the data presented in Fig. 5.3 demonstrate that the truncated channels are functional voltage- and ΔpH-gated H^+-selective channels, validating the $hH_V\Delta N\Delta C$ construct as a good structural target for generating insight into these interesting biophysical phenomena.

5.2.2 $hH_V\Delta N\Delta C$ is biochemically stable in two detergents

Expression of wild type $hH_V\Delta N\Delta C$ was much improved by the N-terminal decaHis-GFP tag. In order to get sufficiently enriched channel for the NMR experiments, it was also necessary to alter the purification protocol. Originally, the purification was carried out similar to that of the HAP5ΔNΔC construct in DM (discussed in Chapter 4), i.e. *via* Co^{2+}-resin immobilized metal affinity chromatography (IMAC), followed by PreScission protease digestion, a second round of Co^{2+}-resin IMAC for removal of the cleaved decaHis-GFP tag and a by final size exclusion chromatography (SEC). However, dialyzing into low salt during overnight PreScission protease digestion and replacing the second IMAC step with an anion exchange chromatography step were sufficient to significantly improve the purity of the $hH_V\Delta N\Delta C$ channel.

I investigated the detergent stability profile of the truncated channel of this highly enriched $hH_V\Delta N\Delta C$. The $hH_V\Delta N\Delta C$ channel was unstable in maltoside detergents,

precipitating after one day at room temperature at high concentrations. However, the truncated channel was highly stable in the lipid-like detergents DHPC and LPPG. In either of these detergents, the truncated channel remained in solution and monodisperse on the SEC column at high concentrations after incubation for several days at room temperature.

During detergent exchange into LPPG, a slow timescale detergent-exchange phenomenon was observed, which manifested as a significant shift in the elution volume of the $hH_V\Delta N\Delta C$ peak (Fig. 5.5). Specifically, after the ion exchange chromatography step in DM the channel was concentrated and run over the SEC column equilibrated in LPPG. During this detergent exchange SEC run the $hH_V\Delta N\Delta C$ channel eluted as a broad peak centered at 12.8 mL (Fig. 5.5A). When this peak was pooled, concentrated and re-run over the SEC column in LPPG, the channel eluted as a doublet with peaks centered at 12.4 and 13.4 mL respectively (Fig. 5.5B). If the same sample was re-run over the SEC column after several hours, the elution profile collapsed into a single sharp peak centered at 13.3 mL, which then remained stable for up to a week at room temperature (Fig. 5.5C). Such a detergent-exchange phenomenon was not observed for exchange of $hH_V\Delta N\Delta C$ from DM to DHPC.

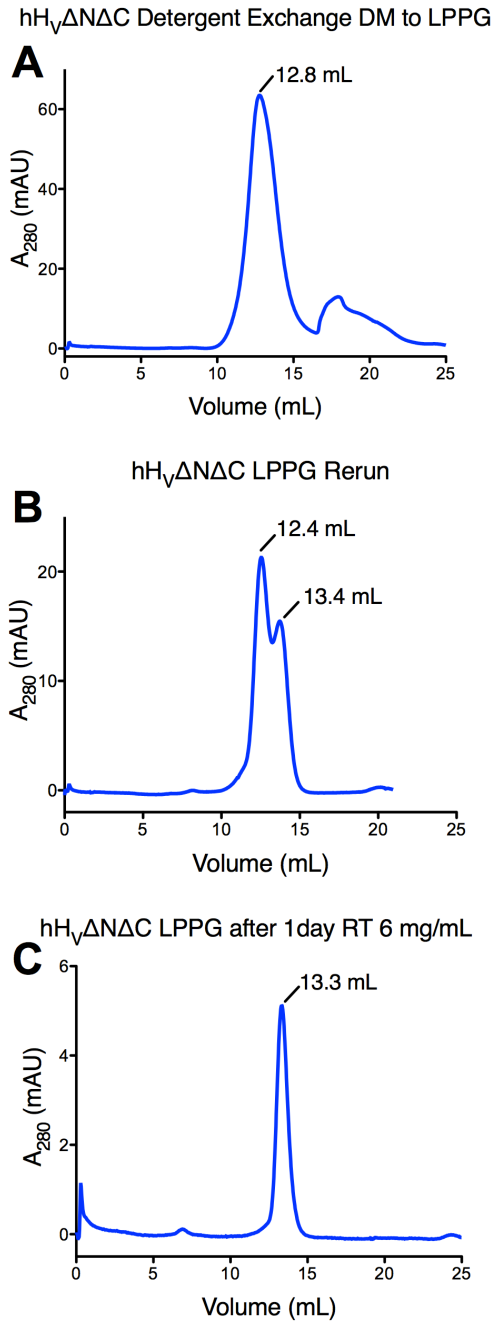

Fig. 5.5 DM to LPPG detergent exchange phenomenon of hH$_V$ΔNΔC

(**A**) SEC chromatogram of hH$_V$ΔNΔC initial detergent exchange from DM to LPPG. (**B**) SEC chromatogram of immediate concentration and rerun of pooled fractions 10-14 mL from (**A**) over SEC column equilibrated in LPPG. (**C**) SEC chromatogram of rerun of pooled fractions 10-14 mL from (**A**) over SEC column equilibrated in LPPG after 1 day incubation at room temperature (RT) at 6 mg/mL.

Due to the large change observed when $hH_V\Delta N\Delta C$ was exchanged into LPPG, we were concerned that we were obtaining either incomplete detergent exchange or a detergent-dependent refolding of the channel, potentially into a non-native conformation. We were able to rule out incomplete detergent exchange as a possible cause by looking at the ^1H peaks corresponding to the detergent in the NMR spectrum. Due to the high concentration of detergent in the concentrated NMR samples, the strongest peaks in the one-dimensional 1H spectrum come from the detergent molecules. If there were incomplete detergent exchange between DM and LPPG, we would expect to see ^1H peaks corresponding to DM molecules in the spectrum. However, only peaks corresponding to LPPG were observed, indicating that complete detergent exchange had occurred. This is also in agreement with the observation that the exchange phenomenon occurs to the concentrated $hH_V\Delta N\Delta C$ samples in the absence of further detergent exchange (i.e. given time the sample will convert to the 13.3 mL peak without further runs over a SEC column equilibrated with LPPG).

When we collected a ^1H-^{15}N HSQC spectrum of the $hH_V\Delta N\Delta C$ construct in LPPG, we observed a highly disperse set of peaks corresponding to the majority of the $hH_V\Delta N\Delta C$ main chain amides as well as all of the asparagine, glutamine, arginine and tryptophan side chains (Fig. 5.6A). Since the quality of the HSQC spectrum is sensitive to the dynamics of the protein, this high-quality spectrum indicated that the channel was in a well-folded stable confirmation (Cavanagh *et al*. 2007). We concluded that the probability of the channel adopting a well-folded stable non-native conformation was low and that, therefore, the conformation of the channel after the detergent exchange phenomenon was likely native.

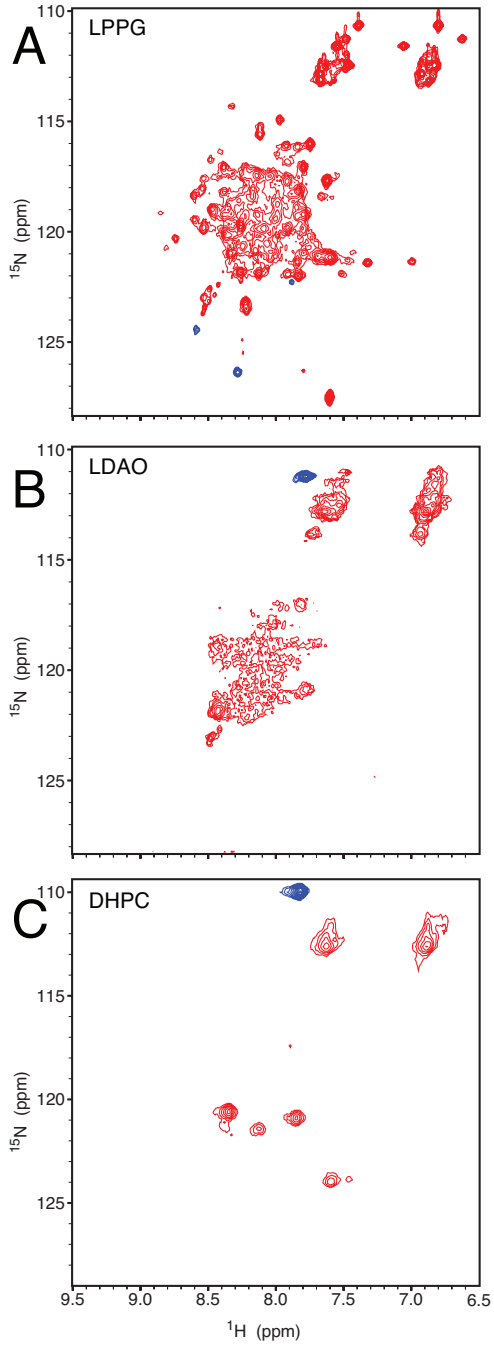

Fig. 5.6 Detergent screen ^{1}H-^{15}N HSQC of ^{15}N labeled hH$_V$ΔNΔC

(**A**) ^{1}H-^{15}N HSQC spectrum of ^{15}N-labeled hH$_V$ΔNΔC in LPPG. (B) ^{1}H-^{15}N HSQC spectrum of ^{15}N-labeled hH$_V$ΔNΔC in LDAO. (C) ^{1}H-^{15}N HSQC spectrum of ^{15}N-labeled hH$_V$ΔNΔC in DHPC. All spectra were collected at 25°C. Peaks that are aliased in the ^{15}N dimension are shown in blue.

Although the $hH_V\Delta N\Delta C$ channel was less stable in LDAO than in LPPG or DHPC, we decided to examine the ^{1}H-^{15}N HSQC spectrum in LDAO because of the high quality spectrum observed for the chimeric HAP5ΔNΔC in this detergent (Fig. 5.1B). However, the ^{1}H-^{15}N HSQC spectrum of $hH_V\Delta N\Delta C$ in LDAO was very weak with only few distinguishable peaks (Fig. 5.6B).

Detergent exchange of $hH_V\Delta N\Delta C$ from DM to DHPC did not result in any equivalent slow exchange phenomenon. During initial detergent exchange into DHPC $hH_V\Delta N\Delta C$ elutes as a single peak centered at 14.8 mL and this peak position does not change significantly with time. However, when we collected a ^{1}H-^{15}N HSQC spectrum in DHPC the quality of the spectrum was poor (Fig. 5.6C.). The poor quality of the ^{1}H-^{15}N HSQC spectrum in DHPC prohibited any further structural analysis of $hH_V\Delta N\Delta C$ by NMR in this detergent. Therefore, we concluded that structural work by NMR on $hH_V\Delta N\Delta C$ would be pursued in LPPG.

5.2.3 Assignment of the $hH_V\Delta N\Delta C$ spectra in LPPG

Resonance assignments for backbone ($^{1}H^{N}$, ^{15}N, $^{13}C'$, and $^{13}C^{\alpha}$) nuclei at 25°C and neutral pH were identified using TROSY HNCA, HNCO and HN(CO)CA. Moreover, ^{15}N-edited ^{1}H–^{1}H nuclear Overhauser effect spectroscopy (NOESY) experiments (Cavanagh *et al*. 2007) were recorded using 70% deuterated $hH_V\Delta N\Delta C$ samples. Isotope labeling of the His-GFP-$hH_V\Delta N\Delta C$ construct was performed according to the same protocol used for the HAP5 constructs (see above and Materials and Methods), with the exception that the concentration of D_2O was lowered from 90% to 70%, greatly improving the expression

with no significant reduction in TROSY spectrum quality. Uniform ^{13}C labeling of the $hH_V\Delta N\Delta C$ construct was accomplished by replacing the glycerol in the growth media and methanol in the expression media with ^{13}C-labeled glycerol and methanol respectively.

In addition to the uniformly labeled samples, we recorded HSQC experiments on samples with different combinations of labeled amino acids so that specific amino acids could be distinguished in crowded regions of the spectra: A, G, F, D/N, L, I, K, E/Q, V and R (for examples see Fig. 5.7A and B). Although bacterial expression had not resulted in any extractable channel for the original hH_V1 constructs (see Chapter 3), we were able to express and purify the His-GFP-$hH_V\Delta N\Delta C$ construct from *Escherichia coli* which, due to significantly reduced metabolic shuffling of labeled atoms into other amino acids, facilitated specific amino acid labeling. Resonance assignments were extended along the side chains using H(C)CH-COSY and ^{13}C-edited and ^{15}N-edited NOESY experiments. Most ambiguities present among the methyl resonances were resolved by repeating the ^{13}C-edited NOESY using methyl-specific labeling on Ile, Leu, and Val residues (Cavanagh *et al*. 2007). Complete backbone resonance assignments (H, N, CA, CO) were determined for 56% of the 138 residues, whereas 77% of residues have main chain amide assignments (Fig. 5.7). Importantly, peaks for 84% have at least some (main chain or side chain) assignments, providing easily accessible probes for nearly every residue within the $hH_V\Delta N\Delta C$ construct.

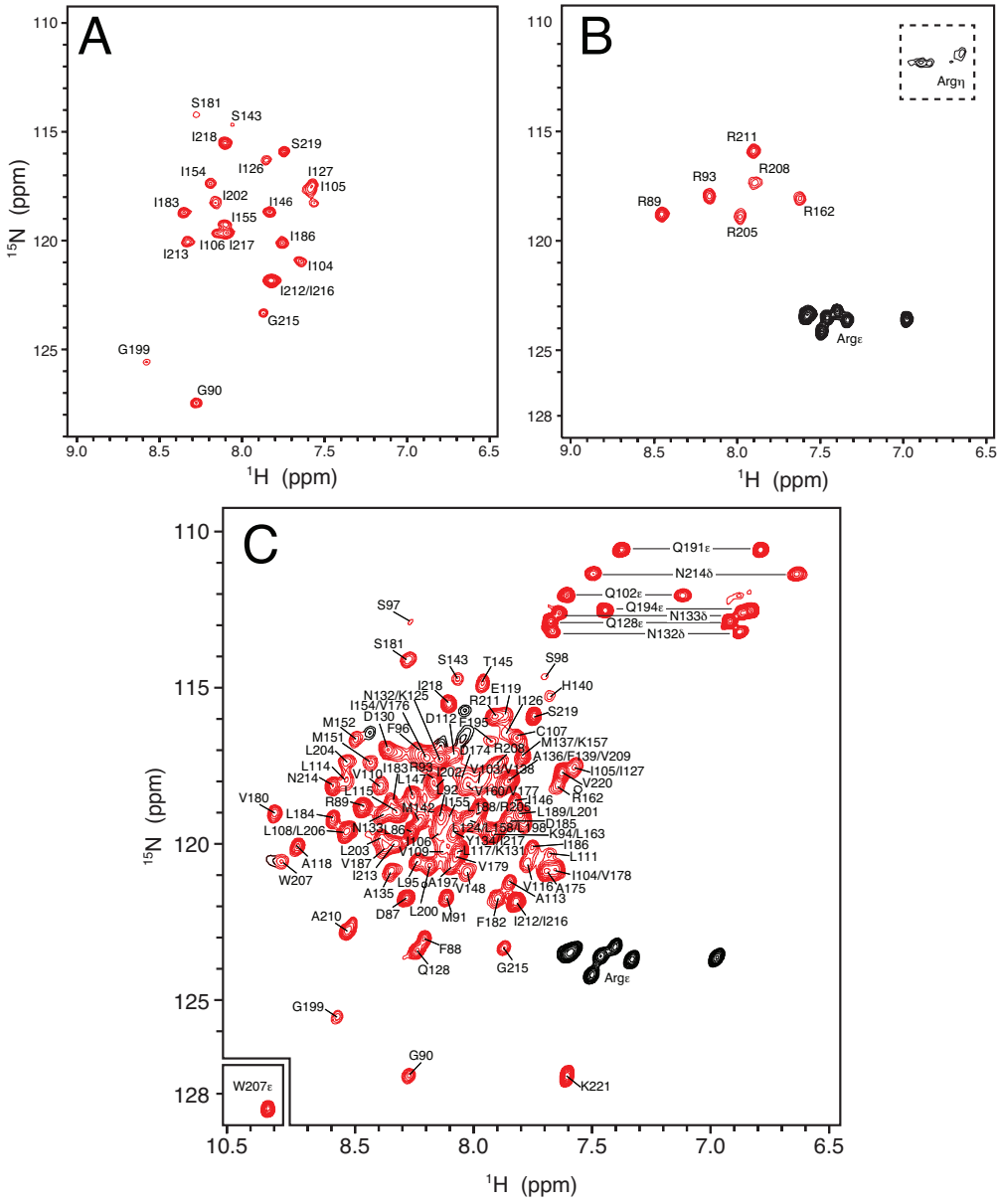

Fig. 5.7 Amide resonance assignments for hH$_V$ΔNΔC in LPPG micelles

^{1}H-^{15}N HSQC spectra of (**A**) ^{15}N-Ile/Gly (^{15}N-Ser is also visible because of metabolic scrambling of ^{15}N-Gly label) and (**B**) ^{15}N-Arg specific amino acid labeled H$_V$ΔNΔC in LPPG. (**C**) ^{1}H–^{15}N HSQC TROSY spectrum at 25°C of ^{2}H-^{15}N labeled hH$_V$ΔNΔC with assignments. Main-chain amide peaks for 106 residues (out of 136 residues expected to be observed; 2 Pro) and N132$^{\delta}$, N133$^{\delta}$, N214$^{\delta}$, Q102$^{\varepsilon}$, Q128$^{\varepsilon}$, Q191$^{\varepsilon}$, Q194$^{\varepsilon}$ and W207$^{\varepsilon}$ side chains have been assigned. Peaks that are unassigned are shown in black. Peaks that are aliased in the ^{15}N dimension include G90, G199, G215 and the Arg$^{\varepsilon}$ resonances.

5.2.4 Secondary structure shows S1-S4 helices plus a S0 helix

Chemical-shift analysis of the assigned main chain resonances allowed for the determination of secondary structure of the $hH_V\Delta N\Delta C$ construct (Fig. 5.8). Patterns of secondary chemical shifts of main chain resonances ($\Delta\delta$ = observed shift – "random coil" shift) report on the secondary structure of the protein (Cavanagh *et al*. 2007; Wishart & Case 2001). By comparing the $\Delta\delta$s of the different main chain atoms of the same amino acid residue, it is possible to get a robust determination of the secondary structure for that residue.

In addition to observing the four transmembrane helices (S1-S4), by examining the $\Delta\delta$s of the $hH_V\Delta N\Delta C$ construct in LPPG we experimentally confirmed the existence of a short N-terminal helix (S0) that precedes the first transmembrane helix S1 (approximately 10 amino acid residue long, R89-S98; Fig. 5.8). Although an analogous S0 helix has been reported in the NMR structure of the isolated VSD of K_VAP (Butterwick & Mackinnon 2010), this was the first observation of this structural feature in H_V channels.

Based on the $\Delta\delta$ observations, we are able to estimate the amino acid residue span of each of the transmembrane helices. According to these data, S1 spans residues V103-D123, S2 starts at residue N133 and continues at least until residue L163, S3 extends at least from residue D174 to L188 and S4 spans residues F195-S219 (Fig. 5.8). The ambiguity in the start position of helix S3 and stop position of helices S2 and S3 derives from the lack of assignments for main chain atoms from amino acid residues within the S2-S3 and S3-S4 loops. Nonetheless, it is clear from these data that the secondary structure of $hH_V\Delta N\Delta C$ in LPPG matches what would be expected for a VSD.

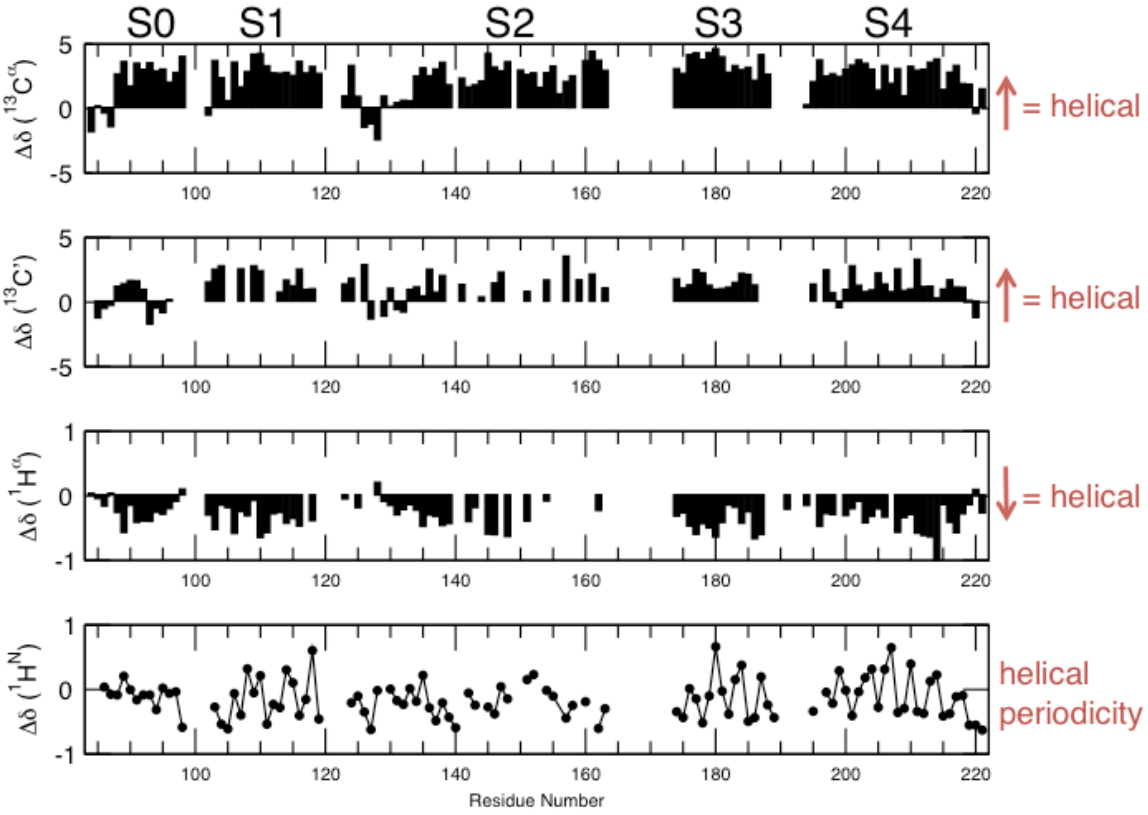

Fig. 5.8 Secondary structure of $hH_V\Delta N\Delta C$

The VSD helices are identified by the pattern of secondary chemical shifts for $^{13}C'$, $^{13}C^{\alpha}$, [$\Delta\delta(^{13}C^{X})$; corrected for ^{2}H isotope shifts (Venters *et al*. 1996) and graphed from – 5 ppm to + 5 ppm] and $^{1}H^{\alpha}$ and $^{1}H^{N}$ [$\Delta\delta(^{1}H^{X})$; graphed from – 1 ppm to + 1 ppm] (Wishart & Case 2001). The helices identified are labeled at the top of the plot and the red arrows to the right of each plot indicate the direction of $\Delta\delta$ that correspond to helical structure.

5.2.5 Through-space measurements indicate a poorly defined tertiary structure

In order to solve the three dimensional structure of the channel, we needed to measure long-range through-space interactions between the different transmembrane helices. The ^{13}C-edited and ^{15}N-edited NOESY experiments gave us some distance restraints; however, due to crowding in the aromatic region of the spectra, we were unable to assign many of the interactions. Therefore, we performed a series of specific labeling experiments for paramagnetic relaxation enhancement (PRE), to better constrain the overall fold and thereby help with the assignments of the observed NOESY peaks.

The electron spin of a stable nitroxide free radical enhances the relaxation of nearby nuclei in a magnetic field (Hilty *et al*. 2004). By introducing a cysteine mutation at a specific site in a cysteine-free background (i.e. C107S) and labeling the cysteine with a paramagnetic nitroxide-free-radical-containing small molecule, it is possible to measure a decrease in the peak intensity of nearby nuclei. This decrease in peak intensity is proportional to the distance between the nucleus and the paramagnetic probe. Through comparison of the spectrum of the paramagnetic-labeled protein to a control spectrum in which the cysteine is modified with a diamagnetic version of the small molecule, it is possible to accurately calculate long-range distances (15-20 Å) between the labeled position and other parts of the protein. These long-range distances can then be added as constraints into a structure calculation.

In order to generate long-range distance constraints for the $hH_V\Delta N\Delta C$ construct, we labeled the channel at five different positions: R100C at the N-terminus of S1; I127C and Y134C in the S1-S2 loop; L173C in the S2-S3 loop and F190C in the S3-S4 loop (Fig. 5.9). The PRE data presented in Fig. 5.9A indicate that the channel was efficiently

labeled at each position. However, significant long-range signal suppression was not apparent. In contrast, when an equivalent position in the S3-S4 loop was labeled on the homologous K_VAP isolated VSD, strong signal suppression was seen for nuclei on the S1-S2 loop, which is what would be expected for a four-helix bundle (Fig. 5.9C). The lack of strong PRE signal for the $hH_V\Delta N\Delta C$ construct indicates the tertiary structure of the channel in LPPG may be poorly defined. In fact, the only suppression observed was between positions on the S1-S2 loop (I127 and Y134) and the C-terminus of S4 (Fig. 5.9A). In the native fold of a VSD, these two regions of the protein should be on opposite sides of the membrane and therefore we would not expect to see any PRE signal between them. The fact that we did see this suppression at both S1-S2 positions, strongly suggests that the $hH_V\Delta N\Delta C$ construct in LPPG was in a non-native conformation.

Our inability to measure strong distance constraints in the $hH_V\Delta N\Delta C$ construct and our observation of likely non-native interactions between the S1-S2 loop and the C-terminus of S4 led us to conclude that structure determination of the channel by NMR under these conditions was infeasible. This approach was therefore abandoned.

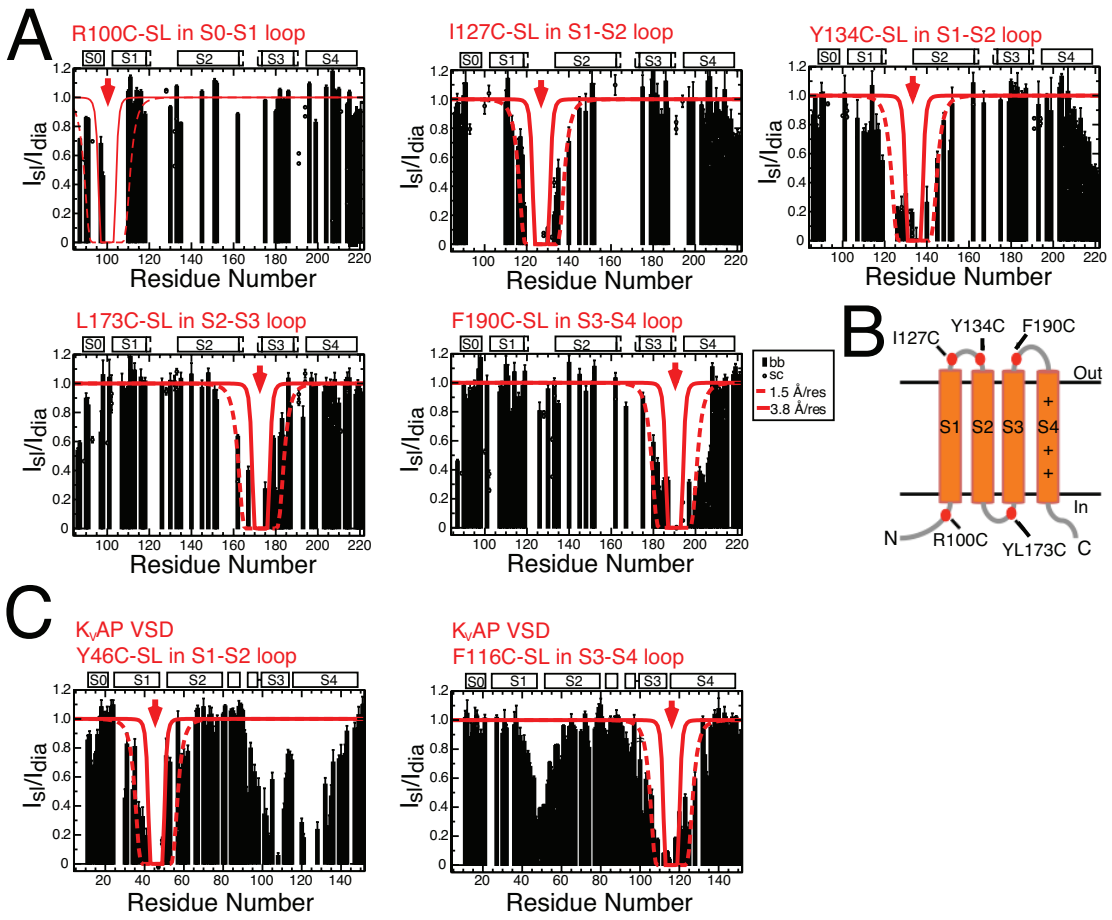

Fig. 5.9 PRE experiments on $hH_V\Delta N\Delta C$

(**A**) PRE data for the different specifically labeled positions along the $hH_V\Delta N\Delta C$ construct. Data are presented as the ratio of peak intensity for the spin-labeled sample (I_{sl}) over the peak intensity for the diamagnetic-labeled sample (I_{dia}) versus amino acid residue number. In each case the red arrow indicates the site of the label. The solid red curves indicate the expected intensity drop near the label site for an extended random coil structure, whereas the dashed red line indicates the expected intensity drop near the label site for a more compact helical structure. (**B**) Schematic of $hH_V\Delta N\Delta C$ topology indicating the positions of the labeling sites. (**C**) Data for the K_VAP isolated VSD with labels at equivalent positions on S1-S2 loop (Y46 in K_VAP equivalent to I127 in H_V) and S3-S4 loop (F116 in K_VAP equivalent to F190 in H_V) demonstrating the expected signal suppression between the two "extracellular" loops that would be expected for a four-helix bundle structure. K_VAP data provided by Dr Joel Butterwick from Butterwick & Mackinnon 2010.

5.3 THE STRUCTURAL NECESSITY OF THE MEMBRANE

The biochemical characterization of the different hH_V1 and chimeric constructs presented in this thesis clearly demonstrates the importance of the lipid bilayer membrane to the maintenance of the native structure of H_V channels. Before pursuing the structure of each of the constructs, we had ensured that they were functional by electrophysiology and again after purification by reconstitution and characterization in the flux assay. However, in all these functional and cross-linking studies, the channels were embedded within a lipid bilayer (either that of a cell membrane or of reconstituted lipid vesicles). In contrast, all structural work was performed on detergent-solubilized channels, i.e. in the absence of lipid membranes. As described throughout the thesis, in every case, these previously functional channels adopted a non-native conformation in detergent.

It is clear, then, that although the channel protein is stable in some detergents the channel structure is unstable when removed from the membrane and that future directions for structural work on H_V channels must focus on membrane-like conditions. Additional crystallography attempts, including future work using the phage-display Fabs discussed in Chapter 4, must focus on detergent-lipid mixtures, bicelle and lipidic cubic phase conditions. Any future work by solution state NMR should only be performed on H_V channels incorporated into lipid nano-disks. It may also be possible to try solid-state NMR on pellets of membranes containing reconstituted H_V channels.

MATERIALS AND METHODS

Preparation of cDNA and mutations for HEK cell transfections

Human H_V1 cDNA (GI: 34783431, a gift from David Clapham, Havard Universtiy) was subcloned into pcDNA4 vector (Invitrogen). Mutations were generated using QuikChange kit (Stratagene). Three additional amino acids (ARG) were introduced into the C-terminus as a byproduct of cloning into the expression vector. These amino acids were later removed for all constructs used for electrophysiological recordings.

Electrophysiological recordings from HEK and CHO cells

Full-length hH_V1 (Fig. 1.6, 4.15 and 5.3), the HAP5 chimera (Fig. 4.15) and the truncated constructs (Fig. 5.3) used for crystallization and NMR were cloned into a pcDNA4 vector (Invitrogen) for mammalian cell expression. All constructs used for recordings shown in Fig. 1.6 and 5.3 contained N-terminal GFP fusions. The hH_V1 and HAP5 constructs used for recordings in Fig. 4.15 had no GFP fusion but were co-transfected with a GFP containing vector in order to facilitate detection of transfected cells. HEK tsA201 cells (ATCC) were maintained in DMEM (Gibco) containing 10% FBS. Cells were transfected using FuGene (Promega) following the manufacturers protocol then, after ~6 hours, were split onto poly-D-lysine-coated glass coverslips (BD BioCoat) and allowed to recover for

~12-24 hrs. After 12-48 hrs, coverslips were transferred to the recording chamber. Immediately before recording, medium was replaced by bath solution. All recordings were performed at room temperature. Recordings were obtained with an Axopatch 200B amplifier (Molecular Devices) using standard whole-cell patch-clamp techniques. Recordings were filtered at 1 kHz with sampling at 10 kHz. Pipettes of 2-5 MΩ resistance were pulled from borosilicate glass and fire polished. Currents were recorded according to the voltage step protocols represented schematically in each figure.

Pipette solution for recordings shown in Fig. 1.6 and 5.3 was: 100 mM Tetramethylammonium chloride (TMACl), 2 mM $MgCl_2$, 100 mM MES (pH 6.5) and 5 mM Glucose (353 mOsm). Bath solutions for recordings shown in Fig. 1.x and 5.x were: 100 mM TMACl, 2 mM $MgCl_2$, 100 mM MES (pH 6.0) and 25 mM Glucose (352 mOsm); 100 mM TMACl, 2 mM $MgCl_2$, 100 mM MES (pH 6.5) and 5 mM Glucose (353 mOsm); 100 mM TMACl, 2 mM $MgCl_2$, 100 mM HEPES (pH 7.0) and 50 mM Glucose (356 mOsm). All solutions had pH adjusted using N-methyl-D-glucamine (NMDG).

Pipette solutions for recordings in Fig. 4.15 was: 64 mM NMDG, 3 mM $MgCl_2$, 1 mM EGTA and 150 mM MES (pH 6.5). The bath solution was: 75 mM NMDG, 1 mM $MgCl_2$, 1 mM $CaCl_2$ and 100 mM HEPES (pH 7.5). These solutions had their pH adjusted with methanesulfonic acid and osmotic concentration matched by addition of glucose.

The recordings shown in Fig. 1.2 were provided by Josefina del Mármol and were produced by the whole-cell patch clamp technique described above with slight modifications. The *Rattus norvegicus* $K_V1.1$ (GI: 24520) subcloned into a pcDNA3.1 vector containing an IRES mCherry was used to transiently transfect CHO cells (ATCC)

by means of lipofectamine 2000 (Life Technologies) according to the manufacturers protocol. Pipette solution was: 150 mM KCl, 10 mM HEPES (pH 7.4), 2 mM $MgCl_2$ and 5 mM EDTA, pH'ed with KOH. Bath solution was: 135 mM NaCl, 15 mM KCl, 10 mM HEPES (pH 7.4), 2 mM $MgCl_2$, and 1 mM $CaCl_2$, pH'ed with NaOH.

Membrane preparation

cDNAs encoding hH_V1 were transfected into tsA201 (HEK293 derivatives) cells using Lipofectamine 2000 (Invitrogen) for 36-48 h. Membranes were prepared as described with modifications (Asano *et al*. 1996). Briefly, cells were washed with phosphate buffered saline with 1 mM EDTA and lysed with a tissue grinder (wheaton) in the presence of protease inhibitors (1 mM PMSF, 1 mg/ml leupeptin, 1 mg/ml aprotinin, 1 mg/ml pepstatin). Lysed cells were briefly sonicated for 10 s in a bath sonicator and then centrifuged at 900 g for 15 min. Supernatants were collected and diluted 4-fold with ice-cold buffer (20 mM HEPES, pH 7.5, 5 mM KCl, 150 mM NaCl, 5 % glycerol, and 1 mM EDTA) and ultra-centrifuged for 90 – 120 min at 130,000 g. After ultra-centrifugation, supernatants were discarded and pellets were resuspended in the same buffer and then homogenized with a tissue grinder (wheaton). Samples were maintained at 4°C at all times.

Cross-linking and Western blotting

For non-specific cross-linking experiments, the amino-group reactive bifunctional cross-linker DSS (Pierce) was used. For each reaction, 20-fold concentrated DSS stocks,

dissolved in dimethylsulfoxide (DMSO), were added to prepared membranes and incubated at room temperature for 20 min; reactions were quenched by the addition of Tris-HCl (pH 8.5) to a final concentration of 100 mM. For copper mediated cross-linking, 6 mM $CuSO_4$ and 1.8 mM o-phenanthroline in water were added to prepared membranes to a final concentration of 300 μM and 900 μM, respectively and incubated at room temperature for 20 min; reactions were quenched by addition of 20 mM N-ethylmaleimide (NEM) and 50 mM EDTA. For cysteine-directed cross-linking, 1 mM stock of 1,3-propanediyl bismethanethiosulfonate (M3M, Toronto Research Chemicals Inc) in DMSO was added to the prepared membranes to a final concentration of 50 μM and incubated on ice for 1 hr; reactions were quenched with 20 mM NEM. Air-oxidized samples, used immediately after membrane preparation, were treated with 10-20 mM NEM to prevent cross-linking during electrophoresis. All the samples were mixed with equal volume of loading buffers containing 4 % (w/v) SDS and 10 % (v/v) b-mercaptoethanol (only for reducing condition), then subjected to SDS-PAGE on 12 % gels, transferred onto polyvinylidene difluoride (PVDF) membrane, and probed with a mixture of two monoclonal antibodies 25H11 and 9C1. Monoclonal antibodies were raised in mice injected with purified hH_V1 protein by standard protocols (Harlow & Lane 1988).

Expresion of hH_V1 in *Pichia Pastoris*

The gene for the full-length human H_V channels (GenBank accession no: **91992153**) with a C-terminal 1D4 tag (ARAAGGTETSQVAPA) was ligated into the PICZ-c vector (Invitrogen Life Technologies). This vector was transformed into a His^+ strain of

SMD1163 *Pichia pastoris* and selected as described (Long S. B., *et al*., 2005). Transformed cells were grown in 1 L cultures of BMG media (Yeast Nirtogen Base, 100 mM sodium phosphate pH 6.3 and 1% glycerol) at 30°C until an optical density of ~20 was reached. BMG media was exchanged for BMM media (BMG with 0.75-1% MeOH instead of glycerol) and grown at 24-27°C for 12-24 hours. Cell pellets were frozen in liquid nitrogen and stored at -80°C until needed. This same expression protocol was used for the chimeric-1D4 and N-terminal-GFP full-length and truncated chimeric and wild type channels.

For expression of ^{15}N labeled protein all ammonium sulfate in the media was replaced with ^{15}N ammonium sulfate. For ^{13}C labeled samples glycerol in the BMG media and methanol in the BMM media were replaced by ^{13}C-glycerol and ^{13}C-methanol respectively. In order to promote maximal expression the cells grown in 70-90% D_2O BMG were only allowed to reach an optical density (measured at 600 nm) of ~5. They were then spun down and resuspended into a half volume of 70-90% D_2O BMM (concentrating the cells twofold) and incubated at 27°C for 16-24 h before harvesting.

Expression of GFP-hH$_V$ΔNΔC in *E. coli* for specific amino acid labeling

To produce amino-acid-specific and methyl-specific labeling patterns samples, we grew XL-1 Blue cells (Stratagene), which were transformed with an expression vector, in LB broth at 37°C until the optical density (measured at 600 nm) had reached ~ 0.8 The cells were then centrifuged for 10 min at 3000 x g and resuspended in a half volume of M9 minimal medium (concentrating the cells twofold) supplemented with and 10 mg/L thiamine and the isotopically enriched amino acid (sodium salt) at 50–100 mg/L, and all

nonlabeled amino acids were included at 100–200 mg/L. Similarly, to specifically label the $Ile^{\delta 1}$ and/or $Leu^{\delta}/Val^{\gamma}$ groups (denoted $^{13}C^{methyl}$), we added 50 mg/L sodium 2-keto-4-13C-butyrate (for Ile) and 100 mg/L sodium 2-keto-3-methyl-d_3-4-^{13}C-butyrate (for Leu/Val) in lieu of their respective amino acids (Tugarinov *et al*. 2006). It should be noted that for Leu^{δ} and Val^{γ} methyl groups labeled in this manner, one group within the pair is $^{13}CH_3$, while the other is $^{12}CD_3$. After 1 h, protein expression was induced by the addition of 0.5 mM isopropyl-β-D-thiogalactopyranoside, and the cells were harvested 12–16 h later.

1D4-purification

Frozen pellets were lysed with a mixer mill (Retsch, Inc. Model MM301) and resuspended in buffer (500 mM NaCl, 50 mM TRIS-HCl, pH 8.5, 2 mM β-mercaptoethanol, 0.1 mg/ml deoxyribonuclease I, 1 μg/ml pepstatin, 1 μg/ml leupeptin, 1 μg/ml aprotinin, 1.0 mM phenylmethysulfonyl fluoride and 2.0 mM Ethylenediaminetetraacetic acid (EDTA). The pH was adjusted to 8.5 with NaOH, and 0.15 g DDM (n-dodecyl-β-D-maltopyranoside, Anatrace) per g of cells was added prior to a 2-3 hour extraction at room temperature followed by centrifugation at 31000 x g for 25 min. Supernatant was added to 1D4 antibody-linked sepharose affinity resin previously equilibrated with buffer A (500 mM NaCl, 50 mM TRIS-HCl (pH 7.5), 1 mM EDTA and 1 mM DDM) and rotated at room temperature for 2 hours. The resin was collected on a column, washed with buffer A (4 x 5 column volumes) and eluted with buffer A containing 0.4 mg/ml 1D4 peptide. Protein was loaded on a Superdex-200 gel filtration column in 20 mM TRIS-HCl (pH 7.5), 150 mM KCl, 50 mM NaCl and 4 mM

DM (n-decyl-β-D-maltopyranoside, Anatrace, anagrade; Buffer B). The fractions corresponding to Hv channels were pooled.

Reconstitution of hH_V1 channels

A mixture of 6:6:3:3:1 of POPC:POPE:POPS:SM:PI (1-Palmitoyl-2-Oleoyl-sn-Glycero-3-Phosphocholine, 1-Palmitoyl-2-Oleoyl-sn-Glycero-3-Phosphoethanolamine, 1-Palmitoyl-2-Oleoyl-sn-Glycero-3-Phospho-L-Serine, Sphingomyelin, and L-a-Phosphatidylinositol, obtained from Avanti) was prepared based on the composition of human neutrophil plasma membrane (Tamura *et al*. 1988). A mixture of 3:1 POPE:POPG can also be used. The lipid mixture was dried under an Argon stream and then resuspended to 10 mg/ml in dialysis buffer (20 mM HEPES (pH 7.0), 150 mM KCl, 10% glycerol, 0.2 mM EGTA and 2 mM 2-mercaptoethanol). The lipid mixture was then sonicated in a bath sonicator three times for 2 minutes. Decylmaltoside (DM) was added to the lipid mixture to 10 mM and rotated at room temperature for 1hr. Protein was added to the lipid mixture in a 1:100 (wt:wt) protein to lipid ratio and an additional 10 mM DM was added. As a control empty vesicles were made in which only dialysis buffer was added to the lipids. The protein-lipid mixture was rotated at room temperature for ~3 hours then placed into dialysis membrane (molecular weight cut off of 50 KDa) and dialyzed in 4 L of dialysis buffer for 5 days at RT exchanging buffer daily. Vesicles were then harvested and flash frozen in liquid nitrogen and stored at -80°C until needed.

Fluorescence based flux assay

The fluorescence data for vesicles containing H_V channels was obtained using a published procedure with the following modification (Zhang & Forgac 1994). Vesicles were thawed in room temperature water and then sonicated once in a bath sonicator for 5 seconds and then diluted 20 fold into flux buffer (20 mM HEPES (pH 7.0), 150 mM NaCl, 7.5 mM KCl, 10% glycerol, 0.2 mM EGTA, 0.5 mg/ml BSA, 2 mM 2-mercaptoethanol and 2 mM ACMA) in a quartz cuvette. Data were collected on a Spex Fluorolog 3-11 spectrofluorometer in time acquisition mode at 30-second intervals with excitation at 410 nm, emission 490 nm, with bandwidth 5 nm and an integration time 2 s. A baseline was collected for 150 s before the addition of 20 nM valinomycin. After the fluorescence stabilized carbonyl cyanide m-chloro phenyl hydrazone (CCCP) was added to 2 mM rendering all vesicles H^+ permeable and a minimum baseline was collected for 150 seconds. Data are scaled by $(F_i - F_{min})/(F_{max}-F_{min})$, where F_{max} is the average value of the starting baseline and F_{min} is the average value of the minimum baseline. $F_{max}-F_{min}$ (the total reduction in fluorescence after CCCP addition) was ~ 25 % for all vesicles.

Sucrose Gradient Flotation Assay

Lipid vesicles containing hH_V1, with protein to lipid ratio 1: 100 (wt:wt), were layered on a sucrose gradient (From top to bottom, 140 µl sample plus 60 µl dialysis buffer, 600 µl 7% sucrose, and 1 ml 27% sucrose in dialysis buffer). The gradients were then centrifuged at 135,000 x g in a Sorvall RP55-S swinging bucket rotor for 2 hours and then fractionated into 8 x ~225 µl fractions. A 15 ml sample of each fraction was then

mixed with 15 ml 2x running buffer and run on a 12% gel (SDS-PAGE) and stained with Coomassie blue.

Mass Spectrometry

Mas spectrometry was performed by the ultra-thin layer method accordind to published protocols (Cadene & Chait 2000). In short protein samples were concentrated to 1 mg/mL then diluted with FWI (3 parts formic acid, 1 part water, 2 parts isopropanol) into 10X final concentration aliquots which were further diluted (1 to 10) with saturated a-cyano-4-hydroxycinnamic acid (4-HCCA) in FWI to final ratios of 1:10, 1:20, 1:50, 1:100 and/or 1:200. 0.5 μL of each sample was spotted onto a stainless steal MALDI sample plate coated with an ultrathinlayer of 4-HCCA. After a visible precipitate had fromed on the bottom of the spots the excess liquid was aspirated away and the spots were washed with 2 μL of 0.1% trifluoro acetic acid (TFA) solution. The samples were then taken for analysis. All spectra were aquired using MALDI time-of-flight mass spectrometer Voyager-DE STR (PE Biosystem, Foster City, CA) operating in linear, delayed extraction mode. This instrument is equipped with a nitrogen laser delivering pulses of ultraviolet light (wavelength 337 nm) at 3 Hz to the matrix spot. Spectra from 200-500 individual laser shots were averaged (using 2-ns data channel width) with software provided by the manufacturer. The spectra were smoothed, calibrated, and analyzed using the program M-over-Z (http://www.proteometrics.com and http://prowl.rockefeller.edu). For more details see:
http://prowl.rockefeller.edu/protocols/ultra-thin-layer.html

decaHis-GFP- construct purification

Frozen pellets were lysed with a mixer mill (Retsch, Inc. Model MM301) and resuspended in buffer (500 mM NaCl, 50 mM TRIS-HCl, pH 8.5, 2 mM β-mercaptoethanol, 0.1 mg/ml deoxyribonuclease I, 0.1 mg/ml pepstatin, 1 μg/ml leupeptin, 1 μg/ml aprotinin and 1.0 mM phenylmethysulfonyl fluoride). The pH was adjusted to 8.5 with NaOH, and DM (n-dodecyl-β-D-maltopyranoside, Anatrace) was added to a final concentration of 80 mM prior to a 1.5 hour extraction at room temperature followed by centrifugation at 31000 x g for 30 min. Supernatant was added to Co^{2+} Talon (CloneTech) IMAC resin equilibrated with buffer A (500 mM NaCl, 50 mM TRIS-HCl, (pH 7.5) 5 mM imidazole and 4 mM DM) and rotated at room temperature for 2 hours. The resin was collected on a column, washed with buffer A (4 x 5 column volumes), further washed with buffer A containing 25 mM imidazole and eluted with buffer A containing 250 mM imidazole.

For the decaHis-GFP-HAP5ΔNΔC construct 2 mM DTT and PreScission protease were added the elution and the sample was incubated at 4°C overnight followed by a second round of Talon resin purification in buffer A from which the flow through was collected and concentrated. This sample was loaded on a Superdex-200 gel filtration column in 20 mM TRIS-HCl (pH 7.5), 200 mM NaCl and 4 mM DM (Buffer B). The fractions corresponding to HAPΔNΔC channels were pooled and concentrated.

For the decaHis-GFP-hH_VΔNΔC construct 2 mM DTT and PreScission protease was added the elution and the sample was incubated on ice for 1 h before being added to 15 kDa MWCO dialysis membrane (Spectrum Labs) and dialyzed overnight at 4°C into low salt buffer (depending on the volume of the decaHis-GFP-hH_VΔNΔC sample, 400

mL of 12.5-30 mM NaCl, 10 mM BisTris (pH 7.0), 2 mM DTT and 4 mM DM) for a final concentration of 50 mM NaCl. The sample was then applied to a Q-sepharose column equilibrated in 50 mM NaCl, 10 mM BisTris (pH 7.0), 2 mM DTT and 4 mM DM buffer. The flow through from the Q-column was collected, concentrated and loaded on a Superdex-200 gel filtration column in 10 mM HEPES, pH 7.0, 50 mM NaCl and 2 mM LPPG or DHPC. The fractions corresponding to HAPΔNΔC channels were pooled and concentrated.

33H1 and 6E1 Fab purification

Antibodies were prepared as described in Brohawn *et al*. with slight modifications (Brohawn *et al*. 2013). Briefly, media supernatant from hybridomas was dialyzed against two changes of 4 L of 10 mM Tris (pH 8.0), 10 mM NaCl in 8-kDa-MWCO dialysis tubing (Spectrum Labs) overnight. Dialyzed samples were spun at 6,000 × g, and the supernatant was applied to a 5-mL Q-Sepharose column (GE Healthcare) equilibrated in 10 mM Tris (pH 8.0), 10 mM NaCl. Antibodies were eluted during a gradient to 10 mM Tris (pH 8.0), 1.0 M NaCl. Eluted antibodies were diluted to 3 mg/mL in PBS. Fab fragments were generated by reaction with papain (1:100 wt:wt) in PBS with 10 mM β-mercaptoethanol, 10 mM L-cysteine HCl, and 10 mM EDTA (pH 7.0) at 37°C for 4 h. Cleaved antibodies were dialyzed against two changes of 4 L of 10 mM Tris (pH 8.0), 10 mM NaCl in 8-kDa-MMCO dialysis tubing overnight. Dialyzed samples were spun at 6,000 × g, and the supernatant was applied to a 5-mL Q-Sepharose column equilibrated in 10 mM Tris (pH 8.0), 10 mM NaCl. Fab fragments were collected in the flow-through.

Crystallization and structure determination of HAP5ΔNΔC/33H1

Pure HAP5ΔNΔC was mixed with pure 33H1 Fab and concentrated (10kDa MWCO, Millipore) to ~15 mg/mL total protein for crystallization. 0.4 μL protein was added to 0.4 μL reservoir (30% PEG400) in hanging drops. The largest crystals appeared within 1 week and grew to full size in 2-3 weeks at 20° C. Crystals were harvested and frozen in liquid nitrogen.

Data were collected at NSLS beamline X29 and processed with HKL2000 (Minor *et al*. 2006). Data were anisotropic and were elliptically truncated and scaled (Strong *et al*. 2006) to 3.9 x 5.1 x 3.8 Å. Molecular replacement solution was found using the program Phaser (McCoy *et al*. 2007) and the 33H1 Fv and Fc as search models. Crystallographic programs from the Phenix and CCP4 suites were used throughout structure determination (Adams *et al*. 2010; Winn *et al*. 2011). Structure figures were generated with Pymol (Schrödinger LLC).

Phage Display Selections

Were performed as described in sections 4.3.1 and 4.3.2 and Sidhu *et al*. 2000. In brief, biotinylation of purified hH_VΔNΔC was performed at 1 mg/mL protein in 200 mM NaCl, 20 mM HEPES (pH 7.0), 5 mM DHPC (Buffer PD). For cysteine specific biotinylation final concentration of 2 mM Biotinylcaproylaminocaproyl-aminoethyl Methanethiosulfonate (BCAC; Toronto Research Chemicals, Inc.) was added to the protein and incubated for 3-4 h at room temperature in the dark, excess BCAC was removed by SEC. For amine specific biotinylation N-hydroxylsuccinimidyl d-biotin-15-

amido-4,7,10,13-tetraoxapentadecylate (NHS-PEO4-Biotin; Thermo Scientific) was added in a molar ratio of 1:3 $hH_V\Delta N\Delta C$: NHS-PEO4-Biotin and incubated at 4°C, samples were used directly without removal of excess reagent.

Detergent based selections: Pre-absorption (negative selection) and selection wells on the 96-well plate (for each selection [positive and negative] the number of wells was: round 1, 8 wells; round 2, 6 wells; round 3, 4 wells; round 4, 2 wells; round 5, 2 wells) were coated overnight at 4°C with 100 μL of 5-25 μg/mL streptavidin or neutravidin in 200 mM NaCl, 20 mM HEPES (pH 7.0) then blocked with 200 μL of 0.5% BSA for 1 h at room temperature. For selections 100 μL of biotinylated $hH_V\Delta N\Delta C$ was added to the positive selection wells at 10 μg/mL in buffer PD and incubated at 4°C for 1h at the same time 100 μL phage library at 10^{12}-10^{13} cfu/mL buffer PD was added to the negative selection wells and incubated at 4°C for 1h. $hH_V\Delta N\Delta C$ solution was removed from positive selection wells and unbound phage were transferred from negative to positive selection wells and incubated at 4°C for 2h. Phage solution was removed from the positive selection wells and the wells were washed with 6X for round 1, 8X for round 2, 10X for round 3 and 15X for rounds 4 and 5 with buffer PD. Bound phage were eluted by adding 100 μL/well of 100 mM HCl and incubating for 5 min at room temperature with shaking. The HCl solution was then added to an eppendorf tube containing 25 μL 1 M Tris-HCl (pH 8) per well (8 wells = 200 μL Tris + 800 μL phage) then 500 μL of this phage solution was added to 7.5 mL of actively growing OPTIMAX cells (OD = 0.5-0.8) in 2YT. Infected OPTIMAX cells were incubated for 30 min at 37°C with shaking then M13K07 helper phage were added to get 10^{10} cfu/ml final and then further incubation for 45 min at 37°C with shaking. The culture was transferred to 35 mL final volume

2YT/carb100/kan25 medium and incubated overnight at 37°C with shaking. Overnight phage cultures were precipitated: spun cultures in 50 ml Falcon tubes 8000 rpm, 15 minutes, added 8.75 ml (1/5 final volume) PEG/NaCl (20% PEG 8000 w/v, 2.5 M NaCl) to supernatant, incubated on ice for 20 minutes, spun 20 min at 24000 g, re-suspended pellets in 1.2 mL volume of buffer PD and transfer to eppendorf tubes, spun again (5 min, 13000 rpm) to remove bacterial debris then transferred supernatant to new tubes (this is input phage for next round of selections). After each round input and output phage were titered: 10 μL of 10-fold serial dilutions of precipitated phage (10 μL phage+ 90 μL 2YT), were added to 90 μL OPTIMAX (OD600 0.5-0.8), incubated for 30 min at 37°C, and then 5 μL of each dilution were spotted plates (carb, kan, tet), final dilutions of 10^{-2} to 10^{-7} and the 10^{-6} to 10^{-11} were used for output and input phage respectively. Plates were incubated overnight at 37°C and colonies were counted the next day.

Vesicle based selections: Performed as for the detergent based selections with the following modifications. Antigen buffer (AB) used was 150 mM KCl, 20 mM HEPES (pH7.0), 5% glycerol. DPPE-biotin-containing empty vesicles were added to the negative selection wells prior to the addition of input phage (see section 4.3.2). The unbound phage from the negative selections were mixed with DPPE-biotin-containing $hH_V\Delta N\Delta C$ vesicles for 1 h at 4°C with shaking prior to quick capture of vesicles and bound phage on streptavidin or neutravidin coated wells (15 min at 4°C) followed by washing and elution.

Isolation of positive binders: The output phage from the final round of selections were mixed with 7.5 mL of actively growing OPTIMAX cells (OD = 0.5-0.8) in 2YT for 30 min at 37°C then diluted and plated onto LB plates/carb100 in order to grow single colonies and incubated overnight at 37°C. Single colonies were picked (96-192 per

library), used to inoculated individual 2 mL cultures of 2YT/carb100 and incubated at 37°C with shaking until OD600 0.5-0.8, then M13K07 helper phage were added and the cultures were incubated overnight at 37°C with shaking. These cultures were spun down to pellet bacterial cell debris and the supernatant was used in ELISAs (like the one shown in Table 4.3). In brief, ELISA plates were coated with streptavidin and blocked with BSA in the same way as the selection plates, four wells were used per the isolated phage clone: BSA alone, empty vesicles and two wells containing $hH_V\Delta N\Delta C$ vesicles. Supernatant from isolated phage cultures were diluted 2-fold with 2 X AB and incubated with antigen (either in detergent or in vesicles) for 1 hr at 4°C with shaking prior to quick capture of biotin on the plates (15 min 4°C with shaking), followed by washes and incubation with primary antibody (either αFLAG or αM13 see Table 4.3). ELISAs were then developed by standard protocols. Isolated phage clones that were positive for binding were sequenced then subcloned into an expression vector for Fab expression and purification.

Phage display Fab expression and purification

Single colonies from *E. coli* BL21 DE3 transformed with the phagemid DNA containing the Fab sequence was grown at 37°C in 25 mL 2YT/amp medium for ~3 hours then used to inoculate 1 L of 2YT/amp media and grown at 37°C until an optical density (measured at 600 nm) of 0.6 was reached. Expression was induced by the addition of 1 mM IPTG and the cells were left overnight at 37°C. Cells were pelleted by centrifugation for 10 minutes at 3,000 x g then fozen in liquid nitrogen and stored at -80°C.

Cell pellets were resuspended in lysis buffer (100 mM NaCl, 20 mM Tris (pH 8.0), 0.1 mg/ml deoxyribonuclease I, 0.1 mg/ml pepstatin, 1 μg/ml leupeptin, 1 μg/ml

aprotinin, 1.0 mM phenylmethysulfonyl fluoride) and lysed by sonication. Cell debris was removed by centrifugation for 40 min at 12,000 rpm. Supernatants were mixed with 2-3 mL of Talon Co^{2+} resin (CloneTech) equilibrated in wash buffer (100 mM NaCl, 20 mM Tris (pH8.0) and 5 mM imidazole) and tumbled for 1-2 h at room temperature. The resin was collected on a column, washed with wash buffer (4 x 5 column volumes), and eluted with wash buffer containing 250 mM imidazole. Sample was then dialyzed into low salt buffer A (10 mM NaCl, 10 mM Tris (pH 8.0)) overnight and then run over a Q-sepharose column. The Q-spharose flow through was collected and concentrated for use in binding experiments.

NMR data collection and analysis

NMR experiments were performed at the New York Structural Biology Center using Bruker Avance or Avance II instruments operating at static magnetic field strengths of 14.1, 18.8 and 21.1 T, equipped with z-shielded gradient triple-resonance TCI or TXI cryogenic probes. The sample temperature was maintained at 25°C during the initial screening of detergent and buffer conditions and for all other experiments. NMR spectra were processed using the NMRPipe software package (Delaglio *et al*. 1995) and analyzed using the program SPARKY (Goddard & Kneller).

Chemical Shift Assignments

Resonance assignments for backbone $^{1}H^{N}$, ^{15}N, $^{13}C'$, and $^{13}C^{\alpha}$, and $^{13}C^{\beta}$ nuclei were identified using three-dimensional (3D) TROSY HNCA (at 21.1 T), HNCO, HN

(CO)CA, and HNCACB (at 18.8 T) experiments (Cavanagh *et al*. 2007; Neri *et al*. 1989) performed on 0.15-0.3 mM ^{2}H, ^{13}C, ^{15}N samples. Also, two-dimensional (2D) TROSY HSQC and 3D ^{15}N-edited NOESY (mixing times τ_{mix} = 80) experiments (at 21.1 T) were recorded on a 0.3 mM ^{2}H, ^{15}N sample. In addition to uniformly labeled samples, 2D HSQC, HNCA, and HNCO experiments (at 18.8 T) were recorded on 0.3 mM samples with varied amino-acid-specific labeling patterns designed to eliminate ambiguities as discussed in section 5.2.3.

Side-chain resonance assignments were based on 3D HC(C)H-COSY ^{13}C-edited (aromatic and aliphatic) and ^{15}N-edited (τ_{mix} = 80 ms) NOESY experiments (at 21.1 T) recorded on 0.5 mM ^{13}C, ^{15}N samples in 99.9% (vol/vol) D_2O and on a 3D ^{15}N-edited ^{1}H–^{1}H NOESY (τ_{mix} = 80 ms) experiment (at 21.1 T) recorded using a 0.4 mM ^{15}N sample. To improve resolution within the Val and Leu methyl regions, we recorded a 3D ^{13}C-edited NOESY (τ_{mix} = 100 ms) experiment on a $^{13}C^{methyl}$-LV sample.

APPENDIX I

This Appendix contains the MATLAB code for my model of H^+ flux into vesicles reconstituted with hH_V1 channels based on the equivalent circuit model found in Moffat *et al*. 2008 (see Chapter 3). Green text that follows a '%' indicate comments which I have used to annotate the code. If you are looking at a PDF file it should be possible to copy and paste the code along with the other functions below into separate text files and save them as simple_flux_V_Na_Cl.m, pt_ffluxbias.m, total_proportional_flux_V.m, channel_dist_theta.m and unscaled_plot.m then use MATLAB to execute the code by typing the command simple_flux_V_Na_Cl(30) in the command window. Currently the conductances for Na^+ and Cl^- are set to zero but this can be adjusted by altering the highlighted variables GNa and GCl.

```
function simple_flux_V_Na_Cl(m)
%calculates the basis set of fluxes for a series of 1 to m
%channels per vesicle
%the basis set is to be use in the programs pt_ffluxbias or
total_proportional_flux_V
%through their global assignment

global time1                %assigns the time vector as a global variable
global sflux                %assigns the sflux matrix as a global variable
global fflux                %assigns the fflux matrix as a global variable

Ki1 = 0.150;                %initial internal concentration of K+ in M
Ko1 = 0.015;                %initial outer concentration of K+ in M
Hi1 = 1e-7;                 %initial internal concentration of H+ in M
Ho1 = 1e-7;                 %initial outer concentration of H+ in M
Nai1 = 1e-4;                %initial internal concentration of Na+ in M
Nao1 = 0.150;               %initial outer concentration of Na+ in M
Cli1 = 0.150;               %initial internal concentration of Cl- in M
Clo1 = 0.165;               %initial outer concentration of Cl- in M
Vo = 0.0008;                %bath volume
Vi = 2.3562e-18;            %volume inside average vesicles (r = 100 nm)
F  = 96485;                 %Faraday constant 9.6485e4 C/mol
R  = 8.3145;                %gas constant 8.3145 V*C/mol*K
T  = 298;                   %absolute temp 298 K
BKd = 0.000000028183829;    %dissociation constant for HEPES buffer pKa 7.55
Bi = 0.02;                  %internal concentration of HEPES buffer
Bo = 0.02;                  %outer concentration of HEPES buffer
GK = 1e-6;                  %K+ conductance through the membrane
```

```
Vmid = 0.04;                %V1/2 of voltage sensor Boltzmann
z = 3;                      %assigns valence for hHv1 voltage sensor Boltzmann


n = 2000000;                %number of interations of loop
dt = 0.001;                 %time step per interation in seconds

%duration of time = n*dt

%builds fflux and sflux matrices
fflux = zeros(m,n+1);
sflux = zeros(m,n+1);

for k = 1:m;        %runs this master loop for each of the different number of
channels
    GH = k*1e-16;   %the proton conductance is equal to the unitary conductance
                    %times the number of channels

    GNa = k*0;      %the Na conductance is equal to the unitary conductance
                    %times the number of channels

    GCl = k*0;      %the Cl conductance is equal to the unitary conductance
                    %times the number of channels

    for j = 1:2;    %run this inner loop twice for each number of channels

        %builds vectors and assigns initial values
        EH = zeros(1,n);
        EK = zeros(1,n);
        ENa = zeros(1,n);
        ECl = zeros(1,n);
        VM = zeros(1,n);
        JH = zeros(1,n);
        JK = zeros(1,n);
        JNa = zeros(1,n);
        JCl = zeros(1,n);
        totHi = zeros(1,n+1);
        totHo = zeros(1,n+1);
        Ki = zeros(1,n+1);
        Ko = zeros(1,n+1);
        Hi = zeros(1,n+1);
        Ho = zeros(1,n+1);
        Nai = zeros(1,n+1);
        Nao = zeros(1,n+1);
        Cli = zeros(1,n+1);
        Clo = zeros(1,n+1);
        Ki(1) = Ki1;
        Ko(1) = Ko1;
        Hi(1) = Hi1;
        Ho(1) = Ho1;
        Nai(1) = Nai1;
        Nao(1) = Nao1;
        Cli(1) = Cli1;
        Clo(1) = Clo1;
        totHi(1) = (BKd + Hi1 + Bi)/(1+(BKd/Hi1));
        totHo(1) = (BKd + Ho1 + Bo)/(1+(BKd/Ho1));

        if j == 1       %changes the value of x for each of the two times
                        %through the loop
            x = 1;      %x is used a a multiplier of the membrane voltage Vm
        else            %depending on the orientation of the channel the
                        %membrane voltage is
            x = -1;     %either positive or negative, this has a large impact
                        %on open probability
        end
```

```
for i = 1:n;    %this loop runs the solver for equivalent circuit
                %differential equation

    EH(i) = ((R.*T)./F).*log(Ho(i)./Hi(i));
    %calculates the equilibrium potential for H+

    EK(i) = ((R.*T)./F).*log(Ko(i)./Ki(i));
    %calculates the equilibrium potential for K+

    ENa(i) = ((R.*T)./F).*log(Nao(i)./Nai(i));
    %calculates the equilibrium potential for Na+

    ECl(i) = -((R.*T)./F).*log(Clo(i)./Cli(i));
    %calculates the equilibrium potential for Na+

    VM(i) = (GH.*EH(i) + GK.*EK(i) + GNa.*ENa(i) +
    GCl.*ECl(i))./(GH+GK+GNa+GCl);   %calculates the membrane potential

    JH(i) = (GH./F).*(VM(i)-EH(i))./(1+exp(-(z*F*(x*VM(i) -
    Vmid)/(R*T))));         %determines flux for H+ mol/s

    JK(i) = (GK./F).*(VM(i)-EK(i));      %determines flux for K+ mol/s

    JCl(i) = -(GCl./F).*(VM(i)-ECl(i));  %determines flux for Cl- mol/s

    JNa(i) = (GNa./F).*(VM(i)-ENa(i));   %determines flux for Na+ mol/s

    totHi(i+1) = totHi(i)-(JH(i).*dt)./Vi; %determines concentration
                                           %change inside for H+

    totHo(i+1) = totHo(i)+(JH(i).*dt)./Vo; %determines concentration
                                           %change outside for H+

    Ki(i+1) = Ki(i)-(JK(i).*dt)./Vi;    %determines concentration
                                        %change inside for K+

    Ko(i+1) = Ko(i)+(JK(i).*dt)./Vo;    %determines concentration
                                        %change outside for K+

    Nai(i+1) = Nai(i)-(JNa(i).*dt)./Vi; %determines concentration
                                        %change inside for Na+

    Nao(i+1) = Nao(i)+(JNa(i).*dt)./Vo; %determines concentration
                                        %change ouside for Na+

    Cli(i+1) = Cli(i)-(JCl(i).*dt)./Vi; %determines concentration
                                        %change inside for Cl+

    Clo(i+1) = Clo(i)+(JCl(i).*dt)./Vo; %determines concentration
                                        %change ouside for Cl+

    Hi(i+1) = (-(Bi-totHi(i+1)+BKd)+sqrt((Bi-totHi(i+1)+BKd).^2 +
    4.*BKd.*totHi(i+1)))./2; %determines the free H+ concentration
                             %inside after buffering

    Ho(i+1) = (-(Bo-totHo(i+1)+BKd)+sqrt((Bo-totHo(i+1)+BKd).^2 +
    4.*BKd.*totHo(i+1)))./2; %determines the free H+ concentration
                             %outside after buffering
end

sig = (1e-6 - Hi)/(1e-6 - 1e-7);     %calculates the internal pH change

if j == 1                            %if the channel is in the slow
                                     %conducting configuration
```

```
            sflux(k,:) = sig;                %assign pHi to sflux of k channels
        else                                 %else
            fflux(k,:) = sig;                %assign pHi to fflux of k channels
        end
    end
end


time1 = 0:1:n;      %time vector
time1 = time1.*dt;  %standardizes the time to seconds

fflux2 = zeros(m,floor((n+1)/100));
sflux2 = zeros(m,floor((n+1)/100));
time2 = zeros(1,floor((n+1)/100));

for r = 1:floor((n+1)/100); %data reduction loop
    sflux2(:,r) = sflux(:,r*100);
    fflux2(:,r) = fflux(:,r*100);
    time2(r) = time1(:,r*100);
end

sflux = sflux2;
fflux = fflux2;
time1 = time2;

figure
plot(time1,fflux,time1,sflux) %plots all 60 flux time courses

pt_ffluxbias
%calls and executes the script pt_ffluxbias (see below)

total_proportional_flux_V
%calls and executes the script total_proportional_flux_V (see below)
```

```
function pt_ffluxbias

%builds pascals triangle *(1/2)^(number of elements in row)
%then if there are any channels in the fast fluxing orientation it takes
%the flux vector from fflux for however many channels there are in that
%orientation, if there are only slow fluxing channels it takes the flux vector
%form sflux for that number of slow fluxing vesicles
%in each case it multiplies the flux by the ratio given by the probability
%of that configuration and then sums all of the fluxes for a given total
%number of channels per vesicle


global time1    %retrieves the value of the time vector from simple_flux_V
global fflux    %retrieves the value of the fflux matrix from simple_flux_V
global sflux    %retrieves the value of the sflux matrix from simple_flux_V
global pflux    %assigns the pflux matrix as a global variable

[m n] = size(fflux);    %uses the dimensions of fflux to assign value to script
                        %components

pflux = zeros(m,n);     %builds pflux matrix

for k = 1:m             %run for each number of channels per vesicle
                        %k defines the total number of channels in this run

    cflux = zeros(1,n); %builds cflux vector

    for j = 0:k;        %j defines the number of fast flux oriented channesl

        f = (factorial(k)/(factorial(j)*factorial(k-j)))*(1/2)^k;
        %f calculates the fraction of vesicles with k channels, j of them
        %in the fast fluxing orientation and (k-j) in the slow fluxing
        %orientation

        if j == 0
            %if there are no channels in the fast fluxing orientation
            cflux = cflux + sflux(k,:)*f;
            %assign the flux as slow flux of k channels
        else
            cflux = cflux + fflux(j,:)*f;
            %assign the flux as fast flux for j channels
            %this assumes that the contribution to flux from fast fluxing
            %channels is >> than that from slow fluxing channels
        end
    end
    pflux(k,:) = cflux; %assigns total flux for k number of channels to pflux
end

figure
plot(time1,pflux)
```

```
function y = total_proportional_flux_V


global time1        %retrieves the value of the time vector from simple_flux_V
global pflux        %retrieves the value of the pflux matrix from pt_ffluxbias
global totalflux    %assigns the totalflux matrix as a global variable
global rho

[m,n] = size(pflux);
%uses the dimensions of fflux to assign value to script components

cp = 0.1;
%cp = [0.1 0.02 0.01 0.002 0.001 0.0005 0.00025 0.000167];
%vector of protein concentration in vescle mixtures
%currently set for 1:100 ratio of protein-to-lipid (see channel_dist_theta
%input) but can be set to any/many protein-to-lipid ratios for example see
%the first comment line directly above.

rho = channel_dist_theta(7.57,100,cp);
%determines the Poisson distribution of number of channels per vesicle by
%running the channel_dist function for lipid concentration of 10 mg/ml and
%average vesicle radius of 50 nm

p = length(cp);
%uses the length of cp to assign value to script components

rho2 = rho(:,2:m+1);
%removes empty vesicle component of rho

totalflux = zeros(p,n); %builds totalflux matrix

for j = 1:p; %for each protein concentration

    fluxp = zeros(m,n); %builds fluxp vector

    rho2(j,:) = rho2(j,:)./sum(rho2(j,:));
    %scales each column of rho2 to its total value

    for i=1:n; %for each column of pflux
        fluxp(:,i) = pflux(:,i).*rho2(j,:)';
        %multiplies dot-wise each column of pflux by the scaled probability
        %for that number of of channels per vesicle given the protein to
        %lipid ratio
    end

    totalflux(j,:) = sum(fluxp);
    %assigns the total flux for each protein to lipid ratio
end


figure
plot(time1,totalflux)
axis([0 max(time1) -0.05 1.05])
xlabel('Time /s')
ylabel('Scaled Vesicle Flux')
title('Scaled Flux by Vesicles Containing Protein for each Protein:Lipid
Ratio')
```

```
function y=channel_dist_theta(cl,r,cp)
%cl final concentration lipids
%r radius of vesicles in nm
%cp final concentration of protein

global  pflux

[m,n] = size(pflux);

p = length(cp);

massl = cl*(10^-3); %mass in grams per 10 mililiter
%mass = mg/ml*(10^-3 g/mg) = g/ml

numlipid = (massl/753.84)*(6.022e23); %number of lipids in sample
%numlipid = (mass lipids in g/ average MW lipid)*Avogadros number


SAlipid = (numlipid*63e-20)/2;
%total surface area of lipid head group in m^2
%factor of 2 remove for bilayer

Nv = SAlipid/(4*pi*(r*1e-9)^2); %calculates the number of vesicles

Np = ((cp*(10^-3))./(2*35000))*6.022e23; %number of channels per ml

f = zeros(p,m);

for i = 0:m;
    f(:,i+1) = ((((Np./Nv).^i).*exp(-
                Np./(Nv*0.85))).*(((0.85)^i)*factorial(i)));
end

f = f*0.85;
f(:,1) = f(:,1)+0.15;


y = f;



function unscaled_plot(tf,rho0)
global time1
global slow

p = length(rho0);

for i = 1:p
    tf(i,:) = tf(i,:)*(1-rho0(i));
    tf(i,:) = tf(i,:)+rho0(i);
end

slow = tf(p,:);

figure
plot(time1,tf)
axis([0 max(time1) -0.05 1.05])
xlabel('Time /s')
ylabel('Scaled Total Flux')
title('Scaled total Flux for each Protein:Lipid Ratio')
```

APPENDIX II

Sequences of all putative H_V channel genes that were synthesized for expression and biochemical stability experiments. Each sequence is named according to its GI number followed by its species. A multiple sequence alignment done using ClustalW of all putative H_V channel genes is also shown compared to the sequence of the Rat K_V1.2 voltage-sensor domain (with its transmembrane helices highlighted in cyan). Conserved residues of possible functional importance are highlighted in yellow (with outliers highlighted in alternate colors).

Sequences of Putative H_V channel Genes

>91992153_Homo_sapiens_(Human)
MATWDEKAVTRRAKVAPAERMSKFLRHFTVVGDDYHAWNINYKKWENEEEEEEEEQPPP
TPVSGEEGRAAAPDVAPAPGPAPRAPLDFRGMLRKLFSSHRFQVIIICLVVLDALLVLA
ELILDLKIIQPDKNNYAAMVFHYMSITILVFFMMEIIFKLFVFRLEFFHHKFEILDAVV
VVVSFILDIVLLFQEHQFEALGLLILLRLWRVARIINGIIISVKTRSERQLLRLKQMNV
QLAAKIQHLEFSCSEKEQEIERLNKLLRQHGLLGEVN

>118344228_Ciona_intestinalis
MEGDNCNKSRHKSHNMINPNYASVRCTQPLPSVIQLRSRNKMIGITEDPSSDSEPVSSN
QPLLLTNLSYEVHTFNDNNNHERPAPQEQSTQNTMISMQSEQKSDRFTASNLGMFQYMK
FEIGEDGDDHEEEAILTNREKLRHILHSKPIHVAIIVLVVLDSFLVVGELLIDLKVIIV
PHGNPAPEILHGFSLSILSIFMVEIALKIIADHRHFIHHKVEVLDAVVVVISFGVDIAL
IFVGESEALAAIGLLVILRLWRVFRIINGIIVTVKTKADDRVHEIKKKNSELELQIHNL
EEKLSQKEQDMSRLHEILRCNNIDIPPTVPLTTSVQIHSTTTASADV

>71897219_Gallus_Gallus_(Chicken)
MSRYLKHFTVVGDDPIQWSNDYQKWENEEEDNGEKDSEIKLEPSRGHVTFQDVMKKLFS
SRRFQIVIVFLVIVDALLVLGELLMDLKIIHPDKYHIAPKVFHYLSLSILTIFLVEVGF
KIFVYGREFFHHKFEVLDSIVVVVSFILDLVLLFREHEFEAVGLLILLRLWRVARIING
IILSVKTRSEQQVSKLKQVNLKLATKVEQLQHSCVEKEQEIERLTRMLKQHGLLSEQT

>6573743_Arabidopsis_thaliana
MNIINTGTVDNVEFSIQNLIKSWCRRRKWRQLCNFSPKQQQEELISINQQWRITLSNFL
ESYQVHLFTIFLLSLDIILTSLELSSSLLSCTSVKKTETENEWFRWGGTVILSILAVKS
MALVVAMGKSFFKQPGCVMDGTLAIVALILQVLLEKKGTGFIVVVSLWRVLRVVETAFE
LSDEAIEVQIDGIISQFQALSKENRTLLETLAEKDEVIKMLEEELNRFKENGDIPFVKP

>116505721_Coprinopsis_cinerea
MPLQIFIDVVFVLVELGYTLFNPNCSELEPRETPVWMEALSITSLALSALLVTEIPITV
WCMGIQYFNPFGAVHWAALHLFDALINLATFILDLVLRGRERELASLLIILRLWRIAKL
VSSVAVATDSLEEEVEARLEATKQELHRTKEELGKVEEEVFNLRQRLATFETKVVSNSA
V

>329664616_Bos_taurus_(Cow)
MATWNEKAVTRRARVAPAERMSKFLKHFTVVGDDYHAWNINYKKWENEEEEEEEQPPPT
EASASAEEGRATDPTPAPAPVPRPRLDFRTTLRKLFSAHRFQVIIICLVVLDALLVLAE
LVLDLKIIEPDKNNYAPKVFHYMSLAILTFFMMEIFFKIFVFRLEFFHHKFEILDTIVV
VISFILDLVLLFREHQFEALGLLILLRLWRVARIINGIIISVKTRSERQLLRLKQINIQ
LATKIQHLEFSCSEKEQEIERLNKLLRQHGLLGEVN

>345790859_Canis_lupis_familiaris_(Dog)
MATWDEKASSRRARVAPAERMSKFLKHFTVVGDDYHAWNVNYKKWENEEDDEEEEQPPP
TAASGEEGRADPTAAPTPRPPLDFRATLRKLFSSHRFQVIIICLVILDALLVLAELILD
LKIIQGDKNNYATKVFHYSSFAILTLFMMEVFLKLFVFRLEFFHHKFEILDTFVVVVSF
ILDLVLLFQKHEFEALGLLILLRLWRVARIINGIIISVKTRSERQLLRLKQMNIQLAAK
IQHLEFSCSEKEQEIERLNKLLRQHGLLGEVN

>148235789_Xenopus_laevis_(Frog)
MAGCLRHFTSVGDDTKKREWKQEDVEVAYEEPLKNTPHPFIASYSFRGALKWLLSSHKF
QIVIICLVILDALFVLVEVLLDLELLAEKVDHIIPEIFHYLSISVLTFFILEIAGKLYA
FRLEFFHHKFEVFDAAIVVISFIIDIVYISREDIFNAVGLLILLRLWRVARIVNGVIVS
VKTRAEEKMHKLKEQKGSLLEKVAQLEQQCAQQEQEIGRLHKLLQEHNVFPAS

>83774308_Aspergillus_oryzae
MASPSDPLLHEHTGPRSLRQRPIYLPEEQGQRIIAQWRRAARDFLSSRRGHYLVLLLVS
VDVACTFADFLIELHVCELTKHGSHVAIGWGVTQKVLAIVGLVFSCLFMLELMVTVFSF
GKGYFSSKFHVFDALVIIVAFGVDVALHGIEEELGSLIVVLRLWRVFKIIEELQSANED
TLEEYEHEIERLRQENTYLRQRLNVSLSNADPMD

>124360845_Medicago_truncatula
MIRVLSILLLTIDLIITILELSSSLVSCKQKINIVEELYFHWIGIGILSIISMKIIALL
VGLGFSFFKHPGYVVDGIVAIGALIMEVFLEKRGGGLLVVVSLWRVIRVVESVFELSDE
AIEAQIEGIVCQFEALKDENIRLLGIINEKDKLIEKLKEELDKCR

>109098724_Macaca_mulatta_(Indian_Monkey)
MATWDEKAVTRRAKVAPAERMSKFLKHFTVVGDDYHAWNINYKKWENEEDEEEEEQPPP
TPASGEEGRVAGPDAAPAPGPAPRAPLDFRGTLRKLFSSHRFQVIIICLVVLDTLLVLA
ELILDLRIIQPDKKNYAAMIFHYMSIAILALFMMEITFKLFVFRLEFFHHKFEILDAVV
VVVSFVLDVVLLFQEHEFEALGLLILLRLWRVARIINGIIISVKTRSERQLLRLKQMNV
QLAAKIQHLEFSCSEKEQEIERLNKLLRQHGLLGEVN

>334327101_Monodelphis_domesticus_(opossum)
MGPKQWNNNSGSHTGSGQEELSEQHRQWVPLKDGSPRAMSRFLRHFTVVGDDHYKWNTR
YKKWDNEDEDDEQPQVPTGPAPGADVPGTESNAVQVPGETVTPPKAPPDFRTVMRKLFG
SHRFQVIIICLVIMDALLVLAELMLDLKIIQPDKDNYAARVFHYLSIAILTFFMIEVAL
KLYVFRLEFFYHKFEILDAVIVIISFVLDIVLLFQEHAFEALGLLILLRLWRVARIING
IIISVKTRSERQLSRLKLINHQLATKIQHLEFSCTEKEQEIERLNKLLRDHGLLE

>109809754_Mus_musculus_(Mouse)
MTSHDPKAVTRRTKVAPTKRMSRFLKHFTVVGDDYHTWNVNYKKWENEEEEEPAPTSA
EGEGNAEGPDAEAGSASTPRQSLDFRSRLRKLFSSHRFQVIIICLVVLDALLVLAELLL
DLKIIEPDEQDYAVTAFHYMSFAILVFFMLEIFFKIFVFRLEFFHHKFEILDAFVVVVS
FVLDLVLLFKSHHFEALGLLILLRLWRVARIINGIIISVKTRSERQILRLKQINIQLAT
KIQHLEFSCSEKEQEIERLNKLLKQNGLLGDVN

>109497399_Rattus_norvegicus_(Rat)
MRGDTIHARGNRLGKGLEAWNAGRMAKQGEAVTRRTKVAPTKRMSRFLKHFTVVGDDYH
TWNVNYKKWENEEDEEEPAPTSAEGEGSAVGPDAEAGSASTPRPSLDFRSRLRKLFSSH
RFQVIIICLVVLDALLVLAELLLDLRIIEPDLSKYSTKVFHYLSLAILAFFVLEISLKV
FVFRLEFFHHKFEILDAIVVVSFVLDLILLFKNHHFEALGLLILLRLWRVARIINGII
ISVKTRSERQILRLKQINLQLATKIQHLEFSCSEKEQEIERLSKLLRQNGLLEDVNVN

>187282419_Strongylocentrotus_purpuratus_(sea_urchin)
MFGFRRLSDTTKPSEGNDQQRVIVKDDSSDSVVSDSHDGHPARTEPLSLREKLHEIMET
QKFHIAILVLVVIDCILVIVELVIDFEVLSQEEGQCNATETDKEEKEVTAANVLHYISI
GILSIFMIELLIKIPVFRMEFFRSKLEVFDGIIIVISFVLDVVSLIYEEQFAVLQLLVL
LRLWRIVRVVNGVILSVETQAKKKIEQQKHLRAEVEHEMEKFRRYCAAQEKEIEVLRNT
LNQHGIQIDDDYVAKKPQFSLNQLNVVVEMNSADKHDTGEDEGEGEEGGGDGNTRRHEK
EREALGEHTITLTTDDNVNTIQADYHPQDTTFT

>50539752_Danio_rerio_(zebra_fish)
MSRYLKHFTAVGDNKSAVPTWHEEDTSHHVTTLHDAPDGLEVSTGQHLGQLSFRDSLRK
LYSTERFQIVVVCLVVLDAIFVLCELLIDLSIIEADHHRIAPQVFHYLSLALLTFFMVE
LAGKIFAYRLEFLHHKFEVFDGIVVVVSFILDIIYISKEDAFDAMGLLILLRLWRVARI
INGILVSVQNRANHRVEKLKEINESLVHQVNELKEQNTKMDQENVRLRALLKDHSIDF

>156364735_Nematostella_vectensis_(sea_anemone)
MESDNQQLVGQLVFDTQSLGERAMDKEIEVEVGDGGGDAQVVSSTPCWHILKDRPRLCE
IIHGQKAQYTIIALVIIDCIIVIAELLVDLEILKVHHDNPAPHILHDVSIAILSLFIIE
LIVKIYAMGMEFFHHKLEVFDGIVVIVSFALDIAFSGGNAAEGASLLIILRLWRVTRIV
NGIILSVKMQDEKKIHHLHKVIEELQEELDRLKTRNAELENELKTLKGTKEEPVAEEAT
T

>156374277_Nematostella_vectensis_(sea_anemone_baby)
MAEKVESVEQTAEDGKRQTFQNLNRRRSTKEWMQGGCGILRTSLGKMLTGITWQFTIIL
LVLVEVAINLVLMCISLNAINDSEQHFASRLLHFVGISILAIFALEVFLKLFALGIEYF
KIEKLEIFDAVIVITALIVEILLSATHTSKAWKSLGFVIGLRLWRVCRVITNIIEFREE
LYELIDESDGRSKRPTSSATETLHTERESLHETK

>338727680_Equus_caballus_(Horse)
MRGASGTEDTKLSAVLGCNYKDTETVTRRPKVAPAERMSKFLRHFTVVGDDYHTWNINY
KKWENEEEEEEEEQAPPAPASGEEGRAAEPTAARVPAPRPPLDFRTMLRKLFSCHRFQV
IIICLVILDALLVLAELILDLKIIEADKNNYVPRVFHYMSLAILTFFMTEVSLKIFVFR
LEFFHHKFEILDAVVVVVSFVLDIVLIFREHEFEALGLLILLRLWRVARIINGIIISVK
TRSERQLLRLKQMNIQLAAKVQHLEFSCSEKEQEIERLNKLLQQHGLLGEVI

>345305006_Ornithorhynchus_anatinus_(Platypus)
MSTPHLGSARFYHLLRFEVSSRASGLRGLRLVIGDLQNFRVTIVCLVIVDALLVLAELL
LDLRIIHPDEKQVAPKVFHYLSICILTFFVVEVVLKMFVYRLEFFHHKFEVLDAVVVII
SFILDLVLLFREHEFEALGLLILLRLWRVARIINGIIISVKTRSEQQLSRLRQANLQLV
AKVQHLEFSCNEKEQEIERLNALLKQHGLIN

>156059386_Sclerotinia_sclerotiorum_(Fungal_pathogen)
MSRRNSDISEHAPLIRASSQPISITSELPYHHTPRLSFSRRLSNGYRKSRSYVRSFLST
RGQHYTVLLLVACDLIGIFADIIINLYQCDNDKEGKTDPIWNEVRVGLGIAGLVFSCLF
MLELIASVWAFGWSKFHCFDATVIVAGFVVDVLLHGIVEEVASLVIVLRLWRFFKIIEE
FSVGAQEQMDVLEERIEQLEMENKRLKKELRKRNDNDNDEDLENGERTR

>145234953_Aspergillus_niger
MRSPSDPLLASESQPLPPGQIYLPDEDDENTQSTEPLIARCRRSARNYLSSRFGHYLVL
FLVSVDVACVFADFLIEIYVCELEKKYKHVPSGWEDAQEALSITGLVFSCLFMLELVVA
VGSFGMSYFSSKFHIFDSAVIIVAFAIDVAMRGLVEELGSLVVVLRLWRVFKIIEELES
ANADSLEEYEREIDRLKEENYLLRRRAEFGSDGVN

ClustalW Alignment

```
91992153_Human              ---------------------------------------------MATWD
118344228_Ciona             MEGDNCNKSRHKSHNMINPNYASVRCTQPLPSVIQLRSRNKMIGITEDPS
71897219_Chicken            ---------------------------------------------------
6573743_Arabidopsis         ---------------------------------------------------
116505721_Coprinopsis       ---------------------------------------------------
329664616_Cow               ---------------------------------------------MATWN
345790859_Dog               ---------------------------------------------MATWD
148235789_Frog              ---------------------------------------------------
83774308_Aspergillus        ---------------------------------------------------
124360845_Medicago          ---------------------------------------------------
109098724_Indian_Monkey     ---------------------------------------------MATWD
334327101_opossum           ---------------------------MGPKQWNNNSGSHTGSGQEELSE
109809754_Mouse             ---------------------------------------------MTSHD
109497399_Rat               ----------------------MRGDTIHARGNRLGKGLEAWNAGRMAKQ
187282419_sea_urchin        ---------------------------------------------------
50539752_zebra_fish         ---------------------------------------------------
156364735_sea_anemone       ---------------------------------------------------
156374277_sea_anemone_baby  ---------------------------------------------------
338727680_Horse             ---------------------------MRGASGTEDTKLSAVLGCNYKD
345305006_Platypus          ---------------------------------------------------
156059386_Fungal_pathogen   ---------------------------------------------------
145234953_Aspergillus       ---------------------------------------------------


91992153_Human              EKAVTRRAKVAPAERMSKFLRHFTVVGDDYHAWNINYKKWENEEEEEEEE
118344228_Ciona             SDSEPVSSNQPLLLTNLSYEVHTFNDNNNHERPAPQEQSTQNTMISMQSE
71897219_Chicken            ---------------MSRYLKHFTVVGDDPIQWSNDYQKWENEEEDNG--
6573743_Arabidopsis         -----------MNIINTGTVDNVEFSIQNLIKSWCRRRKWRQLCNFSPKQ
116505721_Coprinopsis       ---------------------------------------------------
329664616_Cow               EKAVTRRARVAPAERMSKFLKHFTVVGDDYHAWNINYKKWENEE-EEEEE
345790859_Dog               EKASSRRARVAPAERMSKFLKHFTVVGDDYHAWNVNYKKWENEEDDEEEE
148235789_Frog              ---------------MAGCLRHFTSVGDDTKKREWKQEDVEVAYEEPLKN
83774308_Aspergillus        ---------------MASPSDPLLHEHTGPRSLRQRPIYLPEEQGQ----
124360845_Medicago          ---------------------------------------------------
109098724_Indian_Monkey     EKAVTRRAKVAPAERMSKFLKHFTVVGDDYHAWNINYKKWENEEDEEEEE
334327101_opossum           QHRQWVPLKDGSPRAMSRFLRHFTVVGDDHYKWNTRYKKWDNEDEDDEQP
109809754_Mouse             PKAVTRRTKVAPTKRMSRFLKHFTVVGDDYHTWNVNYKKWENEEEEEE--
109497399_Rat               GEAVTRRTKVAPTKRMSRFLKHFTVVGDDYHTWNVNYKKWENEEDEEE--
187282419_sea_urchin        ---------------MFGFRRLSDTTKPSEGNDQQRVIVKDDSSDSVVSD
50539752_zebra_fish         ---------------MSRYLKHFTAVGDNKSAVPTWHEEDTSHHVTTLHD
156364735_sea_anemone       -------MESDNQQLVGQLVFDTQSLGERAMDKEIEVEVGDGGGDAQVVS
156374277_sea_anemone_baby  ---------------MAEKVESVEQTAEDGKRQTFQNLNRRRSTKEWMQG
338727680_Horse             TETVTRRPKVAPAERMSKFLRHFTVVGDDYHTWNINYKKWENEEEEEEEE
345305006_Platypus          --MSTPHLGSARFYHLLRFEVSSRASG----------------------
156059386_Fungal_pathogen   ---------MSRRNSDISEHAPLIRASSQPISITSELPYHHTPRLSFSRR
145234953_Aspergillus       ---------------MRSPSDPLLASESQP--LPPGQIYLPDEDDENTQS
```

```
rKv1.2                                                                ARIIA
91992153_Human             QPPPTPVSGEEGRAAAPDVAPAP---GPAPRAPLDFRGMLRKLFSSHRFQ
118344228_Ciona            QKSDRFTASNLGMFQYMKFEIGEDGDDHEEEAILTNREKLRHILHSKPIH
71897219_Chicken           --------------------EKDSEIKLEPSRGHVTFQDVMKKLFSSRRFQ
6573743_Arabidopsis        QQEELISIN-------------------------QQWRITLSNFLESYQVH
116505721_Coprinopsis      ------------------------------------------------MPL
329664616_Cow              QPPPTEASASAEEGRATDPTPAP---APVPRPRLDFRTTLRKLFSAHRFQ
345790859_Dog              QPPPTAASGEEG-----RADPTA---APTPRPPLDFRATLRKLFSSHRFQ
148235789_Frog             TPHPFIAS-------------------------YSFRGALKWLLSSHKFQ
83774308_Aspergillus       --R----------------------------IIAQWRRAARDFLSSRRGH
124360845_Medicago         ------------------------------------------------MIR
109098724_Indian_Monkey    QPPPTPASGEEGRVAGPDAAPAP---GPAPRAPLDFRGTLRKLFSSHRFQ
334327101_opossum          QVPTGPAPGADVPGTESNAVQVPGETVTPPKAPPDFRTVMRKLFGSHRFQ
109809754_Mouse            --PAPTSAEGEGNAEGPDAEAGS---ASTPRQSLDFRSRLRKLFSSHRFQ
109497399_Rat              --PAPTSAEGEGSAVGPDAEAGS---ASTPRPSLDFRSRLRKLFSSHRFQ
187282419_sea_urchin       SHDGHPA----------------------RTEPLSLREKLHEIMETQKFH
50539752_zebra_fish        APDGLEVSTGQH-----------------LGQLSFRDSLRKLYSTERFQ
156364735_sea_anemone      STP--------------------------CWHILKDRPRLCEIIHGQKAQ
156374277_sea_anemone_baby GCG-------------------------------ILRTSLGKMLTGITWQ
338727680_Horse            QAPPAPASGEE--GRAAEPTAAR---VPAPRPPLDFRTMLRKLFSCHRFQ
345305006_Platypus         ------------------------------LRGLRLVIGDLQNFR
156059386_Fungal_pathogen  LSN----------------------------GYRKSRSYVRSFLSTRGQH
145234953_Aspergillus      TEP----------------------------LIARCRRSARNYLSSRFGH


rKv1.2                     IVSVMVILISIVSFCLETLPIFRDENEDMHGGGVT-/-GYQQSTSFTDPF
91992153_Human             VIIICLVVLDALLVLAELILDLKIIQPDKNN-------------YAAMVF
118344228_Ciona            VAIIVLVVLDSFLVVGELLIDLKVIIVPHGN-------------PAPEIL
71897219_Chicken           IVIVFLVIVDALLVLGELLMDLKIIHPDKYH-------------IAPKVF
6573743_Arabidopsis        LFTIFLLSLDIILTSLELSSSLLSCTSVKKT------------ETENEWF
116505721_Coprinopsis      QIFIDVVFVLVELGYTLFNPNCSELEPRETP-------------VWMEAL
329664616_Cow              VIIICLVVLDALLVLAELVLDLKIIEPDKNN-------------YAPKVF
345790859_Dog              VIIICLVILDALLVLAELILDLKIIQGDKNN-------------YATKVF
148235789_Frog             IVIICLVILDALFVLVEVLLDLELLAEKVDH-------------IIPEIF
83774308_Aspergillus       YLVLLLVSVDVACTFADFLIELHVCELTKHGS-----HVAIGWGVTQKVL
124360845_Medicago         VLSILLLTIDLIITILELSSSLVSCKQKIN-------------IVEELYF
109098724_Indian_Monkey    VIIICLVVLDTLLVLAELILDLRIIQPDKKN-------------YAAMIF
334327101_opossum          VIIICLVIMDALLVLAELMLDLKIIQPDKDN-------------YAARVF
109809754_Mouse            VIIICLVVLDALLVLAELLLDLKIIEPDEQD-------------YAVTAF
109497399_Rat              VIIICLVVLDALLVLAELLLDLRIIEPDLSK-------------YSTKVF
187282419_sea_urchin       IAILVLVVIDCILVIVELVIDFEVLSQEEGQCNATETDKEEKEVTAANVL
50539752_zebra_fish        IVVVCLVVLDAIFVLCELLIDLSIIEADHHR-------------IAPQVF
156364735_sea_anemone      YTIIALVIIDCIIVIAELLVDLEILKVHHDNP-------------APHIL
156374277_sea_anemone_baby FTIILLVLVEVAINLVLMCISLNAINDSEQH-------------FASRLL
338727680_Horse            VIIICLVILDALLVLAELILDLKIIEADKNN-------------YVPRVF
345305006_Platypus         VTIVCLVIVDALLVLAELLLDLRIIHPDEKQ-------------VAPKVF
156059386_Fungal_pathogen  YTVLLLVACDLIGIFADIIINLYQCDNDKEGK-----TDPI-WNEVRVGL
145234953_Aspergillus      YLVLFLVSVDVACVFADFLIEIYVCELEKKYK-----HVPSGWEDAQEAL
                              : ::          .  .                          :
```

```
rKv1.2                      FIVETLCIIWFSFEFLVRFFACPSKAGFFT-----NIMNIIDIVAIIPYF
91992153_Human              HYMSITILVFFMMEIIFKLFVFRLEFFHHK-------FEILDAVVVVVSF
118344228_Ciona             HGFSLSILSIFMVEIALKIIADHRHFIHHK-------VEVLDAVVVVISF
71897219_Chicken            HYLSLSILTIFLVEVGFKIFVYGREFFHHK-------FEVLDSIVVVVSF
6573743_Arabidopsis         RWGGTVILSILAVKSMALVVAMGKSFFKQP-------GCVMDGTLAIVAL
116505721_Coprinopsis       SITSLALSALLVTEIPITVWCMGIQYFNPFGAVHWAALHLFDALINLATF
329664616_Cow               HYMSLAILTFFMMEIFFKIFVFRLEFFHHK-------FEILDTIVVVISF
345790859_Dog               HYSSFAILTLFMMEVFLKLFVFRLEFFHHK-------FEILDTFVVVVSF
148235789_Frog              HYLSISVLTFFILEIAGKLYAFRLEFFHHK-------FEVFDAAIVVISF
83774308_Aspergillus        AIVGLVFSCLFMLELMVTVFSFGKGYFSSK-------FHVFDALVIIVAF
124360845_Medicago          HWIGIGILSIISMKIIALLVGLGFSFFKHP-------GYVVDGIVAIGAL
109098724_Indian_Monkey     HYMSIAILALFMMEITFKLFVFRLEFFHHK-------FEILDAVVVVVSF
334327101_opossum           HYLSIAILTFFMIEVALKLYVFRLEFFYHK-------FEILDAVIVIISF
109809754_Mouse             HYMSFAILVFFMLEIFFKIFVFRLEFFHHK-------FEILDAFVVVVSF
109497399_Rat               HYLSLAILAFFVLEISLKVFVFRLEFFHHK-------FEILDAIVVVVSF
187282419_sea_urchin        HYISIGILSIFMIELLIKIPVFRMEFFRSK-------LEVFDGIIIVISF
50539752_zebra_fish         HYLSLALLTFFMVELAGKIFAYRLEFLHHK-------FEVFDGIVVVVSF
156364735_sea_anemone       HDVSIAILSLFIIELIVKIYAMGMEFFHHK-------LEVFDGIVVIVSF
156374277_sea_anemone_baby  HFVGISILAIFALEVFLKLFALGIEYFKIEK------LEIFDAVIVITAL
338727680_Horse             HYMSLAILTFFMTEVSLKIFVFRLEFFHHK-------FEILDAVVVVVSF
345305006_Platypus          HYLSICILTFFVVEVVLKMFVYRLEFFHHK-------FEVLDAVVVIISF
156059386_Fungal_pathogen   GIAGLVFSCLFMLELIASVWAFG----WSK-------FHCFDATVIVAGF
145234953_Aspergillus       SITGLVFSCLFMLELVVAVGSFGMSYFSSK-------FHIFDSAVIIVAF
                               .  .  ::  :    :                    .*  : :  :

rKv1.2                      ITLGTELAE-/-MSLAILRVIRLVRVFRIFKLSRHSKGLQILGQTLKAS
91992153_Human              ILDIVLLFQ--EHQFEALGLLILLRLWRVARIINGIIISVKTRSERQLLR
118344228_Ciona             GVDIALIFVGESEALAAIGLLVILRLWRVFRIINGIIVTVKTKADDRVHE
71897219_Chicken            ILDLVLLFR--EHEFEAVGLLILLRLWRVARIINGIILSVKTRSEQQVSK
6573743_Arabidopsis         ILQVLLEKK-------GTGFIVVVSLWRVLRVVETAFELSDEAIEVQIDG
116505721_Coprinopsis       ILDLVLRGR----ERELASLLIILRLWRIAKLVSSVAVATDSLEEEVEAR
329664616_Cow               ILDLVLLFR--EHQFEALGLLILLRLWRVARIINGIIISVKTRSERQLLR
345790859_Dog               ILDLVLLFQ--KHEFEALGLLILLRLWRVARIINGIIISVKTRSERQLLR
148235789_Frog              IIDIVYISR--EDIFNAVGLLILLRLWRVARIVNGVIVSVKTRAEEKMHK
83774308_Aspergillus        GVDVALHGI----EEELGSLIVVLRLWRVFKIIEELQSANEDTLEEYEHE
124360845_Medicago          IMEVFLEKR-------GGGLLVVVSLWRVIRVVESVFELSDEAIEAQIEG
109098724_Indian_Monkey     VLDVVLLFQ--EHEFEALGLLILLRLWRVARIINGIIISVKTRSERQLLR
334327101_opossum           VLDIVLLFQ--EHAFEALGLLILLRLWRVARIINGIIISVKTRSERQLSR
109809754_Mouse             VLDLVLLFK--SHHFEALGLLILLRLWRVARIINGIIISVKTRSERQILR
109497399_Rat               VLDLILLFK--NHHFEALGLLILLRLWRVARIINGIIISVKTRSERQILR
187282419_sea_urchin        VLDVVSLIY--EEQFAVLQLLVLLRLWRIVRVVNGVILSVETQAKKKIEQ
50539752_zebra_fish         ILDIIYISK--EDAFDAMGLLILLRLWRVARIINGILVSVQNRANHRVEK
156364735_sea_anemone       ALDIA-FSG--GNAAEGASLLIILRLWRVTRIVNGIILSVKMQDEKKIHH
156374277_sea_anemone_baby  IVEILLSATHTSKAWKSLGFVIGLRLWRVCRVITNIIEFREELYELIDES
338727680_Horse             VLDIVLIFR--EHEFEALGLLILLRLWRVARIINGIIISVKTRSERQLLR
345305006_Platypus          ILDLVLLFR--EHEFEALGLLILLRLWRVARIINGIIISVKTRSEQQLSR
156059386_Fungal_pathogen   VVDVLLHGI----VEEVASLVIVLRLWRFFKIIEEFSVGAQEQMDVLEER
145234953_Aspergillus       AIDVAMRGL----VEELGSLVVVLRLWRVFKIIEELESANADSLEEYERE
                             :::               ::: : ***. :::           .
```

```
91992153_Human              LKQMNVQLAAKIQHLEFSCSEKEQEIERLNKLLRQHGLLGEVN-------
118344228_Ciona             IKKKNSELELQIHNLEEKLSQKEQDMSRLHEILRCNNIDIPPTVPLTTSV
71897219_Chicken            LKQVNLKLATKVEQLQHSCVEKEQEIERLTRMLKQHGLLSEQT-------
6573743_Arabidopsis         IISQFQALSKENRTLLETLAEKDEVIKMLEEELNRFKENGDIPFVKP---
116505721_Coprinopsis       LEATKQELHRTKEELGKVEEEVFNLRQRLATFETKVVSNSAV--------
329664616_Cow               LKQINIQLATKIQHLEFSCSEKEQEIERLNKLLRQHGLLGEVN-------
345790859_Dog               LKQMNIQLAAKIQHLEFSCSEKEQEIERLNKLLRQHGLLGEVN-------
148235789_Frog              LKEQKGSLLEKVAQLEQQCAQQEQEIGRLHKLLQEHNVFPAS--------
83774308_Aspergillus        IERLRQENTYLRQRLNVSLSNADPMD-------------------------
124360845_Medicago          IVCQFEALKDENIRLLGIINEKDKLIEKLKEELDKCR-------------
109098724_Indian_Monkey     LKQMNVQLAAKIQHLEFSCSEKEQEIERLNKLLRQHGLLGEVN-------
334327101_opossum           LKLINHQLATKIQHLEFSCTEKEQEIERLNKLLRDHGLLE----------
109809754_Mouse             LKQINIQLATKIQHLEFSCSEKEQEIERLNKLLKQNGLLGDVN-------
109497399_Rat               LKQINLQLATKIQHLEFSCSEKEQEIERLSKLLRQNGLLEDVNVN-----
187282419_sea_urchin        QKHLRAEVEHEMEKFRRYCAAQEKEIEVLRNTLNQHGIQIDDDYVAKKPQ
50539752_zebra_fish         LKEINESLVHQVNELKEQNTKMDQENVRLRALLKDHSIDF----------
156364735_sea_anemone       LHKVIEELQEELDRLKTRNAELENELKTLKGTK-----------------
156374277_sea_anemone_baby  DGRSKRPTSSATETLHTERESLHETK-------------------------
338727680_Horse             LKQMNIQLAAKVQHLEFSCSEKEQEIERLNKLLQQHGLLGEVI-------
345305006_Platypus          LRQANLQLVAKVQHLEFSCNEKEQEIERLNALLKQHGLIN----------
156059386_Fungal_pathogen   IEQLEMENKRLKKELRKRNDNDNDEDLENGERTR----------------
145234953_Aspergillus       IDRLKEENYLLRRRAEFGSDGVN----------------------------
```

```
91992153_Human              --------------------------------------------------
118344228_Ciona             QIHSTTTASADV----------------------------------------
71897219_Chicken            --------------------------------------------------
6573743_Arabidopsis         --------------------------------------------------
116505721_Coprinopsis       --------------------------------------------------
329664616_Cow               --------------------------------------------------
345790859_Dog               --------------------------------------------------
148235789_Frog              --------------------------------------------------
83774308_Aspergillus        --------------------------------------------------
124360845_Medicago          --------------------------------------------------
109098724_Indian_Monkey     --------------------------------------------------
334327101_opossum           --------------------------------------------------
109809754_Mouse             --------------------------------------------------
109497399_Rat               --------------------------------------------------
187282419_sea_urchin        FSLNQLNVVVEMNSADKHDTGEDEGEGEEGGGDGNTRRHEKEREALGEHT
50539752_zebra_fish         --------------------------------------------------
156364735_sea_anemone       ------------------------------------------EEPVAEEA
156374277_sea_anemone_baby  --------------------------------------------------
338727680_Horse             --------------------------------------------------
345305006_Platypus          --------------------------------------------------
156059386_Fungal_pathogen   --------------------------------------------------
145234953_Aspergillus       --------------------------------------------------
```

```
91992153_Human             ------------------------
118344228_Ciona            ------------------------
71897219_Chicken           ------------------------
6573743_Arabidopsis        ------------------------
116505721_Coprinopsis      ------------------------
329664616_Cow              ------------------------
345790859_Dog              ------------------------
148235789_Frog             ------------------------
83774308_Aspergillus       ------------------------
124360845_Medicago         ------------------------
109098724_Indian_Monkey    ------------------------
334327101_opossum          ------------------------
109809754_Mouse            ------------------------
109497399_Rat              ------------------------
187282419_sea_urchin       ITLTTDDNVNTIQADYHPQDTTFT
50539752_zebra_fish        ------------------------
156364735_sea_anemone      TT----------------------
156374277_sea_anemone_baby ------------------------
338727680_Horse            ------------------------
345305006_Platypus         ------------------------
156059386_Fungal_pathogen  ------------------------
145234953_Aspergillus      ------------------------
```

REFERENCES

Adams, P.D. *et al*., 2010. PHENIX: a comprehensive Python-based system for macromolecular structure solution. *Acta Crystallographica Section D Biological Crystallography*, 66(Pt 2), pp.213–221.

Aggarwal, S.K. & Mackinnon, R., 1996. Contribution of the S4 segment to gating charge in the Shaker K+ channel. *Neuron*, 16(6), pp.1169–1177.

Alabi, A.A. *et al*., 2007. Portability of paddle motif function and pharmacology in voltage sensors. *Nature*, 450(7168), pp.370–375.

Albers, R.W., 1967. Biochemical aspects of active transport. *Annual review of biochemistry*, 36, pp.727–756.

Albright, R.A., Joh, K. & Morais-Cabral, J.H., 2007. Probing the structure of the dimeric KtrB membrane protein. *The Journal of biological chemistry*, 282(48), pp.35046–35055.

Aller, S.G. *et al*., 2004. Eukaryotic CTR copper uptake transporters require two faces of the third transmembrane domain for helix packing, oligomerization, and function. *The Journal of biological chemistry*, 279(51), pp.53435–53441.

Armstrong, C.M. & Bezanilla, F., 1973. Currents Related to Movement of the Gating Particles of the Sodium Channels. *Nature*, 242(5398), pp.459–461.

Asano, S. *et al*., 1996. Functional Expression of Gastric H^+,K^+-ATPase and Site-directed Mutagenesis of the Putative Cation Binding Site and the Catalytic Center. *Journal of Biological Chemistry,* 271, pp.2740–2745.

Barish, M.E. & Baud, C., 1984. A voltage-gated hydrogen ion current in the oocyte membrane of the axolotl, Ambystoma. *The Journal of Physiology*, 352, pp.243–263.

Barrett, J.N., Magleby, K.L. & Pallotta, B.S., 1982. Properties of single calcium-activated potassium channels in cultured rat muscle. *The Journal of Physiology*, 331, pp.211–230.

Berger, T.K. & Isacoff, E.Y., 2011. The pore of the voltage-gated proton channel. *Neuron*, 72(6), pp.991–1000.

Bezanilla, F., 2000. The voltage sensor in voltage-dependent ion channels. *Physiological Reviews*, 80(2), pp.555–592.

Brohawn, S.G., Campbell, E.B. & Mackinnon, R., 2013. Domain-swapped chain connectivity and gated membrane access in a Fab-mediated crystal of the human TRAAK K^+ channel. *Proceedings of the National Academy of Science*, 110, pp.2129–2134.

Brownlee, C. & Taylor, A., 2004. Calcification in coccolithophores: A cellular perspective. In *Coccolithophores*. Berlin, Heidelberg: Springer Berlin Heidelberg, pp. 31–49.

Butterwick, J.A. & Mackinnon, R., 2010. Solution structure and phospholipid interactions of the isolated voltage-sensor domain from KvAP. *Journal of Molecular Biology*, 403(4), pp.591–606.

Byerly, L., Meech, R. & Moody, W., 1984. Rapidly activating hydrogen ion currents in perfused neurones of the snail, Lymnaea stagnalis. *The Journal of Physiology*, 351, pp.199–216.

Bykova, E.A. *et al*., 2006. Large movement in the C terminus of CLC-0 chloride channel during slow gating. *Nature Structural & Molecular Biology*, 13(12), pp.1115–1119.

Cadene, M. & Chait, B.T., 2000. A Robust, Detergent-Friendly Method for Mass Spectrometric Analysis of Integral Membrane Proteins. *Analytical Chemistry*, 72(22), pp.5655–5658.

Capasso, M. *et al*., 2010. HVCN1 modulates BCR signal strength via regulation of BCR-dependent generation of reactive oxygen species. *Nature Immunology*, 11(3), pp.265–272.

Caprini, M. *et al*., 2001. Structural compatibility between the putative voltage sensor of voltage-gated K^+ channels and the prokaryotic KcsA channel. *The Journal of Biological Chemistry*, 276(24), pp.21070–21076.

Carter, N.W. *et al*., 1967. Measurement of intracellular pH of skeletal muscle with pH-sensitive glass microelectrodes. *Journal of Clinical Investigation*, 46(6), pp.920–933.

Cavanagh, J. *et al*., 2007. *Protein NMR Spectroscopy* 2nd ed, Elselvier Academic Press.

Cherezov, V. *et al*., 2007. High-resolution crystal structure of an engineered human beta2-adrenergic G protein-coupled receptor. *Science*, 318(5854), pp.1258–1265.

Cherny, V.V. & DeCoursey, T.E., 1999. pH-dependent inhibition of voltage-gated H^+ currents in rat alveolar epithelial cells by Zn^{2+} and other divalent cations. *The Journal of General Physiology*, 114, pp.819–838.

Cherny, V.V., Markin, V. & DeCoursey, T.E., 1995. The Voltage-Activated Hydrogen-Ion Conductance in Rat Alveolar Epithelial-Cells Is Determined by the Ph Gradient. *Journal of General Physiology*, 105(6), pp.861–896.

Cherny, V.V., Murphy, R. & DeCoursey, T.E., 2003. Properties of single voltage-gated proton channels in human eosinophils estimated by noise analysis and by direct measurement. *The Journal of General Physiology*, 121(6), pp.615–628.

Cole, C., Barber, J.D. & Barton, G.J., 2008. The Jpred 3 secondary structure prediction server. *Nucleic Acids Research*, 36(Web Server issue), pp.W197–201.

Cole, K.S. & Moore, J.W., 1960. Potassium ion current in the squid giant axon: dynamic characteristic. *Biophysical Journal*, 1, pp.1–14.

Cordingley, M.G. *et al*., 1990. Substrate requirements of human rhinovirus 3C protease for peptide cleavage in vitro. *The Journal of Biological Chemistry*, 265(16), pp.9062–9065.

Cukierman, S., 2006. Et tu, Grotthuss! and other unfinished stories. *Biochimica et Biophysica Acta,* 1757, pp.876–885.

Cukierman, S., 2000. Proton mobilities in water and in different stereoisomers of covalently linked gramicidin A channels. *Biophysical Journal*, 78(4), pp.1825–1834.

de Grotthuss C J T, 1806. Sur la décomposition de l'eau et des corps qu'elle tient en dissolution à l"aide de l"électricité galvanique. *Annales de Chimie (Paris)*, (58), pp.54–73.

DeCoursey, T.E., 1991. Hydrogen ion currents in rat alveolar epithelial cells. *Biophysical Journal*, 60(5), pp.1243–1253.

DeCoursey, T.E., 2003a. Interactions between NADPH oxidase and voltage-gated proton channels: why electron transport depends on proton transport. *FEBS letters*, 555(1), pp.57–61.

DeCoursey, T.E., 2003b. Voltage-gated proton channels and other proton transfer pathways. *Physiological Reviews*, 83(2), pp.475–579.

DeCoursey, T.E., 2010. Voltage-gated proton channels find their dream job managing the respiratory burst in phagocytes. *Physiology (Bethesda, Md.)*, 25(1), pp.27–40.

DeCoursey, T.E., 2008. Voltage-gated proton channels. *Cellular and Molecular Life Sciences : CMLS*, 65(16), pp.2554–2573.

DeCoursey, T.E. & Cherny, V.V., 1997. Deuterium isotope effects on permeation and gating of proton channels in rat alveolar epithelium. *The Journal of General Physiology*, 109(4), pp.415–434.

DeCoursey, T.E. & Cherny, V.V., 1996. Effects of buffer concentration on voltage-gated H^+ currents: does diffusion limit the conductance? *Biophysical Journal*, 71(1), pp.182–193.

DeCoursey, T.E. & Cherny, V.V., 1993. Potential, pH, and arachidonate gate hydrogen ion currents in human neutrophils. *Biophysical Journal*, 65(4), pp.1590–1598.

DeCoursey, T.E. & Cherny, V.V., 1998. Temperature dependence of voltage-gated H^+ currents in human neutrophils, rat alveolar epithelial cells, and mammalian phagocytes. *The Journal of General Physiology*, 112(4), pp.503–522.

DeCoursey, T.E., Morgan, D. & Cherny, V.V., 2003. The voltage dependence of NADPH oxidase reveals why phagocytes need proton channels. *Nature*, 422(6931), pp.531–534.

Delaglio, F. *et al*., 1995. NMRPipe: a multidimensional spectral processing system based on UNIX pipes. *Journal of biomolecular NMR*, 6(3), pp.277–293.

Demaurex, N. *et al*., 1993. Proton Currents in Human Granulocytes - Regulation by Membrane-Potential and Intracellular pH. *The Journal of Physiology*, 466, pp.329–344.

Doyle, D.A. *et al*., 1998. The structure of the potassium channel: molecular basis of K^+ conduction and selectivity. *Science*, 280(5360), pp.69–77.

Dutzler, R., 2003. Gating the Selectivity Filter in ClC Chloride Channels. *Science*, 300(5616), pp.108–112.

Dutzler, R. *et al*., 2002. X-ray structure of a ClC chloride channel at 3.0 Å reveals the molecular basis of anion selectivity. *Nature*, 415(6869), pp.287–294.

Eisenberg, D. *et al*., 1984. Analysis of membrane and surface protein sequences with the hydrophobic moment plot. *Journal of Molecular Biology*, 179(1), pp.125–142.

Eytan, G., 1982. Use of liposomes for reconstitution of biological functions. *Biochimica et Biophysica Acta*, 694(2), pp.185–202.

Fedida, D. & Hesketh, J.C., 2001. Gating of voltage-dependent potassium channels. *Progress in Biophysics and Molecular Biology*, 75(3), pp.165–199.

Fellouse, F.A. *et al*., 2007. High-throughput generation of synthetic antibodies from highly functional minimalist phage-displayed libraries. *Journal of Molecular Biology*, 373(4), pp.924–940.

Fiolet, J.W., Bakker, E.P. & van Dam, K., 1974. The fluorescent properties of acridines in the presence of chloroplasts or liposomes. On the quantitative relationship between the fluorescence quenching and the transmembrane proton gradient. *Biochimica et Biophysica Acta*, 368(3), pp.432–445.

Fogel, M. & Hastings, J.W., 1972. Bioluminescence: mechanism and mode of control of scintillon activity. *Proceedings of the National Academy of Sciences*, 69(3), pp.690–693.

Fujiwara, Y. *et al*., 2012. The cytoplasmic coiled-coil mediates cooperative gating temperature sensitivity in the voltage-gated H^+ channel Hv1. *Nature communications*, 3, p.816.

Fujiwara, Y., Kurokawa, T. *et al*., 2013a. Gating of the designed trimeric/tetrameric voltage-gated H+ channel. *The Journal of Physiology*, 591(3), pp.627–640.

Fujiwara, Y., Kohei, T. *et al*., 2013b. Structural Characteristics of the Redox Sensing Coiled-coil in the Voltage-gated H+ Channel. *Journal of Biological Chemistry*, 288(25), pp.17968–17975.

Gatenby, R.A. & Gillies, R.J., 2007. Glycolysis in cancer: A potential target for therapy. *The International Journal of Biochemistry & Cell Biology*, 39(7-8), pp.1358–1366.

Giroux-Widemann, V. *et al*., 1991. Effects of pH on the reactivation of human spermatozoa demembranated with triton X-100. *Molecular Reproduction and Development*, 29(2), pp.157–162.

Goddard, T.D. & Kneller, D.G., SPARKY - NMR Assignment and Intergration Software. Available at: http://www.cgl.ucsf.edu/home/sparky/.

Goldberg, A.F. & Miller, C., 1991. Solubilization and functional reconstitution of a chloride channel from Torpedo californica electroplax. *The Journal of Membrane Biology*, 124(3), pp.199–206.

Goldman, D.E., 1943. Potential, Impedance, and Rectification in Membranes. *The Journal of General Physiology*, 27(1), pp.37–60.

González, C. *et al*., 2013. Molecular mechanism of voltage sensing in voltage-gated proton channels. *The Journal of General Physiology*, 141(3), pp.275–285.

González, C., Koch, H.P. & Larsson, H.P., 2010. Strong cooperativity between subunits in voltage-gated proton channels. *Nature Structural & Molecular Biology*, 17(1), pp.51–56.

Greenblatt, R.E., Blatt, Y. & Montal, M., 1985. The structure of the voltage-sensitive sodium channel. Inferences derived from computer-aided analysis of the Electrophorus electricus channel primary structure. *FEBS letters*, 193(2), pp.125–134.

Griffin, J.L. & Shockcor, J.P., 2004. Metabolic profiles of cancer cells. *Nature Reviews Cancer*, 4(7), pp.551–561.

Gunn, S.A. & Gould, T.C., 1958. Role of Zinc in Fertility and Fecundity in the Rat. *American Journal of Physiology*, 193(3), pp.505–508.

Guy, H.R. & Durell, S.R., 1994. Using sequence homology to analyze the structure and function of voltage-gated ion channel proteins. *Society of General Physiologists series*, 49, pp.197–212.

Hamamah, S. & Gatti, J.L., 1998. Role of the ionic environment and internal pH on sperm activity. *Human Reproduction*, 13(suppl 4), pp.20–30.

Harlow, E. & Lane, D.P., 1988. *Antibodies: A Laboratory Manual*, CSHL Press.

Heginbotham, L., Kolmakova-Partensky, L. & Miller, C., 1998. Functional reconstitution of a prokaryotic K^+ channel. *The Journal of General Physiology*, 111(6), pp.741–749.

Hille, B., 2001. *Ion Channels of Excitable Membranes* Third, Sunderland, MA: Sinauer Associates, Inc.

Hilty, C. *et al*., 2004. Membrane protein-lipid interactions in mixed micelles studied by NMR spectroscopy with the use of paramagnetic reagents. *Chembiochem*, 5(4), pp.467–473.

Ho, B.K. & Gruswitz, F., 2008. HOLLOW: generating accurate representations of channel and interior surfaces in molecular structures. *BMC Structural Biology*, 8, p.49.

Hodgkin, A.L. & Huxley, A.F., 1952a. A quantitative description of membrane current and its application to conduction and excitation in nerve. *The Journal of Physiology*, 117(4), pp.500–544.

Hodgkin, A.L. & Huxley, A.F., 1952b. Currents carried by sodium and potassium ions through the membrane of the giant axon of Loligo. *The Journal of Physiology*, 116(4), pp.449–472.

Hodgkin, A.L. & Huxley, A.F., 1952c. The components of membrane conductance in the giant axon of Loligo. *The Journal of Physiology*, 116(4), pp.473–496.

Hodgkin, A.L. & Huxley, A.F., 1952d. The dual effect of membrane potential on sodium conductance in the giant axon of Loligo. *The Journal of Physiology*, 116(4), pp.497–506.

Hodgkin, A.L. & Katz, B., 1949. The effect of sodium ions on the electrical activity of the giant axon of the squid. *The Journal of Physiology*, 108(1), pp.37–77.

Jiang, Y. *et al*., 2002. Crystal structure and mechanism of a calcium-gated potassium channel. *Nature*, 417(6888), pp.515–522.

Jiang, Y., Lee, A., *et al*., 2003a. X-ray structure of a voltage-dependent K^+ channel. *Nature*, 423(6935), pp.33–41.

Jiang, Y., Ruta, V., *et al*., 2003b. The principle of gating charge movement in a voltage-dependent K+ channel. *Nature*, 423(6935), pp.42–48.

Kapus, A. *et al*., 1993. A pH-Sensitive and Voltage-Dependent Proton Conductance in the Plasma-Membrane of Macrophages. *Journal of General Physiology*, 102(4), pp.729–760.

Kawate, T. & Gouaux, E., 2006. Fluorescence-detection size-exclusion chromatography for precrystallization screening of integral membrane proteins. *Structure*, 14(4), pp.673–681.

Knowles, H.J. & Harris, A.L., 2001. Hypoxia and oxidative stress in breast cancer. Hypoxia and tumourigenesis. *Breast cancer research : BCR*, 3(5), pp.318–322.

Koch, H.P. *et al*., 2008. Multimeric nature of voltage-gated proton channels. *Proceedings of the National Academy of Sciences of the United States of America*, 105(26), pp.9111–9116.

Kohout, S.C. *et al*., 2008. Subunit organization and functional transitions in Ci-VSP. *Nature Structural & Molecular Biology*, 15(1), pp.106–108.

Lee, S.-Y. *et al*., 2005. Structure of the KvAP voltage-dependent K^+ channel and its dependence on the lipid membrane. *Proceedings of the National Academy of Sciences of the United States of America*, 102(43), pp.15441–15446.

Lee, S.-Y., Banerjee, A. & Mackinnon, R., 2009a. Two separate interfaces between the voltage sensor and pore are required for the function of voltage-dependent K^+ channels. *PLoS biology*, 7(3), p.e47.

Lee, S.-Y., Letts, J.A. & Mackinnon, R., 2008. Dimeric subunit stoichiometry of the human voltage-dependent proton channel Hv1. *Proceedings of the National Academy of Sciences of the United States of America*, 105(22), pp.7692–7695.

Lee, S.-Y., Letts, J.A. & Mackinnon, R., 2009b. Functional reconstitution of purified human Hv1 H^+ channels. *Journal of Molecular Biology*, 387(5), pp.1055–1060.

Li, S.J. *et al*., 2010. The Role and Structure of the Carboxyl-terminal Domain of the Human Voltage-gated Proton Channel Hv1. *Journal of Biological Chemistry*, 285(16), pp.12047–12054.

Lishko, P.V. & Kirichok, Y., 2010. The role of Hv1 and CatSper channels in sperm activation. *The Journal of Physiology*, 588, pp.4667-4672.

Lishko, P.V. *et al*., 2010. Acid extrusion from human spermatozoa is mediated by flagellar voltage-gated proton channel. *Cell*, 140(3), pp.327–337.

Lishko, P.V. *et al*., 2012. The control of male fertility by spermatozoan ion channels. *Annual Review of Physiology*, 74, pp.453–475.

Long, S.B. *et al*., 2007. Atomic structure of a voltage-dependent K^+ channel in a lipid membrane-like environment. *Nature*, 450(7168), pp.376–382.

Long, S.B., Campbell, E.B. & Mackinnon, R., 2005. Crystal structure of a mammalian voltage-dependent Shaker family K^+ channel. *Science*, 309(5736), pp.897–903.

Lupas, A., Van Dyke, M. & Stock, J., 1991. Predicting coiled coils from protein sequences. *Science*, 252(5009), pp.1162–1164.

Mackinnon, R., 1991. Determination of the subunit stoichiometry of a voltage-activated potassium channel. *Nature*, 350(6315), pp.232–235.

Mackinnon, R. & Miller, C., 1989. Mutant potassium channels with altered binding of charybdotoxin, a pore-blocking peptide inhibitor. *Science*, 245(4924), pp.1382–1385.

Mackinnon, R. & Yellen, G., 1990. Mutations affecting TEA blockade and ion permeation in voltage-activated K^+ channels. *Science*, 250(4978), pp.276–279.

Mackinnon, R., Heginbotham, L. & Abramson, T., 1990. Mapping the receptor site for charybdotoxin, a pore-blocking potassium channel inhibitor. *Neuron*, 5(6), pp.767–771.

Mahaut-Smith, M., 1989. The effect of zinc on calcium and hydrogen ion currents in intact snail neurones. *Journal of Experimental Biology*, 145, pp.455–464.

Marsh, M.E., 1999. Biomineralization in coccolithophores. *Gravitational and space biology bulletin : publication of the American Society for Gravitational and Space Biology*, 12(2), pp.5–14.

Maruyama, M., 2000. Crystal Structures of the Transposon Tn5-carried Bleomycin Resistance Determinant Uncomplexed and Complexed with Bleomycin. *Journal of Biological Chemistry*, 276(13), pp.9992–9999.

McCoy, A.J. *et al*., 2007. Phaser crystallographic software. *Journal of Applied Crystallography*, 40(4), pp.658–674.

Minor, W. *et al*., 2006. HKL-3000: the integration of data reduction and structure solution – from diffraction images to an initial model in minutes. *Acta Crystallographica Section D Biological Crystallography*, 62(8), pp.859–866.

Moffat, J.C. *et al*., 2008. Proton transport through influenza A virus M2 protein reconstituted in vesicles. *Biophysical Journal*, 94(2), pp.434–445.

Murata, K. *et al*., 2000. Structural determinants of water permeation through aquaporin-1. *Nature*, 407(6804), pp.599–605.

Musset, B. *et al*., 2011. Aspartate 112 is the selectivity filter of the human voltage-gated proton channel. *Nature*, 480, pp.273–278.

Musset, B. *et al*., 2008. Detailed comparison of expressed and native voltage-gated proton channel currents. *The Journal of Physiology*, 586(10), pp.2477–2486.

Musset, B., Capasso, M., *et al*., 2010a. Identification of Thr29 as a critical phosphorylation site that activates the human proton channel Hvcn1 in leukocytes. *Journal of Biological Chemistry*, 285(8), pp.5117–5121.

Musset, B., Smith, S.M.E., *et al*., 2010b. Zinc inhibition of monomeric and dimeric proton channels suggests cooperative gating. *The Journal of Physiology*, 588(Pt 9), pp.1435–1449.

Nelson, R.D. *et al*., 1999. Modular assembly of voltage-gated channel proteins: a sequence analysis and phylogenetic study. *Journal of Molecular Microbiology and Biotechnology*, 1(2), pp.281–287.

Neri, D. *et al*., 1989. Stereospecific nuclear magnetic resonance assignments of the methyl groups of valine and leucine in the DNA-binding domain of the 434 repressor by biosynthetically directed fractional 13C labeling. *Biochemistry*, 28(19), pp.7510–7516.

Nernst, W., 1889. Die elektromotorische Wirksamkeit der Ionen. *Die Ziele der physikalischen Chemie*, 4, pp.129–181.

Nernst, W., 1888. Zur Kinetik in Losung befindlichen Korper. Theorie der Diffusion. *Die Ziele der physikalischen Chemie*, 2(9), pp.613–637.

Noda, M. *et al*., 1984. Primary structure of Electrophorus electricus sodium channel deduced from cDNA sequence. *Nature*, 312(5990), pp.121–127.

Paasche, E., 2001. A review of the coccolithophorid Emiliania huxleyi (Prymnesiophyceae), with particular reference to growth, coccolith formation, and calcification-photosynthesis interactions. *Phycologia*, 40(6), pp.503–529.

Payandeh, J. *et al*., 2012. Crystal structure of a voltage-gated sodium channel in two potentially inactivated states. *Nature*, 486(7401), pp.135–139.

Payandeh, J. *et al*., 2011. The crystal structure of a voltage-gated sodium channel. *Nature*, 475(7356), pp.353–358.

Perozo, E. *et al*., 1993. Gating Currents From a Nonconducting Mutant Reveal Open-Closed Conformations in Shaker K^+ Channels. *Neuron*, 11(2), pp.353–358.

Perozo, E. *et al*., 1992. Gating currents in Shaker K^+ channels. Implications for activation and inactivation models. *Biophysical Journal*, 62(1), pp.160–171.

Persson, H. *et al*., 2013. CDR-H3 diversity is not required for antigen recognition by synthetic antibodies. *Journal of Molecular Biology*, 425(4), pp.803–811.

Perutz, M.F., 1989. Mechanisms of cooperativity and allosteric regulation in proteins. *Quarterly Reviews of Biophysics*, 22(2), pp.139–237.

Pinto, L.H., Holsinger, L.J. & Lamb, R.A., 1992. Influenza virus M2 protein has ion channel activity. *Cell*, 69(3), pp.517–528.

Post, R.L., Hegyvary, C. & Kume, S., 1972. Activation by adenosine triphosphate in the phosphorylation kinetics of sodium and potassium ion transport adenosine triphosphatase. *The Journal of Biological Chemistry*, 247(20), pp.6530–6540.

Qiu, F. *et al*., 2013. Subunit Interactions during Cooperative Opening of Voltage-Gated Proton Channels. *Neuron*, 77(2), pp.288–298.

Ramsey, I.S. *et al*., 2006. A voltage-gated proton-selective channel lacking the pore domain. *Nature*, 440(7088), pp.1213–1216.

Rand, R.P. & Parsegian, V.A., 1989. Hydration forces between phospholipid bilayers. *Biochimica et Biophysica Acta*, 988(3), pp.351–376.

Rasmussen, S.G.F. *et al*., 2010. Structure of a nanobody-stabilized active state of the β2 adrenoceptor. *Nature*, 469(7329), pp.175–180.

Rehm, H. & Tempel, B.L., 1991. Voltage-gated K^+ channels of the mammalian brain. *FASEB J*, 5(2), pp.164–170.

Richard, S.B. *et al*., 2001. Structure of 4-diphosphocytidyl-2-C-methylerythritol synthetase involved in mevalonate- independent isoprenoid biosynthesis. *Nature Structural Biology*, 8(7), pp.641–648.

Rosenbaum, D.M. *et al*., 2007. GPCR engineering yields high-resolution structural insights into β2-adrenergic receptor function. *Science*, 318(5854), pp.1266–1273.

Rost, B. & Riebesell, U., 2004. Coccolithophores and the biological pump: responses to environmental changes. In *Coccolithophores*. Berlin, Heidelberg: Springer Berlin Heidelberg, pp. 99–125.

Saaranen, M. *et al*., 1987. Lead, magnesium, selenium and zinc in human seminal fluid: comparison with semen parameters and fertility. *Human reproduction (Oxford, England)*, 2(6), pp.475–479.

Sakata, S. *et al*., 2010. Functionality of the voltage-gated proton channel truncated in S4. *Proceedings of the National Academy of Sciences of the United States of America*, 107(5), pp.2313–2318.

Sasaki, M., Takagi, M. & Okamura, Y., 2006. A voltage sensor-domain protein is a voltage-gated proton channel. *Science*, 312(5773), pp.589–592.

Schrödinger LLC, The PyMol Molecular Graphics System.

Schuel, H. & Burkman, L.J., 2005. A tale of two cells: endocannabinoid-signaling regulates functions of neurons and sperm. *Biology of Reproduction*, 73(6), pp.1078–1086.

Schwem, B.E. & Fillingame, R.H., 2006. Cross-linking between helices within subunit a of Escherichia coli ATP synthase defines the transmembrane packing of a four-helix bundle. *The Journal of Biological Chemistry*, 281(49), pp.37861–37867.

Seoh, S.A. *et al*., 1996. Voltage-sensing residues in the S2 and S4 segments of the Shaker K^+ channel. *Neuron*, 16(6), pp.1159–1167.

Shapova, Y.A. & Paetzel, M., 2007. Crystallographic analysis of Bacillus subtilis CsaA. *Acta Crystallographica Section D Biological Crystallography*, 63(Pt 4), pp.478–485.

Sharp, L.L., Zhou, J. & Blair, D.F., 1995. Features of MotA proton channel structure revealed by tryptophan-scanning mutagenesis. *Proceedings of the National Academy of Sciences of the United States of America*, 92(17), pp.7946–7950

Sidhu, S.S., Lowman, H.B. & Cunningham, B.C., 2000. Phage display for selection of novel binding peptides. *Methods in enzymology*, 328, pp.333–363.

Smith, S.M.E. *et al*., 2011. Voltage-gated proton channel in a dinoflagellate. *Proceedings of the National Academy of Sciences of the United States of America*, 108(44), pp.18162–18167.

Sokolov, S., Scheuer, T. & Catterall, W.A., 2005. Ion permeation through a voltage-sensitive gating pore in brain sodium channels having voltage sensor mutations. *Neuron*, 47(2), pp.183–189.

Starace, D. & Bezanilla, F., 2004. A proton pore in a potassium channel voltage sensor reveals a focused electric field. *Nature*, 427(6974), pp.548–553.

Strong, M. *et al*., 2006. Toward the structural genomics of complexes: crystal structure of a PE/PPE protein complex from Mycobacterium tuberculosis. *Proceedings of the National Academy of Sciences of the United States of America*, 103(21), pp.8060–8065.

Taglialatela, M. & Stefani, E., 1993. Gating currents of the cloned delayed-rectifier K^+ channel DRK1. *Proceedings of the National Academy of Sciences of the United States of America*, 90(10), pp.4758–4762.

Tamura, M. *et al*., 1988. The superoxide-generating respiratory burst oxidase of human neutrophil plasma membrane. Phosphatidylserine as an effector of the activated enzyme. *The Journal of Biological Chemistry*, 263(33), pp.17621–17626.

Tao, X. *et al*., 2010. A gating charge transfer center in voltage sensors. *Science*, 328(5974), pp.67–73.

Taylor, A.R. *et al*., 2011. A Voltage-Gated H^+ Channel Underlying pH Homeostasis in Calcifying Coccolithophores P. G. Falkowski, ed. *PLoS Biology*, 9(6), p.e1001085.

Tempel, B.L. *et al*., 1987. Sequence of a probable potassium channel component encoded at Shaker locus of Drosophila. *Science*, 237(4816), pp.770–775.

Thomas, R.C. & Meech, R.W., 1982. Hydrogen ion currents and intracellular pH in depolarized voltage-clamped snail neurones. *Nature*, 299(5886), pp.826–828.

Tombola, F. *et al*., 2010. The opening of the two pores of the Hv1 voltage-gated proton channel is tuned by cooperativity. *Nature Structural & Molecular Biology*, 17(1), pp.44–50.

Tombola, F. *et al*., 2006. The twisted ion-permeation pathway of a resting voltage-sensing domain. *Nature*, 445(7127), pp.546–549.

Tombola, F., Pathak, M.M. & Isacoff, E.Y., 2005. Voltage-Sensing Arginines in a Potassium Channel Permeate and Occlude Cation-Selective Pores. *Neuron*, 45(3), pp.379–388.

Tombola, F., Ulbrich, M.H. & Isacoff, E.Y., 2008. The Voltage-Gated Proton Channel Hv1 Has Two Pores, Each Controlled by One Voltage Sensor. *Neuron*, 58(4), pp.546–556.

Tugarinov, V., Kanelis, V. & Kay, L.E., 2006. Isotope labeling strategies for the study of high-molecular-weight proteins by solution NMR spectroscopy. *Nature Protocols*, 1(2), pp.749–754.

Venters, R.A. *et al*., 1996. Characterizing the use of perdeuteration in NMR studies of large proteins: ^{13}C, ^{15}N and ^{1}H assignments of human carbonic anhydrase II. *Journal of Molecular Biology*, 264(5), pp.1101–1116.

Wang, Y. *et al*., 2012. Clinicopathological and biological significance of human voltage-gated proton channel Hv1 over-expression in breast cancer. *Journal of Biological Chemistry*, 287(7), pp.13877-13888.

Wang, Y. *et al*., 2011. Specific expression of the human voltage-gated proton channel Hv1 in highly metastatic breast cancer cells, promotes tumor progression and metastasis. *Biochemical and Biophysical Research Communications*, 412(2), pp.353–359.

Wang, Y., Wu, X., *et al*., 2013a. Human voltage-gated proton channel Hv1: a new potential biomarker for diagnosis and prognosis of colorectal cancer. *PLoS ONE*, 8(8), p.e70550.

Wang, Y., Zhang, S. & Li, S.J., 2013b. Zn^{2+} induces apoptosis in human highly metastatic SHG-44 glioma cells, through inhibiting activity of the voltage-gated proton channel Hv1. *Biochemical and Biophysical Research Communications*, 438(2), pp.312–317.

Warkentin, E. *et al*., 2001. Structures of F420H2:$NADP^+$ oxidoreductase with and without its substrates bound. *The EMBO journal*, 20(23), pp.6561–6569.

Winn, M.D. *et al*., 2011. Overview of the CCP4 suite and current developments. *Acta Crystallographica Section D Biological Crystallography*, 67(Pt 4), pp.235–242.

Winter, A. & Siesser, W.G., 1994. Coccolithophores. *Coccolithophores, Edited by Amos Winter and William G. Siesser, pp. 252. ISBN 0521380502. Cambridge, UK: Cambridge University Press,* July 1994.

Wishart, D.S. & Case, D.A., 2001. Use of chemical shifts in macromolecular structure determination. *Methods in enzymology*, 338, pp.3–34.

Yaroshchuk, A.E., 2000. Dielectric exclusion of ions from membranes. *Advances in colloid and interface science*, 85(2-3), pp.193–230.

Yellen, G. *et al*., 1991. Mutations affecting internal TEA blockade identify the probable pore-forming region of a K^+ channel. *Science*, 251(4996), pp.939–942.

Yu, F.H. & Catterall, W.A., 2004. The VGL-chanome: a protein superfamily specialized for electrical signaling and ionic homeostasis. *Science's STKE : signal transduction knowledge environment*, 2004(253), p.re15.

Yu, H. & Oprian, D.D., 1999. Tertiary interactions between transmembrane segments 3 and 5 near the cytoplasmic side of rhodopsin. *Biochemistry*, 38(37), pp.12033–12040.

Zhang, J. & Forgac, M., 1994. Proton conduction and bafilomycin binding by the V_o domain of the coated vesicle V-ATPase. *Journal of Biological Chemistry*, 269(38), pp.23518–23523.

Zhang, X. *et al*., 2012. Crystal structure of an orthologue of the NaChBac voltage-gated sodium channel. *Nature*, 486(7401), pp.130–134.

Zhou, Y. *et al*., 2001. Chemistry of ion coordination and hydration revealed by a K^+ channel-Fab complex at 2.0 A resolution. *Nature*, 414(6859), pp.43–48.